SAPIENZA
UNIVERSITÀ DI ROMA

Faculty of Mathematical, Physical and Natural Sciences
Doctorate in Earth Science (XXVI Course)

Patrizio Petricca

Control of geometry and kinematics on the state of stress of subduction zones: an application to the Mediterranean region.

Dissertation for the Degree of Doctor of Philosophy

January 24, 2014

Sapienza Universitá di Roma
Dipartimento di Scienze della Terra

Advisor:
Prof. Eugenio Carminati

Referee:
Prof. Guido Gosso

Referee:
Prof. Ana M. M. Negredo

Ph.D. Thesis by
Patrizio Petricca

mail to: patrizio.petricca@uniroma1.it

Sapienza - Università di Roma
Dipartimento di Scienze della Terra
P.le Aldo Moro 5, 00185 Roma
Italy

A Chiara
complice di Tutto...

Contents

1

Introduction

Knowing the stress field at subduction zones is fundamental as here is released most of the seismic energy in the Earth [e.g. *Pacheco and Sykes*, 1992]. In particular, most $M_W > 8.0$ earthquakes (Figure 1.1) originate at shallow depths along the frictional interface between subducting and overriding plates [e.g., *Scholz*, 2002]. This observation emphasizes the crucial role played by the geologic-time scale dynamics of convergent margins over the short-time scale seismogenic processes. Despite an obvious relevance to seismic hazard, knowing the driving forces generating the stress field at subduction zones is a long-standing problem.

In this thesis, by means of 2D and 3D numerical viscoelastic models, I simulated the stress field in convergent plate margins to evaluate which properties control subduction dynamics. Models are built to evaluate the contribution of plate kinematics, geometry of the system, rheology and gravitational forces to the definition of the present-day stress field at different subduction zones. This has been achieved with the development of several sets of generic (i.e., not simulating specific subduction zones) 2D and 3D models. The aim is to analyze the interaction between the subducted slabs and the geodynamic forces (e.g., slab pull, mantle flow, plate convergence) that stress the system, to reproduce the observed stress fields measured in different subduction zones worldwide for both the upper and lower plates at crustal depths and for intermediate and deep subducted lithosphere. The interaction between subducting slabs and the viscosity jump at upper-lower mantle transition has been also investigated. Although generic, model geometries are consistent with natural geometries observed in real subduction zones worldwide. Modelling results are compared with stress data available in the world stress map database for different convergent margins.

To define the stress field affecting the subducting plates, special attention must be paid to the choice of the righteous initial parameters, since from them depend the delicate balance between the applied tectonic

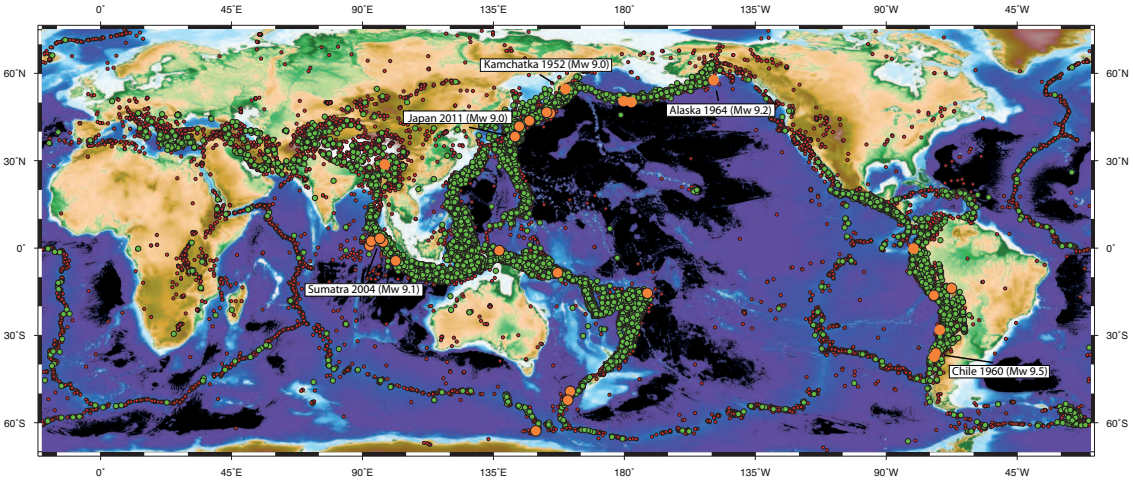

Fig. 1.1. Worldwide topo-bathymetric map (data from NOAA - etopo1) and $M_W > 5.5$ seismicity distribution for the 1973-2013 period. Hypocenters of shallow (red dots), deep (green dots) and with $M_W > 8.0$ (orange dots) earthquakes are from the NEIC catalog (http://neic.usgs.gov). The five greatest earthquakes of the last century are emphasized by the text boxes.

forces and the geometric characteristics of the whole system. For this reason and to validate or reject the observations made for the general cases, the central Mediterranean subduction system was chosen to model a natural subduction zone.

Building and constraining a model requires the knowledge of the real system. Subduction zones are primarily described by their geometry, and today the slab interfaces in the Mediterranean are still uncertain. I defined them reviewing and integrating literature data from various disciplines, collecting geometries into a specifically designed database. Unlike similar databases already available in the literature [e.g., *Heuret and Lallemand*, 2005; *Hayes et al.*, 2012], in the database that I contributed to build the subduction interfaces are fully-parametrized, i.e., characterized by geometric (strike, dip, depth), kinematics and dynamic (rake, slip rate, seismic coupling, maximum earthquake magnitude) parameters. The database so designed, and its on-line publication makes it a valuable tool for the geometric description of active subductions in the Mediterranean area and provide the basis to investigate their seismic hazard.

Thesis outline

In chapter 2, I explain briefly the state of knowledge about the evolution of subduction zones, reviewing the available theories and observations regarding the issues explored in this thesis.

Chapter 3, after an introduction on the state of the art, describes the fundamentals of the finite element method, its application to viscoelastic modelling and the description of the models developed for this thesis.

The results obtained for the generic plate scale models, are described in chapter 4. A comparison between model results and stress data from natural subductions is also provided.

In Chapter 5 the stress field of the Calabrian and Hellenic subductions is reproduced with 3D models. The model geometry of the subductions in the Mediterranean area was constrained using the subduction layer of the database SHARE http://diss.rm.ingv.it/share-edsf/, which I contributed to build. The database is described in appendix A. The results are then compared with all available data.

The conclusions follow in Chapter 6

2

Geodynamic problem

Guideline to the chapter contents

Subduction zones dynamics boasts a huge literature that explores the countless searchable aspects. Such attention arises from the fact that the subduction process is a prime actor in plate tectonics. Convergent margins evolution involves a complex and delicate interplay of active forces and the physical-geometrical parameters. In the following discussion, after a brief introduction, I review the more suitable theories and observations, regarding the issues explored in this thesis. In section 2.2 geometry and dynamics of subducting lithosphere, closely interconnected controlling factors of subduction zones evolution, are discussed. As here the research focuses on the stress field, the knowledges on this topic are widely covered in section 2.3, both regarding the lower plate (section 2.3.1) and the shallow intraplate stress in the upper plate (section 2.3.2). Subduction zone processes requires an accurate quantification of the velocities of the plates and their boundaries. The dynamics of a plate boundary can be thought in a simple relative way considering how one of the two involved plate moves respect to the other, but remains primary controlled by the absolute plate motion relative to the underlying mantle. These topics will be discussed in section 2.4.

2.1 Evolution of convergent margins

2.1.1 Introduction

The evolution of geodynamic systems characterized by plate convergence depends on the balance of driving and resisting forces (Figure 2.1), how these forces change with depth and time, and on its geometry, in turn controlled by plate-scale processes. Driving forces include drag forces, when enhancing plate convergence [e.g., *Davies*, 1977; *Hager and O'connell*, 1978], negative buoyancy forces (i.e., slab pull [e.g., *Forsyth and Uyeda*, 1975; *Davies and Stevenson*, 1992; *Schellart et al.*, 2004]) due to thermal anomalies, metamorphic processes (e.g., basalt-to-eclogite transformation at $\simeq$ 100-250 km [*Ahrens and Schubert*, 1975]), including dehydration, or phase transitions (olivine to-wadsleyite at 410 km [e.g., *Marton et al.*, 1999; *Conrad and Hager*, 1999]). Resisting forces include bending of the lithosphere [e.g., *Buffett*, 2006], frictional and viscous shear forces [*Gurnis et al.*, 2004; *Royden and Husson*, 2006], drag forces, when contrasting plate convergence, positive buoyancy forces again related to phase transitions (serpentinization [*Christensen*, 2004; *Wada et al.*, 2008]; metastable olivine wedge [*Bina et al.*, 2001]; ringwoodite-to-perovskite plus magnesiowustite at 660 km [*Torii and Yoshioka*, 2007]) and anchoring of deepest part of the slab as it penetrates into the more viscous lower mantle [e.g., *Christensen*, 1996; *Goes et al.*, 2008; *Rodríguez-González et al.*, 2009].

In addition, large-scale and local mantle flows also affect the sinking rate and geometry of subducting lithosphere. The weight of each of the driving and resisting forces depends on numerous parameters: e.g., the age of the subducting lithosphere, the rheology and nature (i.e., continental or oceanic) of the plates, the sinking rate, the duration of subduction.

Small changes in the equilibrium among these parameters, principally result in different subduction geometries (see next section) and state of stress (see section 2.3) affecting the lithosphere.

Should not be forgotten that some criticisms are moved in the literature to the real efficiency of the slab pull force [*Doglioni et al.*, 2007]. Recently *Brandmayr et al.* [2011] proposed a new density model for the lithosphere in Italy finding no evidences of negative buoyancy of the subducting slabs with respect to the surrounding mantle. This finding agrees with previous studies [e.g., *Kelly et al.*, 2003; *Anderson*, 2011] in the downgrading of the slab pull as a driving force.

2.2 Geometry and dynamics of subduction

With the huge amount of tomographic studies in subduction zones, it is becoming clear that subducted slabs are not simple 2D features. For example, not only subducted slab shape changes along-dip, but slab dip varies along the length of many arcs, and slab tears, slab windows and detachments [*Carminati et al.*, 1998; *Wortel and Spakman*, 2000; *Faccenna et al.*, 2006] often deform the subducted lithosphere. At least, slab geometry must be described by its dip, lateral extent) and shape (i.e., straight or curved). Although the long term evolution of subduction zones is beyond the scope of this thesis, a brief review of the processes controlling the subduction geometry follows.

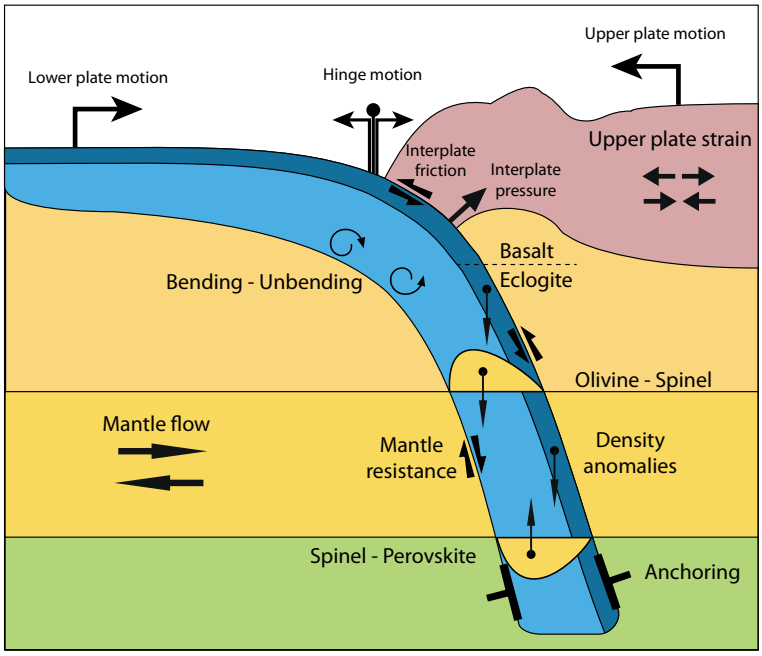

Fig. 2.1. Principal driving and resisting forces for subducting lithosphere. Phase change depths affecting the density of rocks are also indicated. Possible plate kinematics, mantle motions and upper plate strain are indicated by arrows.

Significant effort has been spent in the literature to correlate slab dip with a variety of observables related to subduction zones. *Jarrard* [1986] found for subductions two interesting relations: 1) an excellent correlation between the slab length and the product of the convergence rate and the age of the down-going lithosphere; 2) the subduction of young (i.e., hot and buoyant) lithosphere results in strong coupling between the plates (enhancing higher magnitude earthquakes) compared with that associated with the subduction of old (i.e., cold and heavy) lithosphere. *Cruciani et al.* [2005] re-examined the global correlation

for slab dip finding that slab age and plate convergence rate correlate with slab dip better than slab age or plate convergence rate individually. The relationship between trench rollback and slab age has been examined in a number of studies with conflicting results. There is also a difference in the average dip between slabs where the overriding plate is continental (shallower subductions) or oceanic (steeper subductions) [*Furlong et al.*, 1982; *Jarrard*, 1986; *Lallemand et al.*, 2005]. The slab shape depends also on overridding plate thermal state [*Roda et al.*, 2011; *Rodríguez-González et al.*, 2012]. *Faccenna et al.* [2007] proposed that the motion of the trenches represent the surface manifestation of the resistance encountered by the sinking lithosphere to bend and penetrate within the upper mantle.

The evident differences between shallow and steep subduction zones were used in the literature to discriminate two end member subduction styles: the Chilean-type and the Mariana-type (Figure 2.2) subductions [*Dickinson*, 1978; *Uyeda*, 1981]. In addition to the difference in the slab dip-angle [e.g., *Ricard et al.*, 1991; *Doglioni*, 1993; *Doglioni et al.*, 1999; *Cruciani et al.*, 2005; *Carminati and Doglioni*, 2012], the reverse characteristics from each of the two classes (Chilean vs Mariana) are respectively [*Doglioni et al.*, 2007, and references therein]: maximum depth of seismicity (300 km vs 700 km); state of stress in the back-arc region (compressive vs extensional); state of stress in the slab at intermediate depths (down-dip tensional vs down-dip compressional); structural elevation and vergence of the accretionary wedge (low-elevated single-verging vs high-elevated double-verging); subsidence rate in the foredeep (low vs high); thin- vs thick-skinned tectonics.

Faccenna et al. [2013] have recently proposed that two end-members of subduction exist. The slab-pull type characterized by subduction confined to the upper mantle, rollback trench motion and moderately thick crustal stacks, and the slab-suction type where whole-mantle convection leads to largely thickened crust due to higher drag of plates toward each other.

The asymmetry between the various subduction zones has been related to the efficiency of the slab gravitational pull [e.g., *Anderson*, 2001] or to the differential motion between the mantle and lithosphere [e.g., *Doglioni*, 1990; *Scoppola et al.*, 2006]. As the plates describe an average west-directed global flow [*Doglioni*, 1990; *Doglioni et al.*, 1999], the Chilean-type and Mariana-type subductions are the best example of eastward-dipping (i.e., slab sustained by the relative east-ward mantle flow) and westward-dipping (i.e., slab countered by the relative east-ward mantle flow) subductions (see section 2.4 for further explanation).

Looking at the third dimension, as a matter of fact both arcuate and straight subduction zones exist (Figures 2.3 and 2.4). *Frank* [1968] first noted that the curvature of subduction zone trenches and arcs varies considerably on Earth (Figure 2.3) from concave toward the mantle wedge (e.g., Aleutians-Alaska [figure

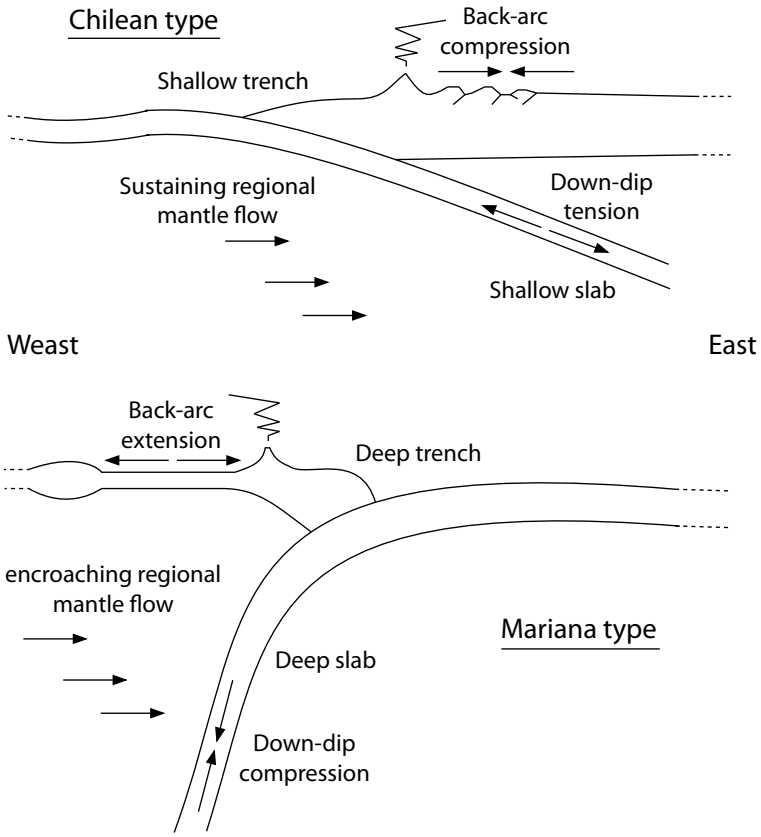

Fig. 2.2. End-member types of subduction zones (after *Uyeda and Kanamori* [1979]), based on the geometry, the subduction direction relative to the mantle flow and the stress field affecting the upper and the lower plates.

2.4a], Scotia, Calabria, Hellenic, North Ryukyu [figure 2.4c], Marianas [figure 2.4f], Sumatra [figure 2.4g]) to straight (e.g., Tonga-Kermadec, South Solomon [figure 2.4b], Central America [figure 2.4d], Vanuatu [figure 2.4e]) to convex (e.g., North Solomon [figure 2.4b], South Ryukyu [figure 2.4c], Central-South America [figure 2.4h], Cascadia). Numerous mechanisms have been proposed to explain the arc-shaped nature of subduction zones: resistance to subduction for relatively buoyant lithosphere [e.g., subduction of aseismic ridge, oceanic plateau, or continental crust; *Vogt*, 1973; *Hsui and Youngquist*, 1985; *Malinverno and Ryan*, 1986]; lateral variations in subduction interface coupling [*Mart et al.*, 2005]; slab rollback-induced toroidal return flow around lateral slab edges [*Faccenna et al.*, 2004; *Schellart et al.*, 2004; *Stegman et al.*, 2006; *Morra et al.*, 2006; *Schellart et al.*, 2007; *Loiselet et al.*, 2009]. According to *Mahadevan et al.* [2010], arcuate arcs occur in steeply dipping lithosphere (i.e., Mariana-type), and straight arcs in shallow dipping lithosphere (i.e., Chilean-type). The most significant exception to these observation is the Tonga-Kermadec subduction zone, straight-shaped and convex trench-ward despite the high angle slab.

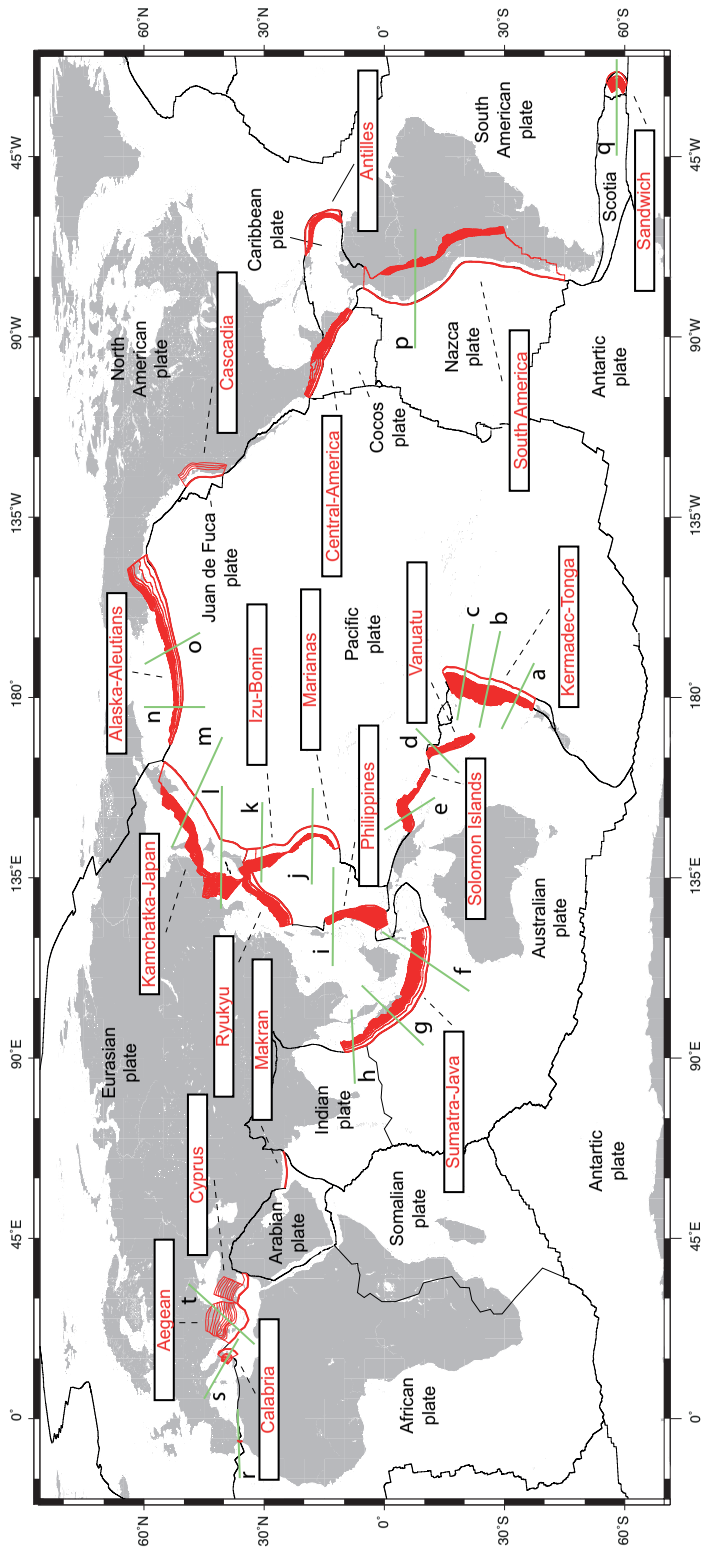

Fig. 2.3 (caption in the next page)

Fig. 2.3. Active subduction zones (red lines and contours) and major plate boundaries (black lines). Calabria, Aegean and Cyprus slab contours are from the SHARE-edsf database (http://diss.rm.ingv.it/SHARE-edsf/). Antilles and South-Philippines slab contours are from the RUM-database (http://rses.anu.edu.au/seismology/projects/RUM/). The remaining subduction contours are from the slab 1.0 database (http://earthquake.usgs.gov/research/data/slab/). The name of the subduction systems are reported in the text boxes. Green lines indicate the location of the sections showed in figure 2.5.

Subduction zones and their associated slabs are limited in lateral extent (250-7400 km). Their three-dimensional geometry evolves over time [*Schellart et al.*, 2007] and can often be quite complex [*Jadamec and Billen*, 2010]. In addition, complex patterns of mantle circulation can develop above slabs [*Honda and Saito*, 2003; *Zhu et al.*, 2009].

Slab width controls two first-order features of plate tectonics: the curvature of subduction zones and their tendency to retreat backwards with time. *Schellart et al.* [2007] proposed that the trench migration rate is inversely related to slab width and depends on the proximity to a lateral slab edge. *Schellart et al.* [2004], *Stegman et al.* [2006] and *Morra et al.* [2006] found that, with progressive slab rollback of narrow to intermediate-width slabs, an arc concave toward the mantle wedge develops. *Schellart et al.* [2007] showed that the slabs with intermediate widths (2000 km) tend to be stationary and straight. There is no relation between radius of subduction zone curvature and slab dip angle. The radius of trench curvature progressively decreases with continuous trench retreat, but starts to increase when trench retreat changes to trench advance [*Schellart et al.*, 2011]. Regardless of the the proposed controlling factor, the along-strike slab geometry appears to be first related to the hinge motion, i.e., it shows respectively a concave or convex shape toward the mantle wedge in case of retreating or advancing trenches. A straight shaped slab evolves in case of stationary trenches.

High-resolution seismic tomography models [e.g., *van der Hilst et al.*, 1997; *van der Hilst*, 1995; *Grand*, 1994; *Widiyantoro et al.*, 1999] suggest various scenarios for deep slab behavior and slab interaction with the transition zone (at 670 km; Figure 2.5). In some subduction zones slabs are observed to penetrate through the upper-lower mantle boundary without any significant deformation (e.g., Kermadec, Java, central America). In other subductions, slabs are horizontally deflected by the boundary (Tonga, Izu-Bonin). Once slabs reach the top of the lower mantle, slab-dip angles can become progressively shallower or steeper if there is an advancing-retreating trench migration [e.g., *Faccenna et al.*, 2001a] because the slab becomes anchored in the higher-viscosity lower mantle. By way of example, seismic tomography has been used to image the slab beneath the Mariana arc penetrating vertically into the lower mantle, whereas beneath the Izu-Bonin arc the slab appears to be deflected horizontally on top of the 670 km interface [*Zhou and Clayton*, 1990; *Fukao et al.*, 1992; *van der Hilst and Seno*, 1993; *Gudmundsson and Sambridge*, 1998;

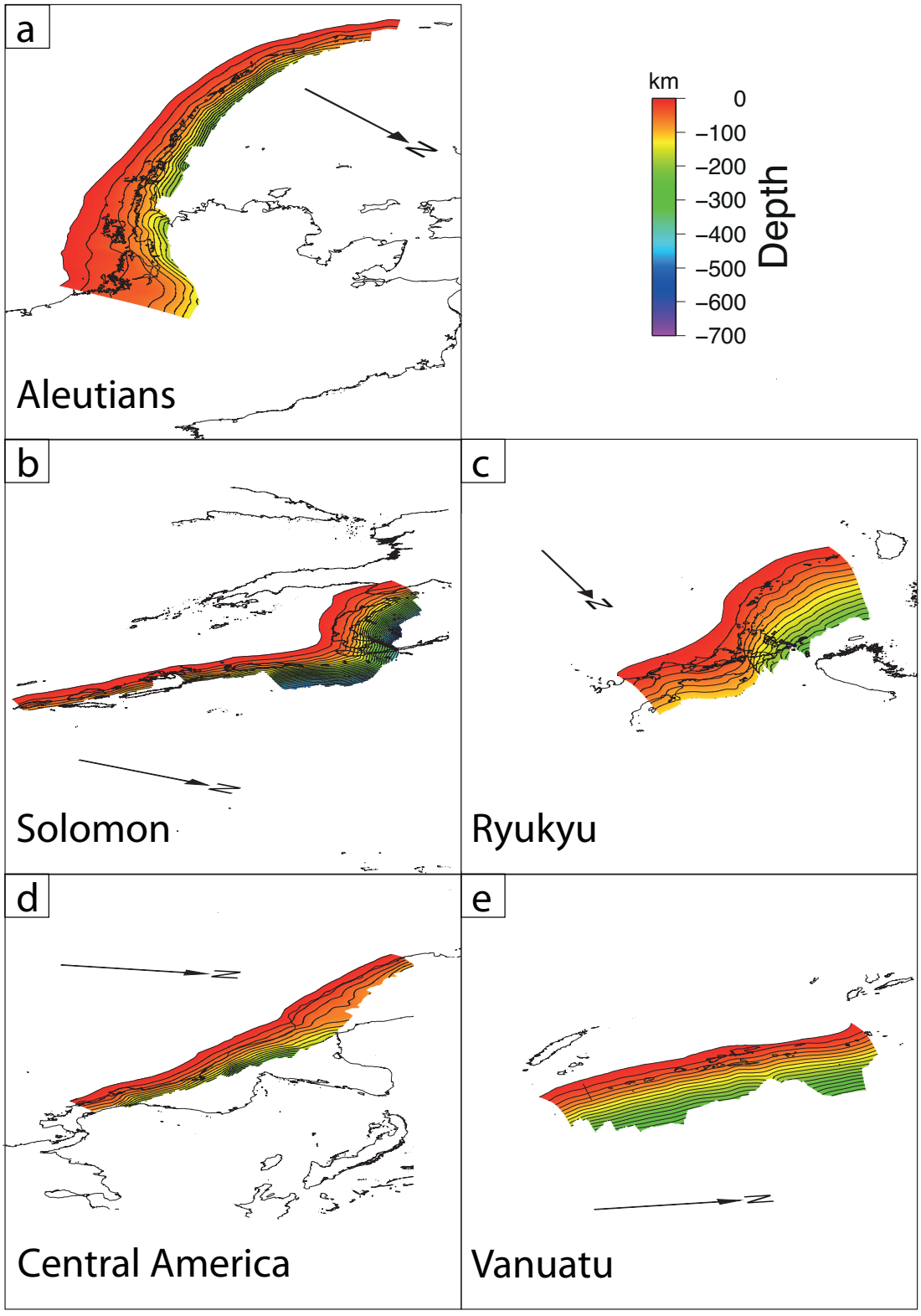

Fig. 2.4 (continued)

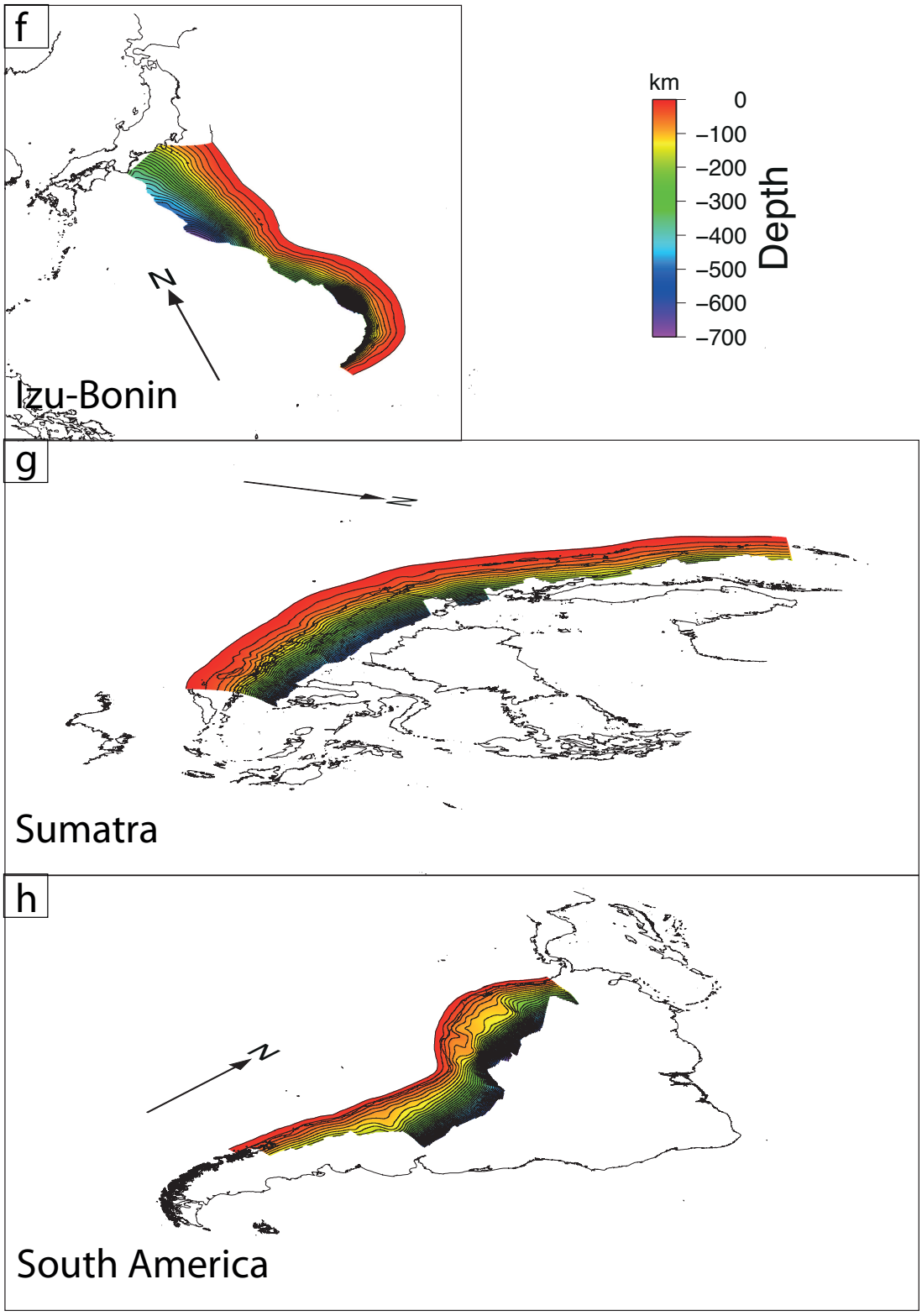

Fig. 2.4 (caption in the next page)

Fig. 2.4. Coastlines and 3D views of selected slab interfaces at depth shown in figure 2.3: a) Aleutians, b) Solomon, c) Ryukyu, d) Central America, e) Vanuatu, f) Izu-Bonin, g) Sumatra and h) South America. Subduction contours are from the slab 1.0 database (http://earthquake.usgs.gov/research/data/slab/). Chosen slabs are representative for the geometries discussed in the text: all linear (Central America, Vanuatu, E-Solomon, N-Izu-Bonin, S-South-America), curved concave (Aleutians, N-Ryukyu, S-Izu-Bonin, Sumatra) and curved convex (N-Solomon, S-Ryukyu, N-South-America) examples are provided (see section 3.8.3 for further explanations).

Widiyantoro et al., 1999; *Miller et al.*, 2005]. To illustrate the variety of slab-lower mantle interactions, a summary of cross-sections across subduction zones is reported in figure 2.5. Most of these geometries will be reproduced and tested in the models presented in this thesis.

2.3 Stress field in subduction zones

The state of stress affecting the lithosphere is mainly revealed by seismicity. On the base of stress regimes, Jarrard [1986] subdivided subduction zones into different classes, with end-members ranging from strongly extensional to strongly compressional. The differences between the two mentioned classes can be found analyzing the stress field within both the lower and the upper plates.

2.3.1 Stress field in the lower plate

The stress field in the lower plates is extremely variable both with depth and among different subduction zones (Figure 2.6). Down-dip variations of stress within slabs, are ruled by tectonic forces acting on the system (Figure 2.1). Shallow seismic events in the trench-outer rise generally indicate a transition from extension to compression with depth [e.g., *Seno and Yamanaka*, 1996]. Extension is consistent with the bending of the plate prior to subduction. Compression at crustal depths is related to the coupling and consequent friction between upper and lower plates and generates the largest earthquakes worldwide (e.g., the 1960 Valdivia earthquake [M_W 9.5], the 2004 Indian Ocean earthquake [M_W 9.3] and the 2011 Tohoku earthquake [M_W 9.0]; Figure 1.1; *Barrientos and Ward* [1990]; *Stein and Okal* [2005]; *Fujii et al.* [2011] and references therein). The reconstructed stress field for intermediate slab depths (focal depths between 100 km and 300 km [*Isacks and Molnar*, 1971]) shows the highest variability, ranging from down-dip extension to down-dip compression. Analyzing the global compilation of the CMTs catalog (for the last upgrade refer to *Ekstrom et al.* [2012]), *Isacks and Molnar* [1971] defined three categories of slab: intermediate extension (IE), intermediate extension-deep compression (IE-DC), and intermediate compression-deep compression

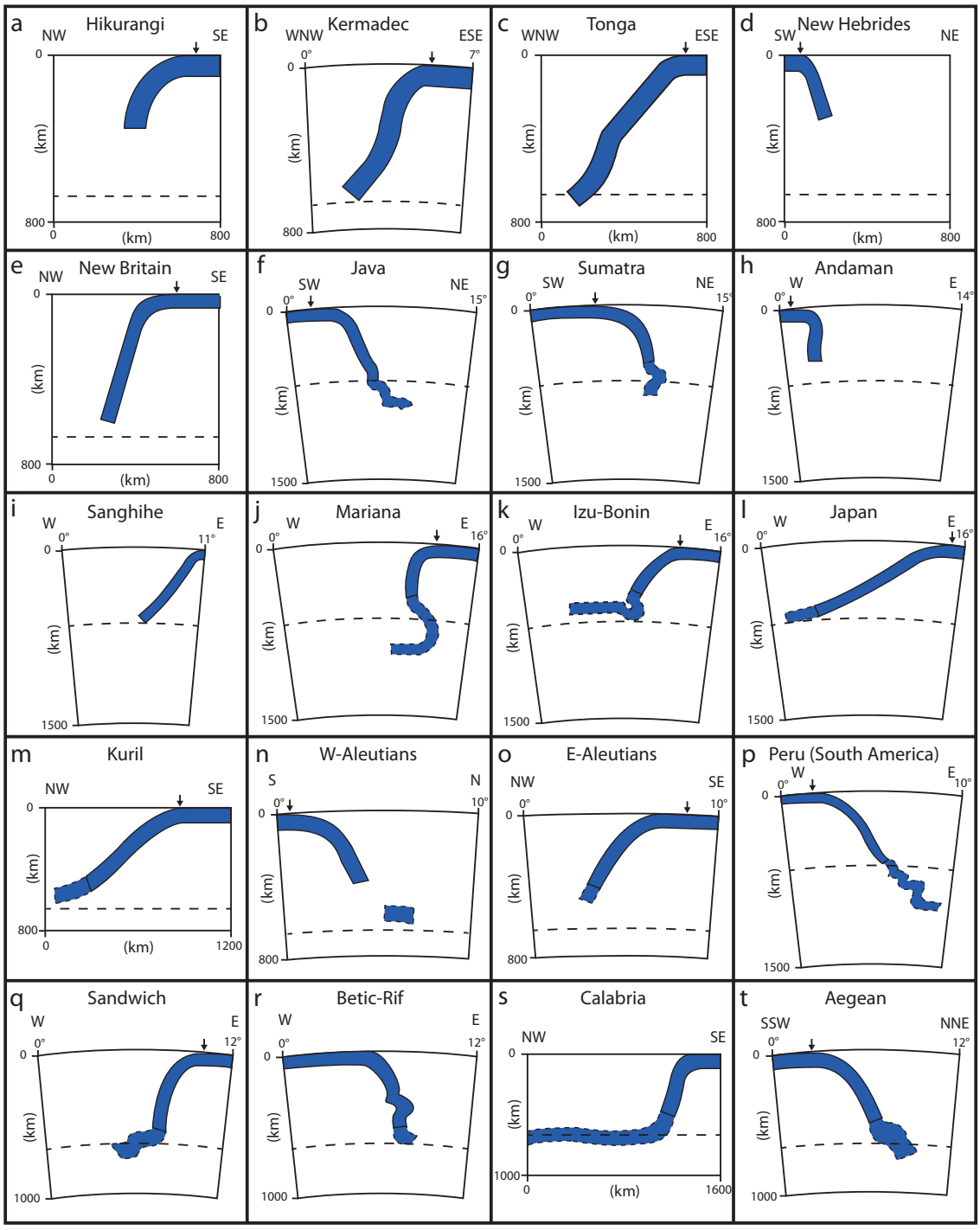

Fig. 2.5. Cross-section showing the slab geometry for a number of well-constrained subduction zones on Earth [after *Schellart et al.*, 2010]. Small arrows indicate the location of the trench. (a) Hikurangi slab; (b) Kermadec slab; (c) Tonga slab; (d) New Hebrides slab; (e) New Britain slab; (f) East Java slab; (g) Sumatra slab; (h) Andaman slab; (i) Sangihe slab; (j) Mariana slab; (k) Izu-Bonin slab; (l) Japan slab; (m) Kuril slab; (n) Aleutian slab; (o) Alaska slab; (p) Southern Peru slab; (q) Scotia slab; (r) Betic-Rif slab; (s) Calabria slab; (t) Hellenic slab. For subductions location refer to figure 2.3

(IC-DC) types. A check using an up-to-date data set and better constrained slab geometries was recently made by *Bailey et al.* [2012], with consistent results (Figure 2.6).

At intermediate depths, bending and unbending (Figure 2.1) have been invoked as the cause of double seismic zones with opposing stresses in the upper and lower interfaces of the slab [*Engdahl and Scholz*, 1977; *Kawakatsu*, 1986], usually showing down-dip compression and extension respectively [*Hasegawa et al.*, 1978]. Analyzing seismological data, *Vassiliou and Hager* [1988] concluded that the state of stress of slabs between 100 and 300 km is regionally dependent. Deep earthquakes (focal depths between 300 km and 700 km) are typically down-dip compressional in all Wadati-Benioff zones that reach the upper-lower mantle transition, reflecting the increasing resistance encountered by the subducting lithosphere [*Isacks and Molnar*, 1969, 1971]. This resistance is related to the viscosity jump and to the thermodynamic effects of the phase change at the 670 km discontinuity. As a first approximation density driven slab-pull should generate down-dip extension in the slab [e.g., *Anderson*, 2001; *Conrad and Lithgow-Bertelloni*, 2002], while viscous resistance to penetration into the lower mantle results in down-dip compression.

The occurrence of down-dip compression at intermediate depths is enigmatic if slab pull is considered as the main driving force in subductions. Its origin was explained by the occurrence of metastable olivine wedges in fast subducting oceanic lithosphere. Such metastable wedge could create negative density anomalies counteracting slab-pull [*Bina*, 1996, 1997]. On the contrary, within slow slabs the conversion of olivine to wadsleyite should occur shallower than 410 km, whereas the conversion of ringwoodite to perovskite and magnesiowustite should occur deeper than 660 km [*Irifune*, 1993], creating opposite forces that compress the lithosphere at these depths (Figure 2.1). A review of available data [e.g., *Doglioni et al.*, 2007] indicates that dominant down-dip extension occurs, at intermediate depths, along E or NE directed (i.e., Chilean-type) subduction zones (e.g., the Nazca plate in Chile subduction zone [*Isacks and Molnar*, 1971; *Rietbrock and Waldhauser*, 2004] and the Cocos plate in Mexican subduction zone [*Manea et al.*, 2006]) and down-dip compression along west directed (i.e., Mariana-type) subductions (e.g., Tonga [*Chen and Brudzinski*, 2001; *Chen et al.*, 2004]) (Figure 2.7). Exceptions to this pattern occur [*Rietbrock and Waldhauser*, 2004] and can be observed in regions of oblique plate convergence and of higher focal mechanism heterogeneity. These regions are located where along-strike changes in slab geometries occur [*Bailey et al.*, 2012].

2.3.2 Shallow intraplate stress field

At shallow depths (5-50 km), the stress field in the upper plates shows high variability (Figure 2.8). What one might expect in a convergent setting, is an overall trench-normal compression. This is true in

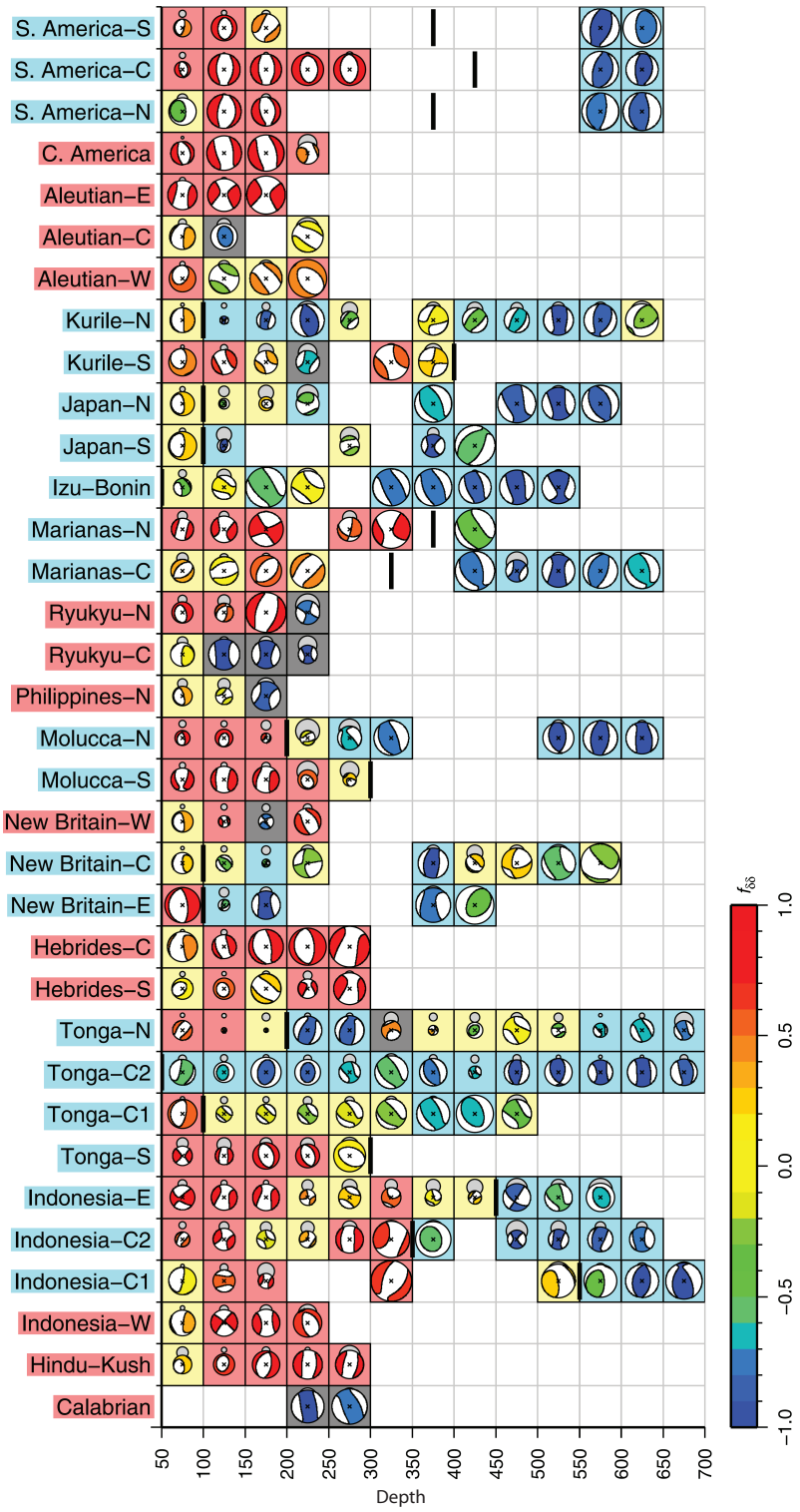

Fig. 2.6. (caption in the next page)

Fig. 2.6. Average source mechanism tensor results for the 50 km depth bins that contain $\leq$ 3 CMTs for 34 subductions [modified after *Bailey et al.*, 2012]. Background colors for the slab labels indicate whether the slab is shallow (i.e., Chilean) or deep (i.e., Mariana) type (see text for explanation). The beach-balls background indicates: down-dip extension (light red), down-dip compression (light blue), oblique orientations (light yellow), other orientations (dark gray). The radius indicates the consistency of orientations among the summed population. For deep slabs, a black solid line indicates the estimated change from extension to compression.

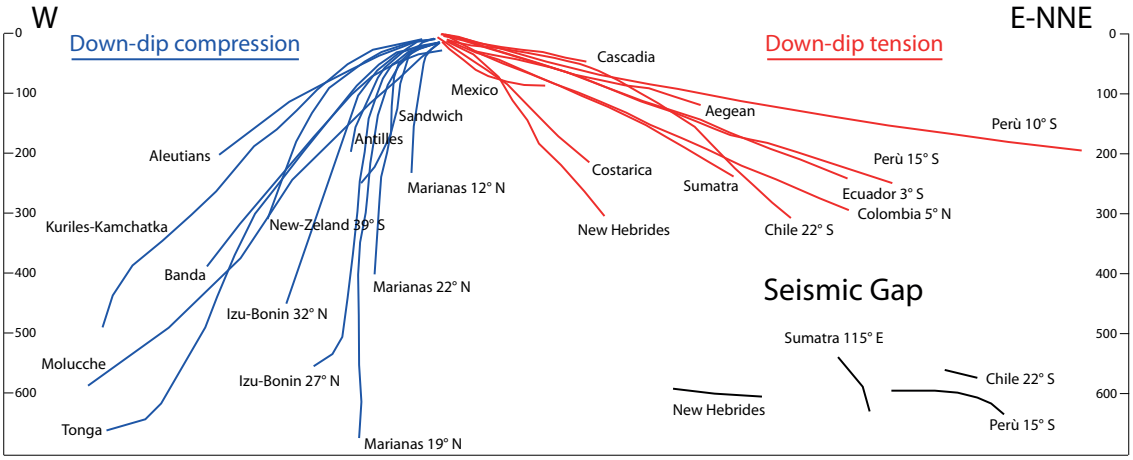

Fig. 2.7. Compilation of the slab dip measured along cross-sections perpendicular to the trench of most subduction zones (modified from *Riguzzi et al.* [2010]). Each line represents the mean trace of the seismicity along every subduction. Intermediate down-dip compression and average higher dip-angles characterize W-directed intra-slab seismicity (blue lines), whereas intermediate down-dip tension and shallower dip-angles characterize the E- or NE- directed slabs (red lines).

many cases, such as compression occurs in the upper plate for several subduction zones (e.g., South America, Sumatra, Central America, Vanuatu and Solomon; see figure 2.8a-e). As a matter of fact, extensional processes characterize the upper plate of many subductions (e.g., Aleutians, Vanuatu, Ryukyu, Mariana and Philippines; see figure 2.8f-j). These tensional stresses characterized by the largest compressive horizontal stress axes (hereafter SHmax) parallel to the slab trench, represent the response to a fundamental process affecting the upper plate tectonics, i.e., the development and evolution of back-arc basins. Trench rollback and slab retreat were identified as the principal mechanisms that origin tensional stresses in the back-arc basins [*Doglioni*, 1991; *Dvorkin et al.*, 1993; *Faccenna et al.*, 1996, 2001a,b; *Jolivet et al.*, 1994; *Doglioni et al.*, 2007], while trench-normal compression occurs when the overriding plate is advancing [*Heuret and Lallemand*, 2005; *Doglioni et al.*, 2007]. The margin curvature appears to control the tectonic regime [*Bonnardot et al.*, 2008], since an oceanward convex shape induces a margin uplift associated with a compressional regime. In contrast, the margin in front of an oceanward concave margin undergoes subsidence and induces an extensional regime in the upper plate. Thus, a slight change in the margin geometry

from convex to linear or even concave would induce a significant variation of the stress regime within the upper plate, especially in the direction of the stress axes. There is an excellent correlation between slab dip and upper plate strain. Back-arc spreading is observed for deep slabs, whereas back-arc shortening occurs only for shallow slabs [*Lallemand et al.*, 2005].

Focusing on the stress axes direction, high variability follows from differences in the geometry of trenches, emphasizing the geometric control over the resulting stress field. The lithosphere in the upper plate shows preferred trench-perpendicular or sub-perpendicular direction for the compressive SHmax axes (see blue axes in figure 2.8a-e), while trench sub-parallel direction is recognized for the normal SHmax axes (see red axes in figure 2.8f-j). This pattern is maintained along the strike of linear trenches (e.g., Chile, Solomon and kermadec) or adapts to the trench curvature or deflections of non-linear trenches (e.g., Sumatra, Aleutians and Mariana). Widespread stress axes rotation affects the lithosphere in regions near the trench tips, appearing to ”wrap” around the slab edges (e.g., North of Vanuatu or East Alaska; see figure 2.8d and f). In addition to the role of trench geometry, effects of the mantle return flow around the edges of the subducting slabs, induced by trench migration, could contribute to the deformation of the shallow lithosphere [*Russo and Silver*, 1994; *Long and Silver*, 2008, 2009].

The stress field affecting the lower plate at shallow depths (5-50 km) is generally represented by axes lying sub-parallel to the subduction trenches (Figure 2.8). Prevailing normal stress regime (red lines in figure 2.8) is consistent with the bending of the plate prior to subduction. Strike-slip and compressional SHmax stress axes (green and blue lines in figure 2.8) do not follow any particular trend, and are mostly detectable around the trench lateral edges. This latters are preferably associated with local mechanisms of lithospheric deformation.

Fig. 2.8. Intraplate stress orientation (0-50 km depth) for the principal subduction zones. Direction of the largest compressive horizontal stress (SHmax) for thrust (blue), normal (red) and strike-slip (green) stress regimes is shown (data after *Heidbach et al.* [2008]. The length of the lines does not contain magnitude information. Plate boundaries (after *Bird et al.* [2008]) and coastlines are shown as black lines. Yellow arrows represent the local relative motion of the global mantle flow (modified from *Doglioni et al.* [1999]). Black arrows indicate the mean dip direction of the subduction interfaces. Note that in the a) South America, b) Sumatra, c) Central America, d) Vanuatu and e) Solomon islands subductions the yellow and black arrows are oriented approximately toward the same direction (i.e., the mantle motion sustain the slab), while for the f) Aleutians, g) Kermadec, h) Ryukyu, i) Izu-Bonin and j) Philippines subductions the yellow and black arrows have opposite directions (i.e., the mantle motion oppose the slab). The various panels are not to the same scale of representation.

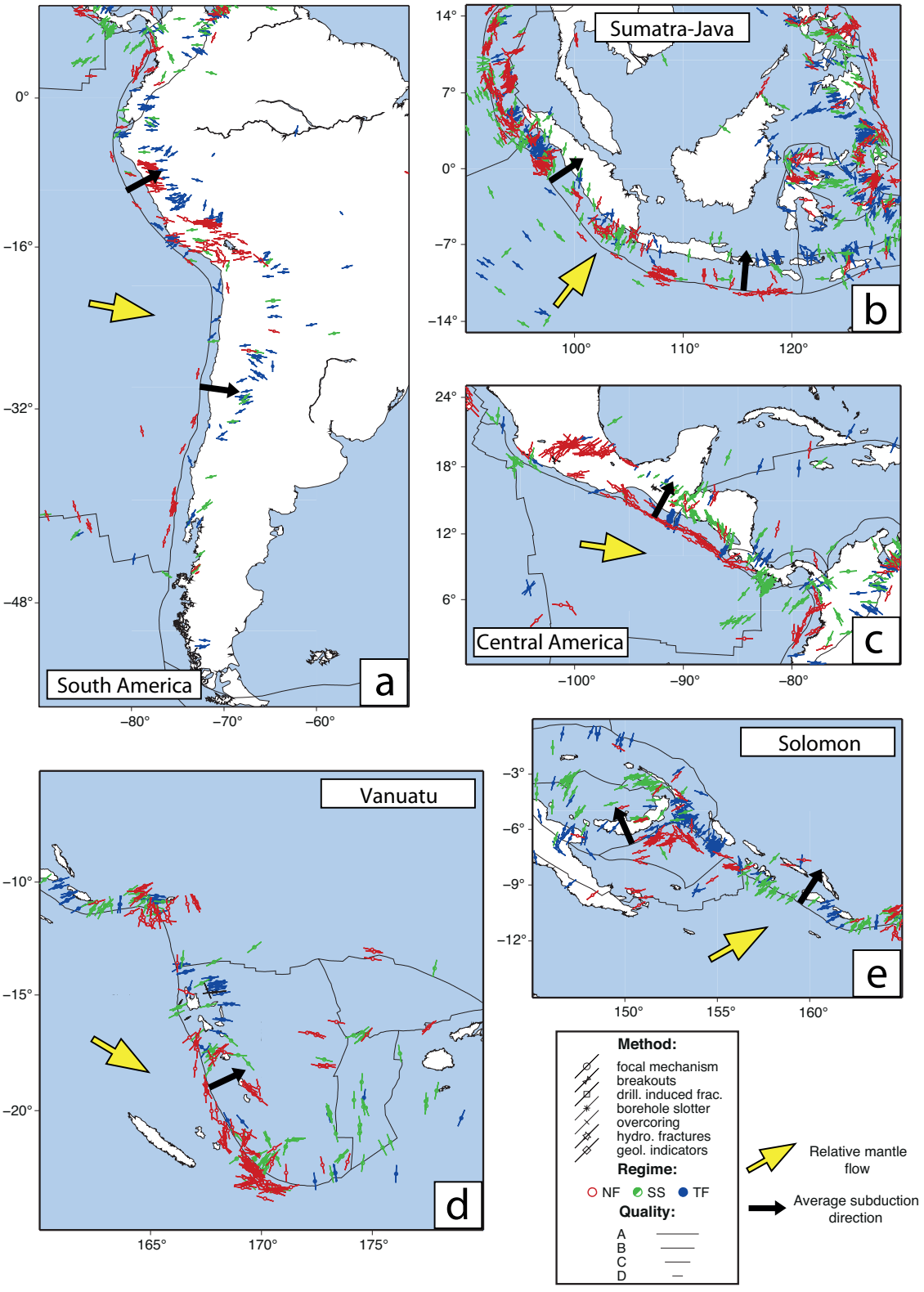

Fig. 2.8 (caption in the previous page)

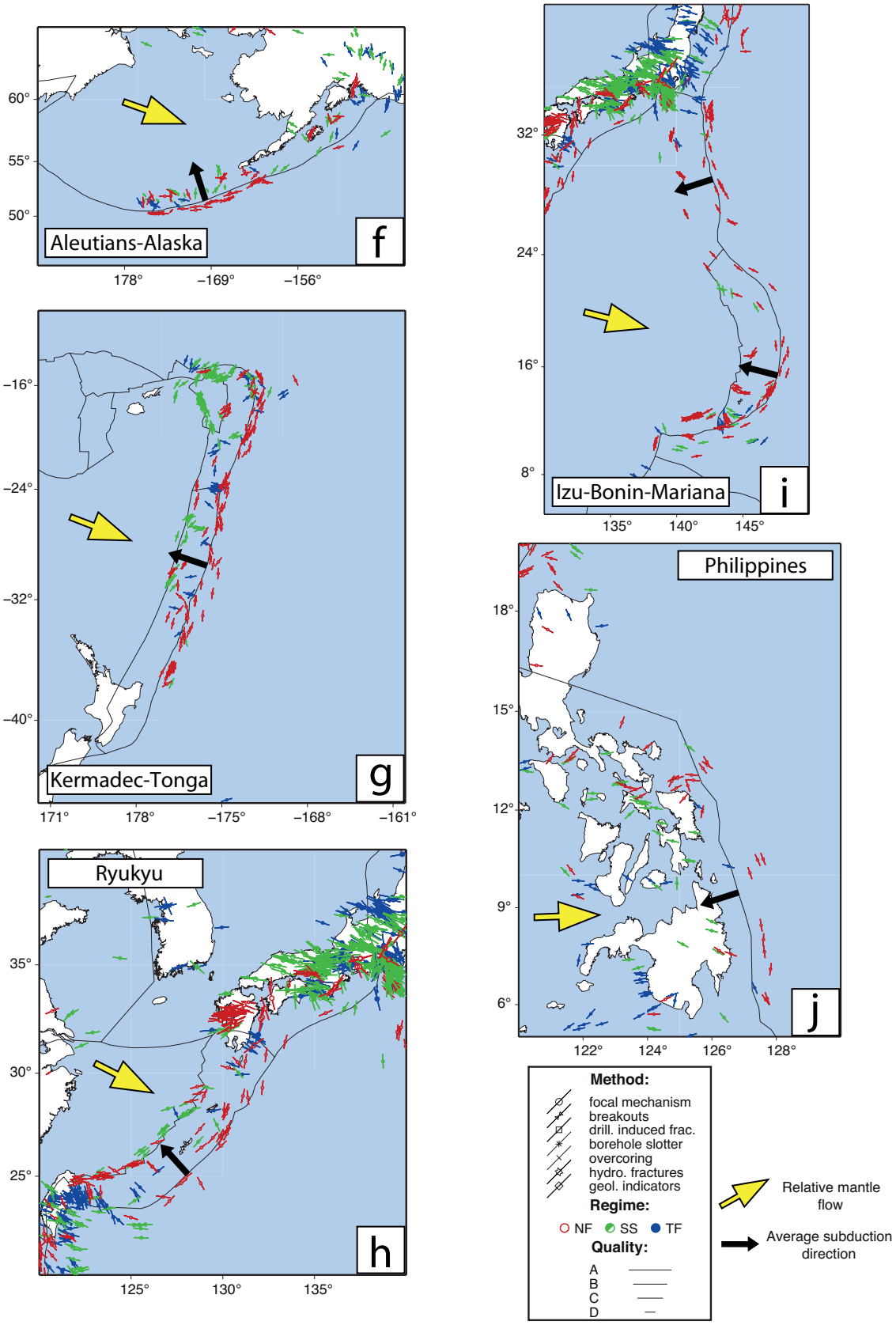

Fig. 2.8 (continued)

2.4 Relative plate kinematics and absolute plate motion

Modelling subduction zone processes requires an accurate quantification of the velocities of the plates and their boundaries. The dynamics of a plate boundary, can be thought in a simple relative way considering how one of the two involved plate moves respect to the other (easily derived from plate motion models). In a destructive margin, relative plate motion is fully described by the motion of the subduction hinge (H) and of the lower plate (L) (both the hinge and the lower plate can converge, diverge or be stationary) with respect to a fixed point (U) in the upper plate [*Doglioni et al.*, 2007] (Figure 2.9).

Following this argument, the subduction rate (i.e., the velocity with which the subducting lithosphere enters the subduction zone V_s) is given by the velocity of the hinge minus the velocity of the lower plate (i.e., $V_S = V_H - V_L$). With this assumption the velocity of subduction increases or decreases respectively when the hinge diverges (i.e., V_H is positive in the equation; figure 2.9a) or converges (i.e., V_H is negative in the equation; figure 2.9b) relative to the fixed (i.e., $V_U = 0$) upper plate.

Combining the different movements, *Doglioni et al.* [2007] obtained numerous kinematic settings that can be compared with real subduction zones worldwide. What is immediately clear analyzing the proposed kinematics is that the subduction hinge mainly diverges along W-directed subduction zones (e.g., figure 2.9a), whereas it converges more frequently along E- or NE-directed subduction zone (e.g., figure 2.9b).

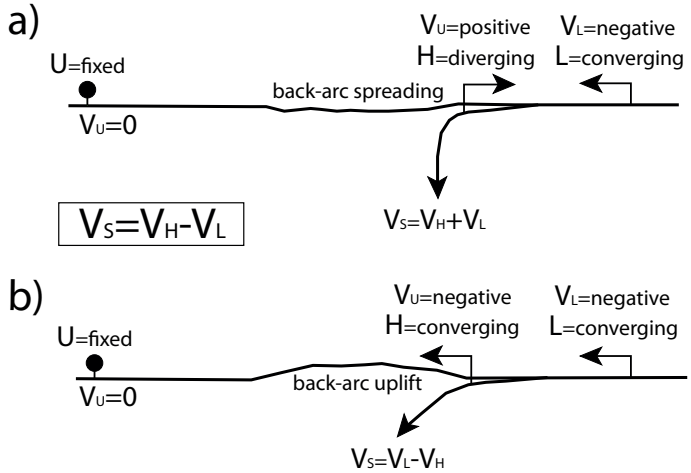

Fig. 2.9. Basic kinematics for a subduction zone (modified from *Doglioni et al.* [2007]) assuming fixed the upper plate U, a converging lower plate L, and a diverging (a) or converging (b) subduction hinge, H. The subduction rate Vs is given by the equation in the box. Vs increases when H diverges relative to the upper plate (a) and extension characterize the back-arc region (typical of W-directed subduction zones), whereas decreases if H converges (b) and compression in the back-arc region is enhanced (typical of E- to NNE-directed subduction zones).

The upper plate is characterized by the occurrence of a back-arc basin in case of diverging hinges or it is shortened in converging hinges realms (as seen in section 2.3.2), regardless the relative motion of the lower plate.

The dynamics of plate margins is, however, primary controlled by the absolute plate motion. Hot spots provide a reference frame for the absolute motion of plates [e.g., *Norton*, 2000]. Hot spot tracks indicate that a relative motion occurs between the lithosphere and the underlying deep, high-viscosity mantle (Net Rotation [e.g., *Ricard et al.*, 1991; *O'Connell et al.*, 1991]), with the asthenosphere likely acting as a detachment layer owing to its low viscosity [e.g., *Panza et al.*, 2010].

The origin of the net rotation goes beyond the scope of this thesis, but it is widely discussed in the literature. Plate motions are widely considered as related to mantle convection [e.g., *Turcotte and Oxburgh*, 1967; *Bercovici*, 2003], driven by buoyancy forces resulting from density anomalies [e.g., *Anderson*, 2001; *Gérault et al.*, 2012]. The tidal drag has been proposed as the driving mechanism [e.g., *Wegener and Skerl*, 1922; *Bostrom*, 1971; *Scoppola et al.*, 2006] although *Jordan* [1974], *Ricard et al.* [1991] and *Ranalli* [2000] demonstrated that this hypothesis is incompatible with present day estimates of upper mantle viscosities. For *Ricard et al.* [1991] the net rotation (NR) is due to differential plate-mantle coupling between oceanic and continental plates.

Several researchers proposed a global or net westward drift of the lithosphere relative to the mantle [e.g., *Bostrom*, 1971; *Gripp and Gordon*, 2002; *Cuffaro and Jurdy*, 2006, Figure 2.11]. The amplitudes of westward drift strongly depend on inversion choices (e.g., Euler poles for slow moving plates, such as Africa, and hot spot selection [*Ricard et al.*, 1991; *O'Neill et al.*, 2005]). Average rates of 4.9 cm/yr have been proposed in the frame of Model HS3 by *Gripp and Gordon* [2002]. According to Model SB04 [*Steinberger et al.*, 2004], if hot spots are allowed to move with respect to each other, the amount of net rotation is about 38% of that predicted by HS3. Amounts of net rotation of about of HS3 are consistent with the observed azimuthal seismic anisotropy [*Becker*, 2008]. A value of 2 cm/yr was proposed by *Ricard et al.* [1991]. Recently, *Crespi et al.* [2007] proposed a new kinematic model and concluded that the net westward drift can be as high as 13.4 cm/yr. In summary, a wide consensus has been reached in the literature about the existence of a westward drift but not about its magnitude.

A debate regarding whether hot spots are deep or shallow features has ensued in literature [*Foulger*, 2005]. If a deep origin is assumed for hot-spots, the plates generally move westward, but the Nazca plate moves eastward with respect to the mantle [e.g., *Gripp and Gordon*, 2002, figure 2.10a]. If their source is shallow, then all of the plates move westward [e.g., *Doglioni et al.*, 1999; *Cuffaro and Doglioni*, 2007, figure 2.10b]. However, these simple kinematic models displaying the net rotation of the lithosphere with

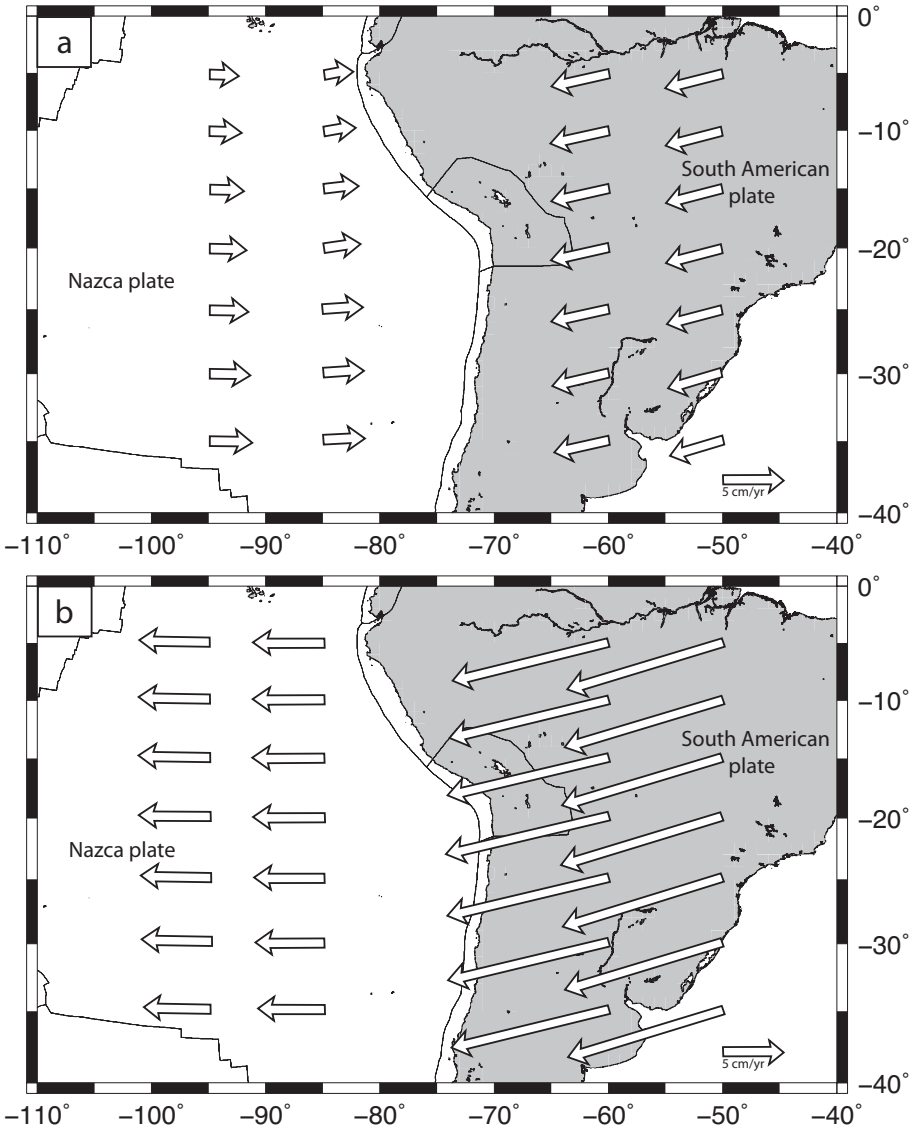

Fig. 2.10. Absolute motions of South America and Nazca plates relative to the mantle in the deep (a) and in the shallow (b) hotspot reference frames (modified from *Doglioni et al.* [2007]).

respect to the mantle could be complicated by other processes, such as net rotation associated currents induced, for example, by continental keels [e.g., *Zhong*, 2001; *Becker*, 2006], or general return flow, which is not necessarily connected to net rotations [e.g., *Hager and O'Connell*, 1981]. These regional flows could be different with respect to the above described global mantle flow.

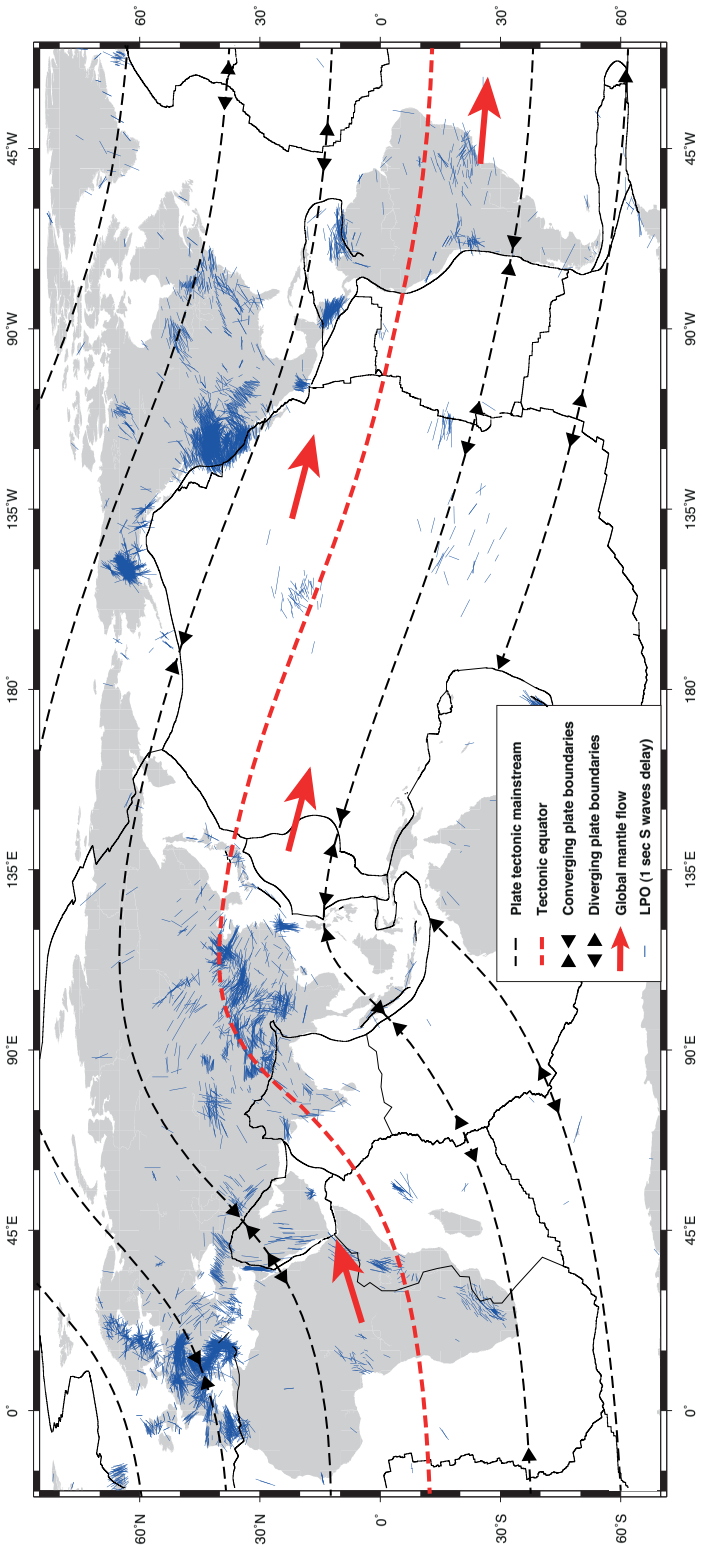

Fig. 2.11 (caption in the next page)

Fig. 2.11. Worldwide shear-wave splitting compilation (data from the splitting database, *Wüstefeld et al.* [2009]). Black dashed lines represent the tectonic mainstream of absolute plate motion (modified from *Doglioni et al.* [1999]; red dashed line is the tectonic equator. The red arrows indicate the relative motion of the global mantle flow.

Measurements of seismic anisotropy represent the most direct observational constraints on mantle flow patterns and its relations with plate motions [e.g., *Silver*, 1996; *Savage*, 1999; *Park and Levin*, 2002; *Long and Becker*, 2010]. Seismic anisotropy in the mantle is generally assumed to be the result of lattice/crystal preferred orientation (LPO/CPO) of mantle intrinsically anisotropic minerals (such as olivine). A worldwide compilation of mantle LPO from *Wüstefeld et al.* [2009] is plotted in figure 2.11.

In regional studies, many issues of smaller-scale mantle circulation in subductions zones can be highlighted by seismic anisotropies. For example, trench-parallel fast azimuths are commonly found in the fore arcs, and progressively rotate to trench perpendicular in the back arc [*Kneller et al.*, 2005; *Long and Silver*, 2009; *Faccenda and Capitanio*, 2013; *Lynner and Long*, 2013]. Along-strike of slabs, fast directions follow the trench curvature as it bends. At the edges of the subduction zone, fast azimuths align in a circular pattern [e.g., *Baccheschi et al.*, 2007; *Long and Silver*, 2009; *Lynner and Long*, 2013], maybe induced by a toroidal mantle flow around the slab edges, due to the roll-back motion of the slabs [*Civello and Margheriti*, 2004; *Schellart et al.*, 2010].

What is clear from the foregoing observations is the strong interaction between the descending lithosphere and the mantle circulation. Mantle motion affects the geometry and the state of stress in subduction systems, while the sinking lithosphere changes locally the global mantle circulation. Small scale mantle flow affects the arcs geometry [e.g., *Faccenna et al.*, 2004] and can explain much of the observed dynamic topography and micro-plate motion [*Faccenna et al.*, 2010]. The effects of mantle circulation on the stress field in subduction zones will be tested.

3

Plate scale numerical models

Guideline to the chapter contents

In this chapter, by means of numerical models, I study the complex and extremely variable state of stress characterizing worldwide subduction zones. Then I discuss the role of driving-resistance forces and plate geometries for generating the stress field. Models are built to evaluate the contribution of plate kinematics (convergence between plates and relative motion between lithosphere and sub-lithospheric mantle), geometry of the system (i.e. curved or linear trench, lateral extent and depth reached by the slab) rheology (effects of viscosities utilized for asthenospheric and lower mantle layers) and gravitational anomalies (e.g. slab pull) to the definition of the present-day stress field at different subduction zones. This has been achieved with the development of 2D (section 3.8.1), "para-3D" (i.e. symmetric in the third dimension: section 3.8.2) and real 3D (i.e. asymmetric in the third dimension: section 3.8.3) generic models. The aim is to analyze the interaction between the subducted slabs and the geodynamic forces that stress the system, to reproduce the observable for both the upper and lower plates at crustal depths and for intermediate and deep subducted lithosphere. The interaction between subducting slabs and the viscosity jump at upper-lower mantle transition has been also investigated (in section 3.8.3). Model geometries are drawn on the basis of real subduction zones characteristics. Model results are compared with data from known convergent margins. The starting-point assumption is that model and real subduction have similar geometric-kinematics features; the end-point must be a stress field comparable with that observed in real subduction zones.

3.1 Introduction

The 2D and 3D modelling presented in this thesis was performed using the finite elements method (FEM), with a viscoelastic approach. My models describe the dynamic evolution in convergent plate margins, simulating the subduction of an oceanic under a continental plate.

The viscoelastic approach, widely used in literature to constrain the state of stress in slabs [*Carminati et al.*, 1999; *Negredo et al.*, 1999b; *Carminati and Petricca*, 2010; *Petricca et al.*, 2013], is here based on a linear Maxwell rheology considered appropriate to reproduce the overall response of a subduction for geological time scales. This kind of approach is able to reproduce the long-term viscous behavior of the lithosphere and mantle, taking into account the elastic flexure on a shorter time-scale. Viscoelastic rheology is useful to study the mechanical response of a structure and the state of stress created by different initial subduction conditions, assuming "a priori" geometries rather than to simulate self-generated geometries (as done by viscous flow models; e.g. *Zhong and Gurnis* [1995]).

The models simulate the dynamic evolution of convergent margins, assuming an initial configuration that reproduces mature stages of the process. The aim is to analyze the interaction between the already subducted slab and the geodynamic forces that stress the system.

3.2 Previous works

Since many physical and geological aspects of subduction remain enigmatic mainly due to limited observations in both time and depth, the subduction process remains one of the most challenging geodynamic processes investigated with numerical techniques [see *King*, 2007; *Billen*, 2008; *Gerya*, 2011, and references therein for a comprehensive list of papers treating this subject].

The choice of the modeling technique depends on the question being addressed and on the observable to be investigated. There are two end-members for modeling subducted slabs: kinematic and dynamic subduction models.

Kinematic models make the assumption of imposed velocities and require careful use of initial and boundary conditions. The input parameters are the properties of subduction zones (e.g., plate rheology, plate velocity, and slab dip). As this approach attempts to isolate the influence of one or a small number of physical parameters on subduction process, kinematic models are often used in seismic, stress field, and petrologic investigations [e.g., *Molnar et al.*, 1979; *Helffrich et al.*, 1989; *Staudigel and King*, 1992;

Peacock et al., 1994; *Peacock*, 1996; *Kirby et al.*, 1996; *Bina*, 1996, 1997; *Carminati et al.*, 1999; *Marton et al.*, 1999; *Negredo et al.*, 1999b; *Marton et al.*, 2005; *Carminati et al.*, 2005].

In dynamic calculations, the plate velocity, slab velocity, and slab dip are not input controls, but rather are results of the modelling and are controlled by imposed forces and assumed rheologies. This makes it more difficult to set up a calculation with a geometry that resembles a specific subduction zone. These dynamic models produce more realistic subduction scenarios (self- generated), but it is often difficult to isolate the influence of individual parameters. Dynamic slab models generally provide lower resolution than kinematic models [*King*, 2007]. Dynamic slab models have been largely used to investigate the factors controlling slab dip [*Gurnis and Hager*, 1988], the interaction of slabs with phase changes [*Christensen and Yuen*, 1984; *Zhong and Gurnis*, 1994; *Christensen*, 1996; *Ita and King*, 1998], the geoid and topographic profiles over subduction zones [e.g. *Davies*, 1986; *King et al.*, 1994; *Zhong and Gurnis*, 1995; *Chen and King*, 1998; *Zhong and Davies*, 1999], the mass transfer between the upper and lower mantle [e.g., *Davies*, 1995; *Christensen*, 1996; *Kincaid and Olson*, 1987; *Kincaid and Sacks*, 1997; *King et al.*, 1997; *Ita and King*, 1998], and the role exerted by mantle flow [*Billen and Gurnis*, 2001, 2003; *Schellart et al.*, 2011].

The evolution of slabs in the mantle can be divided into three stages: subduction initiation, long-term behavior, and subduction cessation. My modelling approach is pointed to analyze the long-term behavior, providing single snapshots at different stages of this time-dependent process. In particular, attention has been focused on slab subduction and bending processes, lateral and depth variability of subduction processes in 3D and overriding plate dynamics. All these aspects have been explored in literature.

Several numerical studies have been performed to address the influence of overriding plate dynamics on subduction process [*van Hunen et al.*, 2000; *van Hunen and van den Berg*, 2004; *Sobolev and Babeyko*, 2005; *Clark et al.*, 2008; *Gerya*, 2011], the resistance to subduction of the slab at depth [*Bellahsen et al.*, 2005; *Schellart*, 2005] and the 3D effects of mantle flow circulation [*Honda and Saito*, 2003; *Zhu et al.*, 2009], of mantle flow over the subduction geometry [e.g., *Schellart et al.*, 2004; *Funiciello et al.*, 2006; *Morra et al.*, 2006; *Schellart et al.*, 2007; *Jadamec and Billen*, 2010].

Large-scale features of subduction zones, i.e. the forebulge motion [e.g., *Melosh and Raefsky*, 1980; *McAdoo et al.*, 1985; *Zhong and Gurnis*, 1994; *Hall and Gurnis*, 2005], the trench geometry [*Morra et al.*, 2006; *Schellart et al.*, 2007], and the shape of the slab [*Hassani et al.*, 1997; *Funiciello et al.*, 2003] have been also investigated using various rheologies, especially with elasto-plastic or visco-plastic behaviors.

By means of kinematic numerical models, a crucial investigated observable is the stress regime of plates and slab in convergent margins. 2D models using elastic or hyper-elastic rheologies [e.g., *Hassani et al.*, 1997; *Bada et al.*, 1998; *Reynolds et al.*, 2002; *Babeyko and Sobolev*, 2008] have been used to investigate

subduction zones at regional scale. Models considering viscoelastic rheologies were made both for the 2D [*Giunchi et al.*, 1996; *Devaux et al.*, 2000; *Carminati et al.*, 2001; *Carminati and Petricca*, 2010] and the 3D [*Negredo et al.*, 1997, 1999a,b; *Hashima et al.*, 2008] cases.

3.3 The finite elements method

When studying a complex physical system, continuous in nature, it is often not possible to determine an analytical solution to the equations that describe its behavior. In these cases, the problem can be addressed using numerical methods for the solution of partial differential equations (PDE's). The first step is to discretize the system, i.e. to divide it into an equivalent system of smaller facilities (elements) for which it is easier to determine the behavior. Their assembly would lead to the real structure. Obviously, smaller components imply: 1) the description of the system approaches the continuous case; and 2) the complexity of the solution increases. It is crucial to look for a good balance between the accuracy required for the solution and the complexity of the studied problem. For a large number of subdivisions is not possible to manually analyze the enormous volume of data and electronic processing is essential. The numerical solution of a system of PDE's can be conveniently transformed into a linear algebra problem and implemented through algorithms on computers.

The finite elements method [e.g., *Ern and Guermond*, 2004] describes the deformation of a system by the solution of partial differential equations in one or more variables and known analytical form, defined in small regions of the "continuum". The solutions are formulated for each elementary unit and combined to obtain the solution for the whole original structure. Once the geometry, the equilibrium laws, the equation of motion and the constitutive relations of materials are properly described, the discrete implementation on the computer is performed. First the whole integration domain is divided into small elements, with a size sufficiently small compared to changes in the quantities to be analyzed. This set of elements forms the mesh.

The process of discretization is done by splitting the model through fictitious surfaces into simple shaped small elements (triangles or quadrilaterals in $2D$; polygons in $3D$), connected together by nodes. For each element a linear combination of functions (shape functions) is solved, with degrees of freedom which represent the unknowns of the problem. The results calculated for each node will give values that are not necessarily those of the original function, but rather the values that provide the least error over all the solution. Interpolation criteria allow to know the solution for each point of the element.

The minimum requirements that the final solution must respect are: 1) the continuity of movement between adjacent elements; and 2) the equilibrium between external and internal forces.

3.4 Governing equations

The fundamental relationship to be considered in this kind of analysis are:

1. compatibility equations: describing the geometric relations between deformation and displacement;
2. constitutive equations: describing the relations link between the state of stress and strain;
3. equilibrium equations: equation of motion that connect stress and applied body forces.

The unknowns (degrees of freedom) to be solved are displacements at nodes, from which the strain ε is calculated using the following compatibility equation:

$$\begin{Bmatrix} \varepsilon_x \\ \varepsilon_y \\ \varepsilon_z \\ \varepsilon_{xy} \\ \varepsilon_{xz} \\ \varepsilon_{yz} \end{Bmatrix} = \begin{Bmatrix} \frac{\delta u}{\delta x} \\ \frac{\delta v}{\delta y} \\ \frac{\delta w}{\delta z} \\ \frac{\delta u}{\delta y} + \frac{\delta v}{\delta x} \\ \frac{\delta u}{\delta z} + \frac{\delta w}{\delta x} \\ \frac{\delta v}{\delta z} + \frac{\delta w}{\delta y} \end{Bmatrix} = \begin{Bmatrix} \frac{\delta}{\delta x} & 0 & 0 \\ 0 & \frac{\delta}{\delta y} & 0 \\ 0 & 0 & \frac{\delta}{\delta z} \\ \frac{\delta}{\delta y} & \frac{\delta}{\delta x} & 0 \\ \frac{\delta}{\delta z} & 0 & \frac{\delta}{\delta x} \\ 0 & \frac{\delta}{\delta z} & \frac{\delta}{\delta y} \end{Bmatrix} \begin{Bmatrix} u \\ v \\ w \end{Bmatrix} \tag{3.1}$$

where ε is the strain tensor and u, v and w are the displacements in x, y and z directions.

The models discussed in this thesis consist of viscoelastic materials, i.e. characterized by an elastic behavior (Hookean) on the short term and by a viscous behavior (Newtonian) for times greater than the relaxation time. The elastic behavior of an isotropic solid is defined by two independent elastic constants λ and μ (Lame parameters), through a matrix D ($_{m=6\ *\ n=6}$) with 12 non-zero components:

$$D = \begin{Bmatrix} \lambda+2\mu & \lambda & \lambda & 0 & 0 & 0 \\ \lambda & \lambda+2\mu & \lambda & 0 & 0 & 0 \\ \lambda & \lambda & \lambda+2\mu & 0 & 0 & 0 \\ 0 & 0 & 0 & \mu & 0 & 0 \\ 0 & 0 & 0 & 0 & \mu & 0 \\ 0 & 0 & 0 & 0 & 0 & \mu \end{Bmatrix} \tag{3.2}$$

applying the relations:

$$\lambda = \frac{E\nu}{(1+\nu)(1-2\nu)} \tag{3.3}$$

$$\mu = G = \frac{E}{2(1+\nu)} \tag{3.4}$$

the matrix of elastic constants D can be expressed as a function of Young's modulus E (or longitudinal elasticity) and Poisson ratio ν (transverse contraction coefficient):

$$\left\{\begin{array}{cccccc}
\frac{E(1-\nu^2)}{(1+\nu)^2(1-2\nu)} & \frac{E\nu}{(1+\nu)(1-2\nu)} & \frac{E\nu}{(1+\nu)(1-2\nu)} & 0 & 0 & 0 \\
\frac{E\nu}{(1+\nu)(1-2\nu)} & \frac{E(1-\nu^2)}{(1+\nu)^2(1-2\nu)} & \frac{E(1-\nu^2)}{(1+\nu)^2(1-2\nu)} & 0 & 0 & 0 \\
\frac{E\nu}{(1+\nu)(1-2\nu)} & \frac{E\nu}{(1+\nu)(1-2\nu)} & \frac{E(1-\nu^2)}{(1+\nu)^2(1-2\nu)} & 0 & 0 & 0 \\
0 & 0 & 0 & \frac{E}{2(1+\nu)} & 0 & 0 \\
0 & 0 & 0 & 0 & \frac{E}{2(1+\nu)} & 0 \\
0 & 0 & 0 & 0 & 0 & \frac{E}{2(1+\nu)}
\end{array}\right\} \tag{3.5}$$

Using the constitutive equation in the case of linear elastic behavior, the stress tensor σ is defined as:

$$\sigma = \left\{\begin{array}{c} \sigma_x \\ \sigma_y \\ \sigma_z \\ \sigma_{xy} \\ \sigma_{xz} \\ \sigma_{yz} \end{array}\right\} = D \left\{\begin{array}{c} \varepsilon_x - \varepsilon_{0x} \\ \varepsilon_y - \varepsilon_{0y} \\ \varepsilon_z - \varepsilon_{0z} \\ \varepsilon_{xy} - \varepsilon_{0xy} \\ \varepsilon_{xz} - \varepsilon_{0xz} \\ \varepsilon_{yz} - \varepsilon_{0yz} \end{array}\right\} \left\{\begin{array}{c} \sigma_{0x} \\ \sigma_{0y} \\ \sigma_{0z} \\ \sigma_{0xy} \\ \sigma_{0xz} \\ \sigma_{0yz} \end{array}\right\} \tag{3.6}$$

where σ_0 and ε_0 are respectively the initial stress and strain of the material considered. The viscous behavior depends on the dynamic viscosity η, representing the coefficient of proportionality between stress σ and the rate of shear deformation of the solid $\dot{\varepsilon}$ (strain rate). The constitutive equation for a Newtonian viscous material is:

$$\sigma = \begin{Bmatrix} \sigma_x \\ \sigma_y \\ \sigma_z \\ \sigma_{xy} \\ \sigma_{xz} \\ \sigma_{yz} \end{Bmatrix} = \eta \begin{Bmatrix} \frac{\delta \varepsilon_x}{\delta t} \\ \frac{\delta \varepsilon_y}{\delta t} \\ \frac{\delta \varepsilon_z}{\delta t} \\ \frac{\delta \varepsilon_{xy}}{\delta t} \\ \frac{\delta \varepsilon_{xz}}{\delta t} \\ \frac{\delta \varepsilon_{yz}}{\delta t} \end{Bmatrix} = \eta \dot{\varepsilon} \tag{3.7}$$

The viscoelastic model has a highly time-dependent behavior, which then becomes a variable with a specific physical meaning. In fact, the constitutive relation of a linear viscoelastic material can be considered by the combination of an elastic behavior on short time scales, and a viscous behavior for longer times of force application. The time limit between the two mechanisms is called relaxation time T_i, and is typical for each material as it depends on the ratio between viscosity and shear modulus:

$$T_i = \frac{\eta}{G_i} \tag{3.8}$$

We can for simplicity account a linear viscoelastic Maxwell body as the in series combination of a spring with stiffness G_i (Hookean spring) and a viscous dash-pot with coefficient of viscosity η_i (figure 3.1).

A stress (σ) applied to the model operates with the same intensity on both the spring and the dash-pot, i.e. $\sigma_{Total} = \sigma_D = \sigma_S$, where σ_D and σ_S are respectively the stress acting over the dash-pot and the spring. The resulting strain is the sum of deformations induced on the dash-pot ε_D and the spring ε_S; the constitutive equation becomes:

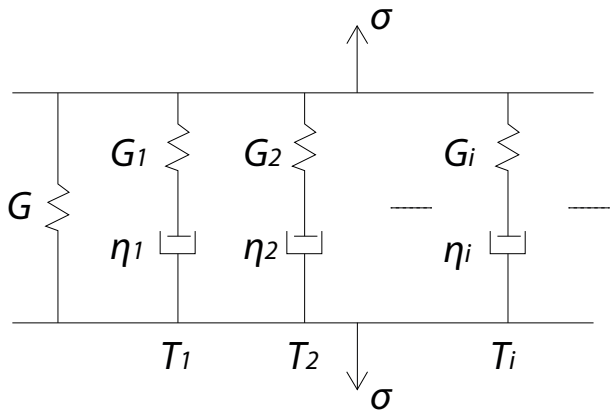

Fig. 3.1. Schematic of the generalized Maxwell model for the viscoelastic rheology.

$$\frac{\delta\varepsilon_{Total}}{\delta t} = \left(\frac{\delta\varepsilon_D}{\delta t}\right) + \left(\frac{\delta\varepsilon_S}{\delta t}\right) = \left(\frac{\sigma}{\eta_i}\right) + \frac{1}{G_i}\left(\frac{\delta\sigma}{\delta t}\right) \tag{3.9}$$

Following this deformation model, when the material undergoes a constant stress application, strain occurs by two components: an instantaneous elastic deformation and a viscous deformation that grows with time (i.e. duration of stress application). The linear Maxwell model is characterized by the decay of stresses exponentially with time, according the relaxation module $\xi_{(t)}$:

$$\xi_t = G_i e^{\frac{-t}{T_i}} \tag{3.10}$$

The equilibrium equations account for the balance of internal and external forces. With F defining the volume forces, the formulation for the 3D case is:

$$\begin{pmatrix} -\frac{\delta\sigma_{xx}}{\delta x} & -\frac{\delta\sigma_{xy}}{\delta x} & -\frac{\delta\sigma_{xz}}{\delta x} \\ -\frac{\delta\sigma_{yx}}{\delta x} & -\frac{\delta\sigma_{yy}}{\delta x} & -\frac{\delta\sigma_{yz}}{\delta x} \\ -\frac{\delta\sigma_{zx}}{\delta x} & -\frac{\delta\sigma_{zy}}{\delta x} & -\frac{\delta\sigma_{zz}}{\delta x} \end{pmatrix} = \begin{pmatrix} F_x \\ F_y \\ F_z \end{pmatrix} \tag{3.11}$$

this relationship in compact form becomes:

$$\nabla\sigma = \mathbf{F} \tag{3.12}$$

3.5 Rheological parameters

The elastic rheological parameters used in this work are based on the Reference Model PREM [*Dziewonski and Anderson*, 1981], while the adopted mantle viscosity values are consistent with literature studies (for the upper mantle: *Spada et al.* [1992]; *Kaufmann and Lambeck* [2000]; *Nakada and Lambeck* [1989]; for the lithospheric mantle: *Houseman and Gubbins* [1997]).

In contrast to *Whittaker et al.* [1992], where the upper lithosphere is considered perfectly elastic, we have modeled this layer by a viscoelastic rheology. The chosen viscosity of the crust yields relaxation times greater than the solution time for the models, so that the crust behaves largely in an elastic way. This choice according to previous studies [*Giunchi et al.*, 1996], avoids unrealistic bending stresses.

Isostatic forces must be addressed in modeling, as they affect the behavior of the tectonic system. However, gravity is not applied as a body force through the models (i.e. it does not act in the absence of other forces applied to the model), but is considered as an adjunctive subdomain condition acting on upper model surface (Winkler foundation; *Williams and Richardson* [1991]). The Winkler foundation is a vertical pressure $-\Delta\rho g v$ (where $\Delta\rho$ is the difference between crust and free air densities, g is the gravity acceleration an v the vertical displacement) that counteracts displacement at the model surface (minus sign). This representation of isostatic forces allows us to easily introduce density variations in the model,

and also reduces its definition only to region affected by gravitational anomalies. The parameters that must be defined for viscoelastic materials are: (1) Bulk modulus K (eq. 3.13) (2) shear modulus G_i (eq. 3.14) and (3) relaxation time T_i (eq. 3.8).

For every region of the model, materials are defined by their elastic properties, raised through the Young modulus E, the Poisson coefficient ν and the dynamic viscosity η. From these we can define the above introduced viscoelastic parameters (bulk and shear modulus), using the following relations:

$$K = \frac{E}{3(1-2\nu)} \tag{3.13}$$

$$G = \frac{E}{2(1+\nu)} \tag{3.14}$$

From these equations it is clear that the rheology of each material can be defined simply on the basis of 3 parameters, which describe the whole elastic and viscous properties: elastic modulus E, Poisson coefficient ν and viscosity η.

The initial rigidity G_0 (i.e. rigidity for time smaller than relaxation time T_i), is always considered null to avoid unrealistic additional stiffness (figure 3.1). In tables 3.1, 3.2, 3.3 and 3.4 are reported the values used for the Earth layers rheological parameters.

3.6 Description of models

The models represent the Earth through two-dimensional sections and three-dimensional portions of a convergent margin and extend from the topographic surface down to a maximum depth of 1000 km. Geometries are all characterized by an oceanic plate that subducts below a continental plate, including the crust, the lithospheric mantle, the asthenosphere, the upper mantle and part of the lower mantle. In agreement with average global values, the continental lithosphere has a thickness of 85 km, including 35 km thick crust and 50 km thick lithospheric mantle. The oceanic lithosphere is 60 km thick due to 10 km

Name	Expression (or Value)	Units	Description
$E_{\ cr}$	$60e^9$	Pa	*Elastic modulus*
$G_{0\ cr}$	0	Pa	*Initial rigidity*
$\eta_{\ cr}$	$1e^{24}$	$Pa\ s$	*Viscosity*
$\nu_{\ cr}$	0.25	$-$	*Poisson coefficient*
$K_{\ cr}$	$4e^4$	MPa	*Bulk modulus*
$G_{i\ cr}$	$3.75e^4$	MPa	*Relaxation time rigidity*
$T_{i\ cr}$	$2.67e^{13}$	s	*Relaxation time*

Table 3.1. Main constants and expressions used for the crust in viscoelastic models. The subscript *cr* indicates the crust.

Name	Expression (or Value)	Units	Description
$E_{\ lit}$	$1.75e^11$	Pa	*Elastic modulus*
$G_{0\ lit}$	0	Pa	*Initial rigidity*
$\eta_{\ lit}$	$5e^{22}$	$Pa\ s$	*Viscosity*
$\nu_{\ lit}$	0.27	$-$	*Poisson coefficient*
$K_{\ lit}$	$1.27e^5$	MPa	*Bulk modulus*
$G_{i\ lit}$	$1.11e^5$	MPa	*Relaxation time rigidity*
$T_{i\ lit}$	$4.5e^{11}$	s	*Relaxation time*

Table 3.2. Main constants and expressions used for the lithosphere (*lit*).

thick crust summed with 50 km of lithospheric mantle. An asthenosphere approximately 200 km thick (i.e. up to a depth of 300 km) was introduced in all the geometries, though often merged in terms of rheology to the underlying mantle.

The choice of introducing in some models an asthenosphere with an average thickness of 200 km is consistent with the results of many studies, which showed that the asthenospheric thickness is in the range of 100 to 400 km [e.g. *Gung et al.*, 2003]. Each layer is therefore characterized by different rheological parameters and thicknesses. Fundamental arrangement in the design phase was to split the subducting slab

Name	Expression (or Value)	Units	Description
$E_{\ um}$	$1.75e^{1}1$	Pa	*Elastic modulus*
$G_{0\ um}$	0	Pa	*Initial rigidity*
$\eta_{\ um}$	$1e^{21}$	$Pa\ s$	*Viscosity*
$\nu_{\ um}$	0.27	$-$	*Poisson coefficient*
$K_{\ um}$	$1.27e^{5}$	MPa	*Bulk modulus*
$G_{i\ um}$	$1.11e^{5}$	MPa	*Relaxation time rigidity*
$T_{i\ um}$	$9e^{9}$	s	*Relaxation time*

Table 3.3. Main constants and expressions used for the upper mantle (*um*).

Name	Expression (or Value)	Units	Description
$E_{\ um}$	$1.27e^{1}1$	Pa	*Elastic modulus*
$G_{0\ um}$	0	Pa	*Initial rigidity*
$\eta_{\ um}$	$1e^{22}$	$Pa\ s$	*Viscosity*
$\nu_{\ um}$	0.27	$-$	*Poisson coefficient*
$K_{\ um}$	$9.2e^{4}$	MPa	*Bulk modulus*
$G_{i\ um}$	$8e^{4}$	MPa	*Relaxation time rigidity*
$T_{i\ um}$	$1.24e^{11}$	s	*Relaxation time*

Table 3.4. Main constants and expressions used for the lower mantle (*lm*).

into subdomains, needed during the process of model setup to force negative buoyancy anomalies (i.e. slab pull; see section 3.7 for initial setting strategies), when included in the models.

Using three-dimensional numerical simulations of free subduction, *Schellart et al.* [2007] showed that the slab width controls two important features of plate tectonics: the curvature of subduction zones and their tendency to retreat backward with time. They also showed that the 3D effect mainly operates close to the lateral edges of slabs. As a consequence, our 2D simulations apply best to portions of wide slabs far from the slab edges. Instead, 3D simulations aim to analyze the real effects in the third dimension. The Models presented in this thesis, in logical order of development, are:

1. 2D models:

two kinds of geometries were used, with steeper (85°) and shallower (35°) dipping slab (figure 3.3). The aim was to analyze the different response to the dynamic solicitation, over the two end-members classes of subduction (i.e steeper Mariana type and shallower Chile type; [*Dickinson*, 1978; *Uyeda*, 1981]) in a plane strain approximation (infinite extent in the third dimension).

With 2D viscoelastic models it was shown that the slab dip angle is not a controlling factor over the resulting stress field [*Carminati and Petricca*, 2010]. For this reason in subsequent stages only the geometry with a steeper slab was used.

2. Para-3D models:

laterally symmetric, obtained by the extrusion in the third dimension of the former 2D model (figure 3.5). This ”intermediate step” between 2D and 3D modelling procedure it was necessary to understand whether the assumptions made in the plane strain approximation could be extended to the third dimension of the space.

3. 3D models with linear trench:

these and the following models are truly three-dimensional, since the slabs are laterally finite. Different lateral extent for the trench (in the range between 500 to 3000 km; figure 3.6) provides a good representation of almost all known case of linear worldwide subduction (e.g. from the laterally short Makran subduction to the 3000 km long Chile subduction).

4. 3D models with curved trench:

these models are meant to simulate convergent margins described by a curved slab shape, a common features of subduction arcs. In a first set of geometries concave downward slabs are simulated (figure 3.7). This geometry of slabs is a typical in retreating hinge subductions (see section 2.2).

Also slabs with concave upward shape (figure 3.8), usually found in advancing hinge subductions, are provided. Different lateral extent for the slab (from 500 km to 3000 km along strike) are assumed in order to represent the variety of natural cases, starting from the smallest Calabrian and Nova Scotia arcs, up to the largest Aleutian and Sumatran arcs.

5. 3D models with variable slab depth:

for both linear and curved trench geometries (with concave or convex slab; figure 3.9) different depths reached by the subducted lithosphere were tested.

These series of models are useful to fully understand the interaction between the subducted slab and the viscosity jump which occurs at the upper-lower mantle transition. Furthermore, these models are fundamental to understand the interactions between the subducting lithosphere and lateral- toroidal mantle flow.

3.7 Body forces and boundary conditions

The forces of subduction dynamics, that can act alternately or simultaneously over the models, are defined as boundary or conditions or as body forces acting on model portions (hereafter subdomains). For a more detailed explanation of the settings for individual models, please refer to the following section 3.8. The forcing processes that were simulated (alternatively or together) are:

- *slab pull*: down pull of the subducting lithosphere induced by gravitational forces due to density anomalies within the slab;
- *mantle flow*: relative flow of the asthenosphere with respect to the lithosphere;
- *plate convergence*.

As already introduced in section 3.6, gravity is not applied as a body force. Instead, it is simulated as a boundary condition applied on surface. The isostatic balance is thus achieved by applying a force F_S (like a spring) perpendicular to each point on the topographic surface, and proportional to the density contrast recorded at the interface between lithosphere and atmosphere:

$$F_S = -gv\left(\rho_{lit} - \rho_{atm}\right) \tag{3.15}$$

where g is the acceleration of gravity, ρ_{lit} and ρ_{atm} are respectively the lithosphere and air densities and v is the vertical displacement at the surface.

Regarding the bottom of the models (located within the lower mantle), it is improper to consider it fixed. To overcome this limitation a Winkler foundation [e.g. *Williams and Richardson*, 1991] was applied at this boundary as well. This kind of boundary condition generates a vertical force that counteracts the overlying model weight. Is easy to introduce the spring stiffness ψ_w defined by its constitutive relation as:

$$\psi_w = \frac{EA}{L} \tag{3.16}$$

where E is the elastic modulus, A and L are respectively the basal area (or basal length in the bi-dimensional case) and model height. Once defined the spring stiffness, I proceeded by setting up a force F_w acting along the basal boundary of the models as:

$$F_w = -\psi_w v \tag{3.17}$$

where v is again the vertical displacement. The minus sign is considered so that the spring balances the vertical movements. A bottom boundary condition fixed in the vertical direction (i.e. only horizontal displacement allowed) was also tested and the solutions were found to be comparable.

This representation of isostatic forces allows to easily introduce gravitational anomalies within the model subdomains. Slab pull, if considered is simulated using this expedient. Given the difficulty in knowing for various subductions worldwide the precise slab pull magnitude, an homogeneous distribution of such gravitational anomalies was used. The chosen values ($60\ kg/m^3$) represent a good average of those proposed in literature, ranging between the $50\ kg/m^3$ obtained by thermo-viscous models [e.g. *Davies and Stevenson*, 1992] in case of slow subductions, up to $100\ kg/m^3$ if eclogitization processes of lower crust gabbroic rocks are taken into account.

When slab pull is included in the simulations, a negative density anomaly of $60\ kg/m^3$ is applied within lithospheric subdomains deeper than 200 km. Some simulations were runned adding the density anomaly at shallower portions of the slab subdomains (from 100 km depth), aimed to understand the effects of slab pull magnitude over the resulting stress field.

Our models do not include rheological and density changes associated with the olivine-spinel phase transition (at approximately 410 km). For a discussion on the contrasting effects of this phase transition on the density anomaly of fast and slowly sinking slabs, the reader is referred to the work of *Bina* [1996, 1997].

Plate convergence and asthenospheric flow, when forced in models, are simulated via prescribed displacement condition over the boundary surfaces (or edges in 2D) of the involved subdomains; i.e., the

velocity can be set applying at the model boundary a horizontal displacement at each time step equal to the velocity multiplied by the duration of time steps.

Using various combinations of boundary and subdomain conditions, it is possible to force:

- convergence of the lower plate (V_{UL}) with fixed upper plate;
- convergence of the upper plate (V_{OL}) with fixed lower plate;
- convergence of both plates ($V_{UL} + V_{OL}$);
- all range of possible relative motion between the lithosphere and the underlying mantle (e.g. subduction and asthenospheric flow toward the same direction (V_{SM}) or toward opposite directions (V_{EM});
- slab pull (F_{sp}).

Additional used boundary conditions in modelling procedures are:

- *free boundary*: free motion is allowed in all directions;
- *roller boundary*: only motion parallel to the edges (in 2D) or planes (in 3D) is allowed;
- *symmetry plane* (3D): the values of variables are symmetric with respect to the plane.

Summarizing about the boundary conditions, common conditions for all simulations are the roller boundary or the Winkler foundation at the base of the models, the free boundary imposed at the sides of the lower mantle and the spring for the isostatic force on the top boundary.

The lithospheric lateral boundaries are kept both fixed in the horizontal direction or alternatively a prescribed displacement is applied to simulate plate convergence (for the upper, the lower or both plates). The same applies to the upper mantle lateral boundaries, in this case to enable the asthenospheric flow relative to the lithospheric layer.

Vertical movements are always allowed for all lateral boundaries. Slab pull is forced in some simulations via a density anomaly limited in few regions of the subducted slabs.

In order to simplify the calculations, in 3D models planes of symmetry were used to halve the geometries and then make the model less time and memory consuming. Roller surfaces (i.e., free lateral and vertical slip) are imposed at the boundary opposite of the symmetry planes in 3D models. Para-3D models instead require two parallel symmetry planes on sides.

Detailed settings for individual models are explained in the next section. The relevant graphic symbols for boundary conditions are reported in figure 3.2.

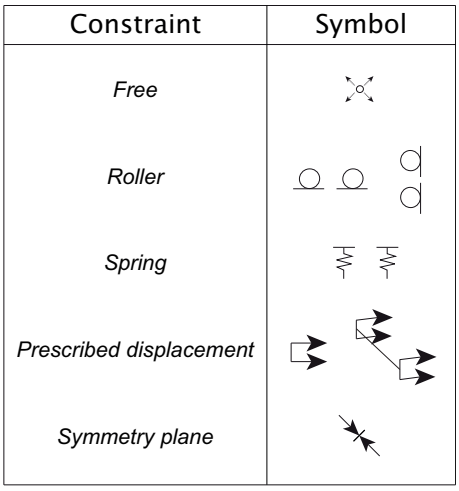

Fig. 3.2. Constraint symbols used for the graphical description of numerical models.

3.8 Models setting

3.8.1 2D models

2D models are calculated in a plane strain approximation, i.e. an infinite and non deformable geometry is considered in the third dimension of the structure. The compatibility equation (3.1) for the two-dimensional case becomes:

$$\left\{ \begin{array}{c} \varepsilon_x \\ \varepsilon_y \\ \varepsilon_{xy} \end{array} \right\} = \left\{ \begin{array}{c} \dfrac{\delta u}{\delta x} \\ \dfrac{\delta v}{\delta y} \\ \dfrac{\delta u}{\delta y} + \dfrac{\delta v}{\delta x} \end{array} \right\} = \left(\begin{array}{cc} \dfrac{\delta}{\delta x} & 0 \\ 0 & \dfrac{\delta}{\delta y} \\ \dfrac{\delta}{\delta y} & \dfrac{\delta}{\delta x} \end{array} \right) \left\{ \begin{array}{c} u \\ v \end{array} \right\} \tag{3.18}$$

Gardi et al. [2002] showed that the stress state of subducting slabs resulting from numerical models is strongly dependent on the geometry. For this reason two different geometries have been used in 2D modelling, characterized by shallow (35° dipping) and steep (85° dipping) slabs. Geometries represent a

2500 km long vertical section of the Earth along the subduction direction from surface down to 1000 km depth (3.3).

Both geometries, representative for the two classes of subduction zone (i.e. Chile and Mariana type; see section 2.2), were drawn for simplicity dipping toward the same direction.

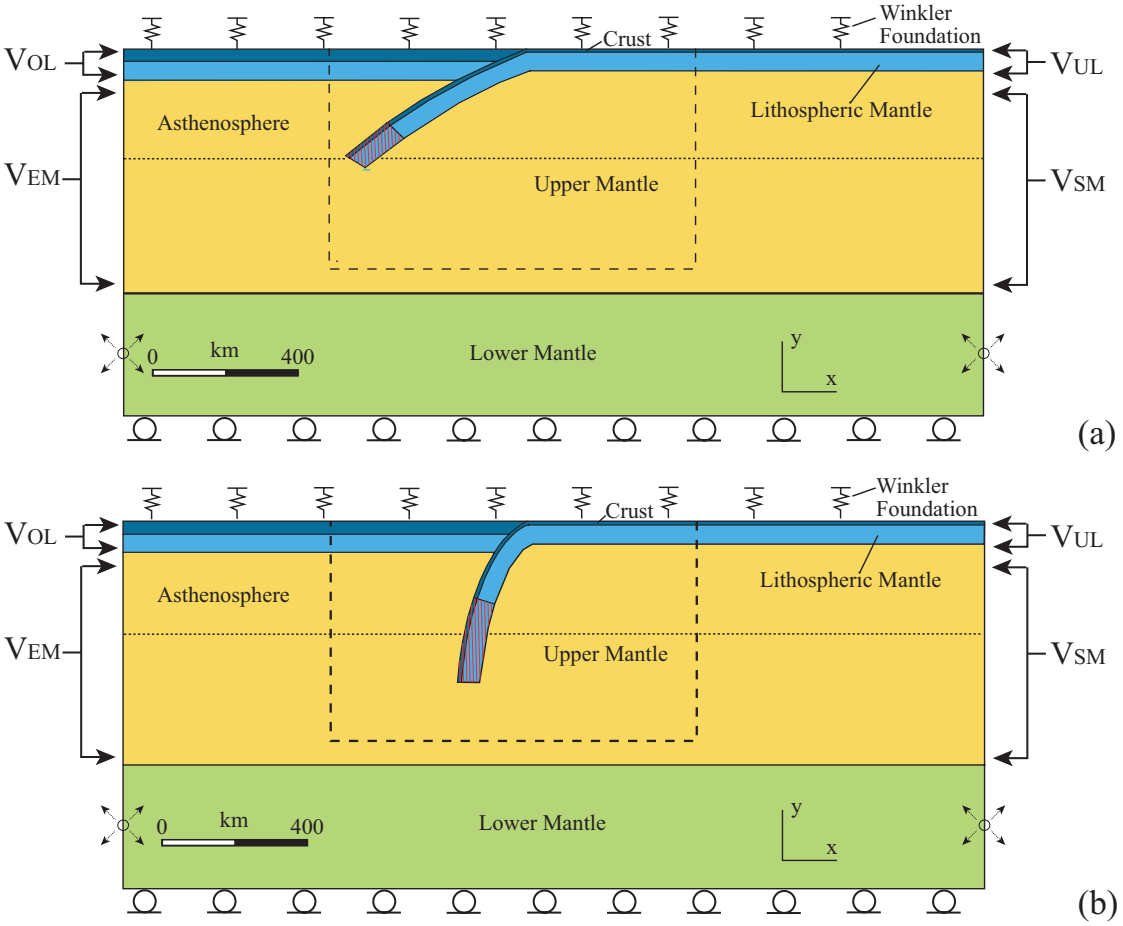

Fig. 3.3. Geometry, materials, and boundary conditions for (a) shallow and (b) steep dipping slabs. In these illustrations a dotted line shows the base of the asthenosphere, when modeled. When modelled, a density contrast was applied to the areas marked by the red grid. The dashed rectangle shows the part of the model shown in Figures of 2D results (section 4.1). V_{OL} (velocity of the overridding plate), V_{UL} (velocity of the underlying plate), V_{EM} (velocity of the mantle at the left boundary, i.e. encroaching the slab), and V_{SM} (velocity of the mantle at the right boundary, i.e. sustaining the slab) indicate velocities applied at the boundaries. Constraint symbols are explained in Figure 3.2.

In the meshing (i.e., discretization) phase it was chosen to use triangular elements, since triangles are characterized by less degrees of freedom and also fit better the geometries. In other words, this choice allows us to decrease the ratio between model complexity and the number of elements.

Given the large dimensions of model geometries (2500 x 1000 km), elements dimensions ranging from 7 km to 50 km have been considered suitable. The mesh is denser in the central portion of the model, with nodal distances between 4 and 8 km within the lithosphere, the slab and in the mantle surrounding the slab. The nodes become progressively less dense in areas distant from the slab, till a maximum nodal distance of approximately 80 km at the bottom of the model (see figure 3.4a).

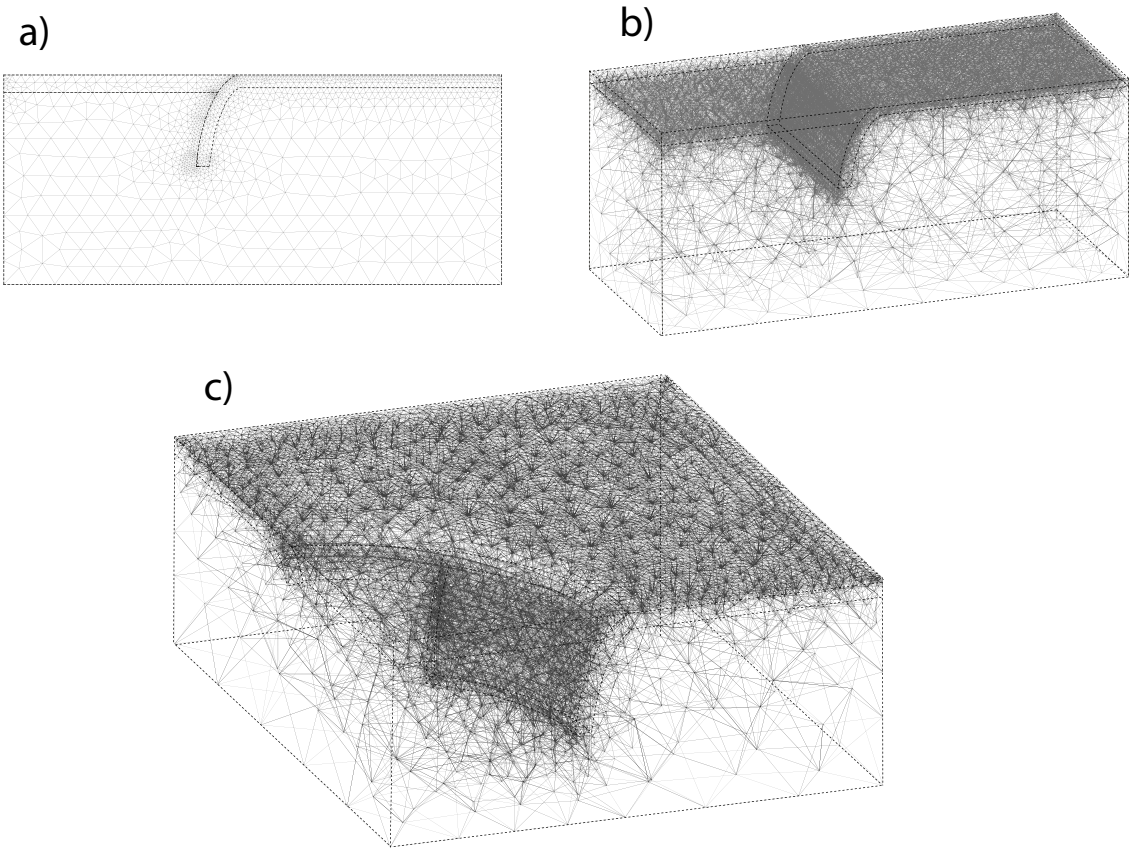

Fig. 3.4. a) 2D, b) para-3D and c) 3D meshes representative for the three class of models described in the text.

3.8.2 Para-3D models

The transition from 2D to 3D modelling is a key step in the finite elements approach. For this reason it is necessary an intermediate phase in which the plane strain assumption made for the bi-dimensional case, is extended to the third dimension of the space. Once checked for compatibility between the solutions obtained in 2D and 3D simulation, it makes sense to develop real 3D models.

The plane strain approximation concept can be somehow maintained when a spatial dimension is added, simply by considering both lateral surfaces of the model (i.e. boundary planes parallel to the extruded section) as symmetry planes (figure 3.5). The infinite extension in the third dimension is then maintained, but three-dimensional deformations become possible. This relatively simple Para-3D geometry is also fundamental to explore the more sensitive discretization process. Moving from 2D to 3D case, the triangular elements become tetrahedrons. This drives to an exponential increase of nodes, unknowns (degrees of freedom) and thus of the complexity of the model. It becomes also more difficult to obtain a qualitatively valid subdivision of the geometry.

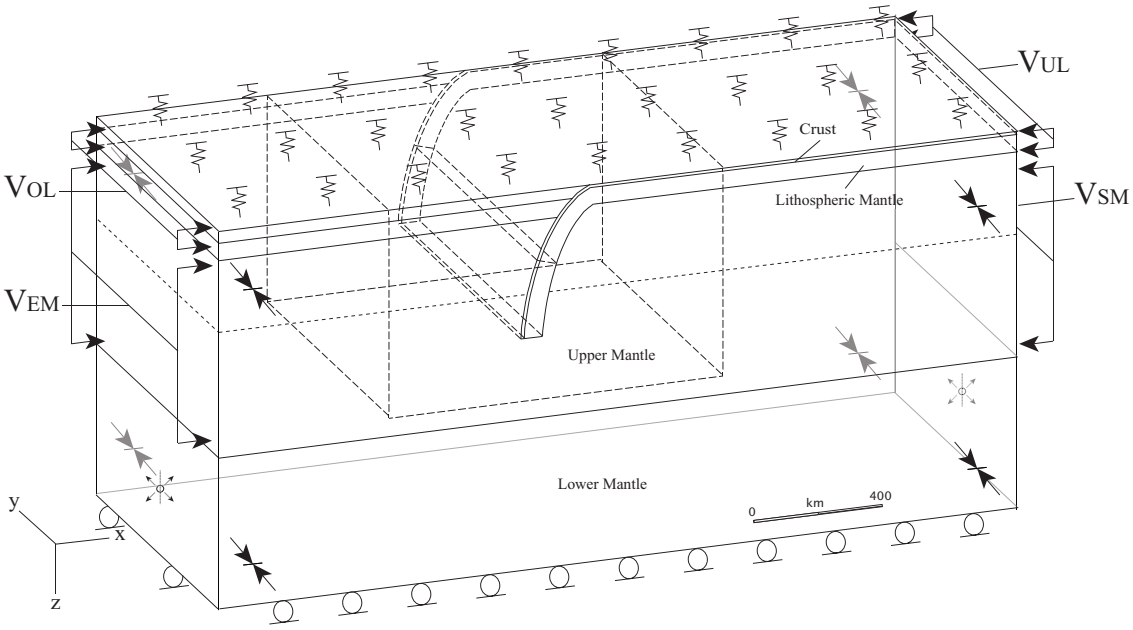

Fig. 3.5. Geometry and boundary conditions for the para-3D model. Symbolic representation of boundary conditions is the same used in Figure 3.3; brhigth symbols refer to hided planes. The front and back (parallel to subduction direction) boundary surfaces are symmetry planes. The dashed plane within the lithosphere separates the lower part of the slab interested by a density contrast, and the upper part with no forced density contrast. The dashed box shows the part of the model where results are shown in section 4.2.

The knowledge gained about 3D meshing, was subsequently used for the even more complicated gridding of the real 3D models. Para-3D model geometry was obtained by extruding in the third dimension (perpendicular to the subduction direction) the steeper section used in 2D modelling.

The para-3D model geometry is 2500 km long, 1000 km deep and 1000 km wide (figure 3.5). The mesh is composed of approximately 10^5 tetrahedral elements (see figure 3.4b) and is described through the solution of $2x10^6$ degrees of freedom. The boundary conditions are analogous to those used in the 2D case, except that are applied to a plane rather than over an edge.

3.8.3 3D models

Fully three-dimensional geometries, characterized by laterally finite extent of the slabs are here described. Unlike 2D and para-3D models that apply best to portions of wide slabs far from the slab edges, with 3D simulations it is possible to investigate also the regions near the lateral tips of subducting lithosphere

These simulations allowed me to investigate the effects of: the lateral extent, the arcuate or linear shape of the slab, the interaction between slab and surrounding mantle, the effects on the resulting stress field of both poloidal and toroidal components of mantle flow and the viscosity of lower mantle as controlling factor in stress definition for deeper regions of drowning slab.

The investigation of all these features requires to design the following four sets of models:

Linear trench 3D models

The slabs are characterized by a linear trend sideways, with total lateral extent of subducted lithosphere (i.e. not halved geometry) of 500 km (figure 3.6.A), 1000 km (figure 3.6.B) and 3000 km (figure 3.6.C).

Fig. 3.6. Geometry and boundary conditions for the linear 3D models with lateral trench extend of A] 250 km B] 500 km and C] 1500 km. Values are referred to halved geometries, i.e. applicable to doubled geometries. The front boundary surfaces are the symmetry planes. Symbolic representation of boundary conditions is the same used in Figure 3.5; bright symbols refer to hided planes. The dashed plane within the lithosphere separates the lower part of the slab interested by a density contrast, and the upper part with no forced density contrast. The dashed box shows the part of the model where results are shown in section 4.3.

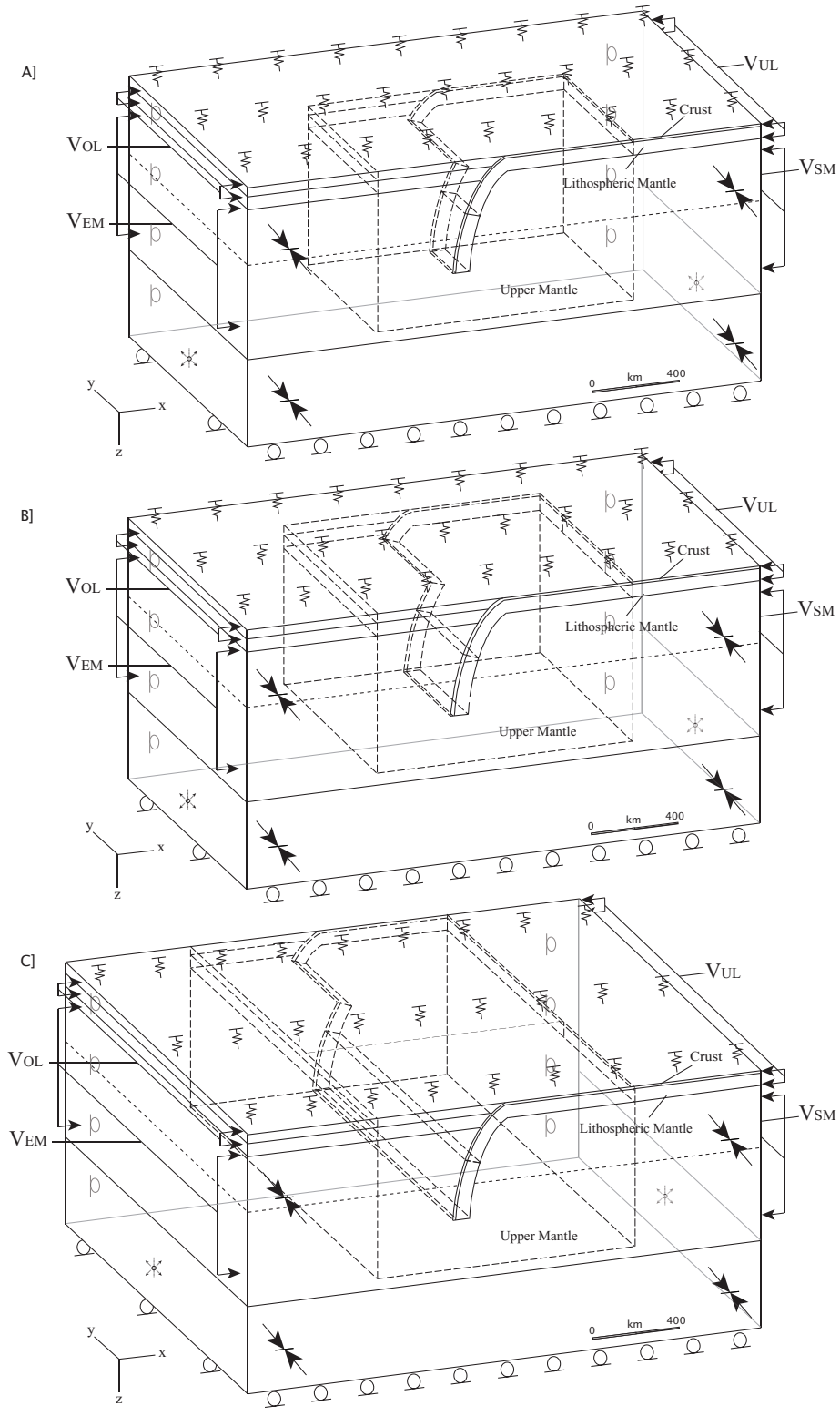

Fig. 3.6. (caption in the previous page)

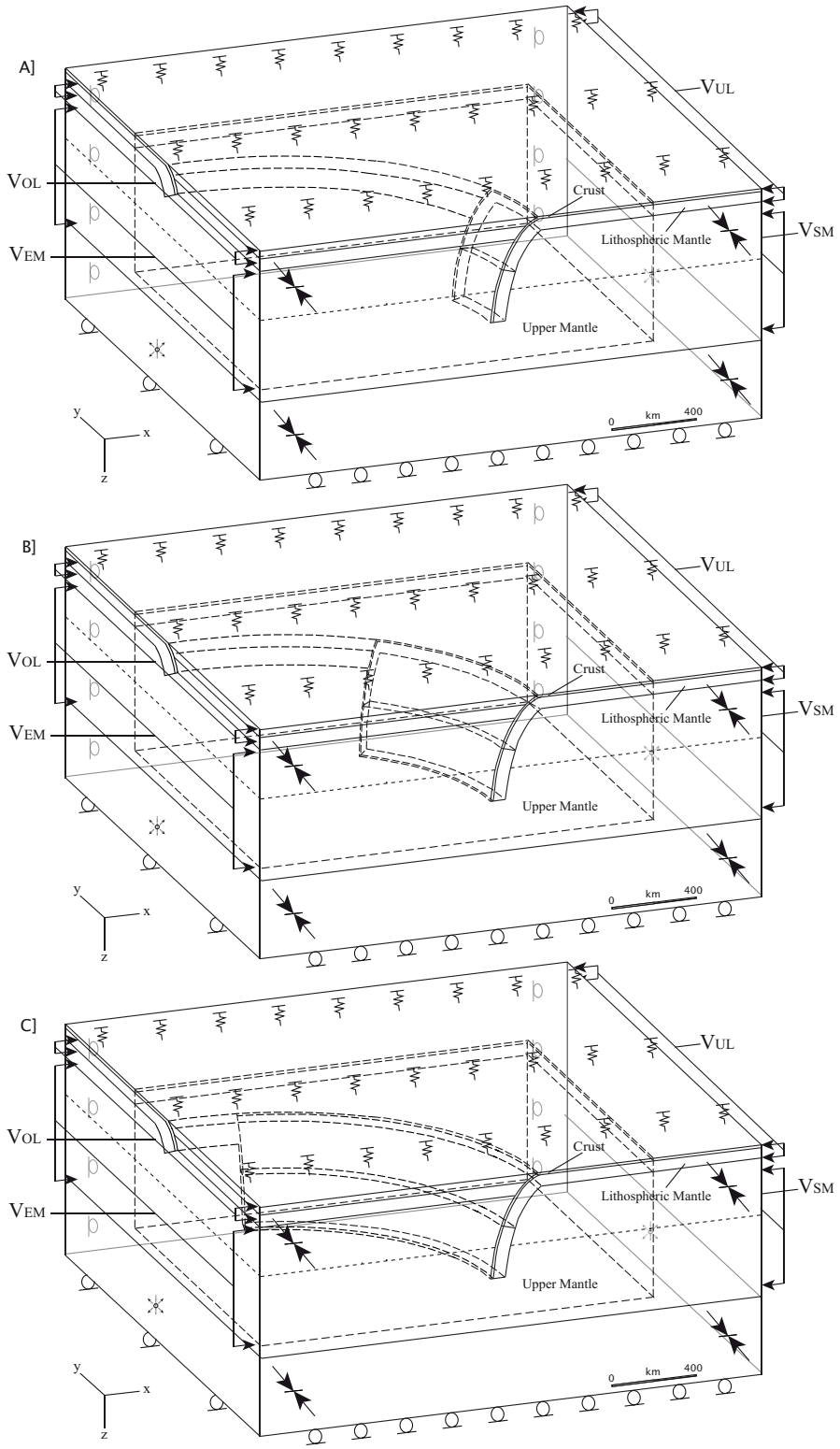

Fig. 3.7. (caption in the next page)

Fig. 3.7. Geometry and boundary conditions for the curved 3D models with down-concave slab. Symbolic representation of boundary conditions is the same used in Figure 3.5; brhigth symbols refer to hided planes. The front boundary surfaces are symmetry planes. The dashed plane within the lithosphere separates the lower part of the slab interested by a density contrast, and the upper part with no forced density contrast. The dashed box shows the part of the model where results are shown in section 4.3.

Curved trench - concave slab 3D models

With these models I simulate convergent margins described by a curved trench with concave downward slab shape (typical of subductions with retreating hinge behavior). Variable trench lateral extent is considered (figure 3.7).

Curved trench - convex slab 3D models

Curved slabs with concave upward shape (that characterize the advancing hinge subductions), are also simulated. Also in this case, geometries exhibit different lateral dimensions (figure 3.8).

3D models with variable depth of the slabs

These models provide a set of different geometries that summarize the previous investigated features. Both linear and curved trench shapes were provided with different depths reached by the subducted lithosphere (figure 3.9). In some models the lithosphere lies over the upper-lower mantle interface, while in others the slab penetrates the lower mantle.

The modelling assumption are the same described above for 2D geometry, with additional boundary conditions required for new lateral boundaries. A symmetry plane condition is imposed to the frontal surfaces of each model (i.e. planes parallel to the subduction direction) and a roller plane condition (fixed in the horizontal direction) is applied to the opposite backside surfaces.

In accordance with the strategy used in the previous phases, all 3D models include a Winkler foundation under the basal plane and an isostatic spring on surface. The lithospheric and asthenospheric boundaries can be either kept free or fixed in the horizontal direction, or alternatively the prescribed displacements were applied to simulate the plate convergence and/or the mantle relative flow.

A full list of developed 3D models, together with meshes statistics can be found in table 3.5. In figure 3.4c a mesh representative for the 3D models is shown.

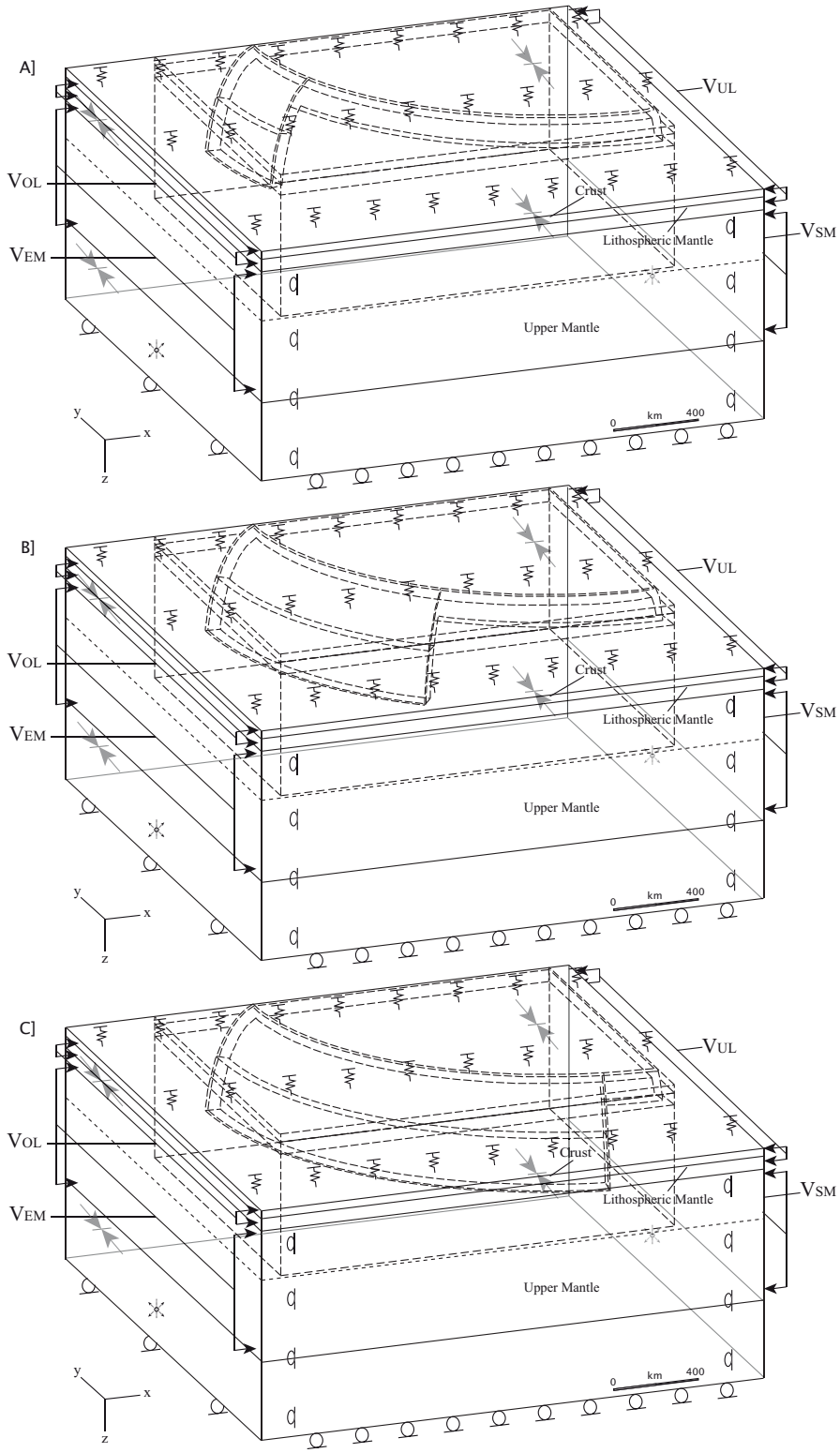

Fig. 3.8. (caption in the next page)

Fig. 3.8. Geometry and boundary conditions for the curved 3D models with up-convex slab. Symbolic representation of boundary conditions is the same used in Figure 3.5; brhigth symbols refer to hided planes. The front boundary surfaces are symmetry planes. The dashed plane within the lithosphere separates the lower part of the slab interested by a density contrast, and the upper part with no forced density contrast. The dashed box shows the part of the model where results are shown in section 4.3.

3.8.4 Solving parameters

Finite element modeling was performed using the software COMSOL Multiphysics (www.comsol.com). For the solution of the PDE's the UMFPACK algorithm has been used.

All the models were initially resolved through a static analysis (static viscoelastic initialization in COMSOL nomenclature). This approach is required to ensure an initial balance between the applied forces and

Model name	Reference figure	Model lenght/width/depth (km)	Slab depth (km)	N° of elements	Degrees of freedom
2D and para-3D					
shallow-2D	3.3a	2350x1000	450	14191	184848
steep-2D	3.3b	2350x1000	450	14426	187902
para-3D	3.5	2350x1000x1000	450	72378	2056536
3D Linear trench					
L3D-500	3.6a	2000x1250x1000	450	68821	1956999
L3D-1000	3.6b	2000x1500x1000	450	83729	2379180
L3D-2000	3.9a	2350x2000x1000	450	66172	1883337
L3D-3000	3.6c	2000x2500x1000	450	145179	4119246
L3D-z500	3.9b	2350x2000x1000	500	59805	1705017
L3D-z600	3.9c	2350x2000x1000	600	62086	1769148
L3D-z670	3.9d	2350x2000x1000	670	64769	1844460
L3D-z670rlb	3.9e	2350x2000x1000	670	150048	4211133
L3D-z670fwd	3.9g	2350x2000x1000	670	158691	4463253
L3D-z800	3.9f	2350x2000x1000	800	67155	1911645
3D Curved trench - concave slab					
CCV3D-20	3.7a	2350x2000x1000	450	42513	1217196
CCV3D-50	3.7b and 3.9h	2350x2000x1000	450	72394	2068629
CCV3D-80	3.7c	2350x2000x1000	450	88983	2538213
CCV3D-50-z500	3.9i	2350x2000x1000	500	68104	1948491
CCV3D-50-z600	3.9j	2350x2000x1000	600	70100	2004711
CCV3D-50-z670	3.9k	2350x2000x1000	670	71588	2046219
CCV3D-50-z670rlb	3.9l	2350x2000x1000	670	119241	3362559
CCV3D-50-z670fwd	3.9m	2350x2000x1000	670	165943	4675113
CCV3D-50-z800	3.9n	2350x2000x1000	800	74310	2122527
3D Curved trench - Convex slab					
CVX3D-20	3.8a	2350x2000x1000	450	46709	1329852
CVX3D-50	3.8b	2350x2000x1000	450	54258	1541325
CVX3D-80	3.8c	2350x2000x1000	450	59166	1678557

Table 3.5. List of developed 2D and 3D models and relative statistics.

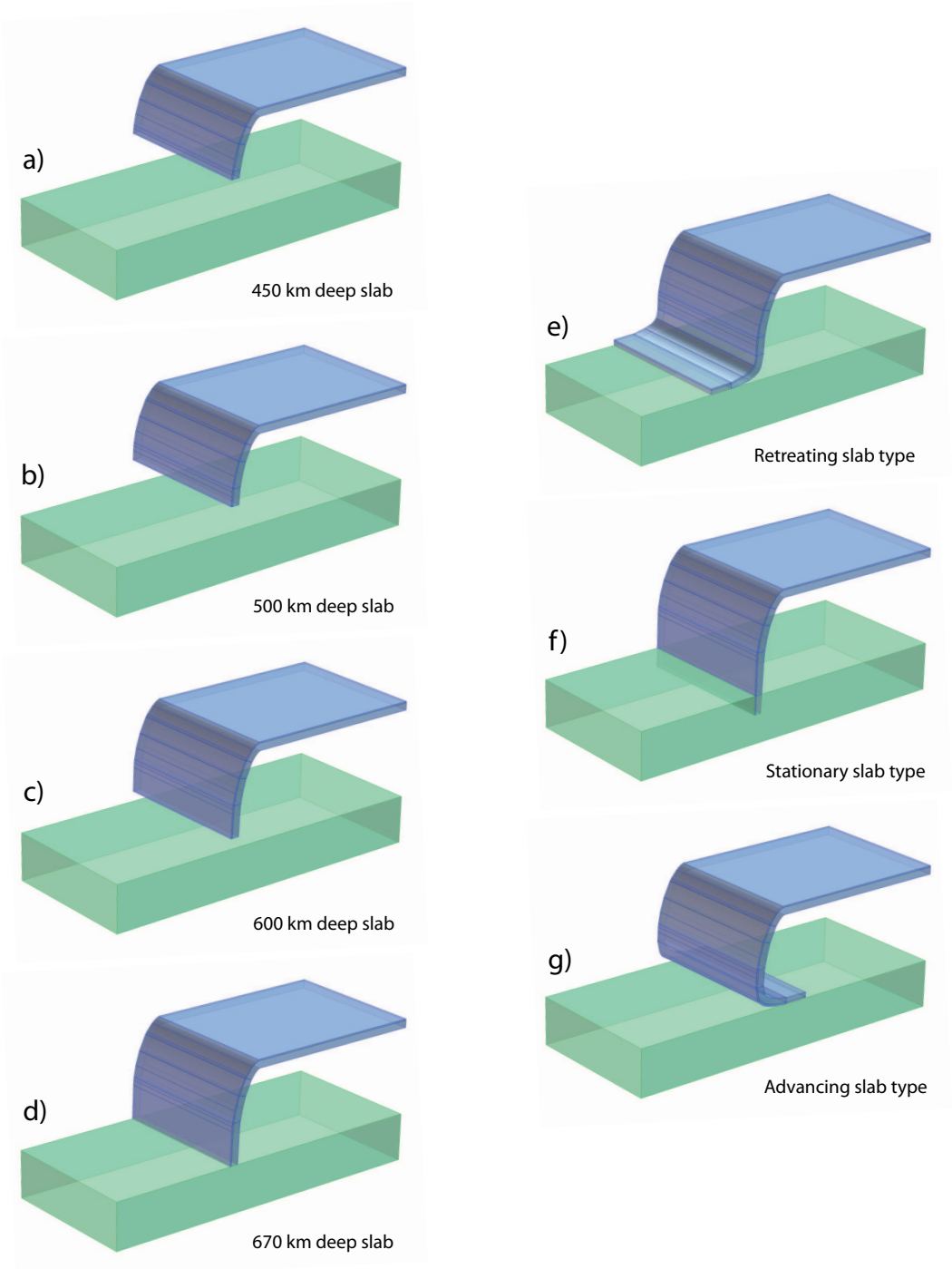

Fig. 3.9 (continued)

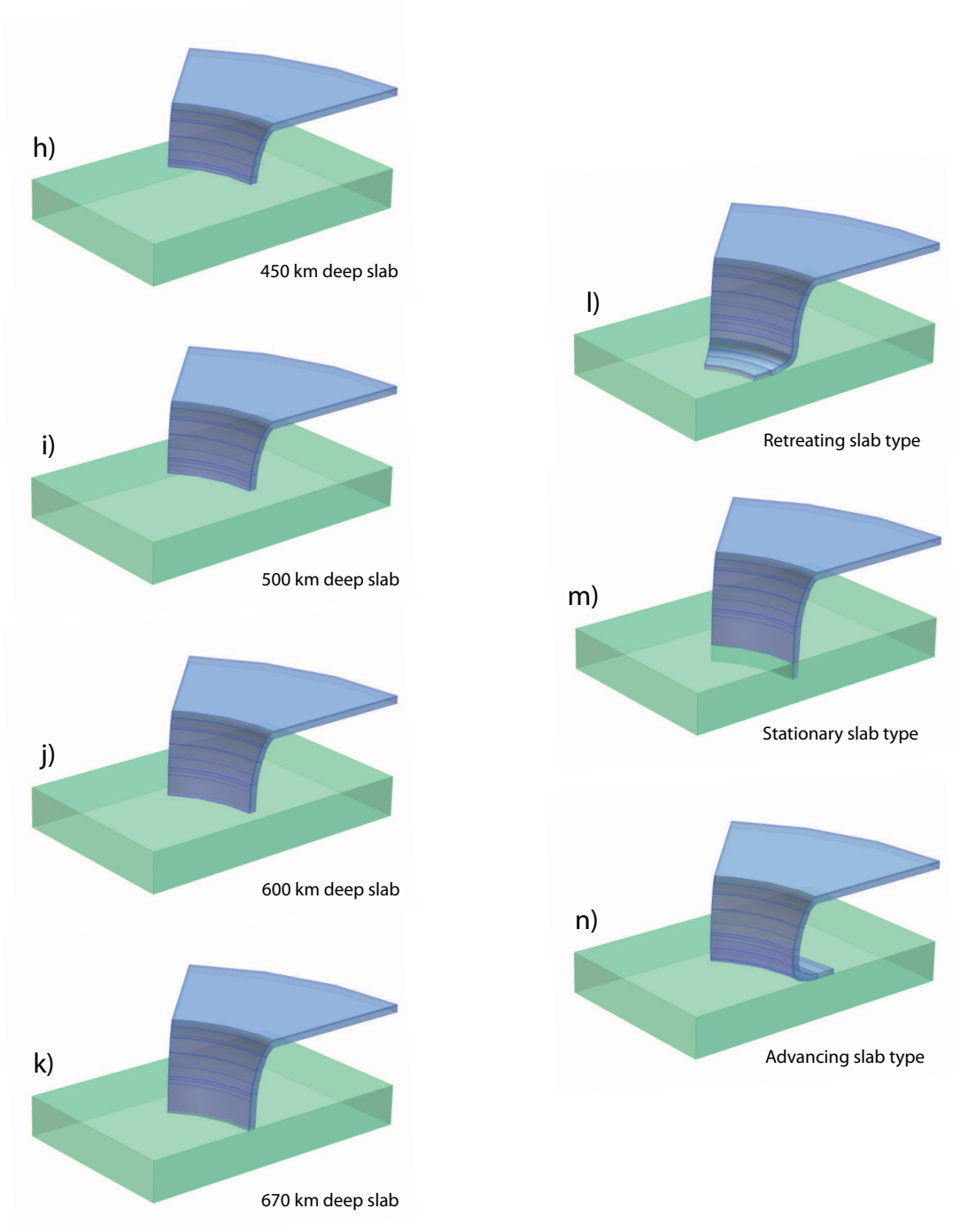

Fig. 3.9 (caption in the next page)

Fig. 3.9. Simplified geometries showing only the descending lithosphere (blue) and the lower mantle (green) in models providing variable depth for the slab. Linear and curved geometries have slab at deep of 450 km (a and h), 500 km (b and i), 600 km (c and j) and 670 km (d and k). Geometries representative of subductions with advancing (e and l), stationary (f and m) or retreating (g and n) trenches (see section 2.2 for the choice of introducing such geometries) are shown. Boundary conditions (not shown) are the same used in previous linear and curved 3D models. The total dimensions of the various geometries are listed in table 3.5.

the internal initial deformation of the system. The static solution is subsequently used as an initial condition for the transient analysis.

The stability of the solutions is always achieved in a time of model evolution of $250\ kyr$, so that the crust behaves largely in an elastic way as it is characterized by higher relaxation times (see sec. 3.6).

All the models results are shown for the 250 kyr time, as in this time frame the model evolves toward a full steady state.

4

Plate scale models results

Guideline to the chapter contents

This chapter describes the results obtained for the plate scale models previously described (Chapter 3). Because of the large amount of performed models, only a part of the whole outputs are here shown. The results of the remaining models are included in the CD-rom accompanying this thesis. Moving from 2D to more complex 3D models, all the suitable interactions between the driving and resisting forces will be investigated. First, using 2D models results (section 4.1), I initially show: 1) the role of the slab pull over the definition of the stress field within the subducted lithosphere (section 4.1.2); 2) the dependency of the stress field affecting the slabs on geometry (dip of the slab) and kinematics (velocity of convergence between upper and lower plates and their absolute velocity with respect to the underlying mantle) of subduction zones (sections 4.1.3 and 4.1.4); 3) the role of varying the rheological parameters (section 4.1.5). All these 2D simulation are intended to reproduce the stress field in regions far from the tips of the subduction system. Afterwards, in section 4.2 I compare these results with those obtained from the para-3D models, to verify the consistency of the 2D and 3D approximations, and to analyze the major differences between the two classes of models. In section 4.3 the solution obtained using real 3D geometries will be discussed. Starting from the reference models and varying the geometry and the initial parameters, first, the stress state affecting the subducting lithosphere (section 4.3.1), and afterward the stress characterizing the upper and the lower plates at shallow depths (section 4.3.3) will be shown. The last section 4.3.3 provides a comparison between models and real cases.

4.1 2D model results

4.1.1 Some introductory remarks

The solutions obtained for the two (steep and shallow; see section 3.8.1) modelled geometries are summarized respectively in tables 4.1 and 4.2. The steep-type models aim to simulate the West directed (e.g., Mariana) subductions while the shallow-type models are representative for the East or North-East directed (e.g., Chilean) subductions (Figure 4.1). The introduction or not (subclass NoG models) of a negative buoyancy (slab pull) as a forcing factor and the systematic variation of the plate and mantle kinematics (Figure 3.3) generated all the listed solutions. I tested various magnitudes for both plate convergence (ranging from 0 cm/yr to 5 cm/yr) and mantle flow (ranging from 0 cm/yr to 8 cm/yr) velocities.

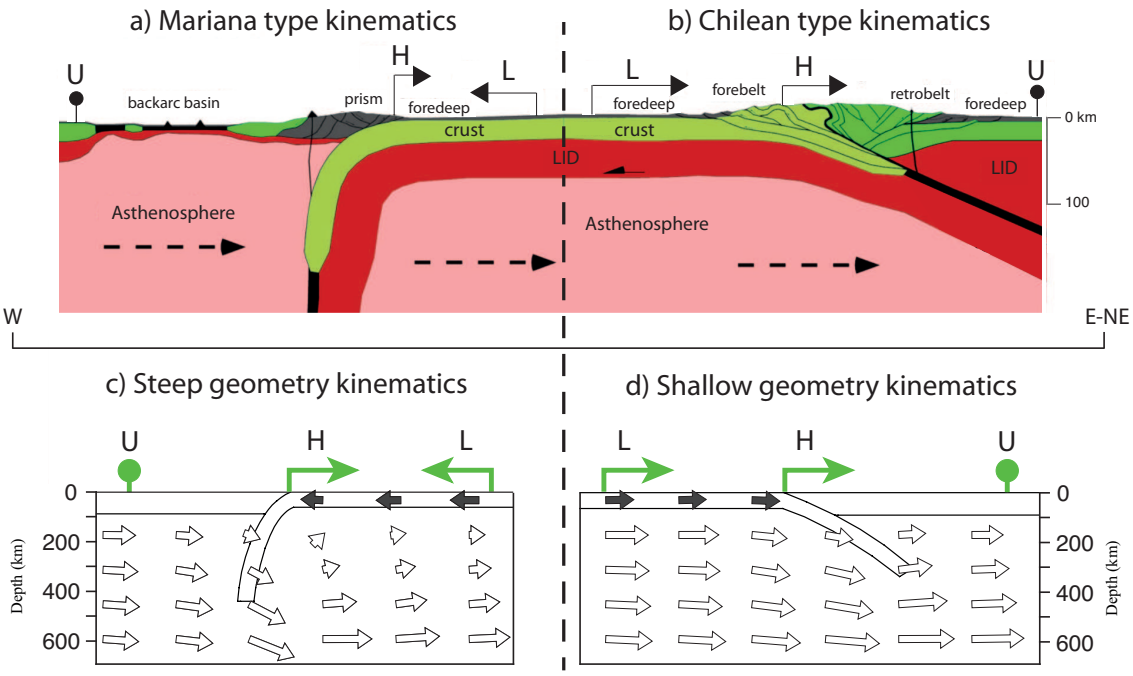

Fig. 4.1. Schematic sections showing a) the Mariana type and b) the Chilean type settings (see section 2.2) and kinematics (see section 2.4). In the first case, the subduction hinge (H) migrates towards the the converging lower plate (L) while the upper plate (U) is fixed; in the second case the subduction hinge (H) migrates towards the fixed upper plate (U). The lower panels show the velocity fields obtained for the lithosphere (black arrows) and the upper mantle (white arrows) in models c) M-windW-convdx and d) C-windE-convdx (see tables 4.2 and 4.1) representative for the two end-members kinematics.

Model name	Slab pull	(U)pper/(L)ower plate convergence	Convergence rate (mm/yr)	Sustaining mantle	Encroaching mantle	Mantle flow rate (mm/yr)
Shallow 2D geometry						
C-nowind	X					
C-nowind-conv	X	$U+L$	$25+25$			
C-nowind-convdx	X	L	50			
C-nowind-convsx	X	U	50			
C-nowind-conv-NoG		$U+L$	$25+25$			
C-nowind-convdx-NoG		L	50			
C-nowind-convsx-NoG		U	50			
C-windW	X				X	80
C-windW-conv	X	$U+L$	$25+25$		X	80
C-windW-convdx	X	L	50		X	80
C-windW-convsx	X	U	50		X	80
C-windW-conv-NoG		$U+L$	$25+25$		X	80
C-windW-convdx-NoG		L	50		X	80
C-windW-convsx-NoG		U	50		X	80
C-windE	X			X		80
C-windE-conv	X	$U+L$	$25+25$	X		80
C-windE-convdx	X	L	50	X		80
C-windE-convsx	X	U	50	X		80
C-windW-conv-NoG		$U+L$	$25+25$		X	80
C-windW-convdx-NoG		L	50		X	80
C-windW-convsx-NoG		U	50		X	80
C-nowind-convdx1	X	L	10			
C-nowind-convdx2	X	L	20			
C-nowind-convdx4	X	L	40			
C-windE4	X			X		40
C-windE4-convdx4	X	L	40	X		40
C-windW4	X				X	40
C-windW4convdx4	X	L	40		X	40
C-windE4-NoG				X		40
C-windE2	X			X		20
C-windE2-convdx4	X	L	40	X		20
C-windE8-convdx4	X	L	40	X		80
C-nowind-heavy	X					
C-windE2-heavy	X			X		20
C-windE4-heavy	X			X		40
C-windE8-heavy	X			X		80

Table 4.1. Compilation of the results obtained for the shallow type 2D-geometry (refer to figure 3.3a). For each solution, the activated forces (X means active) and their magnitudes are listed.

Model name	Slab pull	(U)pper/(L)ower plate convergence	Convergence rate (mm/yr)	Sustaining mantle	Encroaching mantle	Mantle flow rate (mm/yr)
Steep 2D geometry						
M-nowind	X					
M-nowind-conv	X	$U+L$	$25+25$			
M-nowind-convdx	X	L	50			
M-nowind-convsx	X	U	50			
M-nowind-conv-NoG		$U+L$	$25+25$			
M-nowind-convdx-NoG		L	50			
M-nowind-convsx-NoG		U	50			
M-windW	X				X	80
M-windW-conv	X	$U+L$	$25+25$		X	80
M-windW-convdx	X	L	50		X	80
M-windW-convsx	X	U	50		X	80
M-windW-conv-NoG		$U+L$	$25+25$		X	80
M-windW-convdx-NoG		L	50		X	80
M-windW-convsx-NoG		U	50		X	80
M-windE	X			X		80
M-windE-conv	X	$U+L$	$25+25$	X		80
M-windE-convdx	X	L	50	X		80
M-windE-convsx	X	U	50	X		80
M-windW-conv-NoG		$U+L$	$25+25$		X	80
M-windW-convdx-NoG		L	50		X	80
M-windW-convsx-NoG		U	50		X	80
M-nowind-convdx1	X	L	10			
M-nowind-convdx2	X	L	20			
M-nowind-convdx4	X	L	40			
M-windW4	X				X	40
M-windW4-convdx4	X	L	40		X	40
M-windE4	X			X		40
M-windE4convdx4	X	L	40	X		40
M-windW4-NoG					X	40
M-windW2	X				X	20
M-windW2-convdx4	X	L	40		X	20
M-windW8-convdx4	X	L	40		X	80
M-nowind-heavy	X					
M-windW2-heavy	X				X	20
M-windW4-heavy	X				X	40
M-windW8-heavy	X				X	80

Table 4.2. Compilation of the results obtained for the shallow type 2D-geometry (refer to figure 3.3b). For each solution, the activated forces (X means active) and their magnitudes are listed.

4.1.2 Effects of the gravitational slab pull

If no convergence between the upper and lower plates is assumed and if only slab pull is applied (Figures 4.2 and 4.3), the resulting stress field in the slab is controlled by the flexural bending of the sinking plate. It is characterized by down-dip extension in the upper (stretching outer arc) part and by compression in the lower (shortening inner arc) portion of the slab, which is consistent with previous models [e.g., *Giunchi et al.*, 1996; *Carminati et al.*, 1999]. At the tip of the slab, down-dip compression prevails (particularly in the crustal part of the shallow geometry model (Figure 4.2a), due to the mantle resistance to the slab penetration. The upper plate is characterized by weak horizontal extension in Figure 4.3a and compression in Figure 4.2a. This may be due to the fact that the area characterized by density contrast in shallow slabs (Figure 4.2a) is smaller than that in deep slabs (Figure 4.3a) and to different flow patterns in the mantle wedge. Consequently, the down-pull associated with this negative buoyancy would produce a larger slab retreat (and consequently stretching in the upper plate) in the steep slab case. It cannot be excluded, however, that the different model geometry could play a role in the definition of the state of stress of the upper plate.

4.1.3 Effects of the lithospheric convergence

If plate convergence is forced, the lithosphere undergoes an overall compression while the slabs show down-dip tension as in case of only slab pull is active.

Regardless the geometry (compare Figures 4.2d and 4.3d) and the convergence rate (shown in the accompanying material), results show comparable stress directions. The higher the convergence rate the greater the magnitude of the compression affecting the lithosphere. Since the convergence rate affects the stress magnitude rather than its direction [*Carminati and Petricca*, 2010], in the following results I include only models characterized by a converging lower plate and a fixed upper plate.

If convergence at 4 cm/yr rate (i.e., comparable to the mantle flow velocity) is added to slab pull (Figures 4.2d and 4.3d), the state of stress in the slab is only slightly changed with respect to that of Figures 4.2a and 4.3a. The biggest changes are observed in the upper plate, where only horizontal compression occurs. However, in general, the extensional component is slightly decreased in Figures 4.2e and 4.3e with respect to Figures 4.2b and 4.3b both in crustal and lithospheric mantle parts of the slab, whereas down-dip compression is slightly increased in Figures 4.2f and 4.3f with respect to Figures 4.2c and 4.3c.

When the slab pull effects are removed, only a decrease (or disappearance in the shallow-type geometry) of the magnitude of tensional stress within the slab is obtained (shown in the accompanying material), as

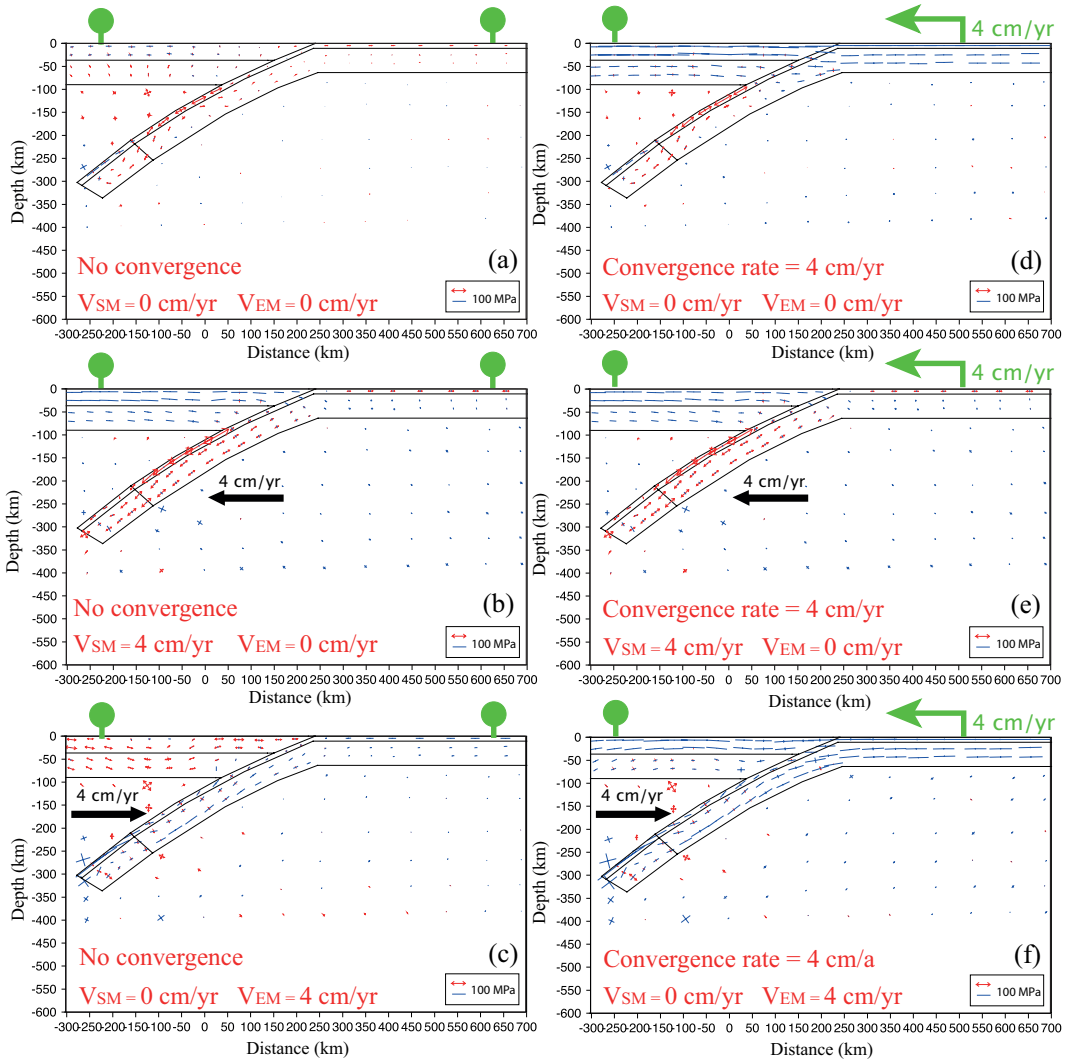

Fig. 4.2. Principal stress axes for models characterized by shallow slabs (geometry of Figure 3.3a). Assuming no convergence between upper and lower plates, the following model results are shown: (a) only slab pull (density contrast) applied, (b) slab pull and 4 cm/yr left directed mantle flow (sustaining the slab), and (c) slab pull and 4 cm/yr right directed mantle flow (opposing the slab dip). Assuming a convergence rate of 4 cm/yr between upper and lower plates, the following model results are shown: (d) only slab pull (density contrast) applied, (e) slab pull and 4 cm/yr left directed mantle flow, and (f) slab pull and 4 cm/yr right directed mantle flow. Blue lines indicate compressional stresses, and red lines indicate extensional stresses.

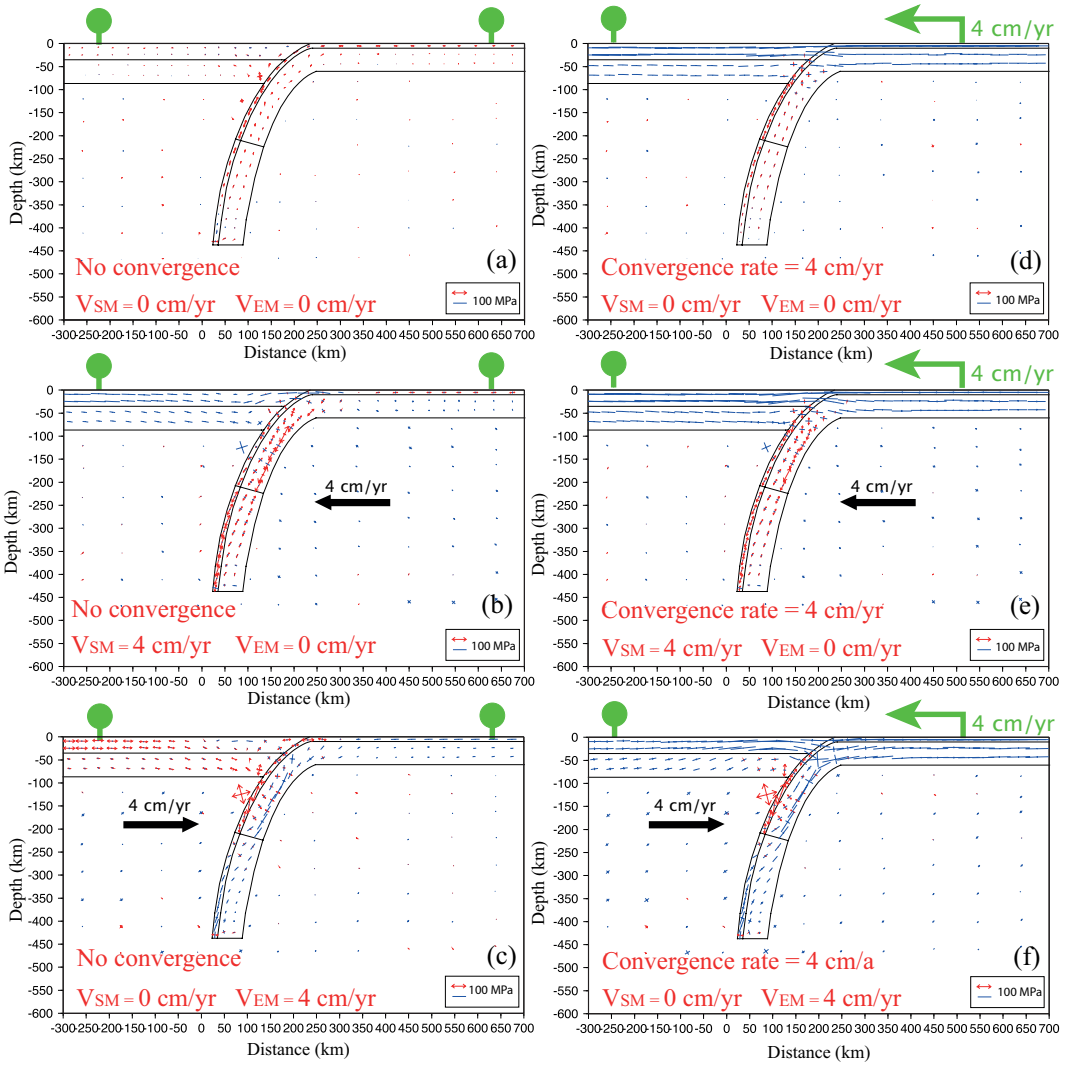

Fig. 4.3. Principal stress axes for models characterized by steep slabs (geometry of Figure 3.3b). Same representation as in Figure 4.2. Assuming no convergence, the following model results are shown: (a) only slab pull (density contrast) applied, (b) slab pull and 4 cm/yr left directed mantle flow (sustaining the slab), and (c) slab pull and 4 cm/yr right directed mantle flow (opposing the slab dip). Assuming a convergence rate of 4 cm/yr, the following model results are shown: (d) only slab pull (density contrast) applied, (e) slab pull and 4 cm/yr left directed mantle flow, and (f) slab pull and 4 cm/yr right directed mantle flow.

expected. This means especially that the compression related to the plate convergence does not propagate deep within the down-going lithosphere.

4.1.4 Effects of mantle flow

If mantle flow (either sustaining, as in Figures 4.2b and 4.3b, or contrasting subduction, as in Figures 4.2c and 4.3c) is applied, then the state of stress of the slab changes radically. Irrespective of the geometry, mantle flow sustaining the subduction is associated with overall down-dip extension. Mantle flow contrasting the subduction induces down-dip compression, which also affects the lithospheric mantle portion of the slab. In models characterized by mantle flow contrasting the subduction (Figures 4.2c and 4.3c), the horizontal extensional component increases in the upper plate, whereas in models in which mantle flow sustains subduction (Figures 4.2b and 4.3b), the horizontal compression drastically increases in the upper plate.

Given the importance of mantle flow rates in the definition of the stress field in the subducting plate and the uncertainties related with the calculation of absolute plate velocities, simulations were performed assuming mantle flow rates varying between 0 and 8 cm/yr, with convergence rates equal to 0 cm/yr and 4 cm/yr.

For simplicity, and in agreement with observations (see figure 4.1b and d), shallow subductions were modeled assuming mantle flow sustaining the slab (Figure 4.4) and steeply dipping subductions (see figure 4.1 a and c) were modeled assuming mantle flow opposing the subduction (Figure 4.5). These results confirm our earlier conclusion about the state of stress in the slab, i.e., in the absence of plate convergence, down-dip extension is enhanced when mantle flow is applied in the same direction of the slab dip (Figures 4.4b-4.4d) and down-dip compression is enhanced when mantle flow opposes the dip of the slab (Figures 4.5b-4.5d). However, Figures 4.4 and 4.5 show that mantle flow rates are also important, since the control exerted by mantle flow on the state of stress within the slab increases with increasing rates. Although small variations (with respect to Figures 4.4a and 4.5a) in the slab state of stress can be observed for mantle flow rates of 2 cm/yr (Figures 4.4b and 4.5b), evident changes are obtained only if mantle flow rates are as large as 4 cm/yr (Figures 4.4c and 4.5c). Faster rates (8 cm/yr, as in Figures 4.4d and 4.5d) further increase these changes. If convergence is forced, down-dip compression is reinforced in models with mantle flow opposing the dip of the slab (Figures 4.5f-4.5h), whereas down-dip extension is only slightly decreased in models assuming mantle flow sustaining the slab. The state of stress in the upper plate along shallow and

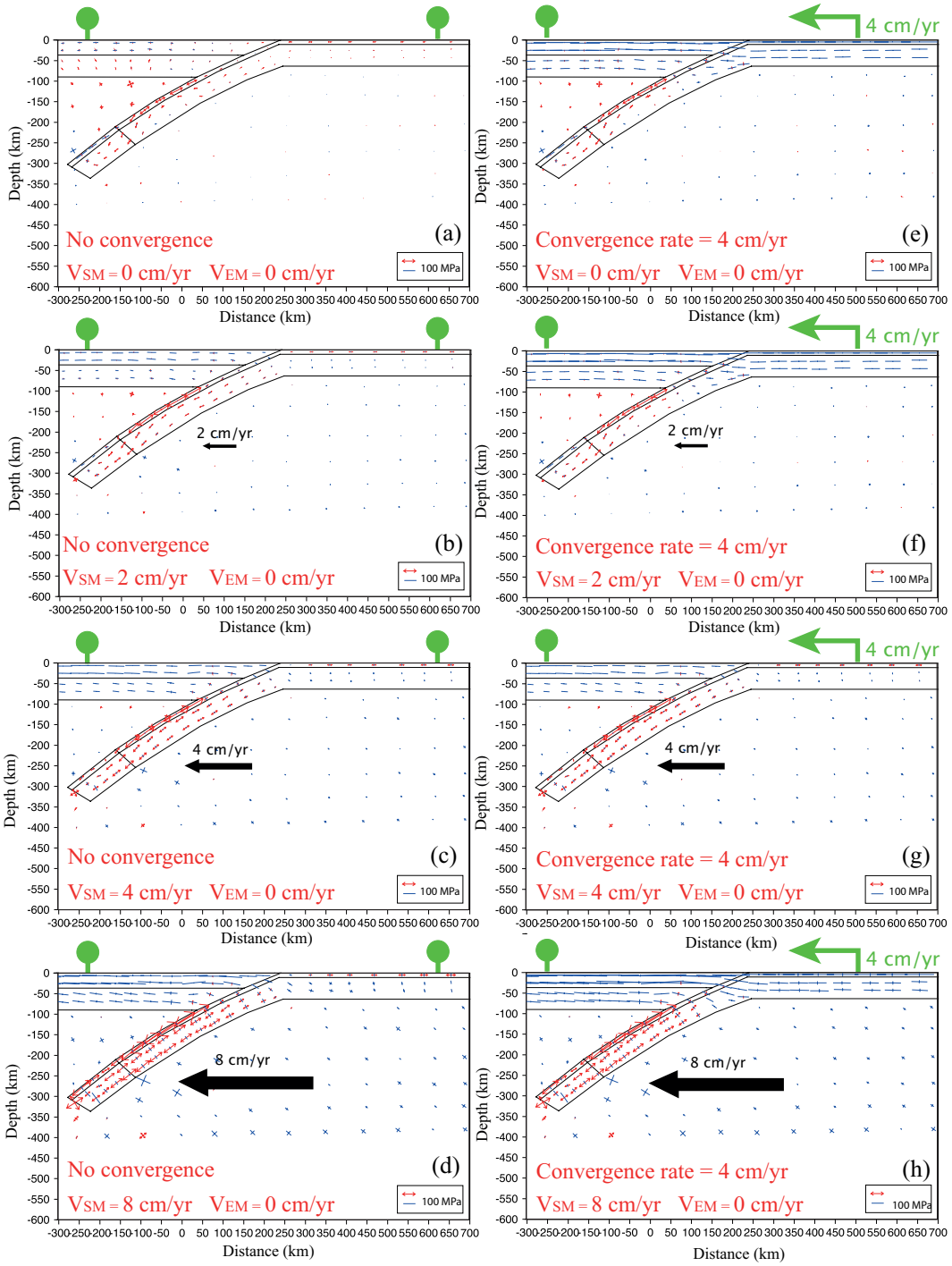

Fig. 4.4. The effects of variable mantle flow rates on the state of stress of subducting slabs and upper plates are shown for models with shallow geometry. In agreement with observations, shallow subductions assuming mantle flow sustaining the slab. (a–d) The mantle flow velocity is increased from 0 to 8 cm/yr, while the convergent rate is kept equal to 0 cm/yr. (e–h) The effects of the same increase of mantle flow rates are tested assuming a convergence rate of 4 cm/yr.

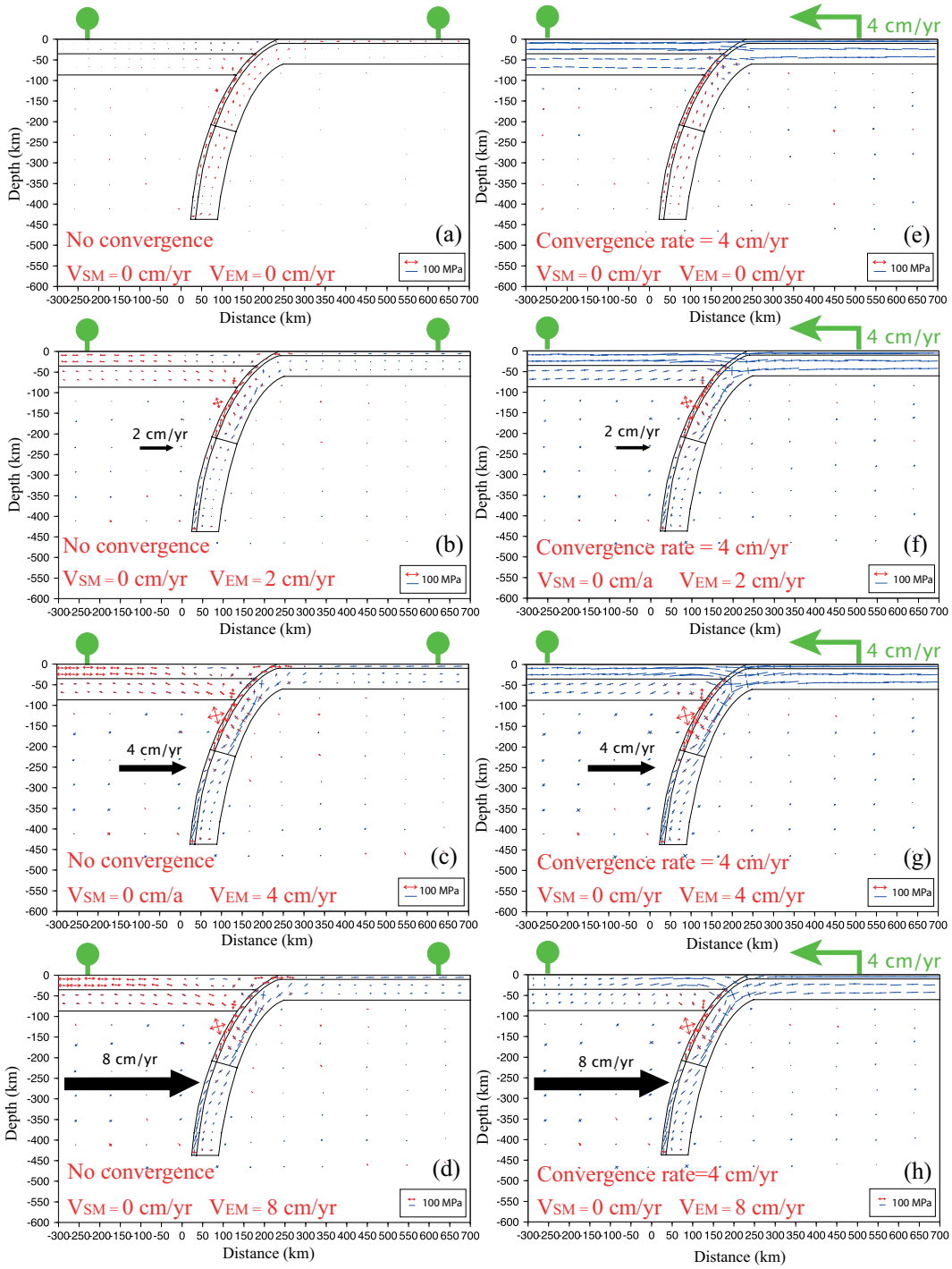

Fig. 4.5. The effects of variable mantle flow rates on the state of stress of subducting slabs and upper plates are shown for models with steep geometry. In agreement with observations, steeply dipping subductions were modeled assuming mantle flow opposing the subduction. (a–d) The mantle flow velocity is increased from 0 to 8 cm/yr, while the convergent rate is kept equal to 0 cm/yr. (e–h) The effects of the same increase of mantle flow rates are tested assuming a convergence rate of 4 cm/yr. Notice that the stress scale in panels d and h is different from that of the other illustrations for a better representation.

steep subductions (characterized in these simulations by sustaining mantle flow) is always compressional (compression increases with increasing mantle flow rate).

4.1.5 Rheological parameters

The models that were run to consider different rheological parameters for both the lithospheric mantle and the asthenospheric layer, are listed in table 4.3. The viscosity of the lithospheric mantle was varied between 10^{21} Pa s and 10^{23} Pa s, assuming mantle flow rates of 4 cm/yr, either sustaining or opposing the slab, according to subduction polarity. A low viscosity of the lithospheric mantle (i.e., 10^{21} Pa s) induces a low accumulation of stress within this layer in the slab (Figures 4.6a and 4.6e). In models characterized by slabs sustained by mantle flow, a lower magnitude of down-dip extension occurs within the lithospheric mantle when low viscosity is assumed for this layer. In models with mantle flow opposing the slab down-dip compression in the slab's lithospheric mantle vanishes when low viscosity is assumed for this layer. The higher the viscosity of the lithosphere the longer the stress axes, i.e. greater extension occurs in sustained slab (Figure 4.6c) and greater compression in case of encroaching mantle flow (Figure 4.6g). The effects on stress magnitudes are also emphasized in the upper plates and bending parts of the slabs.

The effects of introducing a 200 km thick asthenosphere, thus forcing a higher decoupling between the lithosphere and the upper mantle, are shown in Figures 4.6d and 4.6h. In terms of the pattern, the slab stress fields predicted by models including the asthenospheric layer do not differ significantly from those of the reference models (Figures 4.6b and 4.6f). The absence of significant pattern changes is due to the fact that the viscosity contrast between lithosphere and upper mantle ($5\text{x}10^{22}$ versus 10^{21} Pa s) is sufficient enough to provide some decoupling between the subducting slab and mantle wedge. However, the models including the asthenosphere layer show, in the deeper parts of the slab, larger amounts of compression in the crust and weak extension in the lithospheric mantle.

The region characterized by the density contrast, limited in previous described models to the portion of the slab deeper than 200 km, was enlarged in one set of models, starting from 100 km depth. The enlargement of the area of the density anomaly induces an obvious increase of down-dip extension in the slab when no mantle flow is included (Figures 4.7b and 4.7e). This is due to the increased slab pull force. In models with mantle flow sustaining the slab, the increased slab pull further increases the down-dip extension in the slab (4.7c); however, for fast mantle flow encroaching the slab, the amount of down-dip compression within the slab, although decreased by the increased slab pull, is retained (Figure 4.7f).

Model name	Slab pull	(U)pper/(L)ower plate convergence	Convergence rate (mm/yr)	Sustaining mantle	Encroaching mantle	Mantle flow rate (mm/yr)
C-nowind-lit21	X	–	–			
C-nowind-lit23	X	–	–			
C-windW-lit21	X	–	–		X	40
C-windW-lit23	X	–	–		X	40
C-windE-lit21	X	–	–	X		40
C-windE-lit23	X	–	–	X		40
C-nowind-ast17	X	–	–			
C-nowind-ast19	X	–	–			
C-nowind-ast21	X	–	–			
C-windE-ast17	X	–	–	X		40
C-windE-ast19	X	–	–	X		40
C-windE-ast21	X	–	–	X		40
C-windW-ast17	X	–	–		X	40
C-windW-ast19	X	–	–		X	40
C-windW-ast21	X	–	–		X	40
M-nowind-lit21	X	–	–			
M-nowind-lit23	X	–	–			
M-windW-lit21	X	–	–		X	40
M-windW-lit23	X	–	–		X	40
M-windE-lit21	X	–	–	X		40
M-windE-lit23	X	–	–	X		40
M-nowind-ast17	X	–	–			
M-nowind-ast19	X	–	–			
M-nowind-ast21	X	–	–			
M-windE-ast17	X	–	–	X		40
M-windE-ast19	X	–	–	X		40
M-windE-ast21	X	–	–	X		40
M-windW-ast17	X	–	–		X	40
M-windW-ast19	X	–	–		X	40
M-windW-ast21	X	–	–		X	40
C-nowind-heavy	X	–	–			
C-windE2-heavy	X	–	–	X		20
C-windE4-heavy	X	–	–	X		40
C-windE8-heavy	X	–	–	X		80
M-nowind-heavy	X	–	–			
M-windW2-heavy	X	–	–		X	20
M-windW4-heavy	X	–	–		X	40
M-windW8-heavy	X	–	–		X	80

Table 4.3. Compilation of the results obtained for the shallow (C-type) and the steep (M-type) 2D-geometry considering variations in rheological parameters or increasing slab pull force (heavy-type models). The lithospheric mantle viscosity ranges between 10e21 and 10e23 Pa s (lit-type models), while the asthenosphere viscosity ranges between 10e17 an 10e21 Pa s (ast-type models). For each solution, the activated forces (X means active) and their magnitudes are listed.

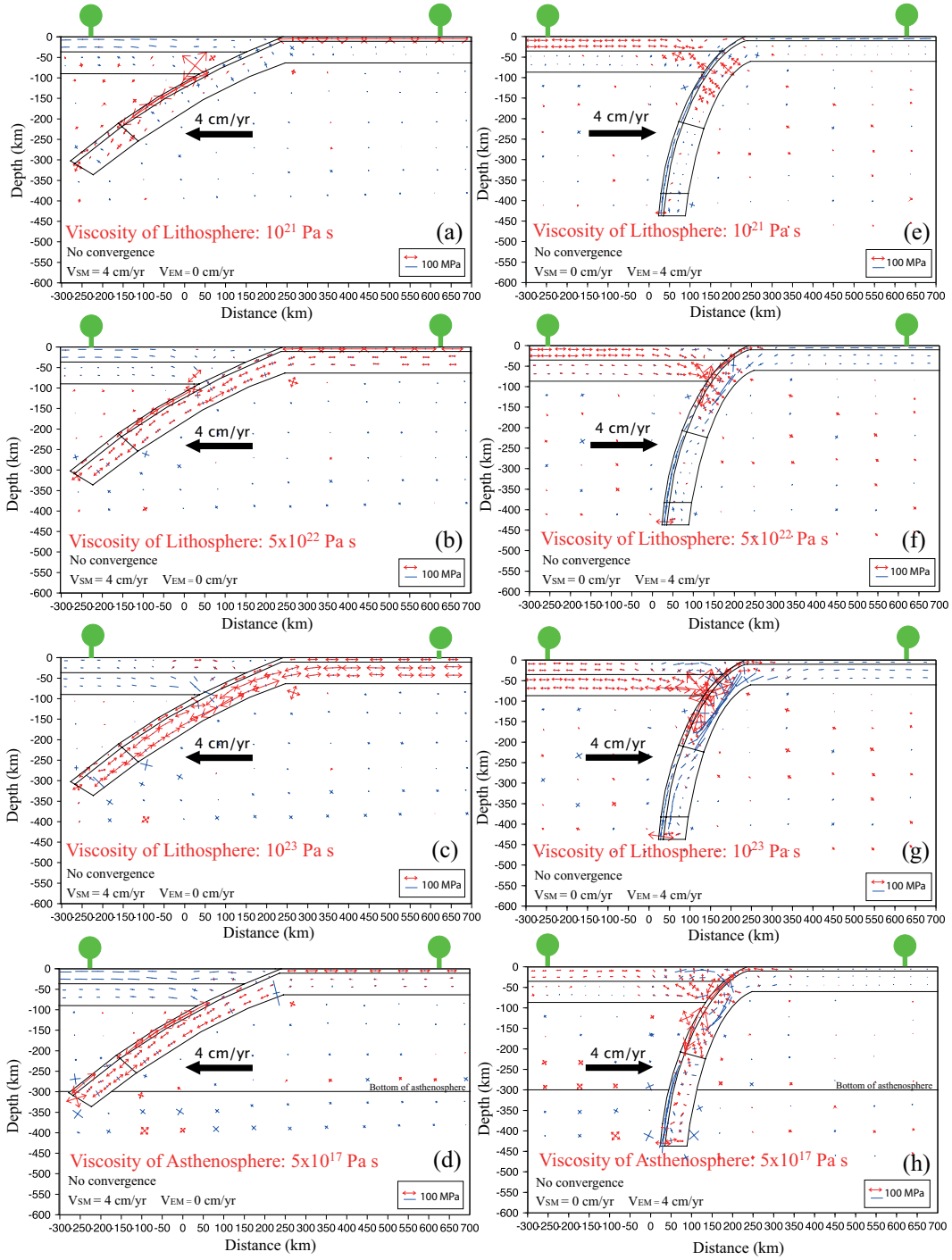

Fig. 4.6. The results of models in which a sensitivity analysis of lithospheric viscosity (a-c and e-g) and a 200 km thick asthenosphere (d and h) are compared with those of the reference models (b and f).

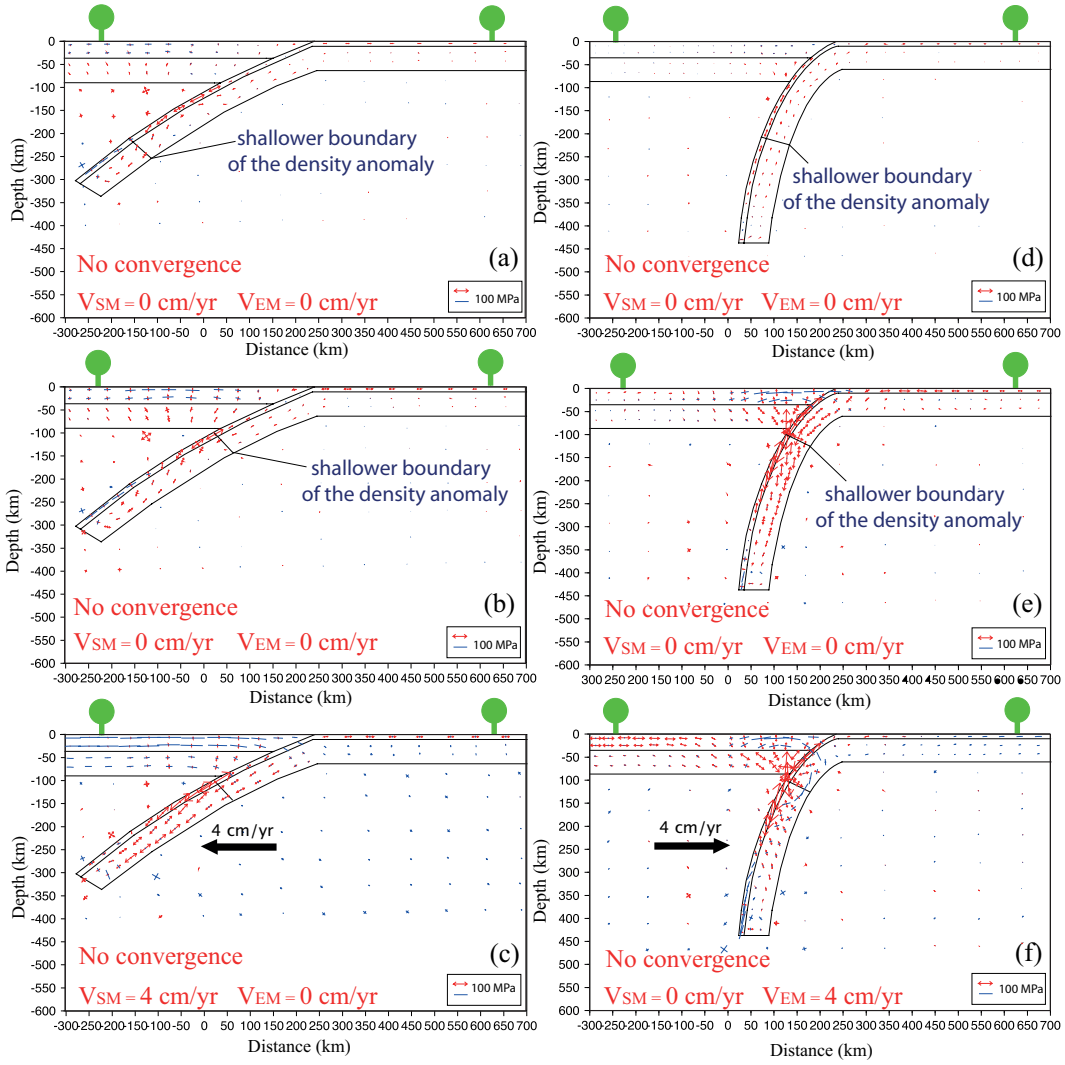

Fig. 4.7. The stress field obtained with models characterized by shallow (a-c) and steep (d-f) slabs with a density anomaly starting at a depth of 200 km (b-c and e-f) and at a depth of 100 km (a and d) are compared. Result of models forcing in addiction a mantle flow are also shown (c and f).

4.2 From 2D to 3D modelling

Proving the consistence between 2D and 3D modelling results is fundamental. At this scope, the end-members of 2D model results (i.e., forcing only by slab pull, sustaining or encroaching mantle flow) and the results obtained with the same kinematics applied to para-3D geometry and to real 3D geometries, are compared. Stress axes are plotted at 5 km and at 50 km depth in the para-3D result. For the sake of simplicity the effects of lithospheric convergence are not taken into account in this phase.

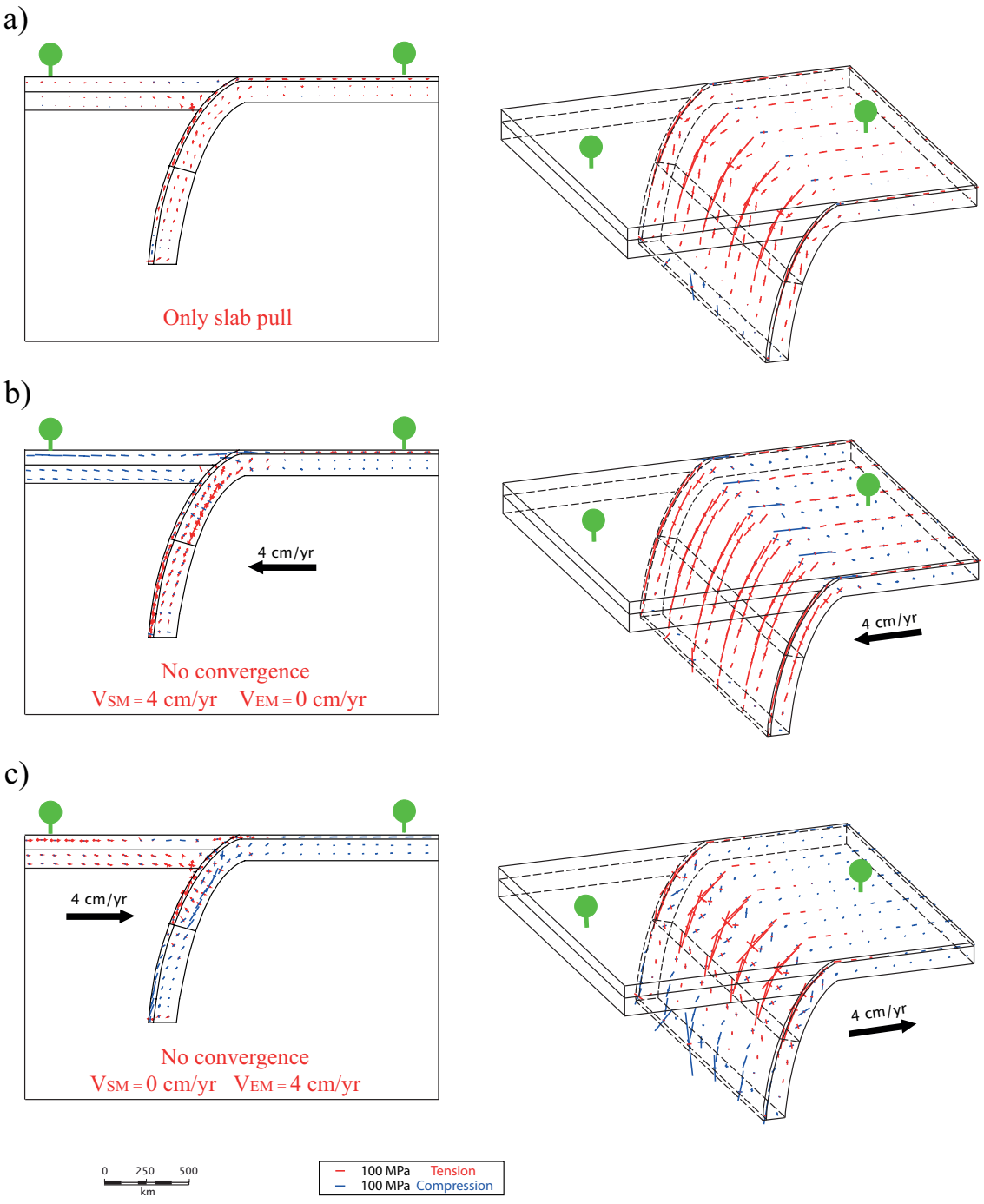

Fig. 4.8 (caption in the next page)

Fig. 4.8. Principal stress axes for 2D (left panels) and para-3D (right panels) models. Assuming no convergence between upper and lower plates, the following model results are compared: (a) only slab pull (density contrast) applied, (b) slab pull and 4 cm/yr left directed mantle flow (sustaining mantle flow), and (c) slab pull and 4 cm/yr right directed mantle flow (encroaching mantle flow). Blue lines indicate compressional stresses, and red lines indicate extensional stresses.

In figure 4.8, the left (results for 2D models) and right (for para-3D models) panels show very similar stress distribution. When slab pull is the only active force, the general down-dip tension observed along the slab for the 2D geometries, is largely reproduced in the three-dimensional case, mostly in the crust. (Figure 4.8a). Also the compression that affect the deeper portion of the subducting slab, is observed in both cases. When mantle flow sustains the sinking lithosphere (Figure 4.8b), longer along-slab oriented tensional axes are observed in the whole slab in the para-3D simulation. The compression, that in the previous case was generated in deeper slab regions, almost vanishes. Downdip compression is enhanced in para-3D model likewise for the 2D simulations, when encroaching mantle kinematics is forced (4.8c).

Compared with 2D results, the para-3D counterparts show higher magnitudes of tensional axes, especially in the shallower slab extrados, certainly induced by bending forces. This inference is supported by the evident increase in magnitude of the principal stress axes observed in case of greater slab retreat (cf. Figures 4.8a and 4.8c). When the mantle flow sustains the slab, magnitude decreases is observed, maybe because the retreat is not allowed (figure 4.8b).

If slab pull and, even more, if sustaining mantle is forced overall tension characterizes the crust at shallow depths. Only near the hinge slight compression generates in the lower plate (Figures 4.8a and b). In case of opposite mantle flow (Figure 4.8c) the same region shows tension axes, while the remaining shallow crust is in compression. Following these observations the stress field affecting the hinge region, i.e. the area of most interaction between the upper and the lower plate, is controlled by the drag effect of the mantle over the lithosphere, that pushes or moves away the plates among them. In the first case the upper plate operates as back-stop for the advancing lower plate, while in the second case the extension occurs following the hinge retreat.

An interesting observation is that, at crustal depth, the horizontal part of the subducting plate is characterized by horizontal trench-perpendicular compression for encroaching mantle flow, whereas when only slab pull or slab pull plus sustaining mantle flow are applied, only trench-perpendicular tension is observed. In addiction for both the 2D and para-3D cases, the unsubducted lithospheric mantle of the lower plate (at depths of ca. 50 km) is always under compression or, at most, neutral. This is always true, regardless of the imposed kinematics (cf. panels in figure 4.8). The upper plate is characterized by tension or compression depending on the imposed kinematics. However, the stress field which concerns the upper plate will be better explored in the next sections. Moving along-strike of slabs, the results of para-3D models highlight

Table 4.4. Compilation of the 3D models results. The prefix of the models name refers to the geometries described in section 3.8.3 (see table 3.5). For each solution, the activated forces (X means active) and their magnitudes are listed.

Model name	Slab pull	(U)pper/(L)ower plate convergence	Convergence rate (mm/yr)	Sustaining mantle	Encroaching mantle	Mantle flow rate (mm/yr)
Linear 3D geometries						
L3D-1000-nowind	X					
L3D-1000-windE2	X			X		20
L3D-1000-windE2-NoG				X		20
L3D-1000-windE2-NoG-convdx		L	40	X		20
L3D-1000-windE4	X			X		40
L3D-1000-windE4-convdx	X	L	40	X		40
L3D-1000-windE4-NoG				X		40
L3D-1000-windE4-NoG-convdx		L	40	X		40
L3D-1000-windE8	X			X		80
L3D-1000-windW2	X				X	20
L3D-1000-windW2-NoG					X	20
L3D-1000-windW2-NoG-convdx		L	40		X	20
L3D-1000-windW4	X				X	40
L3D-1000-windW4-convdx	X	L	40		X	40
L3D-1000-windW4-NoG					X	40
L3D-1000-windW4-NoG-convdx		L	40		X	40
L3D-1000-windW8	X				X	80
L3D-1000-nowind-ast17	X					
L3D-1000-nowind-ast19	X					
L3D-1000-windE4-ast17	X			X		40
L3D-1000-windE4-ast19	X			X		40
L3D-1000-windW4-ast17	X				X	40
L3D-1000-windW4-ast19	X				X	40
L3D-500-nowind	X					
L3D-500-windE2	X			X		20
L3D-500-windE2-NoG				X		20
L3D-500-windE2-NoG-convdx		L	40	X		20
L3D-500-windE4	X			X		40
L3D-500-windE4-convdx	X	L	40	X		40
L3D-500-windE4-NoG				X		40
L3D-500-windE4-NoG-convdx				X		40
L3D-500-windE8	X			X		80
L3D-500-windW2	X				X	20
L3D-500-windW2-NoG					X	20
L3D-500-windW2-NoG-convdx		L	40		X	20
L3D-500-windW4	X				X	40
L3D-500-windW4-convdx	X	L	40		X	40
L3D-500-windW4-NoG					X	40
L3D-500-windW4-NoG-convdx		L	40		X	40
L3D-500-windW8	X				X	80

Table 4.4 (continued)

Model name	Slab pull	(U)pper/(L)ower plate	Convergence rate (mm/yr)	Sustaining mantle	Encroaching mantle	Mantle flow rate (mm/yr)
L3D-3000-nowind	*X*					
L3D-3000-windE2	*X*			*X*		20
L3D-3000-windE2-NoG				*X*		20
L3D-3000-windE2-NoG-convdx		*L*	40	*X*		20
L3D-3000-windE4	*X*			*X*		40
L3D-3000-windE4-convdx	*X*	*L*	40	*X*		40
L3D-3000-windE4-NoG				*X*		40
L3D-3000-windE4-NoG-convdx		*L*	40	*X*		40
L3D-3000-windE8	*X*			*X*		80
L3D-3000-windW2	*X*				*X*	20
L3D-3000-windW2-NoG					*X*	20
L3D-3000-windW2-NoG-convdx		*L*	40		*X*	20
L3D-3000-windW4	*X*				*X*	40
L3D-3000-windW4-convdx	*X*	*L*	40		*X*	40
L3D-3000-windW4-NoG					*X*	40
L3D-3000-windW4-NoG-convdx		*L*	40		*X*	40
L3D-3000-windW8	*X*				*X*	80
Concave 3D geometries						
CCV3D-50-nowind	*X*					
CCV3D-50-windE2	*X*			*X*		20
CCV3D-50-windE2-NoG				*X*		20
CCV3D-50-windE2-NoG-convdx		*L*	40	*X*		20
CCV3D-50-windE4	*X*			*X*		40
CCV3D-50-windE4-convdx	*X*	*L*	40	*X*		40
CCV3D-50-windE4-NoG				*X*		40
CCV3D-50-windE4-NoG-convdx		*L*	40	*X*		40
CCV3D-50-windE8	*X*			*X*		80
CCV3D-50-windW2	*X*				*X*	20
CCV3D-50-windW2-NoG					*X*	20
CCV3D-50-windW2-NoG-convdx		*L*	40		*X*	20
CCV3D-50-windW4	*X*				*X*	40
CCV3D-50-windW4-convdx	*X*	*L*	40		*X*	40
CCV3D-50-windW4-NoG					*X*	40
CCV3D-50-windW4-NoG-convdx		*L*	40		*X*	40
CCV3D-50-windW8	*X*				*X*	80
CCV3D-50-nowind-ast17	*X*					
CCV3D-50-nowind-ast19	*X*					
CCV3D-50-windE4-ast17	*X*			*X*		40
CCV3D-50-windE4-ast19	*X*			*X*		40
CCV3D-50-windW4-ast17	*X*				*X*	40
CCV3D-50-windW4-ast19	*X*				*X*	40

Table 4.4 (continued)

Model name	Slab pull	(U)pper/(L)ower plate	Convergence rate (mm/yr)	Sustaining mantle	Encroaching mantle	Mantle flow rate (mm/yr)
CCV3D-20-nowind	X					
CCV3D-20-windE4	X			X		40
CCV3D-20-windE4-NoG				X		40
CCV3D-20-windW4	X				X	40
CCV3D-20-windW4-NoG					X	40
CCV3D-20-nowind	X					
CCV3D-20-windE4	X			X		40
CCV3D-20-windE4-NoG				X		40
CCV3D-20-windW4	X				X	40
CCV3D-20-windW4-NoG					X	40
CCV3D-80-nowind	X					
CCV3D-80-windE4	X			X		40
CCV3D-80-windE4-NoG				X		40
CCV3D-80-windW4	X				X	40
CCV3D-80-windW4-NoG					X	40
CCV3D-80-nowind	X					
CCV3D-80-windE4	X			X		40
CCV3D-80-windE4-NoG				X		40
CCV3D-80-windW4	X				X	40
CCV3D-80-windW4-NoG					X	40
Convex 3D geometries						
CVX3D-50-nowind	X					
CVX3D-50-windE2	X			X		20
CVX3D-50-windE2-NoG				X		20
CVX3D-50-windE2-NoG-convdx		L	40	X		20
CVX3D-50-windE4	X			X		40
CVX3D-50-windE4-convdx	X	L	40	X		40
CVX3D-50-windE4-NoG				X		40
CVX3D-50-windE4-NoG-convdx		L	40	X		40
CVX3D-50-windE8	X			X		80
CVX3D-50-windW2	X				X	20
CVX3D-50-windW2-NoG					X	20
CVX3D-50-windW2-NoG-convdx		L	40		X	20
CVX3D-50-windW4	X				X	40
CVX3D-50-windW4-convdx	X	L	40		X	40
CVX3D-50-windW4-NoG					X	40
CVX3D-50-windW4-NoG-convdx		L	40		X	40
CVX3D-50-windW8	X				X	80
CVX3D-20-nowind	X					
CVX3D-20-windE4	X			X		40
CVX3D-20-windE4-NoG				X		40

Table 4.4 (continued)

Model name	Slab pull	(U)pper/(L)ower plate convergence	Convergence rate (mm/yr)	Sustaining mantle	Encroaching mantle	Mantle flow rate (mm/yr)
CVX3D-20-windW4	*X*				*X*	40
CVX3D-20-windW4NoG					*X*	40
CVX3D-20-nowind	*X*					
CVX3D-20-windE4	*X*			*X*		40
CVX3D-20-windE4-NoG				*X*		40
CVX3D-20-windW4	*X*				*X*	40
CVX3D-20-windW4-NoG					*X*	40
CVX3D-80-nowind	*X*					
CVX3D-80-windE4	*X*			*X*		40
CVX3D-80-windE4-NoG				*X*		40
CVX3D-80-windW4	*X*				*X*	40
CVX3D-80-windW4-NoG					*X*	40
CVX3D-80-nowind	*X*					
CVX3D-80-windE4	*X*			*X*		40
CVX3D-80-windE4-NoG				*X*		40
CVX3D-80-windW4	*X*				*X*	40
CVX3D-80-windW4-NoG					*X*	40
Linear 3D geometries - Deeper slabs						
L3D-2000-nowind	*X*					
L3D-2000-windE4	*X*			*X*		40
L3D-2000-windW4	*X*				*X*	40
L3D-z500-nowind	*X*					
L3D-z500-windE4	*X*			*X*		40
L3D-z500-windW4	*X*				*X*	40
L3D-z600-nowind	*X*					
L3D-z600-windE4	*X*			*X*		40
L3D-z600-windW4	*X*				*X*	40
L3D-z670-nowind	*X*					
L3D-z670-windE4	*X*			*X*		40
L3D-z670-windW4	*X*				*X*	40
L3D-z670rlb-nowind	*X*					
L3D-z670rlb-windE4	*X*			*X*		40
L3D-z670rlb-windW4	*X*				*X*	40
L3D-z670fwd-nowind	*X*					
L3D-z670fwd-windE4	*X*			*X*		40
L3D-z670fwd-windW4	*X*				*X*	40
L3D-z800-nowind	*X*					
L3D-z800-windE4	*X*			*X*		40
L3D-z800-windW4	*X*				*X*	40

Table 4.4 (continued)

Model name	Slab pull	(U)pper/(L)ower plate convergence	Convergence rate (mm/yr)	Sustaining mantle	Encroaching mantle	Mantle flow rate (mm/yr)
Concave 3D geometries - Deeper slabs						
CCV-z500-nowind	*X*					
CCV-z500-windE4	*X*			*X*		40
CCV-z500-windW4	*X*				*X*	40
CCV-z600-nowind	*X*					
CCV-z600-windE4	*X*			*X*		40
CCV-z600-windW4	*X*				*X*	40
CCV-z670-nowind	*X*					
CCV-z670-windE4	*X*			*X*		40
CCV-z670-windW4	*X*				*X*	40
CCV-z670rlb-nowind	*X*					
CCV-z670rlb-windE4	*X*			*X*		40
CCV-z670rlb-windW4	*X*				*X*	40
CCV-z670fwd-nowind	*X*					
CCV-z670fwd-windE4	*X*			*X*		40
CCV-z670fwd-windW4	*X*				*X*	40
CCV-z800-nowind	*X*					
CCV-z800-windE4	*X*			*X*		40
CCV-z800-windW4	*X*				*X*	40

Table 4.4 (continued)

the first evident effects due to the extrusion in the third dimension. The stress field affecting the lithosphere shows a clear symmetry with respect to central sections of the model, sliced parallel to the subduction direction. Moving away from the center (i.e., slices made at ca. 500 km; figure 4.8) towards the lateral boundary planes, the stress axes show a mirror-like evolution regarding directions and lengths (which decreases). This outcome represents the response to along-strike bending of the slab that, depending on the enhanced driving forces, may be towards the upper plate direction or backward. Slab buckling effects become more evident in real 3D model results, as it will be shown later.

4.3 3D models results

In this chapter, the main results obtained in the 3D modelling phase will be discussed. The kinematics adopted in the 2D modelling, were tested also with the 3D geometries. New conditions have also been

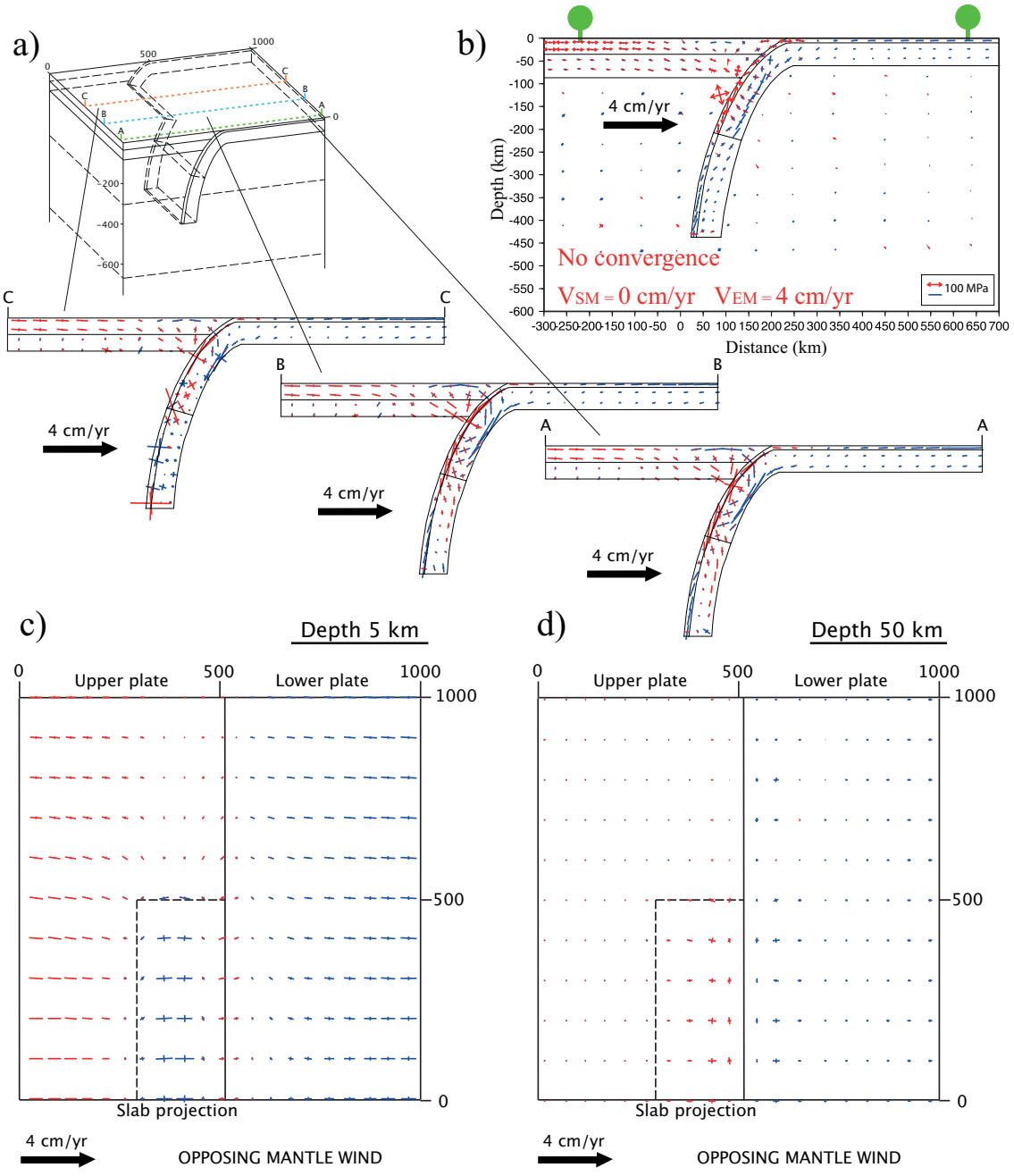

Fig. 4.9. Results of 3D linear model (500 km half width) geometry in which subduction is forced by slab pull plus an encroaching mantle flow. Results are shown along three cross-section of the a) 3D geometry, made at different distances from the symmetry plane (section AA) and moving towards the lateral termination of the slab (section CC). b) Results of 2D model obtained with the same kinematics forced in 3D, are shown for comparison. 3D model stress axes are also plotted in map view at c) crustal (5 km) and at d) lithospheric (50 km) depths within the plates. Blue lines indicate compressional stresses, and red lines indicate tensional stresses.

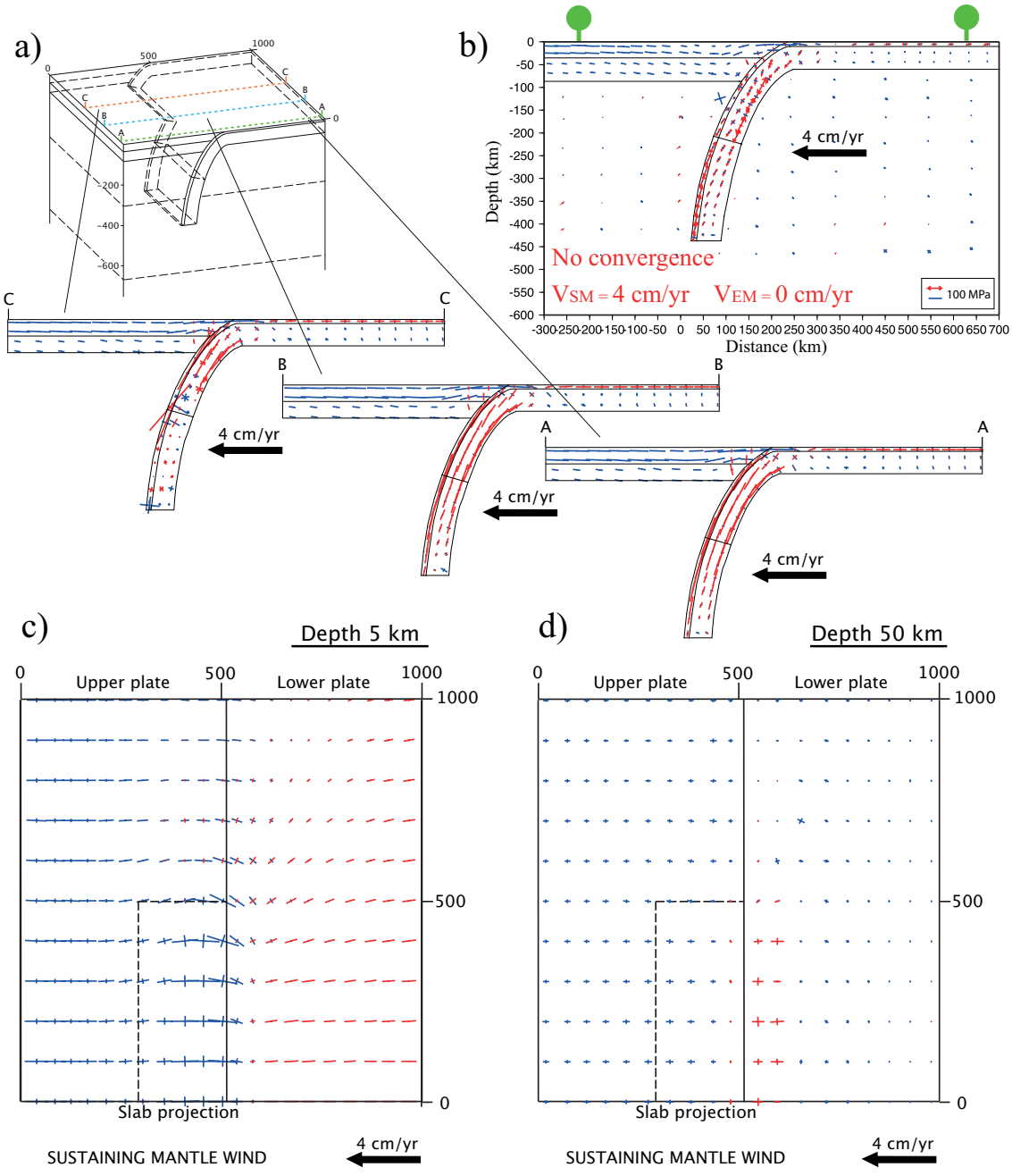

Fig. 4.10. Results of 3D linear model (500 km half width) geometry in which subduction is forced by slab pull plus a sustaining mantle flow. Same representation of figure 4.9. a) 3D geometry; b) Results of 2D model; c) stress axes at crustal depths (5 km); d) stress axes at lithospheric depths (50 km) within the plates of 3D model.

imposed when necessary to investigate issues understandable only in the three-dimensional case. In table 4.4 the complete list of the models run for the 3D geometries can be found.

In figures 4.9 and 4.10 the results obtained from 2D an real 3D simulations are compared. The linear3D-1000 geometry (see table 3.5) is used to build the reference model. For the 3D case, sections built at different distance from the tip of the slab are shown both for sustaining and encroaching mantle flow. As already well recognized in 2D and para-3D model solutions (figures 4.9b and 4.10b), downdip compression in case of opposing mantle flow and down-dip tension in case of sustaining mantle flow, are observed within slabs also in 3D modelling results. In this case, due to the finite lateral extent of the geometry, the stress components vary moving from the central part towards the lateral tip of the slab. In figure 4.9, where an opposite mantle flow is forced, the portion of the slab under compression increases along-strike moving from section A to sections B and C. In addiction, a lateral decrease of tension is observed moving towards the lateral tip of the slab (from section A to section C in figure 4.10b) in case of sustaining mantle flow.

The effects of using real 3D geometries are even clearer in map view. At crustal depths of 5 km (figures 4.9c and 4.10c) it can be observed a widespread rotation of the stress axes that affects wide regions of both plates. This rotation is ruled by the plates geometry, since its maximum is located close to the lateral termination of the subducted lithosphere, where the plates torque becomes significant. Stress regimes for the crust of both plates are comparable with results obtained in 2D simulations. Tension in the upper plate and compression in the lower plate are reproduced in case of opposing mantle flow (cf. figure 4.9b and c); quite the opposite occurs in case of sustaining mantle flow (cf. figure 4.10b and c).

Plate convergence also produces a recognizable effect on the stress regime affecting the upper plate. The region lying over the projection of the slab experiences wide compression within the crust, regardless the adopted kinematics (Figures 4.9c and 4.10c). This compression decreases or vanishes elsewhere in the upper plate.

At greater depths (50 km), the stress affecting the lithosphere (figures 4.9d and 4.10d) clearly decreases in magnitude, but the patterns described for the 5 km depth slices are retained. The results for the 3D models will be shown in detail in the next section.

4.3.1 State of stress and slab geometry

Here I show the results obtained for (hereafter called) narrow (i.e., 250 km half width), intermediate (i.e., 500 km half width) and wide (i.e., 1500 km half width) slab geometries, characterized by linear or curved trench trend. Since the shape of the slab is closely linked to the dynamics of the subduction system

(see section 2.2), the results shown for the linear, the concave and the convex shaped slabs are forced respectively by the solely slab pull (Figure 4.11), by the slab pull plus an opposing mantle flow (Figure 4.12) and by the slab pull plus a sustaining mantle flow (Figure 4.13). However, the three geometries (linear, concave and convex) were tested with all the possible kinematic boundary conditions. The results are shown in the accompanying material and are briefly discussed in the following text as well.

As the linear geometries are concerned, the lateral extent of the slab controls the stress magnitude due to the greater volume affected by a negative gravitational anomaly. The most evident effect is, in the shallow portion of the slab, an increment of the length of down-dip tensional axes, as the bending force increases (cf. figure 4.11a,b and c). The increasing weight of the sinking lithosphere, furthermore enhances compression in the deeper parts of the slab, which reaches maximum levels in the wide geometry case (Figure 4.11c). Moving along-strike, a slight rotation and decrease of the down-dip tensional axes is detected close to the lateral tip of the slabs. The finiteness of the subducted lithosphere in the third dimension produces this lateral variability in the stress field, due to the differential retreat between the central and the side portions of the slabs. These border effects vanish within a few hundreds of km, and consequently affect mostly the narrow slab geometry results (Figure 4.11a) and only limited parts of the larger slab geometries (Figure 4.11c and d).

In case of subduction forced only by slab pull, the findings described for the stress field obtained for linear slab geometries remain valid also when curved geometries are introduced (as shown in the accompanying material). Major changes occur when a mantle flow is applied. Regardless the mantle flow direction and the concave or convex shape of the slab, substantial along-strike deformation occurs within the subducted plate. When a mantle flow opposes (encroaches) a concave-shaped subducting slab (Figure 4.12), down-dip axes are clearly compressional. Further, two kinds of tensional axes are distinguishable: those associated with the down-bending of the lithosphere (as seen for the linear trench models) which characterize the shallow bending region and tend to rotate towards the slab endings; those related to the slab differential retreat induced by the mantle push. The latter is mainly along-strike directed and affects intermediate and deeper regions of the slab. Down-dip and along strike axes at these depths, form compression-tension couples that tend to rotate moving towards the slab tips (Figure 4.12). The larger the lateral extent of the plate the most this effect is evident (cf. figure 4.12a, b and c), until it becomes reversed (i.e., down-dip tension and along-strike compression) in the outermost parts of the subducted lithosphere for the wide geometry.

If a sustaining mantle flow is imposed over a convex slab geometry (Figure 4.13), the following results stand out: tension associated with the slab pull and plate bending still takes place at shallow depths (in this case, however, the inner part of the slab is not characterized by down dip extension); overall down-

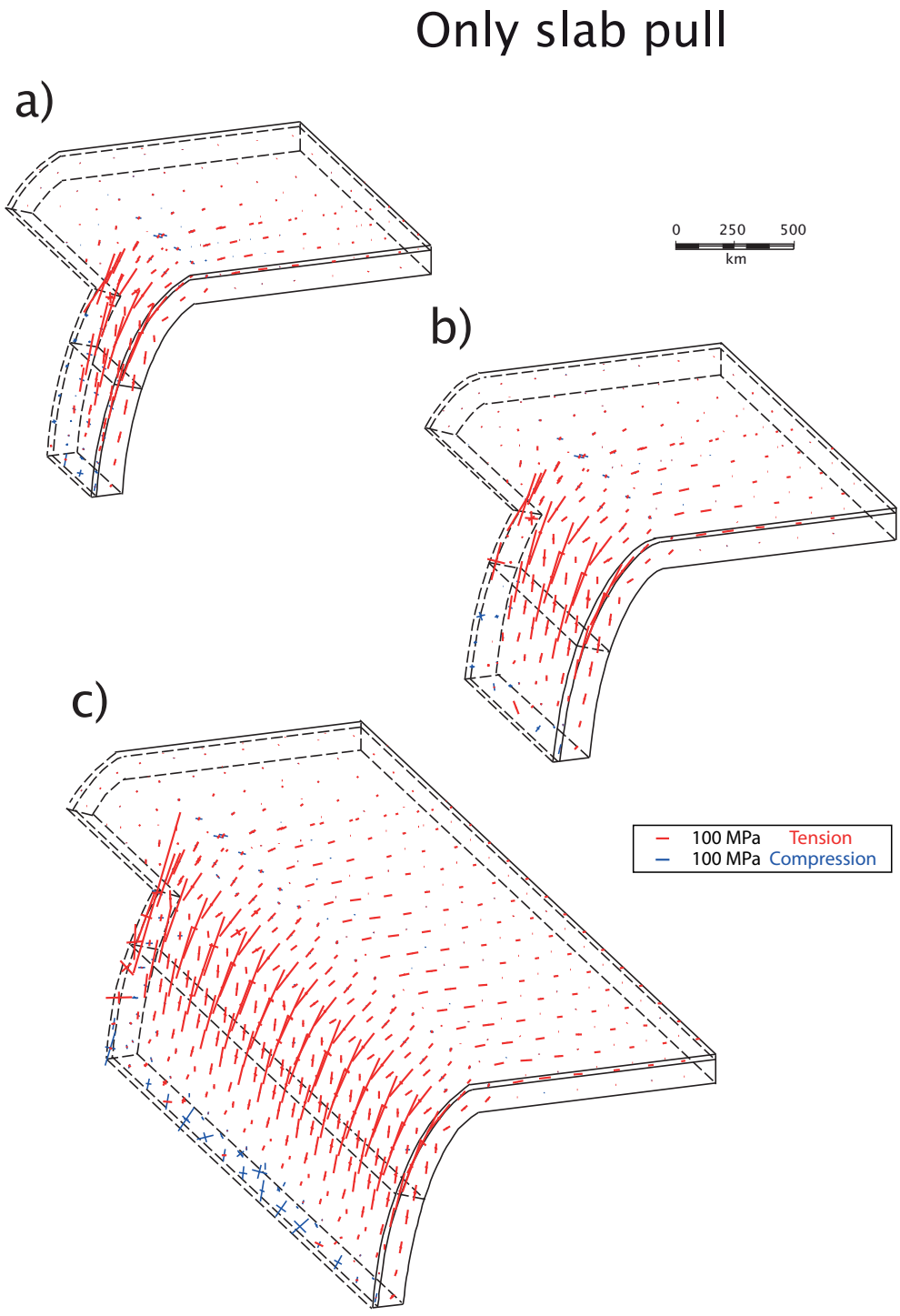

Fig. 4.11. Results of 3D linear models in which subduction is forced only by slab pull. Blue lines indicate compressional stresses, and red lines indicate tensional stresses: a) prospective view of the narrow linear geometry (250 km half width); b) prospective view of the intermediate linear geometry (500 km half width); c) prospective view of the wide linear geometry (1500 km half width). Stress axes are plotted at crustal (5 km) and at lithospheric (50 km) depths within the lower plate, and follow the adopted depths within the sinking slabs. Upper plate is not shown for simplicity.

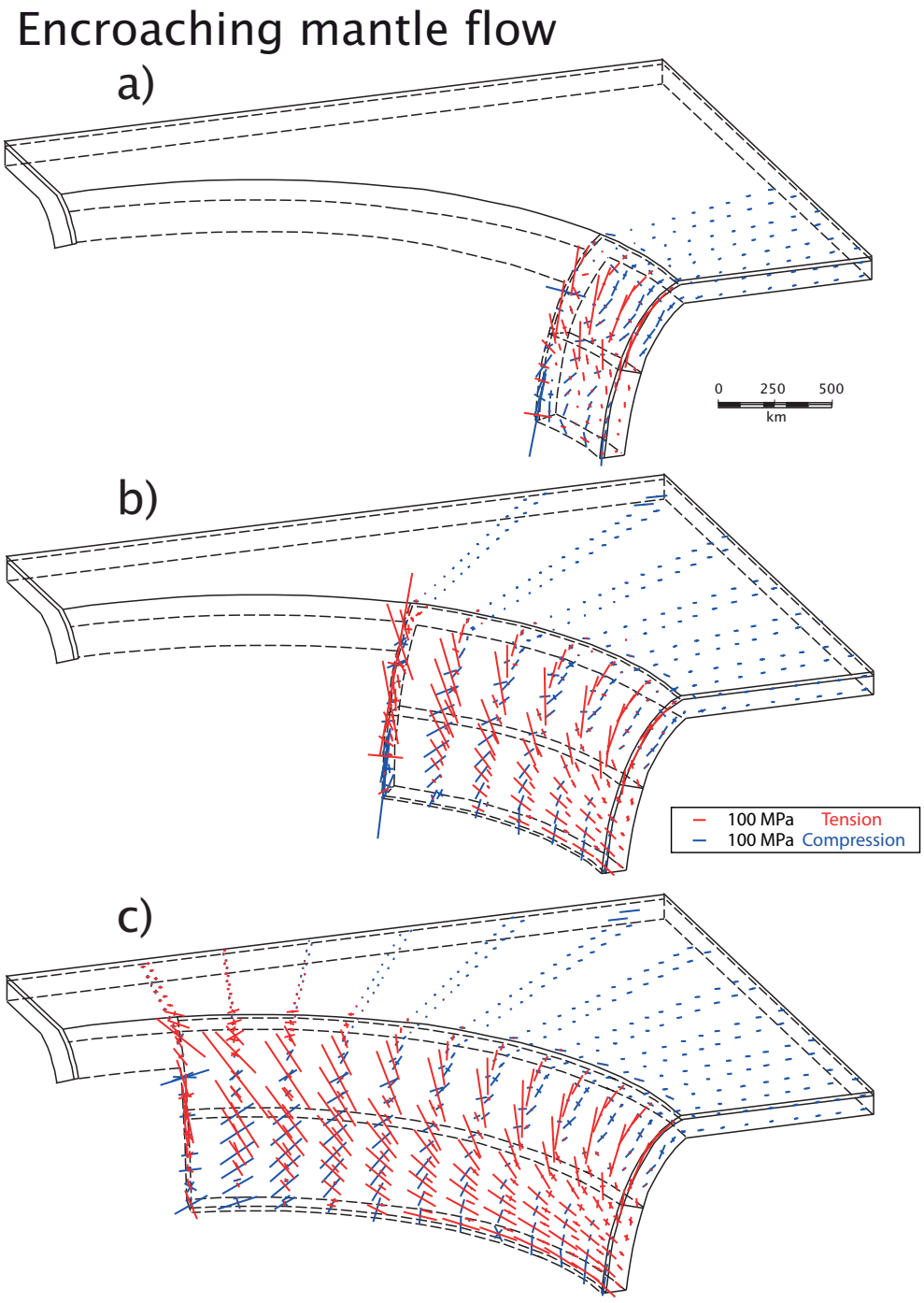

Fig. 4.12. Results of 3D curved (concave slab) models in which subduction is forced by slab pull plus an encroaching mantle flow. Blue lines indicate compressional stresses, and red lines indicate tensional stresses: a) prospective view of the narrow concave geometry; b) prospective view of the intermediate concave geometry; c) prospective view of the wide concave geometry. Stress axes are plotted at crustal (5 km) and at lithospheric (50 km) depths within the lower plate, and follow the adopted depths within the sinking slabs. Upper plate is not shown for simplicity.

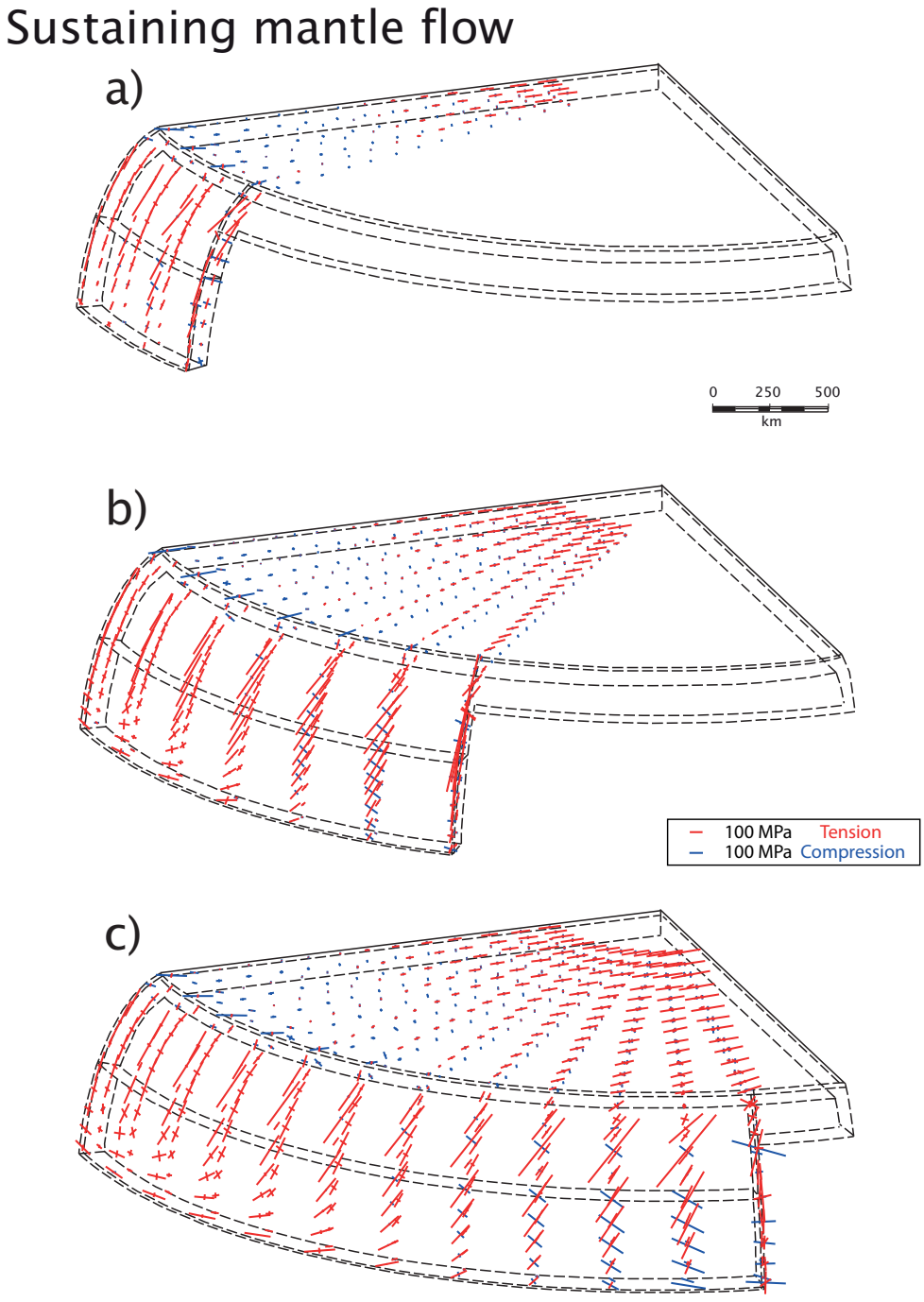

Fig. 4.13. Results of 3D curved (convex slab) models in which subduction is forced by slab pull plus a sustaining mantle flow. Blue lines indicate compressional stresses, and red lines indicate tensional stresses: a) prospective view of the narrow convex geometry; b) prospective view of the intermediate convex geometry; c) prospective view of the wide convex geometry. Stress axes are plotted at crustal (5 km) and at lithospheric (50 km) depths within the lower plate, and follow the adopted depths within the sinking slabs. Upper plate is not shown for simplicity.

dip tension is enhanced in slabs at intermediate and deeper regions; along-strike tension propagates from the central towards the lateral slabs domains. The couples compression-tension observed in the results discussed before, is here replaced by couples tension-tension (respectively down-dip and along-strike). These tension-tension couples show the same stress rotation approaching the slab sides. This is true especially analyzing the wide geometry results (Figure 4.13c), where at the slab edges some sub-horizontal compressional axes are predicted.

Inverting the adopted mantle flow direction for both curved geometries (Figure 4.14), apart for the extension that persists in the extrados bending areas, reverse stress states are obtained. If a sustaining mantle flow forces the subduction of a concave slab (Figure 4.14a), the down-dip compressional and along-strike tensional axes shown in figure 4.12b become down-dip tensional and along-strike compressional. The opposite occurs if an encroaching mantle flow pushes against a convex shaped slab, forcing down-dip compression and along-strike compression within the sinking lithosphere (cf. figures 4.13b and 4.14b). In both cases the along strike compression is due to the fact that the mantle flow tends to force the slab back to a linear geometry. Thus the slab is pushed laterally against the confining mantle and undergoes compression. In addiction, when the mantle flow tends to be parallel to the slab interface (e.g., at the lateral endings of the wide curved slabs; figures 4.12c and 4.13c), along-strike compression or tension occur since the lithosphere is squeezed or stretched in that direction. A wide variability of stress fields occurs within the sinking lithosphere, consistent with the depth-variability in the style of seismicity in slabs.

According to the results described above, the local angle of incidence of the mantle flow over the sinking slabs is the first controlling factor over the state of stress in slabs. When the mantle approaches perpendicular to the slab (e.g., in the innermost regions of the curved slabs), along-strike tension or compression come out in response to the flexure (forward or backward) of the lithosphere depending on the slab longitudinal curvature. In particular along-strike tension occurs in case of slabs curved towards the mantle flow direction (e.g., encroaching mantle over concave slabs and sustaining mantle over convex slabs; figures 4.12 and 4.13), while along-strike compression occurs if the slab has an opposite curvature relative to the mantle flow direction (e.g., sustaining mantle over concave slabs and encroaching mantle over convex slabs; figure 4.14).

These findings remark that the stress axes directions are largely influenced by the subduction geometry, but the stress regime affecting the subducted lithosphere is totally controlled by the mantle flow. The mantle flow rate control also the magnitude of both the down-dip and the along-strike stress; obviously, as already seen for 2D solutions, the higher the speed the greater the length of the stress axes (as shown in the auxiliary material).

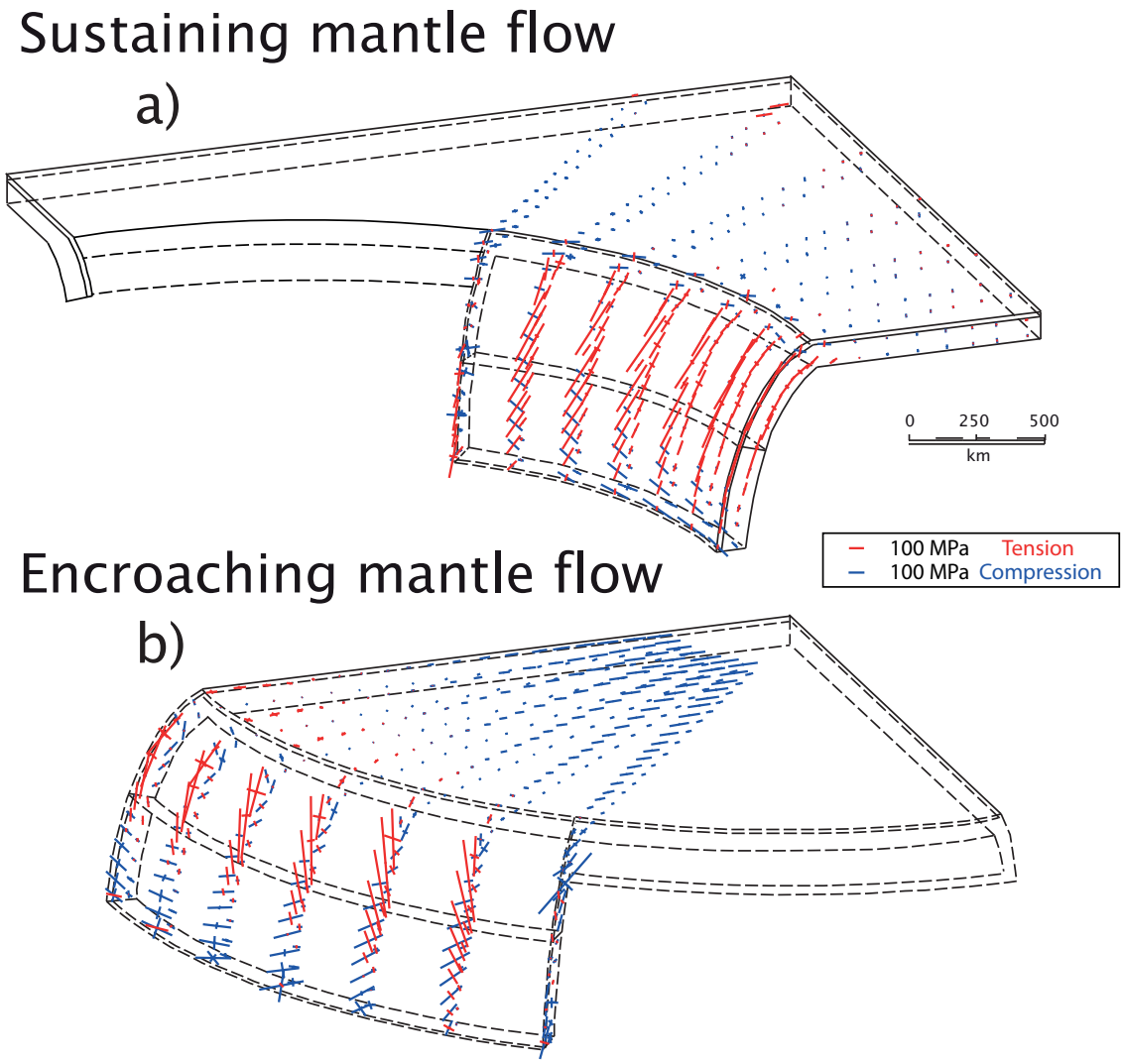

Fig. 4.14. Results of the a) intermediate concave model in which subduction is forced by slab pull plus a sustaining mantle flow and the b) intermediate convex model in which subduction is forced by slab pull plus an encroaching mantle flow. Blue lines indicate compressional stresses, and red lines indicate tensional stresses. Stress axes are plotted at crustal depth (5 km) and at lithospheric depth (50 km) within the lower plate, and follow the adopted depths within the sinking slabs. Upper plate is not shown for simplicity.

4.3.2 Subduction deepening: how the lower mantle controls the stress in slabs

The viscosity jump and the thermodynamic effects of the phase change at the 670 km discontinuity produces viscous resistance to the penetration of slabs at depth. As first noted by *Isacks and Molnar* [1969, 1971], deep earthquakes (focal depths between 300 km and 700 km) are typically down-dip compressional in all Wadati-Benioff zones that reach the upper-lower mantle transition. As explained in section 2.2, tomographic models suggest various scenarios for deep slab behavior and slab interaction with the transition zone, with observed geometries summarized in figure 2.5. In some subduction zones slabs vertically penetrate through the lower mantle, in other cases slabs are horizontally deflected by the 670 km boundary. This deformation produces concave or convex slabs depending on the advancing-retreating trench behavior [e.g., *Faccenna et al.*, 2001a].

Curved and linear slab geometries that reach different depths, and even leaning over or penetrate the 670 km viscous barrier (see figure 3.9), will be used here to discuss the interaction between the lower mantle and the descending lithosphere.

Results for the linear and curved geometries, assuming only slab pull applied (Figures 4.15a-d and 4.16a-d), slab pull and 4 cm/yr mantle flow sustaining the slab (Figures 4.15e-h and 4.16e-h) and slab pull and 4 cm/yr mantle flow opposing the slab dip (Figures 4.15i-l and 4.16i-l), are shown. In both the linear and curved geometries, the sinking slab reaches a depth of 500-600-670 and 800 km. Since the stress affecting the lithospheric mantle in slabs maintains comparable stress field distribution and regime compared with that affecting the subducted crust (see section 4.3), to show the results more clearly the stress axes are plotted only at crustal depths (shallow-most 5 km of the slab).

Summarizing what we have seen in previous sections, results of this series of models regardless of the geometry (see figures 4.15 and 4.16) confirm that:

- due to the slab pull, the bending effects in the stretching outer arc of subducting slabs generate tension at shallow depths (Figures 4.15a-d and 4.16a-d);

Fig. 4.15. Model results with linear trench geometry and different depths reached by the subducting slabs. Starting from the leftmost column panels to the right, slabs are respectively 500, 600, 670 and 800 km deep. The three simulations sequences on each row were obtained assuming only slab pull applied (panels a-d), slab pull and 4 cm/yr mantle flow sustaining the slab (panels e-h) and slab pull and 4 cm/yr mantle flow opposing the slab (panels i-l). Black arrows indicate the mantle flow direction, blue lines the compressional stresses, and red lines the tensional stresses. Stress axes are plotted at crustal depth (5 km) within the lower plate, and follow the adopted depth within the sinking slabs. Upper plate and mantle domains are not shown for simplicity, while the 670 km interface is drawn with thick dashed lines. Ghosted slabs are tracked by black dots.

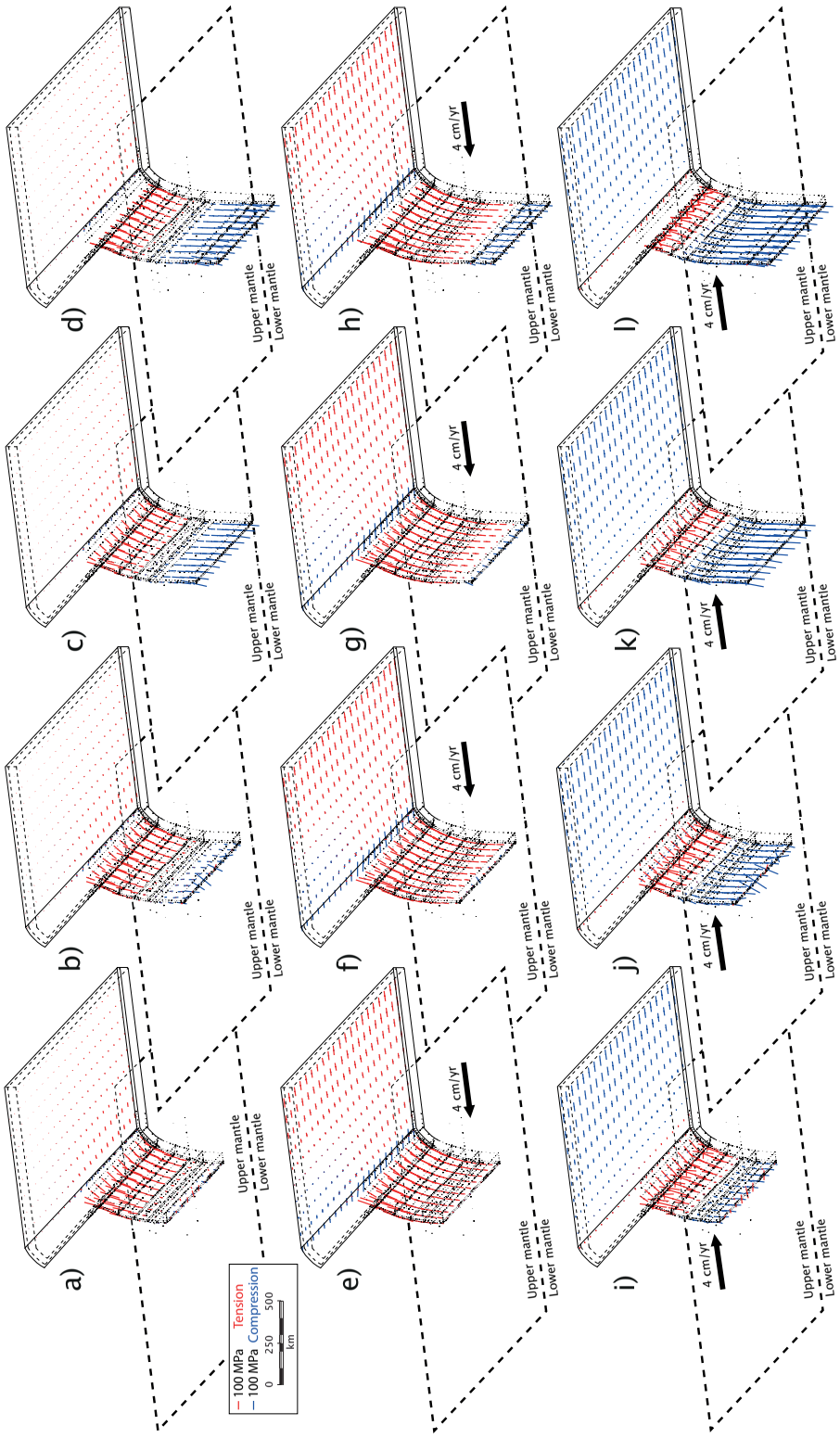

Fig. 4.15 (caption in the previous page)

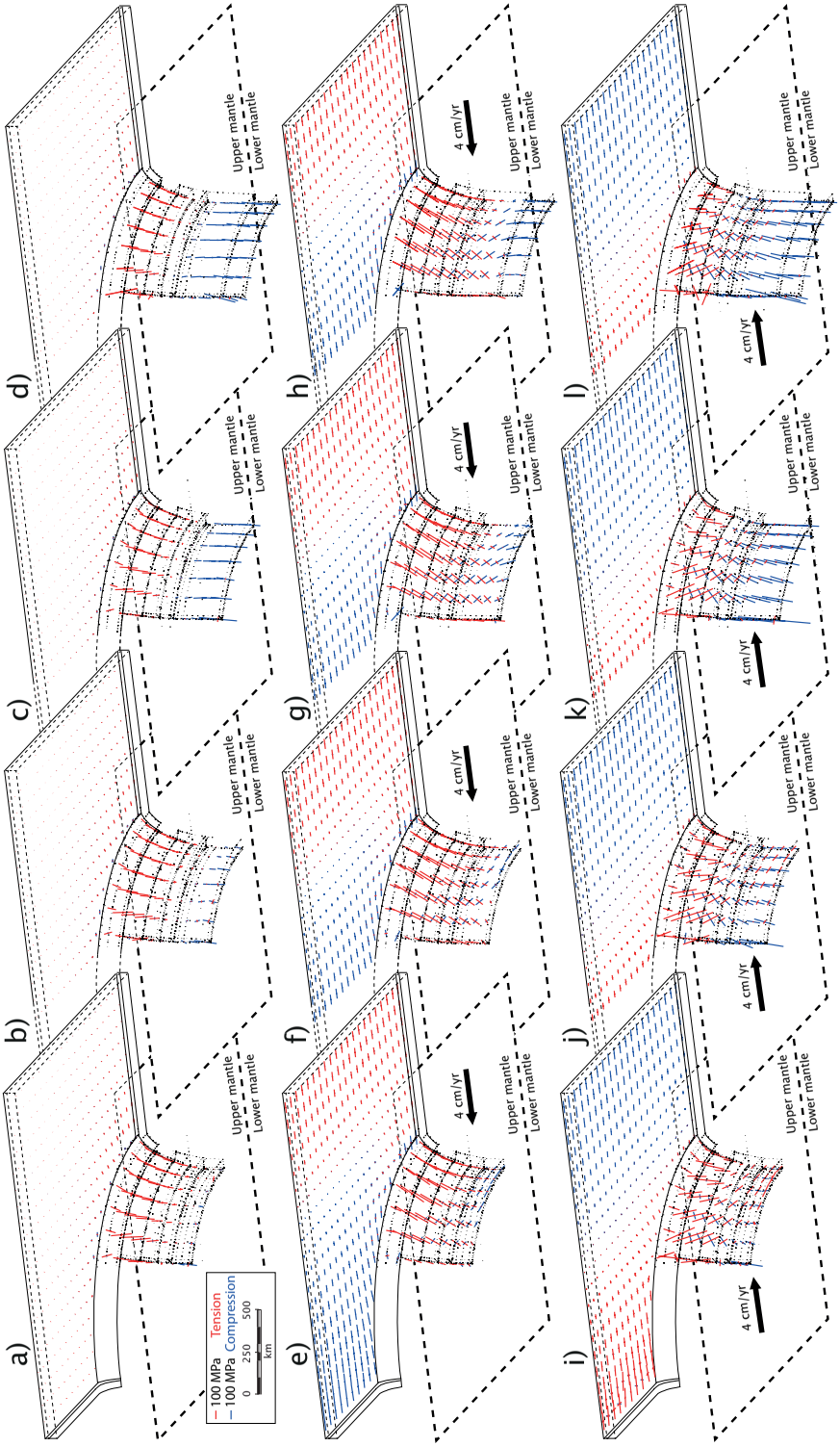

Fig. 4.16 (caption in the next page)

Fig. 4.16. Model results with curved trench geometry and different depths reached from the subducting slabs. Starting from the leftmost column panels to the right, slabs are respectively 500, 600, 670 and 800 km deep. The three simulations sequences on each row were obtained assuming only slab pull applied (panels a-d), slab pull and 4 cm/yr mantle flow sustaining the slab (panels e-h) and slab pull and 4 cm/yr mantle flow opposing the slab (panels i-l). Same representation of figure 4.15.

- tension in the bending region increases (Figures 4.15e-h and 4.16e-h) or decreases (Figures 4.15i-l and 4.16i-l) and down-dip tension or compression characterize the slabs at intermediate depths, depending on the adopted kinematics for the mantle (i.e., sustaining or opposing the slab);
- the longitudinal finiteness and curvature of the subducted lithosphere produces lateral variability in the stress field, that laterally decreases and rotates;
- along-strike stress axes are more developed in case of mantle flow forced over curved slabs (Figure 4.16e-l), since a mantle flow oblique with respect to the sinking lithosphere is applied.

To optimally understand how the lower viscous mantle affects the stress field of the descending lithosphere, only the effects of slab pull are discussed, ruling out at first all the other driving forces. The own weight of the sinking lithosphere enhances compression in its deeper parts, due to the viscous resistance to penetration of slabs at depth. Comparing results obtained with slab depth increasing from 500 km to 800 km (Figures 4.15a-d and 4.16a-d), with the upper-lower mantle interface located at 670 km (representing a one order viscosity jump), lithosphere-lower mantle interactions can be investigated. Despite the slab pull should create tension in the downgoing lithosphere, a veneer of deep compression already appears when the slab reaches 500 km depth and exponentially increases looking at more deeply sunken slabs (Figures 4.15a-d and 4.16a-d). In case of slab pull forcing the subduction, it can be stated that at depth ranging from 500 km to 800 km downdip compression dominates within the lithosphere and mildly propagates upward.

The depth of switch between down-dip tension and compression drastically deepens if mantle flow sustains the slab (Figures 4.15e-h and 4.16e-h). For linear slabs, this change occurs only when the lower plate reaches and exceeds the top of the lower mantle (Figures 4.15g and 4.16g). Compression affecting shallower curved slabs (Figure 4.16f and g) is mainly along-strike directed, and therefore not linked to the viscous resistance to penetration (as previously shown).

When mantle flow encroaches the slab, downdip compression dominates at intermediate and deep depths of both linear and curved slab geometries (Figures 4.15i-l and 4.16i-l). The deeper the slab the greater the compression, that even propagates towards the surface counteracting the stretching due to the bending of the plate (cf. figures 4.15i and l and 4.16i and l). Slab regions crossing the top of the lower mantle, always show down-dip compression. An interesting result is that the stress rotation and the along-

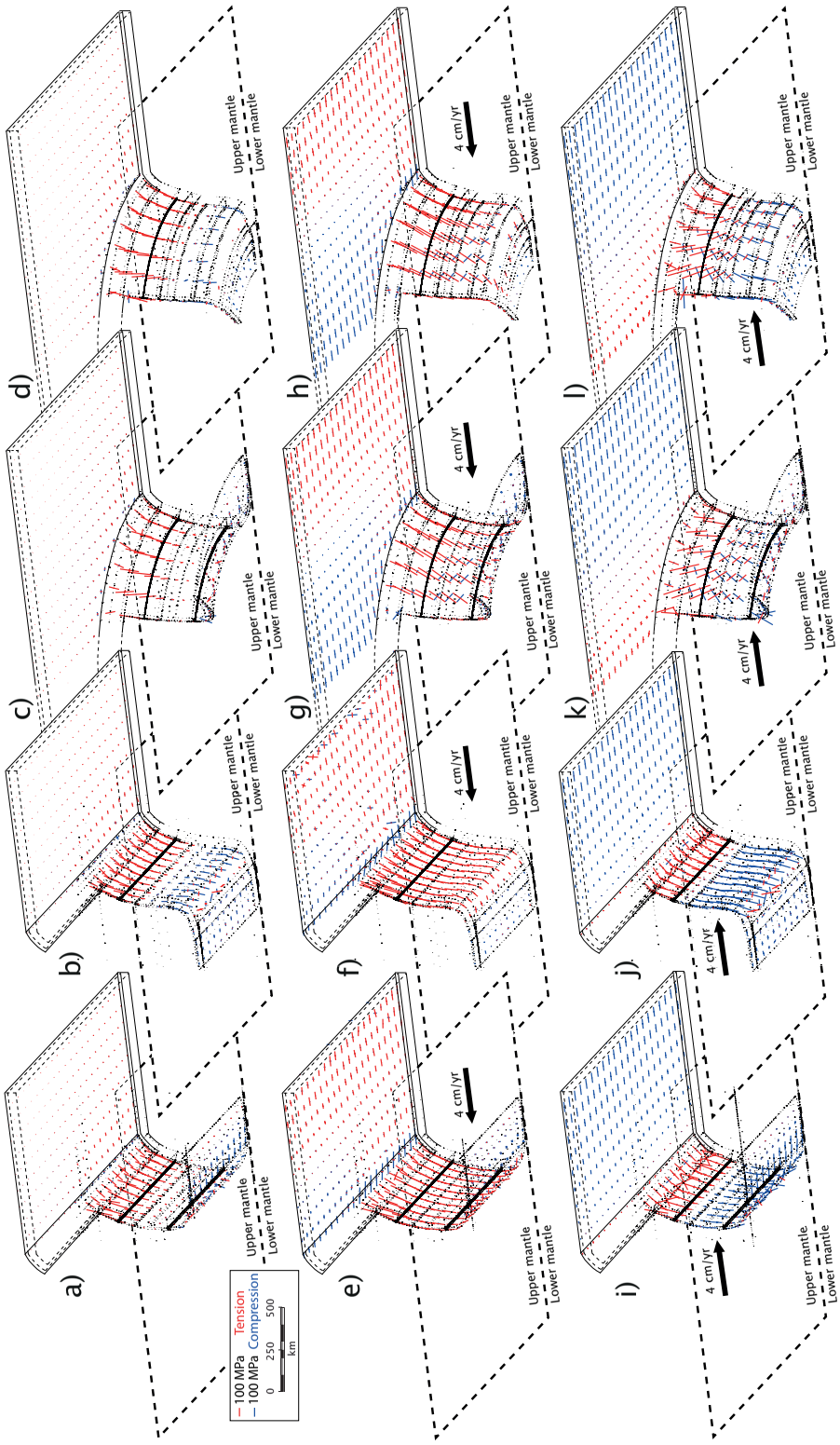

Fig. 4.17 (caption in the next page)

Fig. 4.17. Model results with linear and curved trench geometries with slabs leaning over the upper-lower mantle interface. The panels of the first and third column show solutions for convex (i.e. advancing) slabs, while the panels of the second and fourth column show solutions for concave (i.e. retreating) slabs. The three simulations sequences on each row were obtained assuming only slab pull applied (panels a-d), slab pull and 4 cm/yr mantle flow sustaining the slab (panels e-h) and slab pull and 4 cm/yr mantle flow opposing the slab (panels i-l). Same representation of figure 4.15.

strike deformations almost disappear in the deeper curved slabs, as the lithosphere approaching the 670 km interface (Figure 4.16g-h and k-l). This is explained by considering that the mantle flow can not stretch or compress longitudinally the slab (as for less deep slabs), which is anchored to the lower mantle. Another interesting observation is that, for slabs heavily interacting with the 670 km discontinuity, the slab down-dip compression is transmitted to the entire subducting plate. This finding is very clear in case of forcing only slab pull since, also in the horizontal part of the plate, horizontal trench-perpendicular compression is observed in the bending-domain. The magnitude of such compression increases with increasing depth reached by the slab (i.e., from left to right in figure 4.15). Compression near the slab hinge is often recognizable from stress data in subductions that reach the top of the lower mantle (e.g., cf. the Peruvian part of the south America or the kermadec-Tonga subductions in figure 2.8). Anyhow, this compression emerging from data cannot be attributed with certainty to the lower intraplate stress, as it could represent the stress field at the interface or in the overlying compressional wedge. This uncertainty makes it complicated the correlation between stress data and model results near the hinge in the lower intraplate.

As seen in section 2.2, tomographic models suggest various scenarios for deep slab behavior and slab interaction with the transition zone at 670 km (see figure 2.5). The results described above are representative for slabs that penetrate through the upper-lower mantle boundary without any significant deformation (e.g., Mariana, Kermadec, Java, central America). Another set of models reproduce slabs that are horizontally deflected by that boundary (e.g., Tonga, Izu-Bonin). As suggested by *Faccenna et al.* [2001a], once slabs reach the top of the lower mantle, slab-dip angles can become progressively shallower or steeper if there is an advancing-retreating trench migration, because the slab becomes anchored to the higher-viscosity lower mantle. Both for linear and curved slabs, in figure 4.14 results are shown for models simulating advancing and retreating trench subductions, with the lower plate reaching and leaning over the 670 km interface. Differently from previous results, unexpectedly tension appears in the deep regions of the slab for all considered kinematics (e.g., cf. figures 4.15c, 4.16c and 4.17a-d). Despite the depth, the elastic bending of the lithosphere may be invoked as the cause of the stretching. Tension is here completely controlled by geometry, in particular by the bending of the subducting plate, similarly to what observed for the down-bending at shallow depths. The tensional axes are emphasized in case of mantle flow (encroaching mantle) that is

Fig. 4.18 (caption in the next page)

Fig. 4.18. Map view of the principal stress axes at crustal depth (5 km) within both the lower and the upper plates for 3D models with linear trench geometries and different depths reached by the subducting slabs (i.e., 450 km, 600 km and 800 km). The following model results are compared: assuming only slab pull applied (panels a-c), slab pull and 4 cm/yr mantle flow sustaining the slab (panels d-f) and slab pull and 4 cm/yr mantle flow opposing the slab (panels g-i). No plate convergence is assumed. Black arrows indicate the mantle flow direction, blue lines the compressional stresses, and red lines the tensional stresses. The yellow thick edges represent the symmetry planes of the geometries.

able to drag the lithosphere along the 670 km interface (Figure 4.14e-l). For this kind of geometries, small changes in the stress field also affect the slabs at intermediate depth. Comparing models characterized by slabs resting vertically over the top of the lower mantle (panels c,g and k of figures 4.15 and 4.16), with those where the slabs rest over the same interface (Figure 4.17), what changes in the latter series is that:

- downdip compression decreases (Figure 4.14b and d) or even vanishes (Figure 4.14a and c) in case of subduction forced only by the slab pull;
- compressional axes almost vanishes (Figure 4.14e and h) or become tensional (Figure 4.14f and g) if a sustaining mantle flow is added;
- a general decrease for down-dip compression is observed (Figure 4.14i-l), when the mantle flow opposes the sinking slab.

Further emerges from the results that the deepening of the slabs (and their interaction with the lower mantle) does not affects the stress field for the lithosphere of the upper plate (cf. panels of figure 4.18). As shown in previous sections, this is instead controlled by the trenches longitudinal trend, the plate convergence and the absolute plate motion relative to the underlying asthenosphere. Nonetheless, all maps with the stress field within the plates for the models presented above, are included in the accompanying material. Shallow stress for plates is discussed in the next section.

4.3.3 State of stress within plates and comparison with data

The results so far show that the stress of the upper and lower plates, at lithospheric depths, is primarily controlled by the absolute plate motion relative to the mantle (stress regime), the mantle flow velocity (stress magnitude) and the trench geometry (stress axes direction), rather than by the slab geometry. The plate convergence and its rate, and the viscosity of the lithosphere have a role in determining the stress magnitude. Different configurations of these parameters are recognizable in natural cases of subduction zones. The global mantle flow direction and the slab dip can be toward the same or opposite directions either

with curved or linear trenches (Figure 2.8), and several kinematics are recognized for the convergence of plates. A list of the main subductions and their principal features is provided in table 4.5.

Neglecting the stress magnitude (i.e., plates convergence rates or variations in rheologic parameters are not considered), the results obtained for the three principal kinematics (i.e., assuming only slab pull applied, slab pull and 4 cm/yr mantle flow sustaining the slab and slab pull and 4 cm/yr mantle flow opposing the slab) are here compared with stress data from the World Stress Map database [*Heidbach et al.*, 2008, see figure 2.8]. The stress fields generated at shallow depths (5 km) by models forced only by slab-pull or adding a sustaining or an encroaching mantle flow, are shown in figure 4.19 for both the linear and curved geometries.

Looking at the results for the upper plate, the stress field shows the expected high variability. An overall trench-normal compression emerges in case of only slab pull (Figure 4.19a-c) or if a sustaining mantle flow is forced (Figure 4.19d-f). These are findings observable in Chile-type subductions, e.g., the Central and South America, the Sumatra-Java, the central America and the Solomon subductions (cf. figure 4.20a-d). Modelling results highlight that trench-normal compression is clearly independent on the angle between the mantle flow direction and the trench, but follows the plates interface in its along-strike trend. This is clear comparing results obtained using the same kinematics in models with different initial geometries (i.e., with linear or curved slab; figure 4.20e-g). Shallow compressional axes have a constant (trench-normal) orientation above the straight portions of subduction interfaces (see figure 4.19a, d and g), and rotate following the trench curvature to maintain a trench-perpendicular orientation in curved subductions (see figure 4.19b-c and e-f), despite contextually the mantle flow is away from trench-normalcy. Far from the upper-lower plate boundary (i.e., in undisturbed regions), stress axes tend to be everywhere parallel to the mantle flow. These results are strongly compatible with natural subductions worldwide. The lithosphere in the upper plate of the South America plate margin, shows preferred trench sub-perpendicular direction for the compressive SHmax axes (see blue axes in figure 4.20a). This pattern is laterally maintained along the straight portions of the subduction (e.g., in the Chile region). A clear reorientation of the stress axes coincides with the trench deflection moving northward (i.e. in the South Peru area), following the trench curvature that characterizes the system from then to the North. The same pattern can be recognized in other subductions. The SHmax compressional axes are perpendicular to the straight and continuous trench of the Central America (Figure 4.20c), and to the straight portions of the Solomon subduction trenches (Figure 4.20d). The smooth curvature of the Sumatra-Java subduction (Figure 4.20b), means that the compressional SHmax axes progressively rotate from a NE-SW direction (in its western part) to an approximately N-S direction (to the East), while remaining perpendicular to the plate boundary.

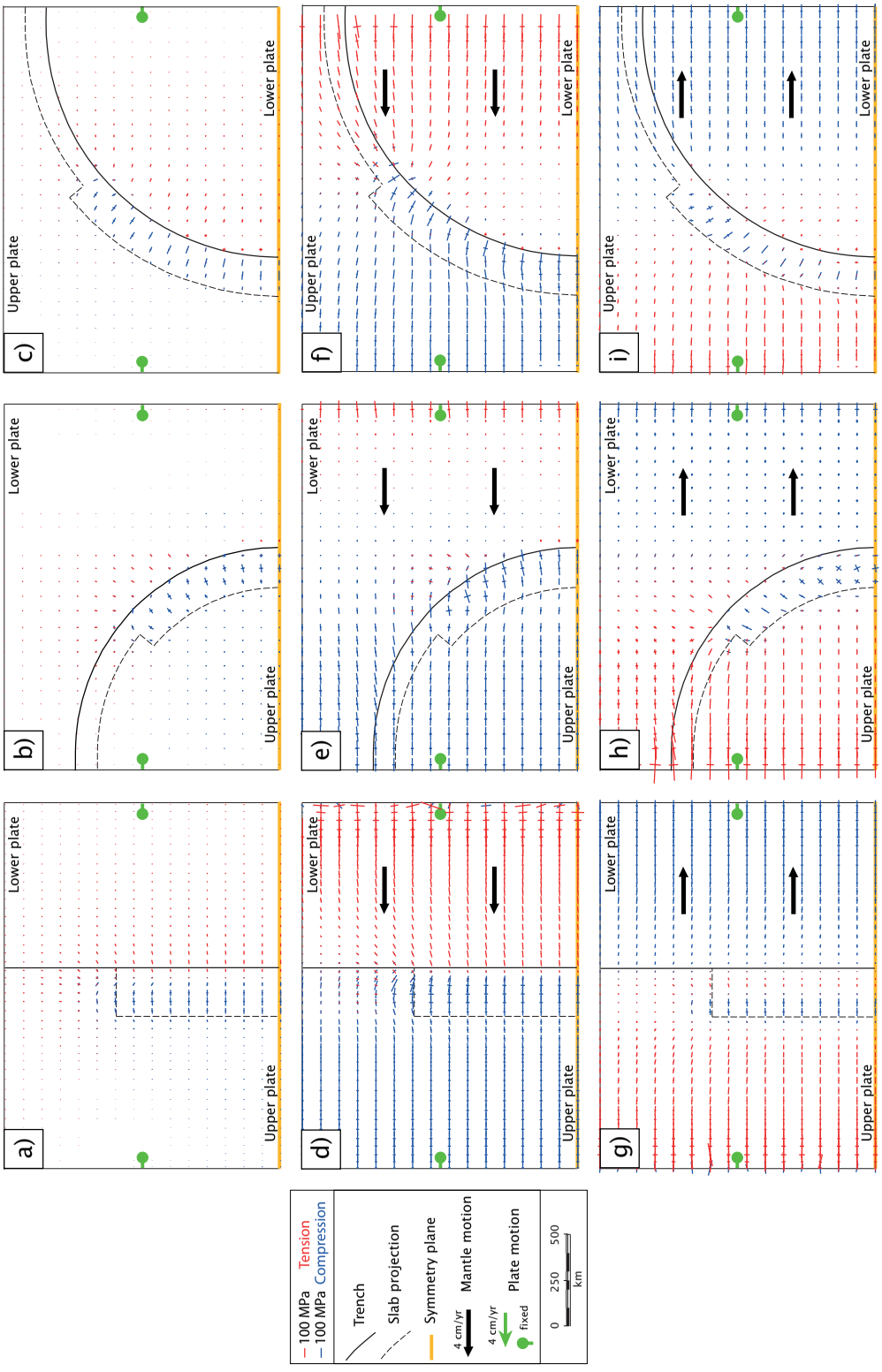

Fig. 4.19 (caption in the next page)

Fig. 4.19. Map view of the principal stress axes at crustal depth (5 km) within both the lower and the upper plates for 3D models with linear and curved trench geometries. The following model results are compared: assuming only slab pull applied (panels a-c), slab pull and 4 cm/yr mantle flow sustaining the slab (panels d-f) and slab pull and 4 cm/yr mantle flow opposing the slab (panels g-i). No plate convergence is assumed. Black arrows indicate the mantle flow direction, blue lines the compressional stresses, and red lines the tensional stresses. The yellow thick edges represent the symmetry planes of the geometries.

Subduction name	Reference figure	Trench shape	Sustaining mantle flow	Encroaching mantle flow	Plate convergence min/max (mm/yr)	Upper plate stress
South America	2.8a	mixed	X		$14-78$	compressional to neutral
Sumatra-Java	2.8b	curved	X		$32-77$	neutral
Central America	2.8c	linear	X		$29-50$	neutral
Vanuatu	2.8d	mixed	X		$54-84$	neutral
Solomon	2.8e	mixed	X		$32-50$	compressional to neutral
Aleutians	2.8f	curved		X	$46-84$	neutral
Kermadec-Tonga	2.8g	linear		X	$145-220$	tensional to neutral
Ryukyu	2.8h	linear		X	$24-63$	tensional to neutral
Izu-Bonin	2.8i	mixed		X	$21-102$	tensional
Philippines	2.8j	linear		X	$97-106$	neutral to compressional

Table 4.5. Compilation of the main subduction zones of figure 2.8 with indications about the trench geometry (i.e., linear, curved or variable along-strike), the mantle flow (relative to the slab dip), the plate convergence [HS3 reference frame; *Gripp and Gordon*, 2002] and the kind of deformation affecting the upper plate.

Models forced by an encroaching mantle flow (Figure 4.19g-i), show for the upper plate results similar to those outlined above. The direction of the stress axes still depend on the geometry of the plate boundary, as they are predicted to rotate in order to remain perpendicular to the trench. Different is the situation concerning the stress field regime. The general compression predicted within the overriding plate by models with sustaining mantle flow, is here turned into overall tension. This finding is consistent with the trench rollback and the slab retreat associated with the Mariana-type subduction, and represents the prerogative for the development of back-arc basins (see section 2.4). Despite the general tensional stress field, a region of the overriding plate is characterized by trench-normal compression. This area is located within the lithosphere lying above the slab projection, and follow again the linear (Figure 4.19g) or curved trend (Figure

Fig. 4.20. Intraplate stress orientation (0-50 km depth) for the Chile-type subduction zones. Direction of the largest compressive horizontal stress (SHmax) for thrust (blue), normal (red) and strike-slip (green) stress regimes is shown for the a) South America, b) Sumatra, c) Central America and d) Solomon subduction zones (data after *Heidbach et al.* [2008]. Same representation as in figure 2.8. Map view of the principal stress axes at crustal depth (5 km) within both the lower and the upper plates obtained by 3D models with linear and curved trench geometries forcing slab pull and 4 cm/yr mantle flow sustaining the slab (panels e-g). Blue lines indicate the compressional stresses, and red lines the tensional stresses. The yellow thick edges represent the symmetry planes of the geometries.

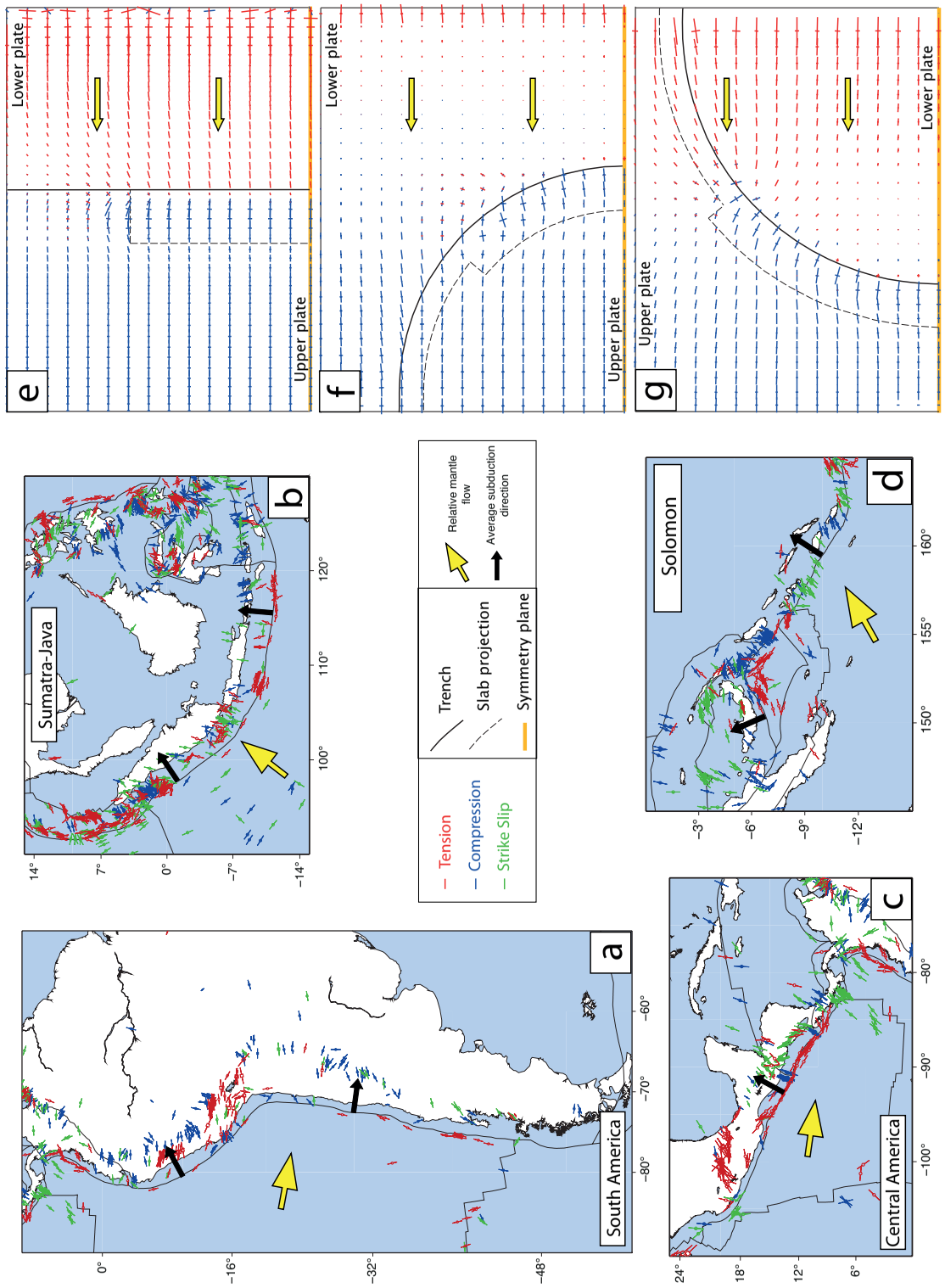

Fig. 4.20 (caption in the previous page)

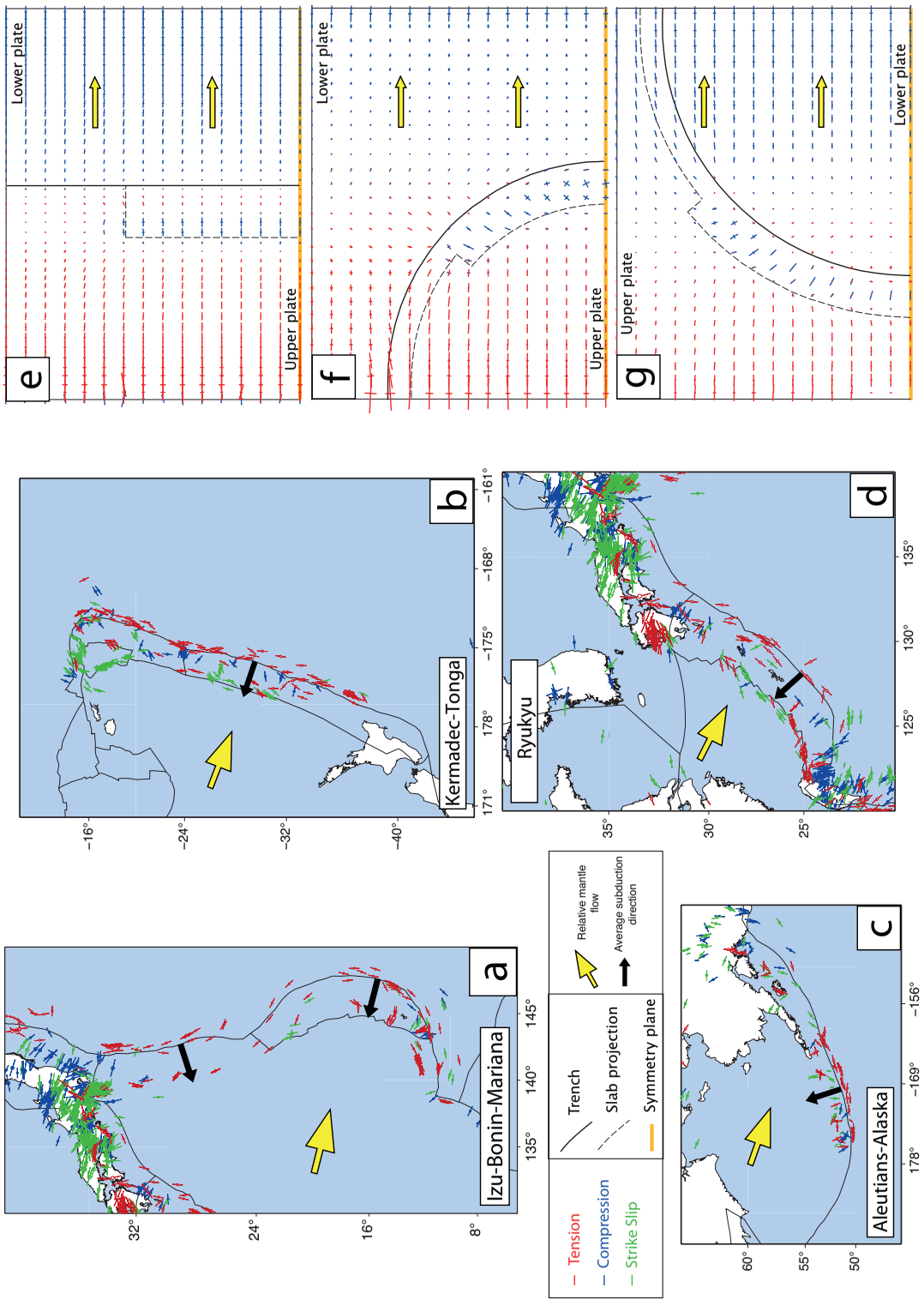

Fig. 4.21 (caption in the next page)

Fig. 4.21. Intraplate stress orientation (0-50 km depth) for the Mariana-type subduction zones. Direction of the largest compressive horizontal stress (SHmax) for thrust (blue), normal (red) and strike-slip (green) stress regimes is shown for the a) Mariana, b) Kermadec, c) Aleutians and d) Ryukyu subduction zones (data after *Heidbach et al.* [2008]. Same representation as in figure 2.8. Map view of the principal stress axes at crustal depth (5 km) within both the lower and the upper plates obtained by 3D models with linear and curved trench geometries forcing slab pull and 4 cm/yr mantle flow opposing the slab (panels e-g). Blue lines indicate the compressional stresses, and red lines the tensional stresses. The yellow thick edges represent the symmetry planes of the geometries.

4.19h-i) of the slab. These models can be compared with real Mariana-type subduction zones (cf. section 2.3). The trench-normal tension obtained with models, is comparable with the SHmax axes parallel to the subduction trench in the Stress Map database (see red axes in figure 4.21a-d). Best example of this kind of lithospheric deformation comes from the Izu-Bonin subduction zone (Figure 4.21a), where the tensional SHmax pattern can be tracked from North to South parallel to the strike of the whole trench. The same situation characterizes the Kermadec and the Aleutians subductions (Figure 4.21b-c), even if it emerges less clearly from data. The trench-normal compression resulting from the models over the slab projection (Figure 4.21e-g), are comparable with stress data from real subductions. Actually, trench-perpendicular compressional axes are recognizable for the upper plate of the Kermadec, the Aleutians and the Ryukyu subductions (Figure 4.21b-d).

Regardless of the kinematics assumed in the models, stress axes direction rotate widely close to the slab lateral tips. This is mainly due to the local mantle flow interacting with the slab (see section 2.4), and then associated with local rather then regional mechanisms of lithospheric deformation. In these areas, the stress axes display a circular pattern around the slab edges of both linear and curved slabs (Figure 4.19a-j). This is a common feature in natural subductions as outlined by stress data. The stress regime is compressional, strike-slip or tensional depending on the kinematics. Best examples are the eastern edge of the Central America (Figure 4.20a), the northern edge of the Kermadec-Tonga (Figure 4.21b), the eastern edge of the Aleutians-Alaska (Figure 4.21c) and the western edge of the Ryukyu (Figure 4.21d).

The modelling results indicate that the stress field affecting the lower plate at shallow depths is generally neutral to tensional when the model is forced only by the slab pull, or in case of sustaining mantle flow (Figure 4.19a-f). Instead, widespread compression is enhanced by mantle flow opposing the sinking slab (Figure 4.19g-i). Stress axes rotation, governed by the trench geometries, is clear also in the lower plate. Few stress data concerning the shallow lower plate are available, and this renders the comparison between modelling results and natural cases difficult. Available data generally show SHmax tensional axes lying sub-parallel to the subduction trenches (Figures 4.20a-d and 4.21a-d), consistent with the bending of the

plate prior to subduction. This bending-drived tension is recognizable in the modelling results, including the case of encroaching mantle flow (e.g., see figures 4.20e-g and 4.21e-g).

From the results shown so far, it is clear the importance of choosing carefully all the initial parameters that contribute to the genesis of a given stress field. The subduction geometry, the plates convergence and the absolute plates motion relative to the underlying mantle, must be selected as accurately as possible for an optimal match between the model and the observables. The aim of the next chapter is to reproduce a subduction in a real setting (the central Mediterranean area), and to compare the results with all available data.

5

An application of 3D modelling to the Calabrian - Aegean subduction system

Guideline to the chapter contents

The outcomes of the plate scale models (investigated in the previous chapter), strongly underline how the stress field affecting a convergent margin depends on the delicate balance between the involved tectonic forces. The aim beyond this chapter is to reproduce a subduction in a real setting, using the observable to constrain the model and validate or refute the observations previously made for the general cases. The Adriatic micro-plate (also called Adria and Apulian plate; figure 5.1) is a good candidate to apply this kind of viscoelastic model approach, as it is down-bent into the opposing subduction zones of the Apennines-Calabria (slab dipping to the west) and Dinarides-Hellenides (slab dipping to the east) at very short distance (ca. 100-150 km). Here I propose a 3D mantle-scale model built to evaluate the contribution of plate kinematics (convergence between Africa and Europe and relative motion between lithosphere and sub-lithospheric mantle) and of the 3D geometry of Calabria-Aegean subduction zones to the definition of present day stress field in the Adriatic Sea and Periadriatic regions of Italy. I also discuss the differences in the stress fields within the Calabrian and Hellenic subducting slabs.

5.1 Introduction

The stress field affecting a convergent margin depends on the delicate balance between the involved tectonic forces and the geometric characteristics of subducting plates. The Adriatic micro-plate is a good candidate to verify the consistency between models outcome and observable, as here different kinematics and geometric features can be found in such a small region. The Adria plate (Figure 5.1) formed as a consequence of the subduction of the Ionian oceanic crust under the southern margin of the European plate. Adria peculiar geodynamics is related to its down-bent into the opposing subduction zones of the Apennines-Calabria (slab dipping to the west) and Dinarides-Hellenides (slab dipping to the east). In addiction the Adriatic region represents the retro-belt foreland of the SE-directed Alpine subduction [*Doglioni and Carminati*, 2002; *Dal Piaz et al.*, 2003], and the foreland basin of the NE-directed Dinaric subduction [*Di Stefano et al.*, 2009]. Paleomagnetism, propagation of transverse waves refracted below the Mohorovic discontinuity, paleoclimatology and palynology suggest that Adria belongs structurally and kinematically to Africa [e.g., *Mantovani et al.*, 1990; *Channell*, 1996; *Mele*, 2001; *Muttoni et al.*, 2001], whereas historical seismicity, geodetic and seismic evidence suggest that Adria is at present an independent micro-plate within the Africa-Eurasia plate boundary zone [*Anderson and Jackson*, 1987; *Nocquet and Calais*, 2003].

The complex geological history of Adria is evident also in its lithosphere, which strongly changes from north to south (along a distance of some 1000 km): it is thinned-continental in the north Adriatic Sea, thick-continental in the south Adriatic Sea, and likely oceanic [*Catalano et al.*, 2001; *Carminati et al.*, 2010] in the Ionian Sea, although a transitional or continental nature for the Ionian basin has been also proposed [*Calcagnile and Panza*, 1979; *Panza et al.*, 2007]. Such paleogeographic features controlled the geometry and evolution of contractional structures associated with fold-and-thrust belts surrounding the Adriatic plate. Indeed the tectonic setting (Figure 5.2) and rheological behavior of Apennines and Dinarides thrust fronts are largely variable, as shown also from several arcs developing along the main trend of both belts. The present-day stress field in the Adriatic plate reflects such variability. By means of 3D numerical model, in this chapter I study the complex state of stress in the Adriatic plate, especially along the Italian Periadriatic area, speculating on the plate-scale sources of stress associated with subduction processes active in the region and discuss the differences in the stress fields within the Calabrian and Hellenic subducting slabs.

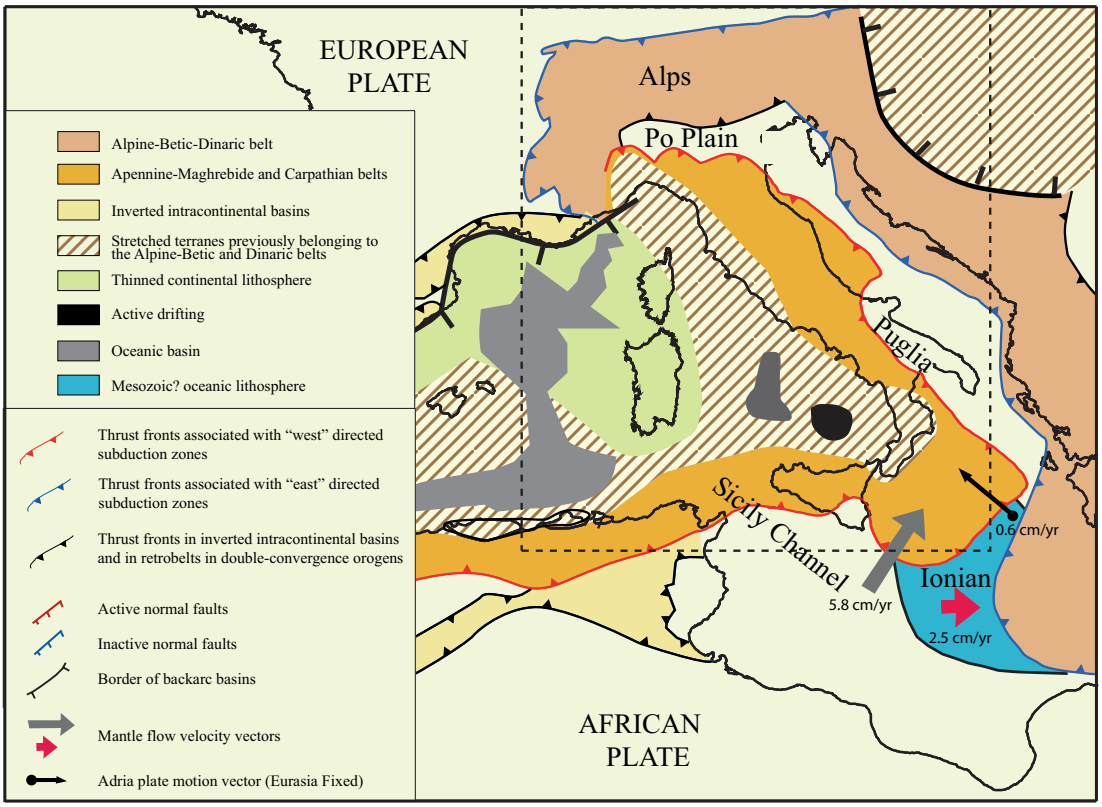

Fig. 5.1. Simplified geodynamic and tectonic map of the Central Mediterranean. The dashed rectangle shows the location of figures 5.2 and 5.3. Mantle motion relative to the lithosphere in the deep [*Gripp and Gordon*, 2002] hotspot reference frame (red arrow) and in the shallow [e.g., *Cuffaro and Doglioni*, 2007] hotspot reference frame (gray arrow) are also shown (see section 5.3 for explanation). Black arrow represents Adria plate motion relative to Eurasia fixed [*Serpelloni et al.*, 2005].

5.2 The stress field from data

In the northern part of the Adriatic plate, stress orientations show a complex pattern (Figure 5.3), with the maximum horizontal stress (SH_{max}) at first approximation perpendicular to the Adria surroundings belts. In the northern part of Adria, the N-S stress axes orientation is consistent with the compressive tectonic activity of Southern Alps thrust and with the dextral strike-slip tectonics of the steeply dipping NW-SE trending faults of northernmost External Dinarides [*Kastelic et al.*, 2008].

Also in the Po Plain, compression is generally N-S, although short wave-length variations of stress axis orientation are determined by the structural undulations of the buried thrust fronts [*Perotti*, 1991; *Doglioni*, 1991; *Montone and Mariucci*, 1999; *Mariucci and Müller*, 2003; *Carminati and Vadacca*, 2010; *Montone*

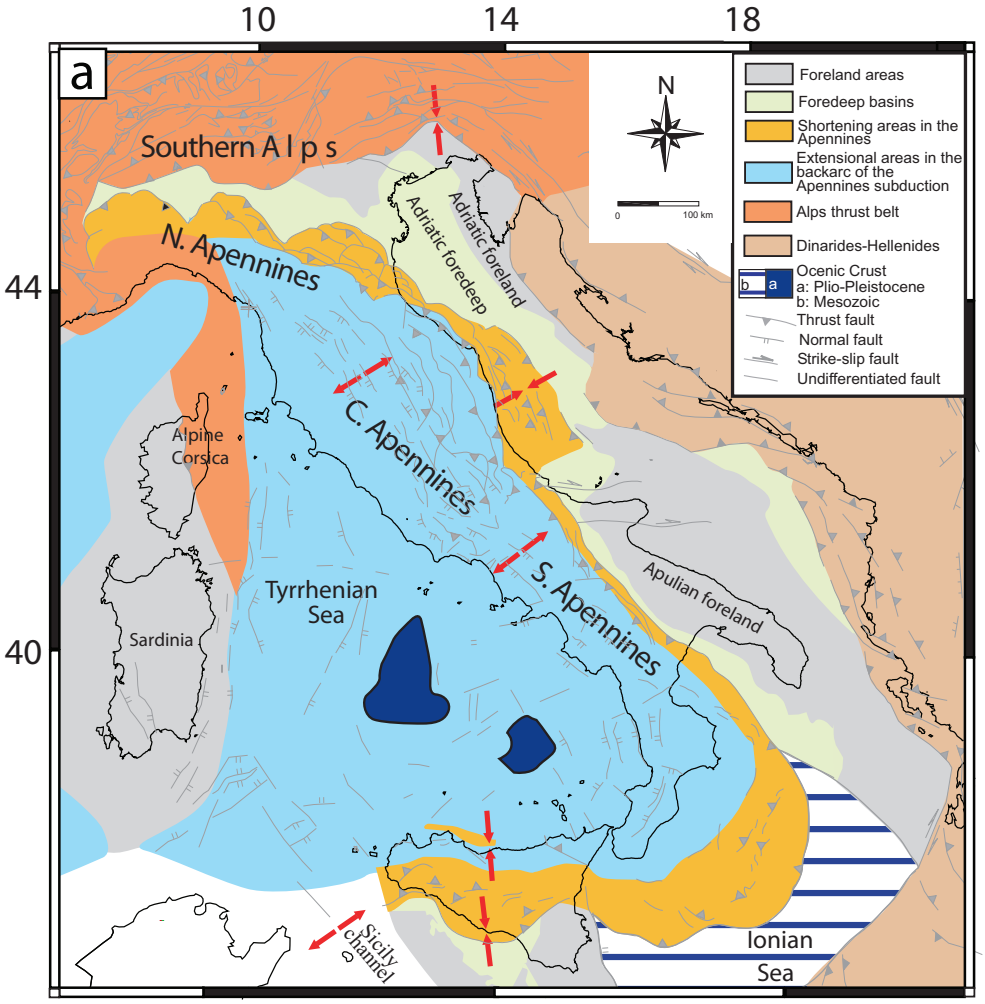

Fig. 5.2. Simplified tectonic map of the Italian area, including the main geographical references (modified from *Carminati and Doglioni* [2012]) and the major faults in the region from the Structural map of Italy [*Bigi et al.*, 1992]. The red arrows illustrate the different tectonic regimes.

et al., 2012]. The N-S orientation of SH_{max} in the Southern Alps documents that the ca. N-S convergence between Africa and Europe is associated with a NW-ward propagation of compressional stresses along the entire Adriatic Plate. The regional state of stress in the southern Po Plain is characterized by approximately NE-SW compression [*Heidbach et al.*, 2008].

The moment tensors of larger earth-quakes, routinely determined based on data by *Group et al.* [2010] and velocity model by *Herrmann et al.* [2011], occur to be compressive with P-axes approximately perpen-

dicular to the thrust faults along the Apennines fronts buried under the Po Plain sediments. The fault plane solutions from polarity analysis of smaller earthquakes are characterized by large strike-slip components [*Frepoli and Amato*, 1997] with P-axes compatible with those of larger earthquakes.

Stress orientations display a rather continuous compression along the outer front of the Apennines, from the Po Plain to the offshore of Calabria and Sicily, and along the External Dinarides, from Croatia to Albania coastlines. However, the state of stress in the Adriatic plate is far from being simple. In the Northern Adriatic, SH_{max} is oriented N-S along the coastline, whereas the maximum compression is perpendicular to the active Apennines outer thrust fronts. According to *Carafa and Barba* [2011] an important role in determining such stress pattern is played by the lateral variation of the strength of the Adriatic lithosphere.

In the Central Adriatic the Apennines front lies adjacent to the Dinarides thrusts [*Scrocca*, 2006] and the widespread compressive deformation affects the sea bottom. The compressive stress regime in the Adriatic micro-plate is also evident from earthquakes occurred in the Central Adriatic Sea [*Herak et al.*, 2005]. In the Southern Adriatic, north of the Tremiti Fault (Figure 5.3), a well-defined cluster of stress measurements indicate NW-SE compression. Stress data show a prevailing NE-SW orientation of SH_{max}. However, some earthquakes, like the 2002 Molise earthquake or 1991 Potenza earthquake indicate a present-day stress field characterized by strike-slip deformation mechanisms with E-W right-lateral faults dissecting the Southern Apennines belt [*Barba et al.*, 2010].

The Southern Apennines are characterized by extension in the sediments scraped off from the subducted Adriatic lithosphere. The SH_{max} axes along the NW-SE trending foredeep are parallel to the main thrusts and suggest that the onshore thrusts may be slightly active or inactive; compression results in continental transpression in the Gargano promontory and across the Mattinata fault zone [*Doglioni*, 1994], where earthquakes show strike-slip mechanisms with a non-negligible compressive component [*Del Gaudio et al.*, 2007]. In southern Apulia and offshore the predicted SH_{max} orientations of *Barba et al.* [2010] mostly trend E-W, but fewer data records are available for this area.

The External Dinarides and Albanides, on the other side of the Adriatic, host strong earthquakes (such as the 1979 M=7.2 Montenegro earthquake), characterized by transpressive to reverse mechanisms [*Benetatos and Kiratzi*, 2006]. Stress data show that External Dinarides and Albanides are undergoing compression perpendicular to the trend of the belt [e.g., *Heidbach et al.*, 2008].

In the Calabrian arc, we observe a gradual rotation of the SH_{max} orientations from NW-SE to NE-SW, following the curvature of the arc. However seismic reflection data support active thrusting perpendicular to the offshore Ionian thrust [*Catalano et al.*, 2001; *Polonia et al.*, 2011], where the accretionary prism, associated with the subduction of the Ionian lithosphere underneath Calabria, is located.

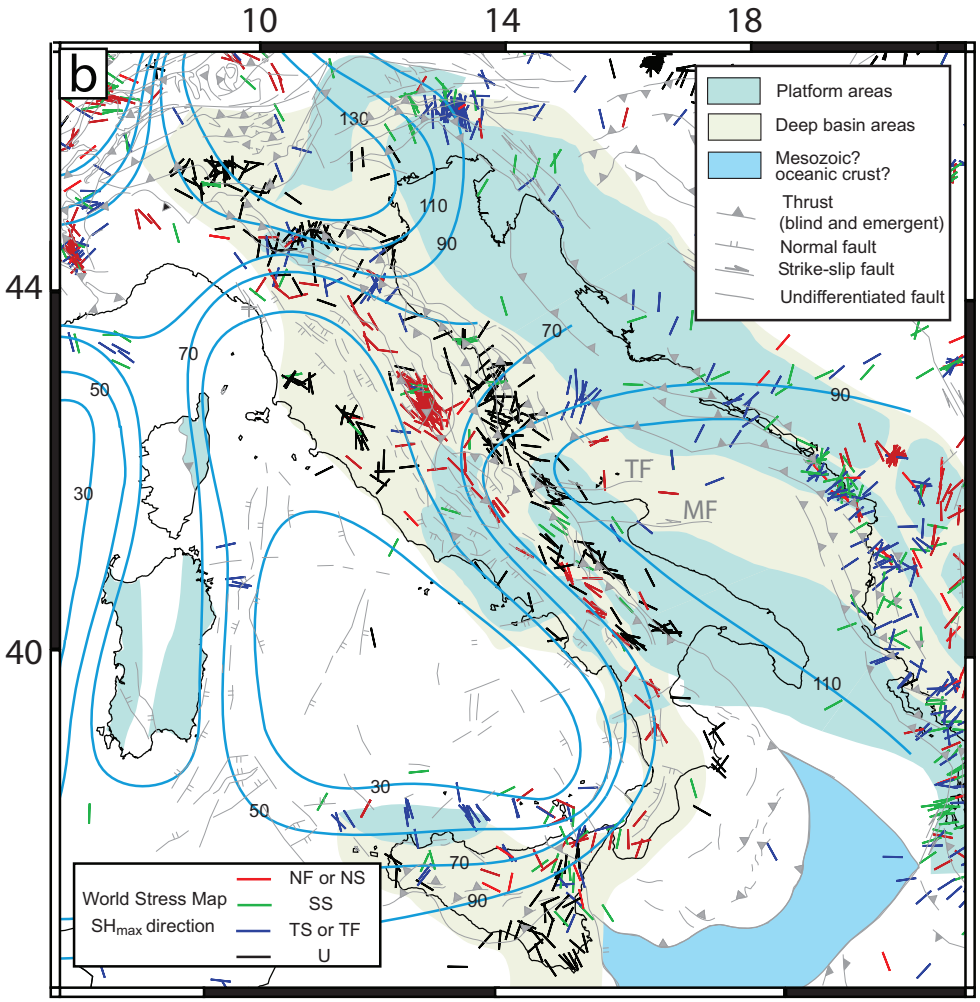

Fig. 5.3. Orientation of SHmax from well breakouts and seismological data (data after *Heidbach et al.* [2008]). The map shows also the Late Liassic-Hauterivian paleogeography of the Italian area (redrawn from *Zappaterra* [1994]). The thickness of the lithosphere (in km) in the Italian area is also shown (after *Panza et al.* [1992]). TF: Tremiti Fault; MF: Mattinata Fault.

In the Sicily Channel, NE-SW trending thrust sheets of the Apennines-Maghrebian accretionary prism crosscut and are crosscut by NW-SE trending normal faults, associated with the Malta-Linosa and Pantelleria rifts, indicating present-day activity of both families of structures [*Corti et al.*, 2006]. These features are poorly constrained by available stress data, but they are clear from available geological and geophysical data.

Finally, sub-crustal seismicity constrains the state of stress at intermediate depths of subducting slabs. The East-directed slab of the Hellenic subduction is characterized by down-dip extension [*Papazachos et al.*, 2005] whereas the West-directed slab of the Calabrian subduction is characterized by compression [*Frepoli et al.*, 2007]. Both slabs consist of the same lithosphere (Ionian) representing a branch of the Tethys Ocean, probably oceanic and Mesozoic in age [*Catalano et al.*, 2001]. As a consequence, the different state of stress cannot be related to differential slab pull in the two subduction zones. Both subductions occurred in the framework of a circa N-S convergence between Africa (to which Adria is kinematically attached) and Europe, as constrained by paleomagnetic data [e.g., *Channell*, 1996; *Muttoni et al.*, 2001]. As the Apennines subduction is concerned, the slab retreat occurred faster in the oceanic Ionian corridor than in the continental parts of the Adriatic Plate [*Carminati et al.*, 2010, and references therein]. This, in turn, produced a larger southeastward advancement (salient) of the thrust front in the offshore of Calabria, a curved Apenninic slab and a first order arc in the Apennines. At the plate scale, the upper crustal stress field at the Apennines front is governed by the curved shape of the Adriatic slab. In figure 5.3, first-order rotations of the stress axes are observed passing from the Southern Apennines to Calabria to Sicily.

The continental portion of the Adriatic plate is also strongly heterogeneous. As the lithospheric thickness is concerned, the southern part of the plate is rather thick (up to 110 km), whereas the lithosphere flooring the central and northern Adriatic Sea is thin (ca 70 km). The thickening of the lithosphere more to the north is related to the Alpine orogeny. Thinner and thicker portions of the Adriatic plate show distinct tectonic signatures [*Doglioni*, 1994]. The Mattinata and Tremiti E-W faults [e.g., *Tondi et al.*, 2005] are the right-lateral lithospheric transfer zones connecting these two tectonic realms (Figure 5.3)

5.3 Calabria-Aegean model description

For the first time a 3D model including both the Apennines-Calabrian and Dinarides-Hellenides subductions is proposed. The models are intended to reproduce first order features of the stress field of the Adriatic plate and of its subducting slabs. Second order features cannot be reproduced by this kind of model that include a simplified geometry of the Adriatic and adjacent plates.

The shape and depth of the Calabrian and Hellenic slabs are constrained using the results of the SHARE (http://diss.rm.ingv.it/share-edsf/) database. This database, which I contributed to build [*Basili et al.*, 2013a] provides geometric, kinematic and dynamic parameters for the Mediterranean subduction (see appendix A). The deeper portions of the slab subducted beneath Calabria were constrained by seismic and tomographic

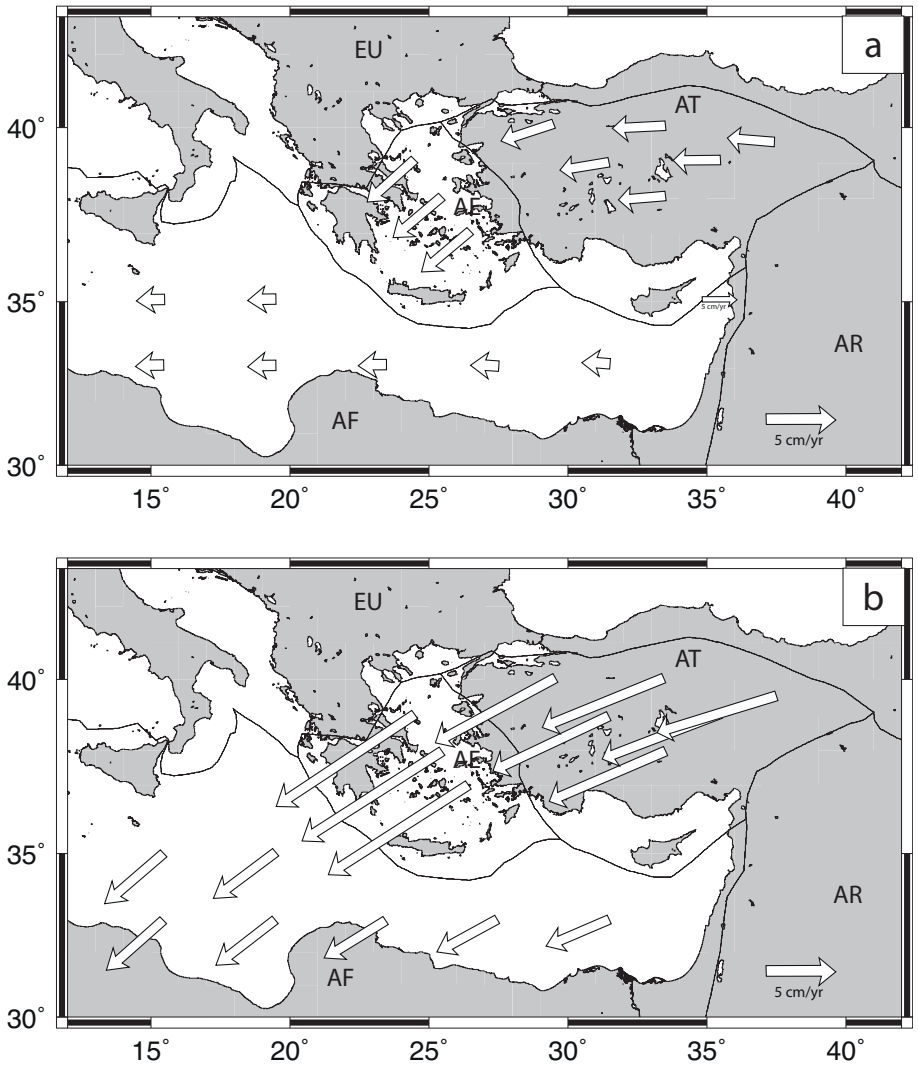

Fig. 5.4. Westward plate motions in the Mediterranean region [after *Doglioni et al.*, 2007] relative to the mantle in the deep (a) and in the shallow (b) hotspot reference frames (see text for explanation). The relative motion of the underlying mantle is represented in figure 5.1. Coastlines and contacts between the tectonic plates are drawn: EU, Eurasian; AF, African; AE, Aegean; AT, Anatolian; AR, Arabian.

[*Barberi et al.*, 2004; *Chiarabba et al.*, 2008] and SKS splitting [*Baccheschi et al.*, 2011] data. Deep seismicity depicts a well-developed near-vertical subducting slab up to 500 km depth. Seismicity distribution and seismic tomography depict a well developed Wadati-Benioff zone beneath the Aegean Sea to a depth up to 300 km [*Benetatos et al.*, 2004; *Bohnhoff et al.*, 2005; *Papazachos et al.*, 2000; *Piromallo and Morelli*, 2003; *Rontogianni et al.*, 2011]. The choice of introducing a shallower Apenninic slab (100 km depth) is

driven by the occurrence of intermediate seismicity beneath the northern Apennines [e.g., *Chiarabba et al.*, 2005], giving some evidences of subduction in the central-North part of the Italian peninsula.

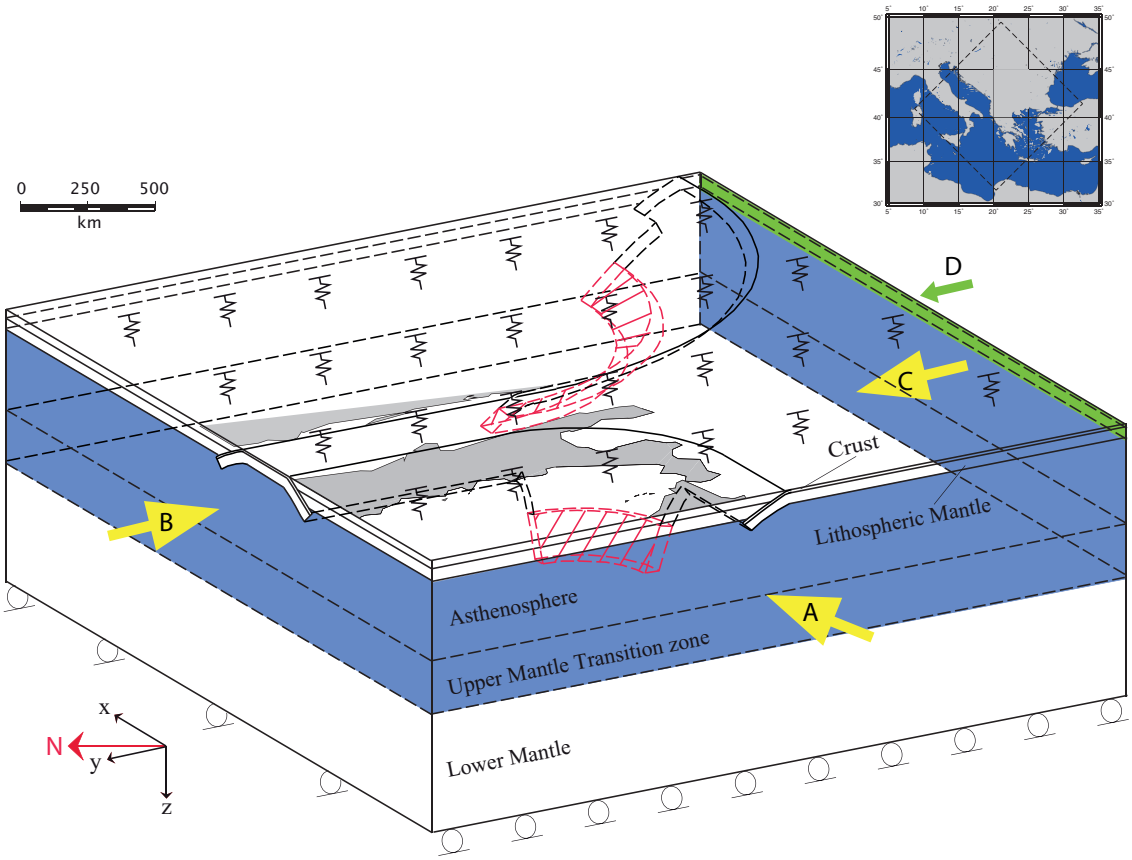

Fig. 5.5. Model geometry, materials and boundary conditions used in the 3D calculations. The circles denote a roller boundary condition. The yellow arrows denote the velocity applied to the mantle boundaries (blue faces) selected to simulate the relative motion between mantle and lithosphere (when modelled). The green arrow denotes the velocity applied to the south-eastern boundary of the Adriatic lithosphere (green boundary) to simulate the motion of the African plate (when modelled). If such velocities are set to zero, only vertical slip along the associated lithospheric boundary and free boundary conditions for the mantle are allowed. For the remaining lithospheric boundaries only vertical slip is permitted. The springs represent the buoyant restoring force applied at the surface (Winkler foundation; see section 3.5). When a density contrast was applied to simulate slab pull, is forced only for the red gridded subdomains. Italy is represented as model scale reference. The dashed rectangle in the upper panel shows the extension of the model. North is indicated within the reference axes (red arrow).

Plate kinematics, both in terms of relative convergence between plates and in terms of relative motion between lithospheric plates and deeper mantle, is fundamental in our modelling. The present-day relative convergence between Africa and Europe is constrained by GPS data, which show Europe-Africa NW di-

rected convergence rates ranging from 3 to 8 mm/yr at the longitude of the Calabrian Arc front [*DeMets et al.*, 1994; *McClusky et al.*, 2003; *D'Agostino and Selvaggi*, 2004; *Serpelloni et al.*, 2005; *Devoti et al.*, 2008]. At the longitude of the Hellenic arc, velocities of 5-9 mm/yr were calculated [*DeMets et al.*, 1994; *Le Pichon et al.*, 1995; *Cocard et al.*, 1999; *Bird*, 2003; *McClusky et al.*, 2003; *Kreemer and Chamot-Rooke*, 2004; *Reilinger et al.*, 2006; *Ganas and Parsons*, 2009].

As relative motions between lithosphere and mantle are concerned, the Adriatic-Ionian lithosphere moves "westward" with respect to the mantle in all of the hot spots reference frames [*Doglioni et al.*, 2007]. It is clear that owing to the dip direction of the slabs with respect to the absolute plate motion, Calabrian West-dipping slab oppose the relative mantle flow, whereas the Hellenic East-dipping slab accompanies the relative mantle flow, possibly controlling the stress field within the slabs. The magnitude of westward drift of the lithosphere in this region strongly depends on inversion choices (see section 2.4). For the Mediterranean region, if a deep origin is assumed for hot spots (figure 5.4a), the Adriatic-Ionian plate generally moves westward (and the relative mantle flow is east-directed) in an E-W direction at approximately 2.5 cm/yr (represented with the red arrow in figure 5.1) according to Model HS3 [*Gripp and Gordon*, 2002]. If their source is shallow (figure 5.4b), then the plate moves southwestward (and the relative mantle flow moves toward N-E as indicated with the gray arrow in figure 5.1) at approximately 5.8 cm/yr [e.g., *Cuffaro and Doglioni*, 2007]. Both mantle-lithosphere relative kinematics, i.e. referred to deep (hereafter kinematics type-1) and shallow (hereafter kinematics type-2) hot spots origin, were tested in our calculation (Figure 5.1).

5.3.1 Model set-up

Finite element modeling was performed using the software COMSOL Multiphysics (www.comsol.com) with a viscoelastic approach (see section 3.1). The compatibility, equilibrium and constitutive equations for a viscoelastic Maxwell body (see section 3.4 for further explanations) are solved simultaneously. Isostatic forces are addressed in the modelling as adjunctive subdomain conditions (see section 3.5). Following the approach used for the 3D plate-scale models (see chapter 3), each layer is characterized by the rheological parameters and thicknesses showed in table 5.1.

The geometry of the model (Figure 5.5) includes in a realistic way the Calabrian and Hellenic subducting slabs and the portion of the Adriatic plate corresponding with the Adriatic Sea. The northern part of the plate (Po Plain and Southern Alps front) is simplified. The contact between the Adriatic Plate and the European Plate is modelled as a fixed model boundary, reproducing the collision in the Alps as a sort

of back-stop. This plate scale model includes crust, lithospheric mantle, asthenosphere, upper and lower mantle (Figure 5.5), modelled as viscoelastic layers.

Zhong and Gurnis [1994] and *Zhong et al.* [1998] showed that the inclusion of a fault along the subduction boundary was important for the reproduction of trench morphology. *Giunchi et al.* [1996] showed that in viscoelastic models, the unlocking of this plate scale fault can be obtained by a slip condition on the nodes of the elements belonging to the slab and upper mantle, while maintaining the contact between the two parts of the fault. I used this approach for the present study. The contact between upper and lower plates is modelled as a single subduction fault, considered unlocked in all the calculation. This choice is motivated as I am interested to the regional stress field (compression or tension axes direction), rather than stress magnitude (controlled by the upper-lower plate coupling). *Giunchi et al.* [1996] models also showed that, for the Adriatic region only considering unlocked plate interfaces reproduce the principal geodynamic features highlighted by available data.

To avoid boundary effects, our geometries have lateral and depth extension larger than the interest domains, that are the subducting slabs and the lithosphere in the area representing the Adriatic and Ionian regions. The bottom of the models is located at 1000 km. Our simulations focus on the stress field within the slab at shallow and intermediate depths rather than on the interaction between the slabs and the viscosity jump at the upper-lower mantle transition. The model geometries also provide a considerable distance between the tip of the sinking slabs and the 670 km depth interface.

Layer	**Young modulus (Pa)**	**Viscosity (Pa s)**	**Poisson's ratio**	**Thickness (km)**
Crust	6×10^{10}	1×10^{24}	0.25	Lower plate: 10 Upper Plate: 35
Lithospheric mantle	1.75×10^{11}	5×10^{24}	0.27	Lower plate: 50 Upper plate: 50
Asthenosphere	1.27×10^{11}	5×10^{17} 1×10^{19} 1×10^{21}	0.27	200
Upper mantle	1.75×10^{11}	1×10^{21}	0.27	370
Lower mantle	1.27×10^{11}	1×10^{22}	0.27	330

Table 5.1. Main constants and expressions used for the Calabria-Aegean model.

The Calabrian slab dip approximately 80° up to 500 km depth, while the Hellenic slab is less steeper (35° dipping) and reaches 300 km depth. Slab domains have been divided in subdomains to facilitate the inclusion of buoyancy anomalies that reproduce slab pull forces.

Mechanical boundary conditions are the following:

1. The bottom of the model (normally located at 1000 km in the lower mantle) is fixed in the vertical direction (free horizontal slip is allowed). However, in some models (to investigate the sensitivity of the model respect the application of different boundary conditions) the mantle flow was simulated applying a drag to the base of the upper mantle (results shown in the auxiliary material). In these cases, the bottom of the model coincides with the 670 km discontinuity, it was fixed in the vertical and a horizontal motion, consistent with the mantle flow vectors, was applied along this boundary.
2. The boundaries of the lithosphere are kept fixed in the horizontal direction (free vertical slip allowed), with the exception of the lithospheric SE boundary (Figure 5.5), where horizontal velocity was applied (if not otherwise indicated) to simulate convergence between the two plates (in both cases slip along the vertical is allowed). The assumed convergence rate between upper and lower plates, when applied, is 6 mm/yr in a NW direction, consistent with previous regional kinematics studies [*Westaway*, 1990; *McClusky et al.*, 2003; *Serpelloni et al.*, 2005], as discussed above.
3. The lateral boundaries of the upper mantle are either left free, both in terms of displacement and forces (when no mantle flow is simulated), or alternatively a horizontal velocity (ranging from 1 cm/yr to 10 cm/yr in different models) is applied with different azimuthal angles, to simulate the effects of mantle motion relative to the lithosphere, obtaining a resultant flow direction and magnitude in agreement with the predictions of *Doglioni et al.* [2007] for the central Mediterranean region. In the models in which mantle flow is simulated by a drag applied at the base of the upper mantle, the lateral boundaries of the upper mantle were left free.
4. The lateral boundaries of the lower mantle are always set free.

The finite element mesh consists of ca. 134000 tetrahedral elements and 50000 triangular boundary elements, which provides a total of 3802623 degrees of freedom. The mesh is denser (nodal distance between 10 and 40 km) in the regions of the model of most interest (i.e. slabs and lower plate's lithosphere), and becomes progressively less dense moving away from these domains (maximum nodal distance of 500 km in the lower mantle). In any case the stability of the solution was tested against mesh refinements.

Model ID	E directed mantle flow (type 1 kinematics)	NE directed mantle flow (type 2 kinematics)	Plate convergence	Extra features	N Adriatic Plate: NW-ward propagation of compression	S Adriatic Plate: NE-SW compression	Sicily Channel: NE-SW tension	Calabrian slab: downdip compression	Hellenic slab: downdip tension
1	No	No	No	Only slab pull	No	No	Yes	No	Yes
2	No	No	Yes		Yes	No	No	No	Yes
3	Yes	No	Yes		No	No	Yes	Yes	Yes
4	Yes	No	No	No plate motion	No	No	Yes	Yes	Yes
5	Yes	No	Yes		No	No	Yes	Yes	Yes
6	Yes	No	No	No plate motion	No	No	Yes	Yes	Yes
7	No	Yes	Yes		Yes	No	Yes	Yes	Yes
8	No	Yes	Yes		Yes	Yes	Yes	Yes	Yes
9	No	Yes	No	No plate motion	Yes	No	Yes	Yes	Yes
10	No	Yes	Yes	No slab pull	Yes	Yes	Yes	Yes	Yes
11	No	Yes	Yes		Yes	Yes	Yes	Yes	Yes
12	No	Yes	Yes		Yes	No	Yes	Yes	Yes
13	No	Yes	Yes		Yes	No	Yes	Yes	Yes
14	No	Yes	Yes	Asthen. 10^{19} $Pa\ s$	Yes	Yes	Yes	Yes	Yes
15	No	Yes	Yes	Asthen. 10^{17} $Pa\ s$	Yes	Yes	Yes	Yes	Yes
16	No	Yes	Yes	Asthen. 10^{19} $Pa\ s$	Yes	Yes	Yes	Yes	Yes
17	Yes	No	Yes	No lower mantle	No	No	Yes	Yes	Yes
18	Yes	No	No	No lower mantle	No	No	Yes	Yes	Yes
19	Yes	No	Yes	No lower mantle	No	No	Yes	Yes	Yes
20	No	Yes	Yes	No lower mantle	No	No	Yes	Yes	Yes
21	No	Yes	Yes	No lower mantle	No	No	Yes	Yes	Yes
22	No	Yes	Yes	No lower mantle	Yes	No	Yes	Yes	Yes
23	No	Yes	Yes	No lower mantle	Yes	No	Yes	Yes	Yes

Table 5.2. Compilation results and first order features of the stress field in the Adriatic plate reproduced by the various configurations.

The evolution time of the model is 250 kyr, considered to be appropriate to describe the global response of the system for the represented geodynamic setting. In this time frame the model evolves towards a steady state. Especially with regard to the crust, the use of a viscoelastic rheology does not exclude its elastic behavior, being the evolution time greater than the crust relaxation time. All the model results are shown for the 250 kyr time.

Several configurations (varying lithosphere and mantle kinematics, applied forces and rheological parameters) were tested (list of model results is provided in table 5.2). Here I display the results for a limited number of such configurations. The remaining modelling results are provided in the accompanying material. The capability of the various configurations to reproduce the first order features of the stress field in the Adriatic plate is shown in table 5.2. Successful models will have to reproduce: 1) downdip compression in the slab subducting underneath Calabrian; 2) downdip tension in the slab dipping under the Aegean arc; 3) NW-ward propagation of compression in the northern Adriatic plate; 4) NE-SW compression in the southern Adriatic plate; 5) tension in the Sicily Channel.

5.4 Model results

In a first set of models, configurations in which the forcing factors acting in the region were added one at a time (first slab pull, then plate convergence and later mantle flow) are adopted. This strategy allows to evaluate the impact of each single forcing factors on the present-day stress field.

Figure 5.6 shows the principal stress axes predicted by a model, in which subduction is forced only by negative buoyancy associated with the applied density contrast (slab pull), neglecting plate kinematics. The resulting stress field is produced by the retreat and down pull of slabs under they own weight. The different shapes adopted for the Calabrian and Hellenic subductions, lead to different stress fields within these slabs. The lithosphere sinking below Calabria shows overall downdip tension (Figure 5.6a), whereas the slab below the Aegean shows downdip tension at shallow and intermediate depths (0-300 km) and changes to downdip compression at greater depths (Figure 5.6b). Deeper compression is due to the higher mantle resistance to the penetration of the bigger and less steep (larger slab-mantle contact area) Hellenic slab. The Adriatic plate crust (flat part of the Adriatic plate) is characterized by overall tension (Figure 5.6c), with stress axes that tend to be perpendicular to subduction fronts and then to rotate according to their geometric shape. Tension at crustal levels propagates in the Adriatic region, albeit with magnitude that progressively decreases northwards. Within the slabs, some minor compression grows parallel to the

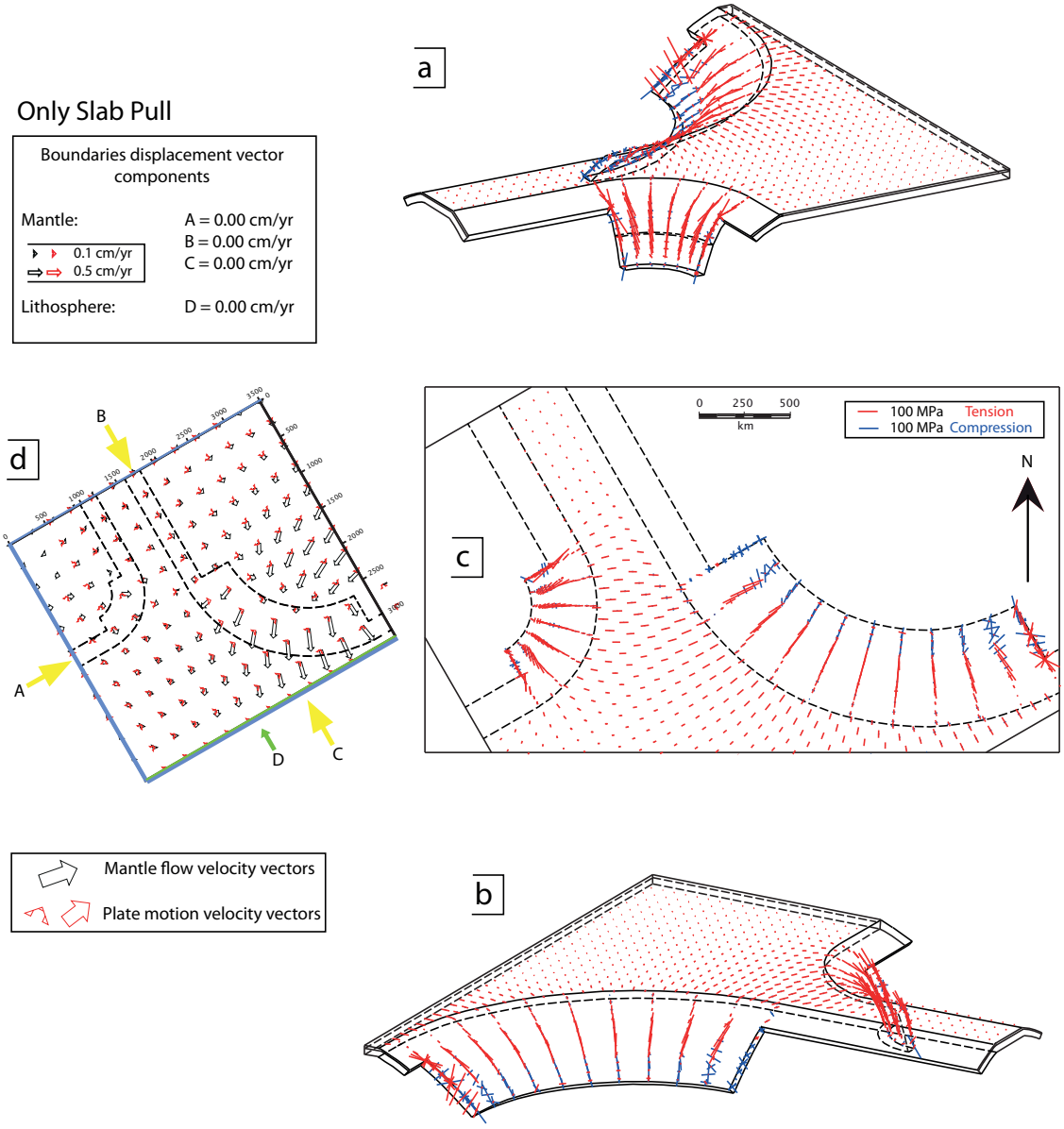

Fig. 5.6. Results of 3D model in which subduction is forced only by slab pull. Blue lines indicate compressional stresses, and red lines indicate tensional stresses: (a) with a prospective view from W (Calabrian slab focused); (b) with a prospective view from NE (Hellenic slab focused) (c) in map. Stress axes are plotted at crustal depth (5 km) within the flat portion of the geometry (Adriatic plate), and follow the crustal depth of the sinking slabs (i.e. stress axes are plotted 5 km down the Calabrian and Hellenic subduction interfaces); Upper plate is not shown for simplicity. (d) Horizontal velocity distribution; the velocities applied at boundaries are represented with yellow (for the upper mantle) and green (for the lithosphere) arrows (see figure 5.5). Red and dark-gray arrows represent the generated velocity field for lithosphere and mantle respectively. In the upper panel are reported for each boundary the values used for the component of velocity field. The resultant vectors are also drawn. Figure shows that, if only slab pull is activated the resulting tensional stress field is controlled by the retreat and down pull of the slabs under they own weight.

subduction trench, possibly generated by the along strike bending of the slabs as it occurs in the central parts of the upper slabs interface (more evident in the slab below Calabrian). The velocity field at crustal depths (5.6d) shows a convergent pattern towards the slabs, due to trench suction force, most clearly around the Aegean region that exerts a higher pull. The simultaneous effect of slab pull and roll-back generates a non-homogeneous velocity field at higher depths. Velocity vectors show that a passive flow is generated for the mantle. Mantle material tend to converge towards the slab interfaces under the suction forces exerted by slabs sinking and retreat. Slabs retreat also generates forces that pushing away the mantle behind them.

If, keeping applied slab pull forces, a northwestward plate motion of 6 mm/yr (consistent, both in direction and amplitude, with GPS data and global plate models for the central Mediterranean area) is applied at SE lithospheric boundary (Figure 5.5), the crustal stress field changes radically. A widespread NW-SE oriented compression characterizes the crust and propagates northward through the Adriatic region (Figure 5.7c). Also the region of the Sicily Channel is characterized by NW-SE oriented compression. Tensional axes are predicted with a smaller magnitude, compared to the case with only slab pull. The stress axes rotation along the front of subductions are still clear. The stress field within the slabs does not undergo substantial modifications compared to the previous model at intermediate depths and deeper regions. Compression arises at shallower depths ($<$100 km), in response to the opposite forces that stress the model at the slab hinges due to the effects of plate convergence and mantle resistance to slabs sinking (Figures 5.7a and b). The orientation of the principal stress axes for the lithosphere is primarily controlled by the horizontal velocity field of the plate (generally north- to northwest-directed), in turn influenced by the model geometries. Analyzing the velocity field at mantle depths (Figure 5.7d), is clear that it is still generated in response of slabs sinking and retreat due to the negative buoyancy of the slabs.

If mantle flow, either simulating the type-1 (as in figure 5.8) or the type-2 (as in figure 5.9) kinematics, is summed to the previous applied forces, then the resulting state of stress is markedly different. In both cases mantle flow contrasting the Calabrian subduction induces compression within the slab (Figures 5.8a and 5.9a). The Hellenic slab shows again downdip tension at intermediate depths, and a smaller compression (compared to previous results) near the lower tip of the slab (Figures 5.8b and 5.9b). These results suggest that the state of stress in the slabs is heavily controlled by the adopted mantle kinematics rather than by the slab pull. The deformation pattern of the slabs can be separated into predominant intermediate downdip compression for the west-directed Calabrian subduction (e.g., Encroaching mantle flow) and predominant intermediate downdip extension for the east-directed Hellenic subduction (e.g., sustaining mantle flow).

The mantle flow direction is crucial, because the amount of downdip compression or tension within the subducted lithosphere depends on the angle of incidence of the flow on the sinking lithosphere. This

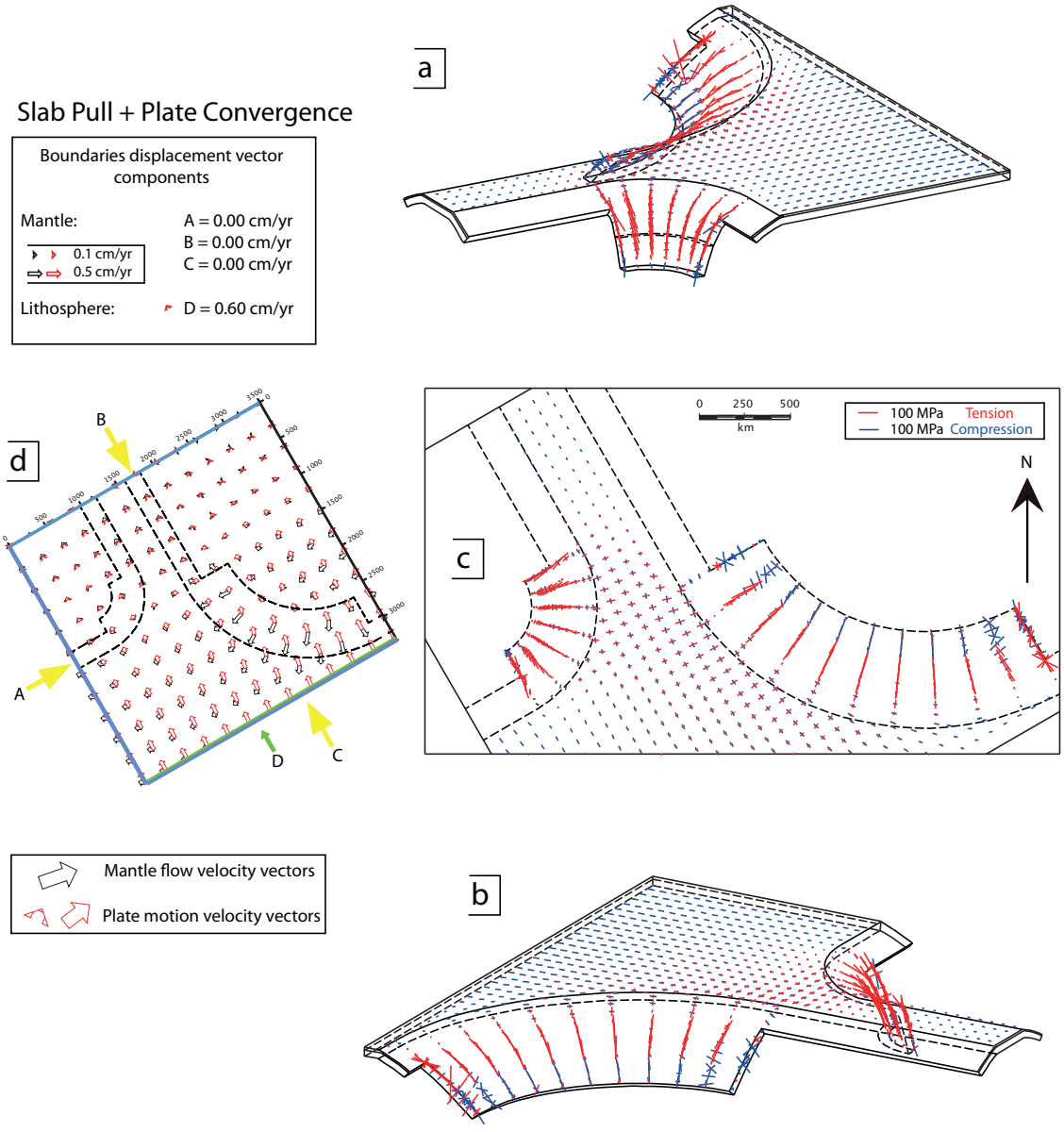

Fig. 5.7. Results of the 3D model that includes slab pull and plate convergence. Same representation as in figure 5.6. Assuming a convergence rate of 6 mm/yr between upper and lower plates, a widespread NW-SE directed compression characterizes the crust and propagates northward through the Adriatic region. Overall downdip tension characterize Calabrian and Hellenic slabs, due to the slab pull force.

is evident comparing results obtained from the two different mantle kinematics, i.e. type-1 (the Adriatic-Ionian plate moves westward relative to the mantle in a E-W direction, consistent with HS3 model; *Gripp and Gordon* [2002], and type-2 (the Adriatic-Ionian plate moves southwestward respect the mantle; *Cuffaro and Doglioni* [2007].

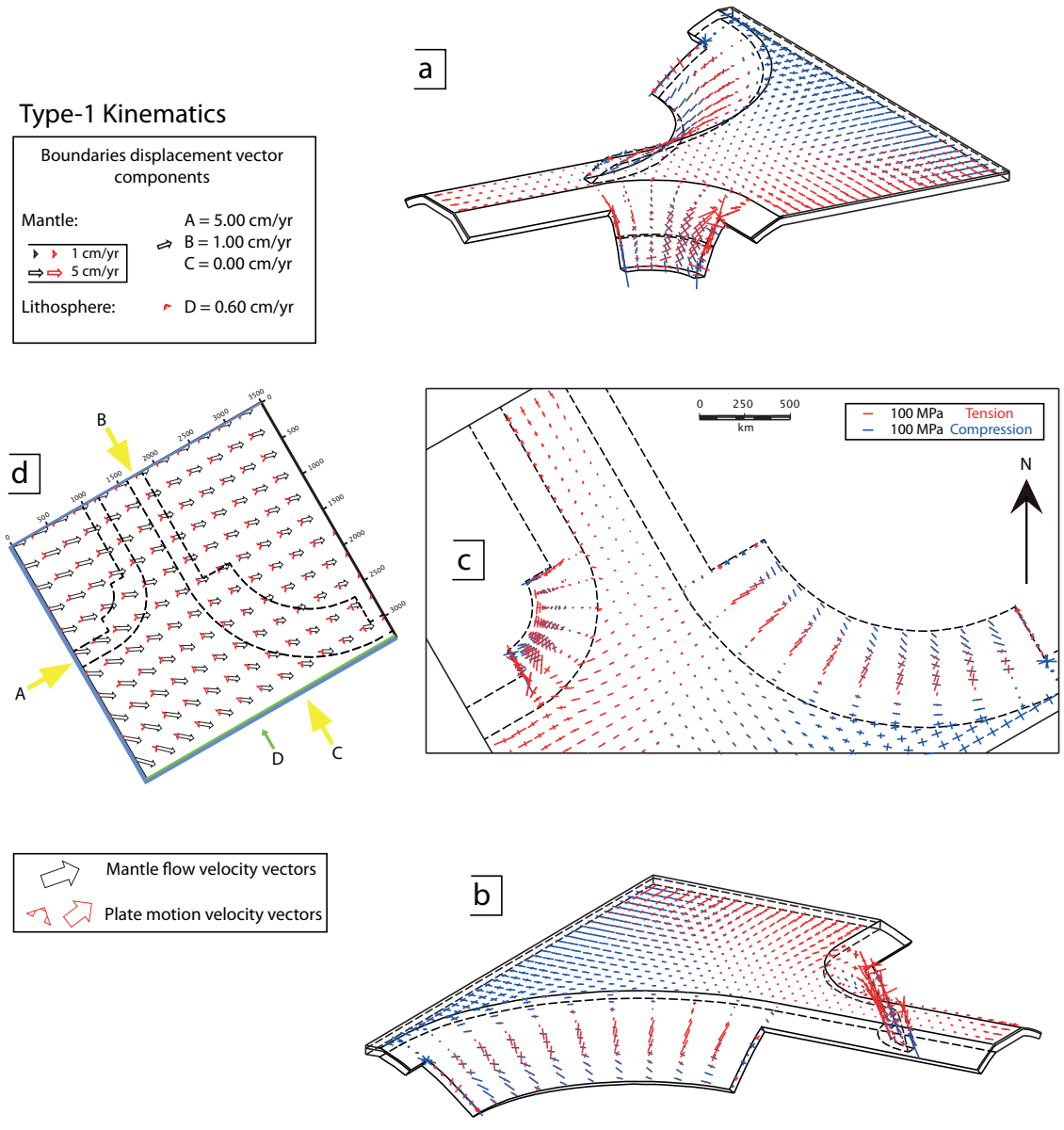

Fig. 5.8. Results of the 3D model that includes slab pull, plate convergence and E-W directed mantle flow (type-1 kinematics; see text for details). Same representation as in figure 5.6. Notice that E directed mantle flow produces downdip compression within the Calabrian slab (as encroach it).

Type-1 kinematics (Figure 5.8d) provides a mantle flow that sustain the Hellenic slab and generates main downdip tension within the subducted lithosphere. Some along-strike compression occurs at the eastern parts of the slab, where the mantle flow tends to be parallel to the subduction geometry (Figure 5.8b). With type-2 kinematics (Figure 5.9d), mantle flow sustain the Hellenic slab in a perpendicular direction, enhancing overall downdip tension (Figure 5.9b). The slab below Calabria, regardless the adopted kinematics, shows a large portion of downdip compression (Figures 5.8a and 5.9a). The magnitude of compression is larger if the type-2 kinematics is adopted (Figure 5.9a), owing to greater mantle flow velocities (about twice compared to the type-1 kinematics flow velocity).

Given the importance of the mantle flow rates in the definition of the stress field in the subducting plate, simulations were performed assuming mantle flow velocities ranging from 1 to 10 cm/yr (results shown in auxiliary material), both for type-1 and type-2 kinematics. This investigation highlighted that variations of the mantle flow velocity do not affect the distribution and direction of the resulting stress axes, which are, however, increased proportionally in magnitude (as for the former 2D and generic 3D models).

The mantle flow direction is also crucial in the definition of the stress field within the crust of the flat part of the plate. Type-1 kinematics (Figure 5.8d) simulates a stress field with widespread tension, with the exception of the SE region of the plate near the Aegean trench (Figure 5.8c), where compression occurs. Here the stress field is related to the interaction of mantle flow (it is to be noted that longer compressional axis are near-parallel to the flow vectors) and lithospheric convergence with the arcuate geometry of the Hellenic slab (the principal stress axes exhibit variable orientation, accompanying the shape of the trench). Type-1 kinematics predicts a tensional stress field in the Sicily channel, but does not provide the northwards propagation of compression through the Adriatic region.

The model with type-2 kinematics (Figure 5.9d) shows the best fitting with the observations. Calabrian and Hellenic slabs show respectively downdip compression and tension (Figures 5.9a and b), consistent with available data for the regions and previous studies (e.g., *Frepoli et al.* [2007] for the Calabrian subduction; *Papazachos et al.* [2005] for the Hellenic subduction). The modelled state of stress within the Adriatic crust, shows all the variability in orientation and style observed from data: NW-ward propagation of compression in the northern Adriatic plate; NE-SW compression in the southern Adriatic plate; NE-SW tensional axes characterize the Sicily channel.

The sensitivity of the solution on the adopted viscosity for the asthenosphere was also tested. In different simulations, viscosity was varied between 5^{17} Pa s and 1^{19} Pa s (see additional material). Similarly to what was observed for different velocities, a decrease of viscosity produces the same distribution of

stress axes but with smaller magnitude. This is due to the reduced coupling between the lithosphere and underlying mantle (lower drag force affects plates).

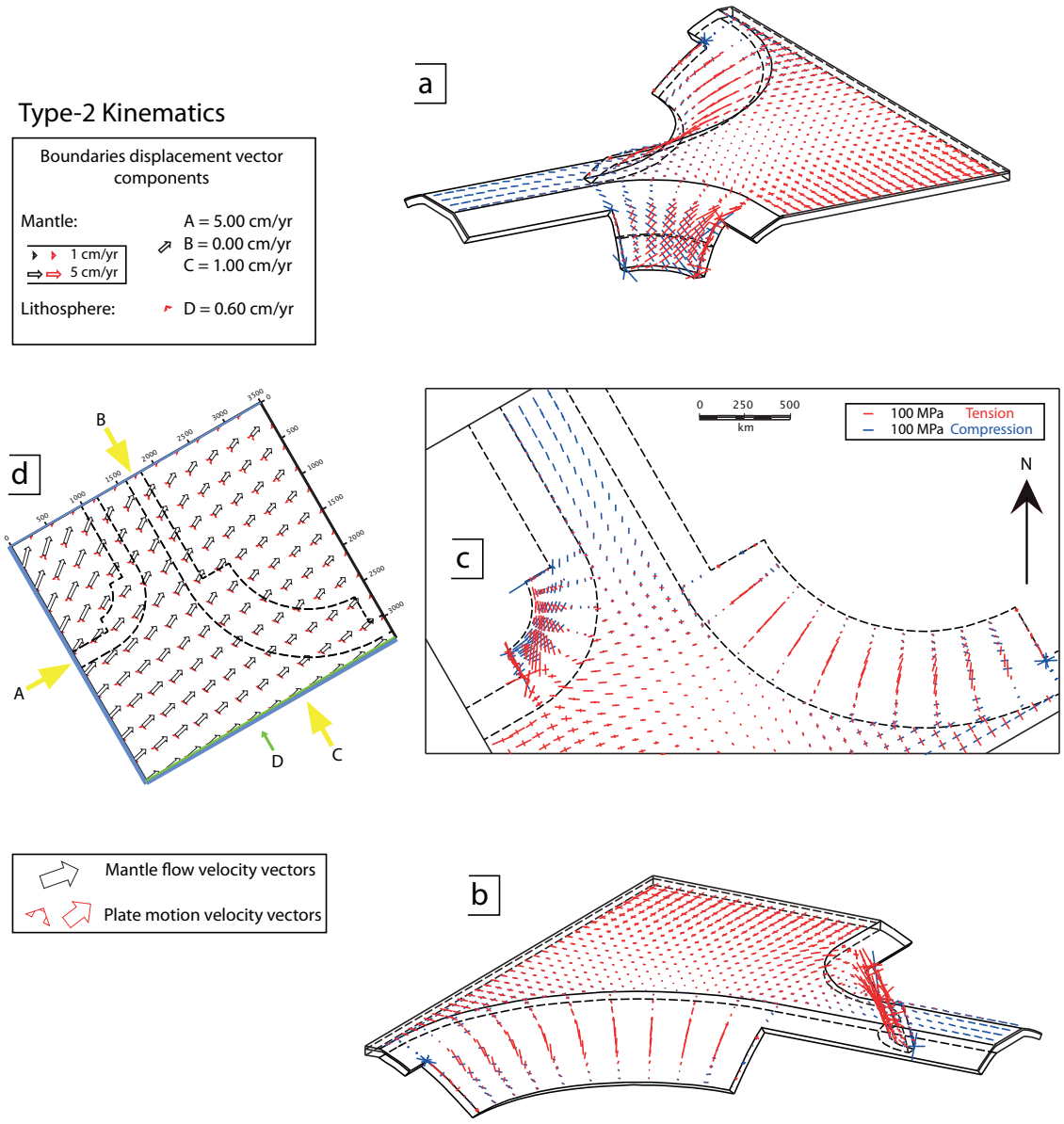

Fig. 5.9. Results of the 3D model that includes slab pull, plate convergence and SW-NE directed mantle flow (type-2 kinematics; see text for details). Same representation as in figure 5.9. Notice that the NE directed mantle flow enhances downdip compression within the Calabrian slab, increases downdip tension in the Hellenic slab and predicts: NW-ward propagation of compression in the northern Adriatic plate; NE-SW compression in the southern Adriatic plate; NE-SW tensional axes in the Sicily channel.

From modelling results, it is evident that the mantle flow is a prime actor in the definition of state of stress, both within slabs and Adriatic Plate. Applying type-2 kinematics to the model (i.e., referred to shallow hot spots reference frame as in *Cuffaro and Doglioni* [2007]), all the principal stress field features are reproduced. The lithospheric convergence does not affect substantially the resulting state of stress, if mantle flow is simulated. This is explained by the fact that the considered plate convergence is one order of magnitude smaller with respect the mantle velocities. This leads the Adriatic plate to get dragged by the faster mantle flow. Drag forces are fundamental to create the tensional field in the Sicily channel, and is a mechanism that can explain the development of rifting processes in a mainly convergent setting. The viscosity of the asthenosphere does not affect the style and orientation of the stress field, but it controls the magnitude of the principal stresses. Slab pull, if any [*Brandmayr et al.*, 2011] is a secondary actor, because it is easily counteracted in case of slab encroaching mantle flow (e.g., for the Calabrian subduction), or its effects add up to those of sustaining mantle flow drag (e.g., for the Hellenic subduction).

6

Discussion and conclusions

In this thesis, by means of 2D and 3D viscoelastic numerical models, I studied the state of stress characterizing subduction zones worldwide, and discussed the role of driving/resisting forces and plate geometries in generating the stress field. Finally, I compared models results with available geophysical observations from different subduction zones worldwide.

2D modeling results show that, if slab pull is the only active force the resulting stress field in the slab is controlled by the flexural bending of the sinking plate. As expected, it is characterized by down-dip tension in the upper part (stretching outer arc) and by compression in the lower portion (shortening inner arc) of the slab. Irrespective of the slab geometry, if a mantle flow sustaining the dip of the subducting slab is added, prevalent down-dip tension occurs within the slab. Mantle flow contrasting the subduction induces down-dip compression, which also affects the lithospheric mantle portion of the slab. In models characterized by mantle flow contrasting the subduction, the horizontal tensional component increases in the upper plate, whereas in models in which mantle flow sustains subduction, the horizontal compression drastically increases in the upper plate. These results are explained by the fact that, mantle flow encroaching the slab pushes the slab backward and downward, inducing a larger retreat of the deepest part of the slab and larger sinking of the slab bottom with respect to models forced only by the density anomaly. The consequent greater slab bending implies an higher stretching of the outer arc and shortening of the inner arc of the slab. In contrast, mantle flow sustaining the slab pushes the tip of the slab forward, unbending and stretching it. In addition, the upper plate is stretched or compressed following respectively the retreat or advance of the lower plate, which results in the observed tension or compression. The mantle flow rates are also important, since the control exerted by mantle flow on the state of stress within the slab increases with increasing rates.

If convergence between the upper and subducting plates is imposed, the lithosphere at shallow depths undergoes an overall compression, while the slabs retain the stress field (i.e., down-dip tension or compression) governed by the imposed mantle flow direction (i.e., sustaining or encroaching the slab). The higher the convergence rate the greater the magnitude of the compression affecting the lithosphere. It is further emphasized that the compression related to the plate convergence does not propagate deep within the down-going lithosphere. However, convergence influences the state of stress of the upper plate, inducing overall horizontal compression, even when mantle flow opposes the slab, provided that the convergence rate is comparable or larger than the mantle flow velocity. These results indicate that the stress field regime in the upper plate can be significantly affected by plate convergence, whereas the state of stress in the slab is mainly controlled by the absolute motion of the mantle with respect to the plates.

The retreat or advance (depending on the direction of the mantle flow) of the slab is larger if an asthenosphere low-viscosity zone is included in the model. This is explained by the faster velocity with which the mantle flow impacts the slab, due to the more efficient decoupling between the lithosphere and underlying mantle. The larger slab distortion associated with models including the low-viscosity zone explains the larger stress magnitude predicted by these models, compared to that predicted by models not including a strong decoupling between the lithosphere and the mantle. In terms of the pattern, the slab stress fields predicted by models including the asthenospheric layer do not differ significantly from those without the asthenosphere. The absence of significant pattern changes is due to the fact that the viscosity contrast between lithosphere and upper mantle, in the latter case, is sufficient to provide effective decoupling between the subducting slab and mantle layer.

Focusing on 3D model results, if the slab-pull is the only operating force, the lateral extent of the slab controls the stress magnitude. Larger slabs correspond to larger stresses, due to the greater volume affected by a negative gravitational anomaly. The most evident effects are a greater tension in the shallow portion of the slab, as the bending increases, and a greater compression in the deeper parts of the slab. Because of the finite lateral extent of the geometry, the stress components vary moving from the central part towards the lateral tip of the slabs. Major changes occur when mantle flow is applied. Regardless the mantle flow direction and both in the case of linear or curved shaped slabs, substantial along-strike deformation occurs within the subducted plate. The finiteness of the subducted lithosphere in the third dimension produces this lateral variability in the stress field, due to the differential retreat or advance between the central and the side portions of the slabs. When mantle flow opposes the subducting slab, down-dip axes are clearly compressional, while they are down-dip tensional in case of slab sustained by mantle flow. Further, two kinds of stress axes are distinguishable: those associated with the down-bending of the lithosphere, that

will always generate in the slab shallow regions regardless of the slab geometry and the mantle kinematics; those related to the slab differential retreat/advance induced by the mantle push. The latter are mainly along-strike directed, affect intermediate and deeper regions of the slab and depend on the adopted geometry; the following cases can be recognized:

- *linear slab*: along-strike tension generates in case of sustaining or encroaching mantle flow;
- *concave downward slab*: along-strike tension generates in case of encroaching mantle flow, while along-strike compression generates in case of sustaining mantle flow;
- *convex upward slab*: along-strike compression generates in case of encroaching mantle flow, while along-strike tension generates in case of sustaining mantle flow.

Down-dip and along-strike axes at intermediate and deeper depths, form couples that tend to rotate approaching the slab sides. The larger the lateral extent of the plate the most this effect is evident, until it becomes reversed (i.e., the down-dip axes become sub-horizontals and the along-strike axes become sub-verticals). According to these findings, along-strike tension or compression come out in response to the flexure (forward or backward) of the lithosphere depending on the slab longitudinal curvature. Along-strike tension occurs in case of slabs curved towards the mantle flow direction while along-strike compression occurs if the slab has an opposite curvature relative to the mantle flow direction. 3D results suggest that the stress axes directions are largely influenced by the subduction geometry, but the stress regime affecting the subducted lithosphere is totally controlled by the mantle flow.

The viscosity jump associated with the transition between upper and lower viscous mantle affects the stress field within slabs, when the descending lithosphere approaches the 670 km interface. Due to the viscous resistance to penetration of slabs at depth, the own weight of the sinking lithosphere enhances compression in its deeper parts. In case of slab pull forcing the subduction, already when the slab reaches depths of 500 km, downdip compression dominates within the lithosphere and propagates upward. The depth interval of the slab in which stress is affected by the lower mantle-slab interaction drastically deepens if mantle flow sustains the slab. When mantle flow encroaches the slab, downdip compression dominates at intermediate and deep depths of slabs. The deeper the slab the greater the compression. If the subducting lithosphere approaches or penetrates the upper part of the lower mantle, the previously discussed stress rotation and the along-strike deformations almost disappear in the deeper parts of curved slabs. This is obvious considering that the mantle flow can not stretch or compress longitudinally the slab that is anchored to the more viscous lower mantle. Further, if sinking slabs are horizontally deflected and lie onto the upper-lower mantle boundary, tension appears in the deep regions of the slab. Despite the depth, the elastic

bending of the lithosphere may be invoked as the cause of the stretching. Tension is here completely controlled by geometry, in particular by the deep bending of the subducting plate.

The results for the upper and the lower plate at crustal depths (i.e., 5-50 km), are strongly compatible with stress data from natural subductions worldwide (i.e., the World Stress Map database, *Heidbach et al.* [2008]). Models results predict trench-normal compression within the upper plate and neutral to tensional down-dip stress in the lower plate, when only slab pull or slab pull plus sustaining mantle flow is forced. Trench-normal axes follows the plates interface in its linear or curved along-strike trend. Far from the upper-lower plate boundary, stress axes tend to become parallel to the mantle flow (when active). Stress axes rotation, governed by the trench geometries, occurs also in the lower plate. These findings are consistent with stress data from the Chile-type subductions (e.g., the Central and South America, the Sumatra-Java, the central America and the Solomon). For example, the lithosphere in the upper plate of the South America plate margin, shows preferred trench sub-perpendicular direction for the compressive SHmax axes. This pattern is laterally maintained along the straight portions of the subduction (e.g., in the Chile region). A clear reorientation of the stress axes coincides with the trench deflection moving northward (i.e. in the South Peru area), following the trench curvature that characterizes the system from then to the North. The same pattern can be recognized in other subductions with different geometries (Central America, Solomon and Sumatra-Java).

Models forced by an encroaching mantle flow, show again a geometric-control over the stress field at shallow depths, as the stress axes are predicted to rotate in order to remain perpendicular to the trench. Instead, the stress field regime differs. Overall tension in the upper plate and compression in the lower plate are predicted. These findings are consistent with the trench retreat and the slab roll-back associated with the Mariana-type subduction, and is the prerogative for the development of back-arc basins. This kind of lithospheric deformation is found from stress data in the Izu-Bonin subduction, where the tensional SHmax pattern can be tracked from north to south, parallel to the strike of the whole trench. The same situation characterizes the Kermadec and the Aleutians subductions.

Close to the slab lateral tips, mantle flow highly interacts with the slab edges. The local toroidal and poloidal components of the mantle flow produce significant torsional deformation in the lower plate. For this reason, in these areas the stress axes display a circular pattern around the slab edges, regardless of the slab geometry and the imposed kinematics. This is a common feature in natural subductions as outlined by stress data. Best examples comes from subduction zones in Central America, Tonga and Aleutians.

The models results are also consistent with the stress field observed from data within the upper plate of natural subductions. Available data generally show SHmax tensional axes lying sub-parallel to the sub-

duction trenches, consistent with the bending of the plate prior to subduction. This pull-driven tension is recognizable in all the modelling results.

The outcomes of the plate scale models underline how the stress field affecting a convergent margin depends on the delicate balance between the involved tectonic forces. For this reason a 3D mantle-scale model, in a real tectonic setting, was built to evaluate the contribution of plate kinematics (convergence between Africa and Europe and relative motion between lithosphere and sub-lithospheric mantle) and of the 3D geometry of Calabria-Aegean subduction zones, in order to define the present day stress field in the Adriatic Sea and Periadriatic regions of Italy. The shape and depth of the Calabrian and Hellenic slabs were constrained using data collected in the SHARE database (http://diss.rm.ingv.it/share-edsf/), which I contributed to build (see appendix A).

3D models for the Mediterranean area include Africa-Eurasia convergence and slab pull forces, but show that mantle flow with respect to the lithosphere is a major factor forcing the state of stress of the Apennines and Aegean slabs and of the Adriatic Plate. The best fitting 3D model, simulating a southwestward motion of the Adriatic plate with respect to the sub-lithospheric mantle at approximately 5.8 cm/yr [e.g., *Cuffaro and Doglioni*, 2007], reproduces the main features of the stress field in the Adriatic Sea and surrounding areas, namely: downdip compression for the West-directed Calabrian slab (due to encroaching mantle flow) and downdip tension for the East-directed Hellenic slab (due to sustaining mantle flow); NW-ward propagation of compression in the northern Adriatic plate; NE-SW compression in the southern Adriatic plate; tension in the Sicily Channel. From my 3D model results it is also clear that mantle drag at the base of the lithosphere is fundamental to create the tensional field in the Sicily channel. This mechanism can explain the development of rifting processes in a mainly convergent setting. The results of numerical models performed for the Mediterranean subductions, allow me to conclude that:

1) the relative motion between lithosphere and mantle enhances the onset of NW-SE oriented compression within the Adriatic plate, consistent with compressional seismicity in the eastern Southern Alps, and of ENE-WSW tension in the Sicily channel, consistent with active rifting in the area;
2) downdip compression in the slab below Calabria and downdip extension in the slab below the Aegean are controlled by the eastward mantle flow in the region.

Summarizing, the results of 2D and 3D models presented in this thesis highlight or confirm that:

- due to the slab pull, the bending effects generate tension at shallow depths in the stretching outer arc of subducting slabs;
- tension in the bending region of the slab increases or decreases and down-dip tension or compression characterize the slabs at intermediate depths, depending on the adopted kinematics for the mantle, i.e., sustaining or opposing the slab, respectively;
- the longitudinal finiteness and the curvature of the subducted lithosphere produce lateral variability in the stress field, that decreases and rotates towards the tips of the slabs;
- along-strike stress axes develop in case of mantle flow forced over curved slabs, since a mantle flow oblique with respect to the sinking lithosphere is applied;
- along-strike tension or compression at intermediate and deeper regions of curved slabs depend on the interaction between the subduction geometry and the mantle flow direction. Tension generates in case of sustaining mantle flow and convex upward slabs or in case of encroaching mantle flow and concave downward slabs; compression is predicted in case of sustaining mantle flow and concave downward slabs or in case of encroaching mantle flow and convex upward slabs;
- at intermediate and deeper regions of curved slabs, down-dip and along-strike axes form couples that tend to rotate approaching the slab sides. The more the lateral extend of the slab the most this effect is evident;
- the higher viscosity of the lower mantle affects the stress field within slabs enhancing compression in their deeper parts that can also propagates upward within the subducting lithosphere;
- the results for the upper and the lower plate at crustal depths (i.e., 5-50 km), are consistent with stress data from subductions worldwide.

Appendix

A

The database of the active Mediterranean subductions

A.1 Introduction

Subduction zones are known to generate earthquake ruptures of several types: those generated at the slab interface, those generated within the slab (intra-slab and outer-rise), and those that propagate from the slab interface into the upper plate [e.g., megasplays *Satake and Tanioka*, 1999]. Subduction-related earthquakes follow different scaling laws [*Strasser et al.*, 2010] zand rheology [*Bilek and Lay*, 1999] with respect to crustal earthquakes.

Despite in subduction zones is released most of the worldwide seismic energy, hazard studies do not take subduction sources into the right consideration. A key step to involve subduction into hazard studies, requires knowledge of the geometry of the interfaces and of all the geometric and seismic parameters. Several authors have described the variability in mechanical behavior and geometry of subduction plates [e.g., *Ruff and Kanamori*, 1980; *Peterson and Seno*, 1984; *Pacheco et al.*, 1993; *Conrad and Lithgow-Bertelloni*, 2004], and compilations for subductions geometries are available in literature, such as the SLAB 1.0 [*Hayes et al.*, 2012], the SubMAP [*Heuret and Lallemand*, 2005], or the RUM [*Gudmundsson and Sambridge*, 1998] databases. In spite of this, our knowledge of this surface and related geometric and behavior parameters, is still uncertain for the Mediterranean region. The Mediterranean is located at the intersection between the Eurasian, African, Aegean, Anatolian and Arabian plates (Figure A.1). In three regions, namely the Calabrian, the Hellenic, and Cyprus arcs, deep and intermediate seismicity defines Wadati-Benioff zones well described in literature [e.g., *Isacks and Molnar*, 1971]. To take into account the contribution of potential earthquakes in the Mediterranean area and, to provide a tool for estimating the seismic-tsunamic hazard and to provide a reference of data for geodynamic models, a new tool was developed, integrated as a layer of the European Database of Seismogenic Faults [*Basili et al.*, 2013a]. It was specifically designed dur-

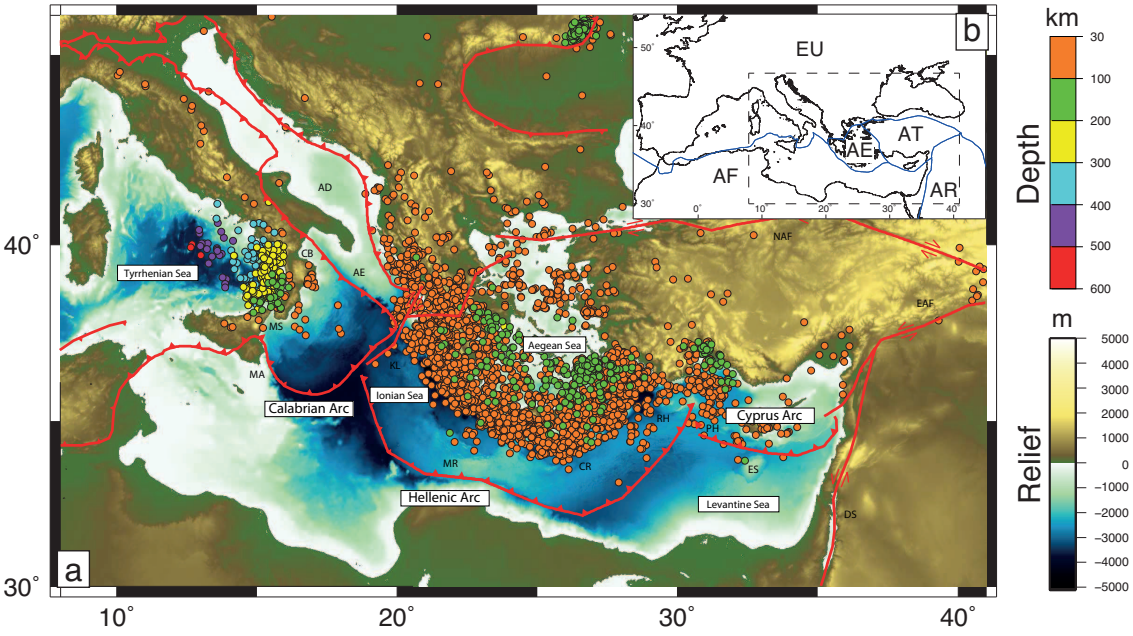

Fig. A.1. a) Seismotectonic map of the central-eastern Mediterranean. Earthquake hypocenters are from the National Earthquake Information Center catalog NEIC. The red lines are the main tectonic features; AD, Adria plate; AE, Adria escarpment; CB, Catanzaro basin; MS, Messina strait; MA, Malta escarpment; KL, Kephallonia-Lefkada fault; MR, Mediterranean ridge; CR, Crete; RH, Rhodes; ES, Eratostene seamount; PH, Paphos fault; DS, Dead Sea fault; EAF, East Anatolian fault; NAF, North Anatolian fault. b) tectonic plates sketch-map. The blue lines represent the boundaries of tectonic plates. Plates: EU, Eurasian; AF, African; AE, Aegean; AT, Anatolian; AR, Arabian.

ing the course of the project SHARE (http://www.share-eu.org/), to which I participated as the regional database manager for the Northern Africa area, for the subduction layer implementation and the Calabria slab compilation [*Basili et al.*, 2011]. The Subduction source is a simplified representation of the plates interface at convergent boundaries, based on geological and geophysical data. The subduction interfaces are fully-parametrized, and following the philosophy of DISS - Database of Individual Seismogenic Sources [*Basili et al.*, 2008], subductions have been characterized by geometric (strike, dip, depth), kinematic and dynamic (rake, convergence rate, seismic coupling, maximum earthquake magnitude) parameters.

A.2 The Mediterranean active subductions - tectonic setting

The central portion of the Mediterranean sea is tectonically dominated by the interaction of the African, Eurasian, and Aegean plates (Figure A.1b). It is mainly constituted by an ancient oceanic crust (called

Ionian) ranging in age from Triassic to Cretaceous [*Finetti et al.*, 1982; *Catalano et al.*, 2001; *Finetti and Del Ben*, 2005], connected with the African and Adriatic plate. The Ionian oceanic crust is subducted beneath the European plate in the Calabrian Arc, below the Aegean plate in the Hellenic Arc and below the Anatolian Plate in the Cyprus Arc (Figure A.1a). The boundary between Africa and Eurasia crosses the Mediterranean basin with an articulated shape and various characteristics due to differences in the crustal nature and the presence of microplates such as the Aegean and Anatolia plates. Along this boundary, the presence of well-developed slabs of subducting oceanic crust is known essentially in three segments, namely the Calabrian, the Hellenic and the Cyprus (or Cyprean) arcs.

Although the slabs belong to the same plate, the Calabrian, Hellenic and Cyprian subductions are different in terms of geometry and behavior. The well know Hellenic slab and the less investigated Cyprean slab dip to the northeast at a shallow angle [circa $20 - 30°$, *Papazachos et al.*, 2000; *Suckale et al.*, 2009], whereas the Calabrian slab is much steeper [circa $70 - 80°$; e.g., *Chiarabba et al.*, 2008] and dips to the northwest, as a consequence of the different orientation with respect of the global plate motion according to *Doglioni* [1990] (see section 2.2). Convergence rates are in the order of 35 mm/yr in the Hellenic Arc [*Reilinger et al.*, 2006] and 1-5 mm/yr in the Calabrian Arc [*D'Agostino and Selvaggi*, 2004; *Devoti et al.*, 2008; *Serpelloni et al.*, 2010; *D'Agostino et al.*, 2011], difference due to the fast SW motion of the Aegean and Anatolia plates. Wide and thick accretionary wedges developed in both zones as a consequence of the subduction processes thereby deforming the thick sediment cover accumulated over time onto the Ionian crust. Away from the subduction of the Ionian oceanic crust, collision of continental crust is active along the coast of northern Greece and Albania, in Sicily, and to the north of the Calabrian Arc. Intracontinental deformation occurs in the Sicily Channel and continues in the Sirt Gulf [Libya, *Corti et al.*, 2006; *Serpelloni et al.*, 2007]. A promontory of continental crust of the African plate, often referred to as the Adria microplate, separates the northward continuation of the Calabrian-Hellenic subduction zones.

A.2.1 The Calabrian arc

The Calabrian Arc represents a portion of the complex plate boundary between the Eurasian and Adria plates formed as a consequence of the subduction of the Ionian oceanic crust under the southern margin of the European plate. Paleomagnetism, S-waves refracted below the Mohorovic discontinuity, paleoclimatology and palynology suggest that Adria belongs structurally and kinematically to Africa [e.g., *Mantovani et al.*, 1990; *Channell*, 1996; *Muttoni et al.*, 2001; *Mele*, 2001], whereas historical seismicity, geodetic and seismic evidence suggest that Adria is at present an independent microplate within the Africa-Eurasia

plate boundary zone [*Anderson and Jackson*, 1987; *Nocquet and Calais*, 2003]. The Calabrian subduction process occurred in the framework of a circa N-S convergence between Africa (to which Adria is kinematically attached) and Europe, as constrained by paleomagnetic data [e.g., *Channell*, 1996; *Muttoni et al.*, 2001]. The subduction zone is located between the Tyrrhenian Sea (to the East) and the Ionian Sea (to the West) and stretches for about 300 km between the Southern Apennines and Sicily (Figure A.1b). The subduction of oceanic crust, as highlighted by seismicity, appears to be still active only in a narrow portion of the Calabrian Arc, near its southwestern end, between the Catanzaro Basin and the Messina Strait, where a steep NW dipping Wadati-Benioff zone is recognized [*Selvaggi and Chiarabba*, 1995]. In geodynamic reconstructions it is a segment of the larger Apennines-Maghrebides subduction zone [*Gueguen et al.*, 1998; *Faccenna et al.*, 2004]. To the North, although convergence is still active, the sedimentary cover of the African continental margin has been wedged into the Calabrian Arc and thrusted towards the foreland. Seismic profiles across the Ionian Sea highlight the fold-and-thrust structure of the eastern margin of the Calabrian Arc and of the 300 km wide accretionary SE verging wedge that spans into the Ionian Sea for about 400 km [*Minelli and Faccenna*, 2010; *Polonia et al.*, 2011], laterally confined by the Apulia and Malta escarpments. The complex geodynamics of the region is reflected in the variability of the deformation styles that affects the Italian peninsula. In an overall convergent settings, the Calabrian subduction zone is also characterized by extensional and transcurrent realms. An active back-arc basin developed in the Tyrrhenian Sea since the Middle Miocene [*Wortel and Spakman*, 2000; *Faccenna et al.*, 2005], related to the retreat of the Calabrian slab toward SE. The narrow configuration of the slab may have been attained by lateral tearing during the last phases of the slab roll-back [*Faccenna et al.*, 2011], but a control of paleogeography has been suggested (Carminati et al., 2012). In this view the narrow Wadati-Benioff zone occurs where a narrow corridor of Mesozoic oceanic lithosphere of the Neotethys subducted. The slab retreat occurred faster in this corridor than in the continental parts of the Adriatic Plate [*Carminati et al.*, 2010, and references therein]. This, in turn, produced a larger southeastward advancement of the thrust front in the offshore of Calabria.

A.2.2 The Hellenic arc

The Hellenic Arc is the active boundary where the African plate, to the south, is subducted beneath the Aegean plate, to the north. It stretches NW-SE between the Kephallonia-Lefkada shear zone and the southeastern corner of the island of Crete, where it changes abruptly its strike and continues towards the NE to the island of Rhodes (Figure A.1b). Here, this structure links with the Cyprus arc. The Hellenic

subduction zone is characterized by an active volcanic arc in the Aegean Sea, a non-volcanic arc along the Ionian Islands, Crete and Rhodes, a forearc basin known as the Hellenic Trench and a large accretionary wedge in its outer part, called the Mediterranean Ridge. The accretionary wedge extends above the Ionian oceanic crust for more than 200 km to the African continental margin [*Huguen et al.*, 2001; *Kukowski et al.*, 2002; *Polonia et al.*, 2002; *Chamot-Rooke et al.*, 2005; *Yem et al.*, 2011]. The northwestern end of the Hellenic Arc is located in the Ionian Islands and is characterized by a large NE-SW striking shear zone, which accommodates the different styles and velocities of deformation occurring to the north and south. The main fault in this zone is the Kephallonia-Lefkada strike-slip fault that marks the boundary between the oceanic subduction domain to the South and continental collision to the North, this last caused by the presence of the thick continental Apulian block [*Shaw and Jackson*, 2010]. At the opposite end, in the Rhodes Basin, the relationship with the Cyprus Arc is still matter of debate, also for the unclear nature of this structure.

A.2.3 The Cyprus arc

The Cyprus arc is the active boundary where the African plate, to the south, is subducted beneath the Anatolian plate, to the north. It stretches NW-SE between the Dead Sea Fault, to the SE, and the Rhodes Basin, to the NW. Here, this structure links with the Hellenic Arc (Figure A.1b). The Cyprus subduction zone is probably the less known in the Mediterranean area. No well-defined volcanic arc exists. It seems to be evolving towards continental collision, at least in its eastern portion [*Imprescia et al.*, 2012], as the crust in the Levantine Basin is not properly oceanic but more probably thinned continental in nature. The accretionary wedge is in part deformed by the impact with the Eratostene Seamount, which is entering the subduction zone. The eastern end of the Cyprus Arc is located against the Dead Sea Fault zone, which in turn ends against the Eastern Anatolia Fault zone. At the opposite end, in the Rhodes Basin, as previously mentioned, the relationship with the Hellenic Arc is still matter of debate, also for the unclear nature of the Cyprus subduction itself. The continuity of the subduction front is interrupted west of the Island of Cyprus by the dextral strike-slip Paphos Fault, which marks the boundary between the oceanic domain subducting to the west and the collision to the east.

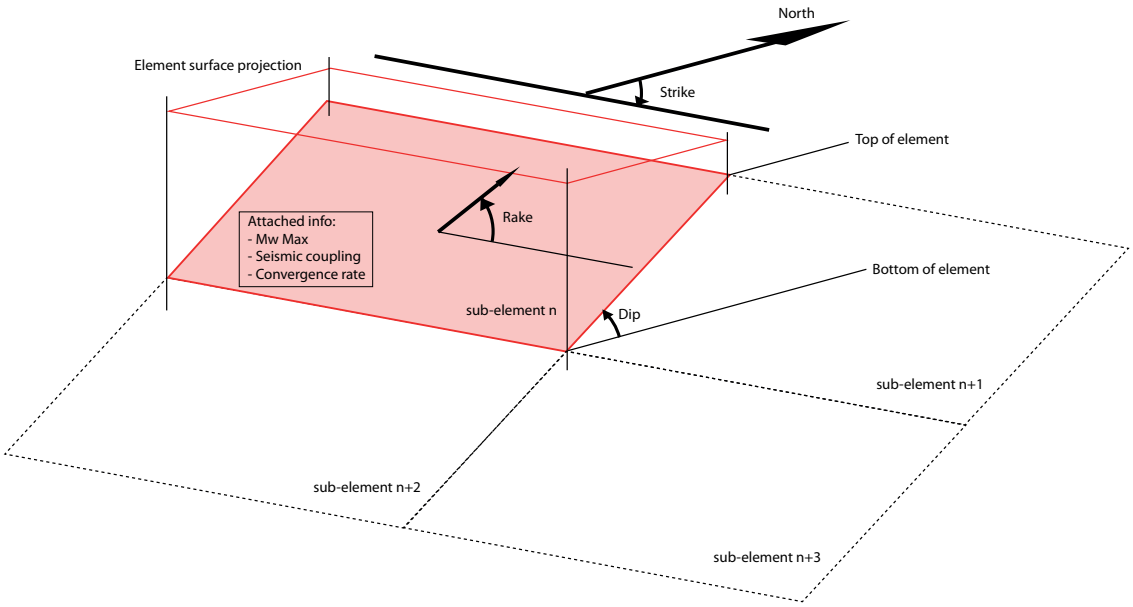

Fig. A.2. Schematic representation of subelements that constitute the subduction interface.

A.3 Technical description of the subduction layer

The subduction database was designed using the software MapInfo and MapBasic (http://www.mapinfo.com/). The idea was to integrate the SHARE database, with a layer that includes a model of the plates interface at convergent boundaries, based on geological and geophysical data. The plate interfaces are mapped as collection of free-form polygons with a variable number of nodes (Figure A.2). Each single polygon, or sub-element, represents a portion of the entire surface of the subducting plate from the outer limit of the trench to the lower tip of the dipping slab. This scheme includes portions of the slab at depths that probably exceed those useful for hazard assessment. However, this condition has to be determined a posteriori. In addition, modeling techniques (e.g., finite elements approach of this thesis) benefit from the availability of data about the whole subduction. Each sub-element has consistent geometric and kinematic characteristics and is bounded by lines of constant depth except for the uppermost line when it coincides with the seafloor. Similarly to crustal seismogenic sources provided by the DISS 3.1 database [*Basili et al.*, 2008], subductions are characterized by geometric (strike, dip, depth) and behavior (rake, slip rate, seismic coupling, maximum earthquake magnitude) parameters (see figure A.2 and table A.1). These parameters are given for all sub-elements and their range of variability within the entire subduction is also stored in a summary table.

Field name	Description	Units
Min Depth	Depth of the sub-element upper edge from sea level	km
Max Depth	Depth of the sub-element lower edge from sea level	km
Min Strike	Minimum direction (between 0 and 2π) clockwise from North	degrees
Max Strike	Maximum direction (between 0 and 2π) clockwise from North	degrees
Min Dip	Minimum dip angle (between 0 and $\pi/2$) from the horizontal	degrees
Max Dip	Maximum dip angle (between 0 and $\pi/2$) from the horizontal	degrees
Convergence azimuth	Convergence direction (between 0 and 2π) clockwise from North	degrees
Convergence Rate	Range of values of convergence as a function of time	mm/yr
Seismic Coupling	Seismic/aseismic factor (between 0-1)	Scalar
Max Magnitude (M_w)	Value of the maximum observed magnitude of the sub-element	Scalar

Table A.1. Parameters provided for each subdomain of the subduction.

Differently from crustal seismogenic sources, some parameters have a peculiar role. Seismic coupling, although very difficult to estimate, is supposed to provide a relation between plate convergence and earthquake production at the slab interface (i.e., gives an estimate of how much of the available tectonic energy is released as earthquakes). Earthquake magnitude parameters is supplied to capture the maximum observed magnitude produced at single sub-element of the slab interface and taken as a reference for the whole system. In the subduction table, also NULL values are allowed. This condition is acceptable because various parameters may not be applicable in every sub-element that constitute a subduction record, e.g., in the deeper portion of the slab or in case of slab windows. Table A.2 illustrates the specific attributes stored for the whole subduction system. The parametric information stored for each sub-element, an used to characterize the whole subduction to which they belong, are described in table A.1. Geological and geophysical data used for estimating the values of parameters include interpreted seismic profiles, gravity and tomography data, receiver function Moho depth determinations and earthquake focal mechanisms and hypocenter

Field name	Description	Units
General Information		
ID Source	ID assigned to the record	–
Source Name	Subduction system name	–
Compilers	Name(s) of the compiler(s) of the record	–
Contributors	Name(s) of the contributor(s) of the record	–
Latest Update	Date of the last update of the record	–
Parametric Information		
Min Seismogenic Depth	Depth of the subduction interface upper seismogenic edge from sea level	km
Max Seismogenic Depth	Depth of the subduction lower seismogenic edge from sea level	km
Dip direction	Cardinal dipping point	–
Convergence azimuth	Values of convergence direction (between 0 and 2π) clockwise from North	degrees
Convergence Rate	Range of values of convergence as a function of time	mm/yr
Max Magnitude	Value of the maximum magnitude calculated from sub-elements (Mw)	Scalar

Table A.2. General and parametric informations describing the subduction system.

determinations. To give an idea of available density of constraining data, those used for the Calabrian slab are reported in table A.3 and also graphically shown in figure A.3.

A.4 Interface geometries

The geometries defined for the three active subductions in the Mediterranean region, are shown in figure A.4. Shape and depth of the subducting Calabrian slab or, more in general, of the contact between the two plates, are constrained by gravity, seismic and tomographic data and seismicity data as well (see Table A.3 and Figure A.3 for details). The geometry of the first 50 km depth is inferred from regional geological and seismological data, mainly seismic profiles [*Van Dijk et al.*, 2000; *Finetti and Del Ben*, 2005; *Scrocca et al.*, 2005; *Minelli and Faccenna*, 2010; *Pepe et al.*, 2010], P-waves velocities [*Di Stefano et al.*, 1999], residual topography [*Gvirtzman and Nur*, 2001], gravity anomalies [*Tiberti et al.*, 2005] and paleomagnetic data [*Cifelli et al.*, 2007; *Mattei et al.*, 2007; *Cifelli et al.*, 2008]. In the Ionian Sea, this portion of the plate contact dips toward NW about 2-8 degrees under the accretionary wedge and becomes steeper (up to 20

Geologic/Geophysic method	**General constrained features**	**Specific constrained parameters**	**References and number/color as represented in figure A.3**
inversion of body waves	tomography profiles	slab geometry	*Chiarabba et al.* [2008] [1-light green]
seismicity location	distribution of seismicity	slab geometry	*Chiarabba et al.* [2005] [2-yellow]
high resolution regional array	tomography	velocity model	*Faccenna et al.* [2011] [3-light blue]
interpretation of seismic lines	seismic profiles	accretionary wedge geometry	*Minelli and Faccenna* [2010] [4-dark blue]
interpretation of seismic lines	seismic profiles	accretionary wedge geometry	*Pepe et al.* [2010] [5-brown]
interpretation of seismic lines	seismic profiles	accretionary wedge geometry	*Scrocca et al.* [2005] [6-orange]
seismic and wells database	seismic profiles	structural model	*Van Dijk et al.* [2000] [7-purple]
S waves splitting	anisotropy maps	slab position	*Baccheschi et al.* [2011] [8-dark green]
topography and isostasy	isobaths map	moho depth and lithospheric thickness	*Gvirtzman and Nur* [2001] [9-pink]
inversion of surface waves data	vertical cross sections	Structural model and V_s distribution	*Pontevivo and Panza* [2006] [10-red]
moment tensors	focal mechanisms	geometric and behavior parameters	*Serpelloni et al.* [2010] [11-black]

Table A.3. List of methods and references selected for constrained parameters of Calabria slab interface.

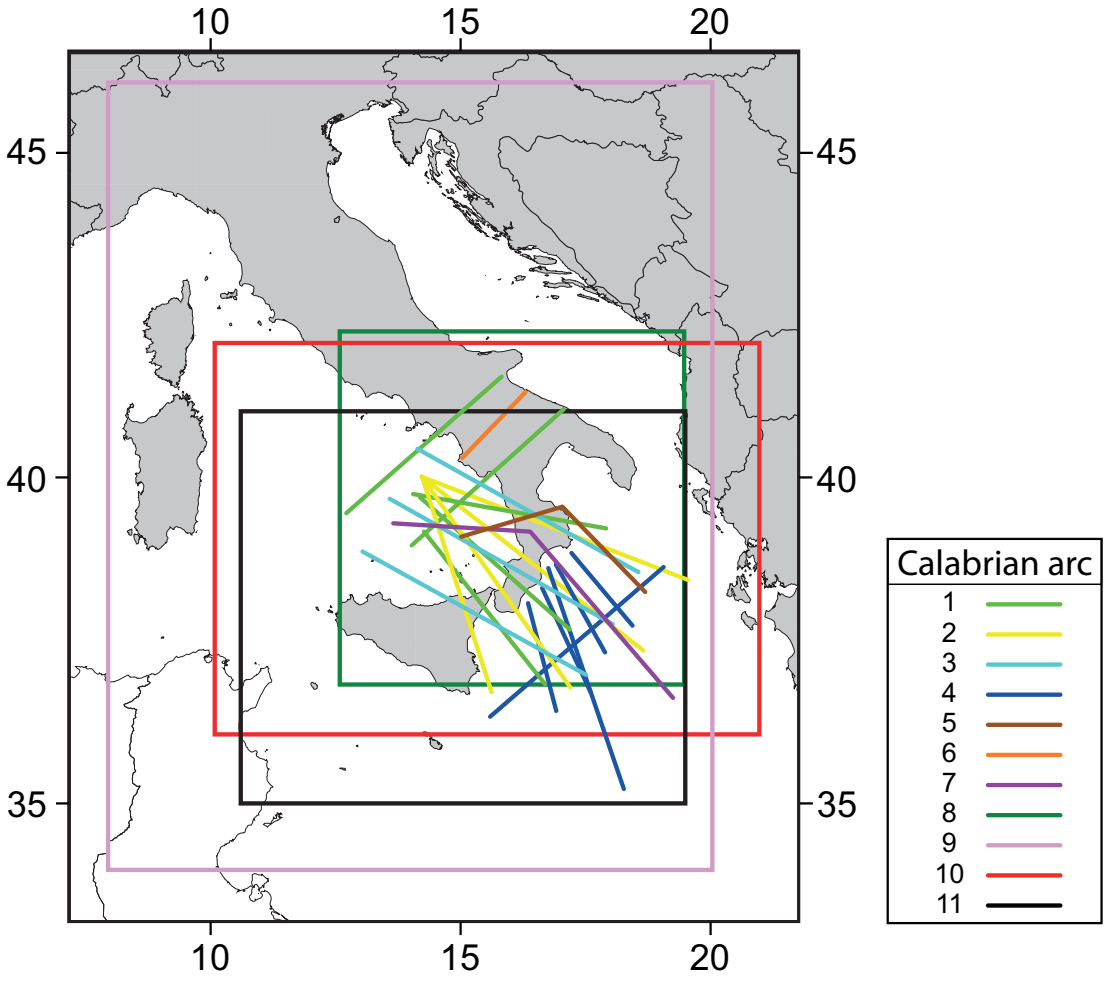

Fig. A.3. Schematic representation and data coverage for the Calabrian subduction zones. Boxes and lines are numbered and outlined by different colors following the references used in this study as reported in table A.3.

degrees) at depth greater than 10-12 km. It is assumed to operate by nearly pure thrusting and represents the region where interface earthquakes took place. Earthquake locations are consistent with the slab geometry model derived from other data. Deeper portions of the subduction interfaces were constrained by seismic and tomographic [*Barberi et al.*, 2004; *Chiarabba et al.*, 2005, 2008] SKS splitting data [*Baccheschi et al.*, 2008, 2011]. Deep seismicity and tomography data depict a well-developed slab up to 500 km depth. Intermediate and deep earthquakes are distributed along a 70° N-NW dipping Wadati-Benioff plane that

can be followed down to 450 km depth [*Chiarabba et al.*, 2005]. The seismically active portion of the slab has a lateral extent of only 250 km from the southern Apennines to the western Aeolian Islands. Tomographic images reveal the presence of a continuous high velocity body beneath the Calabrian Arc, confirming the northwestward subduction of the Ionian lithosphere beneath the southern Tyrrhenian Sea. The slab is sub-horizontal at shallow depth, then dips steeply NW in the upper mantle, and finally flattens to lie on top of the upper-lower mantle discontinuity below the Tyrrhenian Sea [*Lucente et al.*, 2006; *Wortel and Spakman*, 2000; *Cimini*, 1999; *Piromallo and Morelli*, 2003; *Montuori et al.*, 2007; *Chiarabba et al.*, 2008; *Monna and Dahm*, 2009; *Piana Agostinetti and Amato*, 2009].

In the Hellenic region, the seismicity distribution depicts a Wadati-Benioff zone beneath the Aegean Sea down to a depth of about 180 km [*Hatzfeld and Martin*, 1992; *Benetatos et al.*, 2004; *Bohnhoff et al.*, 2005; *Papazachos et al.*, 2000; *Rontogianni et al.*, 2011]. Earthquake locations are consistent with the slab geometry model derived from other data such as seismic profiles or tomography [*Meier et al.*, 2004; *Suckale et al.*, 2009]. Interface earthquakes concentrate at depth between 15 and 45 km in the center of the arc [15-20 at the northwestern termination, *Taymaz et al.*, 1990; *Shaw and Jackson*, 2010; *Heuret et al.*, 2011]. P-axes azimuth of interface earthquakes generally agree with the plate convergence direction indicated by GPS velocity vectors [*McKenzie*, 1978; *Jackson and McKenzie*, 1988; *Taymaz et al.*, 1990; *Papazachos et al.*, 1999; *Benetatos et al.*, 2004], also in the eastern Hellenic arc where plate convergence is taken up by oblique slip motion on the subduction plane [*Shaw and Jackson*, 2010]. Shape and depth of the subducting slab beneath the Aegean plate are also constrained by gravity and seismic data, as well as seismicity data. The African oceanic crust lies beneath the deformed sediments of the Mediterranean Ridge at a depth of 16 km [*Makris and Yegorova*, 2006], then, approaching Peloponnese and the Island of Crete, it begins to dip beneath the Aegean plate with an angle of about 20°, as imaged by seismic lines (Bohnhoff et al., 2001), receiver functions analysis (Meier et al., 2007) and results from combined seismic techniques models [*Meier et al.*, 2004] or velocity-gravity models [*Casten and Snopek*, 2006; *Makris and Yegorova*, 2006]. The hinge of the slab is approximately located beneath the Hellenic Trench. In the western portion of the Hellenic Arc, the crusts of the two plates are in contact to a depth of about 30-35 km, which roughly corresponds to the thickness of the Aegean crust. Conversely, in the eastern portion of the Hellenic arc, where the slip motion is mainly oblique, a mantle wedge seems to divide the two plates to the hinge of the subducting slab [*Casten and Snopek*, 2006; *Makris and Yegorova*, 2006]. The position of the subducting slab beneath the Aegean plate is constrained by receiver functions analyses of P and S waves that show the topography of the Africa Moho discontinuity at a depth between 35 and 200 km [*Sodoudi et al.*, 2006]. Also tomographic images of P and S velocity variations confirm the presence of a slab dipping with a

shallow angle until a depth of at least 120 km [*Papazachos and Nolet*, 1997; *Li et al.*, 2003; *Suckale et al.*, 2009]. Tomography elaborations image the presence of a large fast body beneath the Aegean Sea, reaching the 660 km discontinuity beneath the northern border of Greece and the eastern coast of the Black Sea [*Piromallo and Morelli*, 2003; *Dilek and Sandvol*, 2009; *Suckale et al.*, 2009].

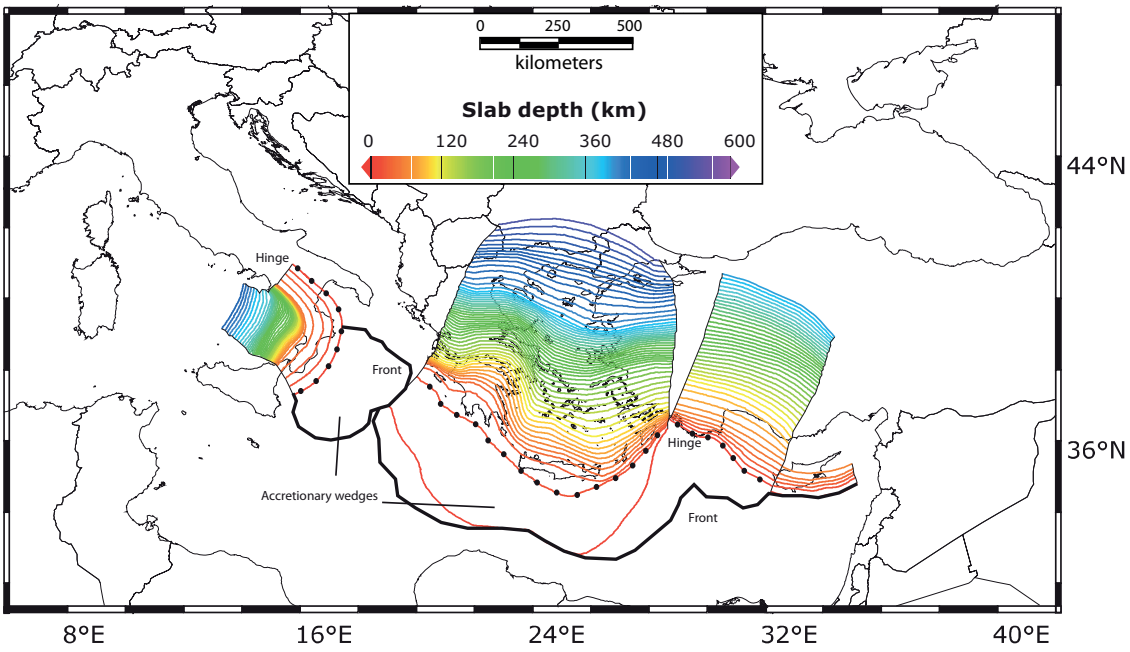

Fig. A.4. Main subduction zone interfaces colored according to depth. Black dots are drawn over the slab hinges projection. The thick black lines represent the subduction fronts.

The Cyprus slab belongs to the eastern Mediterranean active subduction. Seismicity distribution indicates the occurrence of a slab beneath Anatolia down to a depth of about 140 km in the western part of the arc, while in the eastern portion no earthquakes are recorded beyond 60 km depth [*Kalyoncuoğlu et al.*, 2011]. The shallowest structures of the Cyprus Arc are imaged in the seismic lines. The plate contact is clearly imaged only in the central portion of the arc, immediately south of the Cyprus Island [*Vidal et al.*, 2000; *Schattner*, 2010]. The bouguer gravity anomaly pattern seems to be consistent with the presence of a subducting slab until at least 50 km depth [*Ergün et al.*, 2005]. At greater depth, tomography highlights a fast body beneath Anatolia down to about 400 km in correspondence with the southern coast of the Black Sea. A deeper cold body is also imaged at depth between 400 and 800 km [*Dilek and Sandvol*, 2009]. In the eastern portion of the Cyprus arc, a discontinuity in the cold body is interpreted as an indication of slab

detachment [*Faccenna et al.*, 2006], maybe induced by the collision of the Eratostene Seamount with the Anatolia plate margin.

A.5 Kinematic and behavior parameters

According to GPS velocities and current plate models, relative motion between the subducting African plate and the Calabrian arc itself results in a convergence rate of 2-5 mm/yr [*D'Agostino and Selvaggi*, 2004; *Devoti et al.*, 2008; *Serpelloni et al.*, 2010; *D'Agostino et al.*, 2011]. Information on seismic coupling values [i.e., qualitative measures of the interaction between the two plates at subduction zones; see *Ruff and Kanamori*, 1983, for explanations] is not available in the literature for the Calabrian subduction interface, due to the lack of well constrained seismic events for the region [*Heuret et al.*, 2011]. For this reason it has been chosen to use a zero value (i.e., minimum interaction between plates at the interface) for the entire subdomain deeper than 125 km. A seismic coupling value of 1 (i.e., maximum interaction between plates at the interface) was used for the plate interface as it represents the region of higher interest for hazard. In the past centuries, the area has been stuck by several $M_w > 6$ earthquakes [CPTI11, *Rovida et al.*, 2011]. A maximum magnitude M_w 7.1 was adopted for the Calabrian subduction zone, based on the magnitude of the largest historical earthquake that took place in the area.

At longitudes of the Hellenic arc, the subducting Africa plate moves toward N-NW at 5-9 mm/yr while the overriding Aegean plate moves toward the SW at 30-33 mm/yr, both values relative to fixed Eurasia [*DeMets et al.*, 1994; *Le Pichon et al.*, 1995; *Cocard et al.*, 1999; *Bird*, 2003; *McClusky et al.*, 2003; *Kreemer and Chamot-Rooke*, 2004; *Reilinger et al.*, 2006; *Ganas and Parsons*, 2009]. These relative motions result in a convergence rate of 35 mm/y in the western part of the arc. In the eastern part, where relative motion becomes oblique, and here the lateral component is of about 10 mm/yr. GPS velocities of the Aegean plate progressively decrease toward the northwest, where the subduction zone approaches its lateral termination in the Ionian Islands [*Hollenstein et al.*, 2008]. The subduction rate of the Western Hellenic Arc is estimated at about 40 mm/yr by *Agostini et al.* [2010], considering a convergence rate of 50 mm/yr. Seismic coupling of the Hellenic subduction is generally considered to be weak [*Becker and Meier*, 2010; *Reilinger et al.*, 2010; *Rontogianni*, 2010; *Shaw and Jackson*, 2010; *Heuret et al.*, 2011]. *Laigle et al.* [2004] suggest a possible lateral variation of seismic coupling along the Hellenic Arc structure [*Laigle et al.*, 2004]. The Hellenic subduction is supposed to have generated one of the largest earthquake of the entire Mediterranean, which occurred in the 365 AD, with an estimated M_w larger than 8 [e.g., *Guidoboni*

Calabrian Arc		
General Information		
ID Source	ITSD001	
Source Name	Calabrian Arc	
Compiler(s)	Petricca P.	
Contributor(s)	Petricca P.	
	Tiberti M.M.	
	Basili R.	
Latest Update	30/05/2011	
Parametric Information		**Evidence**
Min Seismogenic Depth (km)	10	Inferred from tectonic and seismological considerations
Max Seismogenic Depth (km)	60	Inferred from tectonic and seismological considerations
Dip direction	NW	Based on geophysical data from various authors
Convergence azimuth (deg)	275-310	Based on geodetic data from various authors
Convergence Rate (mm/yr)	1-5	Based on geodetic data from various authors
Max Magnitude (M_w)	7.1	Inferred from regional tectonic considerations

Hellenic Arc		
General Information		
ID Source	GRSD001	
Source Name	Hellenic Arc	
Compiler(s)	Tiberti M.M.	
	Tiberti M.M.	
	Kastelic V.	
	Basili R.	
Latest Update	13/05/2011	
Parametric Information		**Evidence**
Min Seismogenic Depth (km)	15	Based on seismological data from various authors
Max Seismogenic Depth (km)	45	Based on seismological data from various authors
Dip direction	NNE	Based on geophysical data from various authors
Convergence azimuth (deg)	20-40	Based on geodetic data from various authors
Convergence Rate (mm/yr)	23-35	Based on geodetic data from various authors
Max Magnitude (M_w)	8.4	Based on the largest associated earthquake

Cyprus Arc		
General Information		
ID Source	CYSD001	
Source Name	Cyprus Arc	
Compiler(s)	Tiberti M.M.	
	Kastelic V.	
Contributor(s)	Tiberti M.M.	
	Kastelic V.	
Latest Update	13/05/2011	
Parametric Information		**Evidence**
Min Seismogenic Depth (km)	10	Inferred from tectonic and seismological considerations
Max Seismogenic Depth (km)	60	Inferred from tectonic and seismological considerations
Dip direction	NNE	Based on geophysical data from various authors
Convergence azimuth (deg)	30-40	Based on geodetic data from various authors
Convergence Rate (mm/yr)	9-18	Based on geodetic data from various authors
Max Magnitude (M_w)	7.5	Inferred from regional tectonic considerations

Table A.4. General and parametric informations describing the subduction systems.

et al., 2007]. Whether this earthquake occurred on the subduction plane or not, is still a matter of debate [*Papadimitriou and Karakostas*, 2008; *Ganas and Parsons*, 2009; *Stiros*, 2010].

In the Cyprus region, the subducting Africa plate moves toward N-NW at 5-9 mm/yr while the overriding Anatolian plate moves westwards at 21 mm/y relative to fixed Eurasia [*Reilinger et al.*, 2006]. These relative motions result in convergence ranging from 7 to 18 mm/yr moving along the trench from east to west [*Reilinger et al.*, 2006; *Wdowinski et al.*, 2006]. The subduction rate is estimated to be about 10 mm/yr by *Agostini et al.* [2010]. The Paphos fault is thought to accommodate about 10 mm/yr of differential velocity between east and west. The Cyprus area has been affected by many destructive earthquakes in historical times [*Cagnan and Tanircan*, 2010]. The largest known earthquakes in the Cyprus area are those occurred in 1222 with M_w 6 and M_w 7.5 [CFTI4Med, *Guidoboni et al.*, 2007]. Seismic coupling estimates are not available for the Cyprus subduction [*Heuret et al.*, 2011]. The specific attributes for the Calabria, the Hellenic and the Cyprus subduction systems are provided in table A.4.

The described subduction database is currently integrated as a layer of the European Database of Seismogenic Faults [*Basili et al.*, 2013a]; it is published on-line and accessible via the following link: http://diss.rm.ingv.it/share-edsf/.

The significance of such a tool is evident, for example, by the use that was made in this thesis to constrain the model geometries of the numerical models dedicated to the Mediterranean area (see section 5). It was also used as the basis for studies of tsunami hazard [e.g., *Basili et al.*, 2013b].

List of Tables

List of Figures

References

Agostini, S., C. Doglioni, F. Innocenti, P. Manetti, and S. Tonarini (2010), On the geodynamics of the aegean rift, *Tectonophysics*, *488*(1), 7–21.

Ahrens, T. J., and G. Schubert (1975), Gabbro-eclogite reaction rate and its geophysical significance, *Reviews of Geophysics*, *13*(2), 383–400.

Anderson, D. (2001), Top-down tectonics?, *Science*, *293*(5537), 2016–2018.

Anderson, D. L. (2011), Hawaii, boundary layers and ambient mantle—geophysical constraints, *Journal of Petrology*, *52*(7-8), 1547–1577.

Anderson, H., and J. Jackson (1987), Active tectonics of the adriatic region, *Geophysical Journal of the royal Astronomical society*, *91*(3), 937–983.

Babeyko, A., and S. Sobolev (2008), High-resolution numerical modeling of stress distribution in visco-elasto-plastic subducting slabs, *Lithos*, *103*(1), 205–216.

Baccheschi, P., L. Margheriti, and M. Steckler (2007), Seismic anisotropy reveals focused mantle flow around the calabrian slab (southern italy), *Geophysical Research Letters*, *34*(5).

Baccheschi, P., L. Margheriti, and M. Steckler (2008), Sks splitting in southern italy: Anisotropy variations in a fragmented subduction zone, *Tectonophysics*, *462*(1), 49–67.

Baccheschi, P., L. Margheriti, M. Steckler, and E. Boschi (2011), Anisotropy patterns in the subducting lithosphere and in the mantle wedge: A case study—the southern italy subduction system, *Journal of Geophysical Research: Solid Earth (1978–2012)*, *116*(B8).

Bada, G., S. Cloetingh, P. Gerner, and F. Horvath (1998), Sources of recent tectonic stress in the pannonian region: inferences from finite element modelling, *Geophysical journal international*, *134*(1), 87–101.

Bailey, I., L. Alpert, T. Becker, and M. Miller (2012), Co-seismic deformation of deep slabs based on summed cmt data, *Journal of Geophysical Research: Solid Earth (1978–2012)*, *117*(B4), B04,404.

Barba, S., M. Carafa, M. T. Mariucci, P. Montone, and S. Pierdominici (2010), Present-day stress-field modelling of southern italy constrained by stress and gps data, *Tectonophysics*, *482*(1), 193–204.

Barberi, G., M. Cosentino, A. Gervasi, I. Guerra, G. Neri, and B. Orecchio (2004), Crustal seismic tomography in the calabrian arc region, south italy, *Physics of the Earth and Planetary Interiors*, *147*(4), 297–314.

Barrientos, S. E., and S. N. Ward (1990), The 1960 chile earthquake: inversion for slip distribution from surface deformation, *Geophysical Journal International*, *103*(3), 589–598.

Basili, R., G. Valensise, P. Vannoli, P. Burrato, U. Fracassi, S. Mariano, M. M. Tiberti, and E. Boschi (2008), The database of individual seismogenic sources (diss), version 3: summarizing 20 years of research on italy's earthquake geology, *Tectonophysics*, *453*(1), 20–43.

Basili, R., V. Kastelic, P. Petricca, and M. Tiberti (2011), Database of active faults and seismogenic sources, project share, seismic hazard harmonization in europe, *Deliverable* $D3.4$. *Available at: http://www.share-eu.org/sites/default/files/*$D3.4\_SHARE.pdf$.

Basili, R., V. Kastelic, M. Demircioglu, D. Garcia Moreno, E. Nemser, P. Petricca, S. Sboras, G. Besana-Ostman, J. Cabral, T. Camelbeeck, R. Caputo, L. Danciu, H. Domac, J. Fonseca, J. Garcia-Mayordomo, D. Giardini, B. Glavatovic, L. Gulen, Y. Ince, S. Pavlides, K. Sesetyan, G. Tarabusi, M. Tiberti, M. Utkucu, G. Valensise, K. Vanneste, S. Vilanova, and J. Wossner (2013a), The european database of seismogenic faults (edsf) compiled in the framework of the project share, http://diss.rm.ingv.it/share-edsf, doi:10.6092/INGV.IT-SHARE-EDSF.

Basili, R., M. Tiberti, V. Kastelic, F. Romano, A. Piatanesi, J. Selva, S. Lorito, et al. (2013b), Integrating geologic fault data into tsunami hazard studies, *Natural Hazards and Earth System Science*, *13*(4), 1025–1050.

Becker, D., and T. Meier (2010), Seismic slip deficit in the southwestern forearc of the hellenic subduction zone, *Bulletin of the Seismological Society of America*, *100*(1), 325–342.

Becker, T. (2008), Correction to azimuthal seismic anisotropy constrains net rotation of the lithosphere, *Geophysical research letters*, *35*(L08308), doi:10.1029/2008GL033946.

Becker, T. W. (2006), On the effect of temperature and strain-rate dependent viscosity on global mantle flow, net rotation, and plate-driving forces, *Geophysical Journal International*, *167*(2), 943–957.

Bellahsen, N., C. Faccenna, and F. Funiciello (2005), Dynamics of subduction and plate motion in laboratory experiments: Insights into the "plate tectonics" behavior of the earth, *Journal of Geophysical Research: Solid Earth (1978–2012)*, *110*(B1), B01,401.

Benetatos, C., and A. Kiratzi (2006), Finite-fault slip models for the 15 april 1979 (mw 7.1) montenegro earthquake and its strongest aftershock of 24 may 1979 (mw 6.2), *Tectonophysics*, *421*(1), 129–143.

Benetatos, C., A. Kiratzi, C. Papazachos, and G. Karakaisis (2004), Focal mechanisms of shallow and intermediate depth earthquakes along the hellenic arc, *Journal of Geodynamics*, *37*(2), 253–296.

Bercovici, D. (2003), The generation of plate tectonics from mantle convection, *Earth and Planetary Science Letters*, *205*(3), 107–121.

Bigi, G., M. Coli, D. Cosentino, M. Parotto, A. Praturlon, R. Sartori, P. Scandone, and E. Turco (1992), Structural model of italy, sheet 4, scale 1: 500,000. cnr quaderni de "la ricerca scientifica", 114, *Monografie finali, Progetto finalizzato "Geodinamica*, *3*.

Bilek, S. L., and T. Lay (1999), Rigidity variations with depth along interplate megathrust faults in subduction zones, *Nature*, *400*(6743), 443–446.

Billen, M. I. (2008), Modeling the dynamics of subducting slabs, *Annual Review of Earth and Planetary Sciences*, *36*, 325–356.

Billen, M. I., and M. Gurnis (2001), A low viscosity wedge in subduction zones, *Earth and Planetary Science Letters*, *193*(1), 227–236.

Billen, M. I., and M. Gurnis (2003), Comparison of dynamic flow models for the central aleutian and tonga-kermadec subduction zones, *Geochemistry, Geophysics, Geosystems*, *4*(4).

Bina, C. (1996), Phase transition buoyancy contributions to stresses in subducting lithosphere, *Geophysical research letters*, *23*, 3563–3566.

Bina, C. (1997), Patterns of deep seismicity reflect buoyancy stresses due to phase transitions, *Geophysical research letters*, *24*, 3301–3304.

Bina, C. R., S. Stein, F. C. Marton, and E. M. Van Ark (2001), Implications of slab mineralogy for subduction dynamics, *Physics of the Earth and Planetary Interiors*, *127*(1), 51–66.

Bird, P. (2003), An updated digital model of plate boundaries, *Geochemistry, Geophysics, Geosystems*, *4*(3).

Bird, P., Z. Liu, and W. K. Rucker (2008), Stresses that drive the plates from below: Definitions, computational path, model optimization, and error analysis, *Journal of Geophysical Research: Solid Earth (1978–2012)*, *113*(B11).

Bohnhoff, M., H.-P. Harjes, and T. Meier (2005), Deformation and stress regimes in the hellenic subduction zone from focal mechanisms, *Journal of Seismology*, *9*(3), 341–366.

Bonnardot, M.-A., R. Hassani, E. Tric, E. Ruellan, and M. Régnier (2008), Effect of margin curvature on plate deformation in a 3d numerical model of subduction zones, *Geophysical Journal International*,

173(3), 1084–1094.

Bostrom, R. (1971), Westward displacement of the lithosphere, *Nature*, *234*, 536–538.

Brandmayr, E., I. Marson, F. Romanelli, and G. F. Panza (2011), Lithosphere density model in italy: no hint for slab pull, *Terra Nova*, *23*(5), 292–299, doi:10.1111/j.1365-3121.2011.01012.x.

Buffett, B. A. (2006), Plate force due to bending at subduction zones, *Journal of Geophysical Research: Solid Earth (1978–2012)*, *111*(B9).

Cagnan, Z., and G. B. Tanircan (2010), Seismic hazard assessment for cyprus, *Journal of seismology*, *14*(2), 225–246.

Calcagnile, G., and G. Panza (1979), Crustal and upper mantle structure beneath the apennines region as inferred from the study of rayleigh waves, *Journal of Geophysics*, *45*, 319–327.

Carafa, M., and S. Barba (2011), Determining rheology from deformation data: The case of central italy, *Tectonics*, *30*(2).

Carminati, E., and C. Doglioni (2012), Alps vs. apennines: The paradigm of a tectonically asymmetric earth, *Earth-Science Reviews*, *112*(1), 67–96.

Carminati, E., and P. Petricca (2010), State of stress in slabs as a function of large-scale plate kinematics, *Geochemistry, Geophysics, Geosystems*, *11*(4), Q04,006.

Carminati, E., and L. Vadacca (2010), Two-and three-dimensional numerical simulations of the stress field at the thrust front of the northern apennines, italy, *Journal of Geophysical Research: Solid Earth (1978–2012)*, *115*(B12).

Carminati, E., M. Wortel, W. Spakman, and R. Sabadini (1998), The role of slab detachment processes in the opening of the western–central mediterranean basins: some geological and geophysical evidence, *Earth and Planetary Science Letters*, *160*(3), 651–665.

Carminati, E., C. Giunchi, A. Argnani, R. Sabadini, and M. Fernandez (1999), Plio-quaternary vertical motion of the northern apennines: insights from dynamic modeling, *Tectonophysics*, *18*(4), 703–718.

Carminati, E., F. T. Augier, and S. Barba (2001), Dynamic modelling of stress accumulation in central italy: role of structural heterogeneities and rheology, *Geophysical Journal International*, *144*(2), 373–390.

Carminati, E., A. Negredo, J. Valera, and C. Doglioni (2005), Subduction-related intermediate-depth and deep seismicity in italy: insights from thermal and rheological modelling, *Physics of the earth and planetary interiors*, *149*(1-2), 65–79.

Carminati, E., M. Lustrino, M. Cuffaro, and C. Doglioni (2010), Tectonics, magmatism and geodynamics of italy: what we know and what we imagine, *Journal of the Virtual Explorer*, *36*, 8.

Casten, U., and K. Snopek (2006), Gravity modelling of the hellenic subduction zone—a regional study, *Tectonophysics*, *417*(3), 183–200.

Catalano, R., C. Doglioni, and S. Merlini (2001), On the mesozoic ionian basin, *Geophysical Journal International*, *144*(1), 49–64.

Chamot-Rooke, N., A. Rabaute, and C. Kreemer (2005), Western mediterranean ridge mud belt correlates with active shear strain at the prism-backstop geological contact, *Geology*, *33*(11), 861–864.

Channell, J. (1996), Palaeomagnetism and palaeogeography of adria, *Geological Society, London, Special Publications*, *105*(1), 119–132.

Chen, J., and S. D. King (1998), The influence of temperature and depth dependent viscosity on geoid and topography profiles from models of mantle convection, *Physics of the earth and planetary interiors*, *106*(1), 75–92.

Chen, P., C. Bina, and E. Okal (2004), A global survey of stress orientations in subducting slabs as revealed by intermediate-depth earthquakes, *Geophysical Journal International*, *159*(2), 721–733.

Chen, W., and M. Brudzinski (2001), Evidence for a large-scale remnant of subducted lithosphere beneath fiji, *Science*, *292*(5526), 2475–2479.

Chiarabba, C., L. Jovane, and R. DiStefano (2005), A new view of italian seismicity using 20 years of instrumental recordings, *Tectonophysics*, *395*(3), 251–268.

Chiarabba, C., P. De Gori, and F. Speranza (2008), The southern tyrrhenian subduction zone: Deep geometry, magmatism and plio-pleistocene evolution, *Earth and Planetary Science Letters*, *268*(3), 408–423.

Christensen, N. I. (2004), Serpentinites, peridotites, and seismology, *International Geology Review*, *46*(9), 795–816.

Christensen, U. R. (1996), The influence of trench migration on slab penetration into the lower mantle, *Earth and Planetary Science Letters*, *140*(1), 27–39.

Christensen, U. R., and D. A. Yuen (1984), The interaction of a subducting lithospheric slab with a chemical or phase boundary, *Journal of Geophysical Research: Solid Earth (1978–2012)*, *89*(B6), 4389–4402.

Cifelli, F., M. Mattei, and F. Rossetti (2007), Tectonic evolution of arcuate mountain belts on top of a retreating subduction slab: The example of the calabrian arc, *Journal of Geophysical Research: Solid Earth (1978–2012)*, *112*(B9).

Cifelli, F., M. Mattei, and M. Della Seta (2008), Calabrian arc oroclinal bending: The role of subduction, *Tectonics*, *27*(5).

Cimini, G. B. (1999), P-wave deep velocity structure of the southern tyrrhenian subduction zone from nonlinear teleseismic traveltime tomography, *Geophysical research letters*, *26*(24), 3709–3712.

Civello, S., and L. Margheriti (2004), Toroidal mantle flow around the calabrian slab (italy) from sks splitting, *Geophysical research letters*, *31*(10).

Clark, S., A. Levander, M. Magnani, and C. Zelt (2008), Negligible convergence and lithospheric tearing along the caribbean–south american plate boundary at 64 w, *Tectonics*, *27*(6).

Cocard, M., H.-G. Kahle, Y. Peter, A. Geiger, G. Veis, S. Felekis, D. Paradissis, and H. Billiris (1999), New constraints on the rapid crustal motion of the aegean region: recent results inferred from gps measurements (1993–1998) across the west hellenic arc, greece, *Earth and Planetary Science Letters*, *172*(1), 39–47.

Conrad, C., and C. Lithgow-Bertelloni (2002), How mantle slabs drive plate tectonics, *Science*, *298*(5591), 207–209.

Conrad, C. P., and B. H. Hager (1999), Effects of plate bending and fault strength at subduction zones on plate dynamics, *Journal of Geophysical Research: Solid Earth (1978–2012)*, *104*(B8), 17,551–17,571.

Conrad, C. P., and C. Lithgow-Bertelloni (2004), The temporal evolution of plate driving forces: Importance of "slab suction" versus "slab pull" during the cenozoic, *Journal of Geophysical Research: Solid Earth (1978–2012)*, *109*(B10).

Corti, G., M. Cuffaro, C. Doglioni, F. Innocenti, and P. Manetti (2006), Coexisting geodynamic processes in the sicily channel, *Special Papers-Geological Society of America*, *409*, 83.

Crespi, M., M. Cuffaro, C. Doglioni, F. Giannone, and F. Riguzzi (2007), Space geodesy validation of the global lithospheric flow, *Geophysical Journal International*, *168*(2), 491–506.

Cruciani, C., E. Carminati, and C. Doglioni (2005), Slab dip vs. lithosphere age: no direct function, *Earth and Planetary Science Letters*, *238*(3), 298–310.

Cuffaro, M., and C. Doglioni (2007), Global kinematics in deep versus shallow hotspot reference frames, *Special Papers - Geological Society of America*, *430*, 359.

Cuffaro, M., and D. M. Jurdy (2006), Microplate motions in the hotspot reference frame, *Terra Nova*, *18*(4), 276–281.

D'Agostino, N., S. Mantenuto, E. D'Anastasio, R. Giuliani, M. Mattone, S. Calcaterra, P. Gambino, and L. Bonci (2011), Evidence for localized active extension in the central apennines (italy) from global positioning system observations, *Geology*, *39*(4), 291–294.

Dal Piaz, G. V., A. Bistacchi, and M. Massironi (2003), Geological outline of the alps, *Episodes*, *26*(3), 175–180.

Davies, G. F. (1977), Whole-mantle convection and plate tectonics, *Geophysical Journal of the Royal Astronomical Society*, *49*(2), 459–486.

Davies, G. F. (1986), Mantle convection under simulated plates: effects of heating modes and ridge and trench migration, and implications for the core-mantle boundary, bathymetry, the geoid and benioff zones, *Geophysical Journal International*, *84*(1), 153–183.

Davies, G. F. (1995), Penetration of plates and plumes through the mantle transition zone, *Earth and Planetary Science Letters*, *133*(3), 507–516.

Davies, J. H., and D. Stevenson (1992), Physical model of source region of subduction zone volcanics, *Journal of Geophysical Research: Solid Earth (1978–2012)*, *97*(B2), 2037–2070.

Del Gaudio, V., P. Pierri, A. Frepoli, G. Calcagnile, N. Venisti, and G. Cimini (2007), A critical revision of the seismicity of northern apulia (adriatic microplate—southern italy) and implicationsfor the identification of seismogenic structures, *Tectonophysics*, *436*(1), 9–35.

DeMets, C., R. G. Gordon, D. F. Argus, and S. Stein (1994), Effect of recent revisions to the geomagnetic reversal time scale on estimates of current plate motions, *Geophysical Research Letters*, *21*, 2121–2194.

Devaux, J., L. Fleitout, G. Schubert, and C. Anderson (2000), Stresses in a subducting slab in the presence of a metastable olivine wedge, *Journal of Geophysical Research: Solid Earth (1978–2012)*, *105*(B6), 13,365–13,373, doi:10.1029/1999JB900274.

Devoti, R., F. Riguzzi, M. Cuffaro, and C. Doglioni (2008), New gps constraints on the kinematics of the apennines subduction, *Earth and Planetary Science Letters*, *273*(1), 163–174.

Di Stefano, R., C. Chiarabba, F. Lucente, and A. Amato (1999), Crustal and uppermost mantle structure in italy from the inversion of p-wave arrival times: geodynamic implications, *Geophysical Journal International*, *139*(2), 483–498.

Di Stefano, R., E. Kissling, C. Chiarabba, A. Amato, and D. Giardini (2009), Shallow subduction beneath italy: Three-dimensional images of the adriatic-european-tyrrhenian lithosphere system based on high-quality p wave arrival times, *Journal of Geophysical Research: Solid Earth (1978–2012)*, *114*(B5).

Dickinson, W. R. (1978), Plate tectonic evolution of north pacific rim, *Journal of Physics of the Earth*, *26*, 1–19.

Dilek, Y., and E. Sandvol (2009), Seismic structure, crustal architecture and tectonic evolution of the anatolian-african plate boundary and the cenozoic orogenic belts in the eastern mediterranean region, *Geological Society, London, Special Publications*, *327*(1), 127–160.

Doglioni, C. (1990), The global tectonic pattern, *Journal of Geodynamics*, *12*, 21–38.

Doglioni, C. (1991), A proposal for the kinematic modelling of w-dipping subductions-possible applications to the tyrrhenian-apennines system, *Terra Nova*, *3*(4), 423–434.

Doglioni, C. (1993), Some remarks on the origin of foredeeps, *Tectonophysics*, *228*(1), 1–20.

Doglioni, C. (1994), Foredeeps versus subduction zones, *Geology*, *22*, 271–274.

Doglioni, C., and E. Carminati (2002), The effects of four subductions in ne italy, *Memorie di Scienze Geologiche*, *54*, 1–4.

Doglioni, C., P. Harabaglia, S. Merlini, F. Mongelli, A. Peccerillo, and C. Piromallo (1999), Orogens and slabs vs their direction of subduction, *Earth-Science Review*, *45*, 167–208.

Doglioni, C., E. Carminati, M. Cuffaro, and D. Scrocca (2007), Subduction kinematics and dynamic constraints, *Earth-Science Reviews*, *83*(3), 125–175.

Dvorkin, J., A. Nur, G. Mavko, and Z. Ben-Avraham (1993), Narrow subducting slabs and the origin of backarc basins, *Tectonophysics*, *227*(1), 63–79.

Dziewonski, A. M., and D. L. Anderson (1981), Preliminary reference earth model, *Physics of the earth and planetary interiors*, *25*(4), 297–356.

D'Agostino, N., and G. Selvaggi (2004), Crustal motion along the eurasia-nubia plate boundary in the calabrian arc and sicily and active extension in the messina straits from gps measurements, *Journal of Geophysical Research: Solid Earth (1978–2012)*, *109*(B11).

Ekstrom, G., M. Nettles, and A. Dziewonski (2012), The global cmt project 2004–2010: Centroid-moment tensors for 13017 earthquakes, *Physics of the Earth and Planetary Interiors*, *200*, 1–9.

Engdahl, E., and C. Scholz (1977), A double benioff zone beneath the central aleutians: An unbending of the lithosphere, *Geophysical Research Letters*, *4*(10), 473–476.

Ergün, M., S. Okay, C. Sari, E. Zafer Oral, M. Ash, J. Hall, and H. Miller (2005), Gravity anomalies of the cyprus arc and their tectonic implications, *Marine geology*, *221*(1), 349–358.

Ern, A., and J.-L. Guermond (2004), *Theory and practice of finite elements*, vol. 159, Springer.

Faccenda, M., and F. Capitanio (2013), Seismic anisotropy around subduction zones: Insights from three-dimensional modeling of upper mantle deformation and sks splitting calculations, *Geochemistry, Geophysics, Geosystems*.

Faccenna, C., P. Davy, J.-P. Brun, R. Funiciello, D. Giardini, M. Mattei, and T. Nalpas (1996), The dynamics of back-arc extension: An experimental approach to the opening of the tyrrhenian sea, *Geophysical Journal International*, *126*(3), 781–795.

Faccenna, C., T. W. Becker, F. P. Lucente, L. Jolivet, and F. Rossetti (2001a), History of subduction and back-arc extension in the central mediterranean, *Geophysical Journal International*, *145*(3), 809–820, doi:10.1046/j.0956-540x.2001.01435.x.

Faccenna, C., F. Funiciello, D. Giardini, and P. Lucente (2001b), Episodic back-arc extension during restricted mantle convection in the central mediterranean, *Earth and Planetary Science Letters*, *187*(1),

105–116.

Faccenna, C., C. Piromallo, A. Crespo-Blanc, L. Jolivet, and F. Rossetti (2004), Lateral slab deformation and the origin of the western mediterranean arcs, *Tectonics*, *23*(1).

Faccenna, C., L. Civetta, M. D'Antonio, F. Funiciello, L. Margheriti, and C. Piromallo (2005), Constraints on mantle circulation around the deforming calabrian slab, *Geophysical Research Letters*, *32*(6).

Faccenna, C., O. Bellier, J. Martinod, C. Piromallo, and V. Regard (2006), Slab detachment beneath eastern anatolia: A possible cause for the formation of the north anatolian fault, *Earth and Planetary Science Letters*, *242*(1), 85–97.

Faccenna, C., A. Heuret, F. Funiciello, S. Lallemand, and T. W. Becker (2007), Predicting trench and plate motion from the dynamics of a strong slab, *Earth and Planetary Science Letters*, *257*(1), 29–36.

Faccenna, C., T. W. Becker, S. Lallemand, Y. Lagabrielle, F. Funiciello, and C. Piromallo (2010), Subduction-triggered magmatic pulses: A new class of plumes?, *Earth and Planetary Science Letters*, *299*(1), 54–68.

Faccenna, C., P. Molin, B. Orecchio, V. Olivetti, O. Bellier, F. Funiciello, L. Minelli, C. Piromallo, and A. Billi (2011), Topography of the calabria subduction zone (southern italy): Clues for the origin of mt. etna, *Tectonics*, *30*(1).

Faccenna, C., T. W. Becker, C. P. Conrad, and L. Husson (2013), Mountain building and mantle dynamics, *Tectonics*.

Finetti, I., and A. Del Ben (2005), Crustal tectono-stratigraphic setting of the adriatic sea from new crop seismic data, *CROP, Deep Seismic Exploration of the Mediterranean Region (ed. Finetti I R.)(Elsevier, 2005)*, pp. 519–547.

Finetti, I., et al. (1982), Structure, stratigraphy and evolution of central mediterranean, *Boll. Geofis. Teor. Appl*, *24*(96), 247–312.

Forsyth, D., and S. Uyeda (1975), On the relative importance of the driving forces of plate motion, *Geophysical Journal International*, *43*(1), 163–200.

Foulger, G. R. (2005), *Plates, plumes, and paradigms*, vol. 388, Geological Society of Amer.

Frank, F. (1968), Curvature of island arcs, *Nature*.

Frepoli, A., and A. Amato (1997), Contemporaneous extension and compression in the northern apennines from earthquake fault-plane solutions, *Geophysical Journal International*, *129*(2), 368–388.

Frepoli, A., G. Selvaggi, C. Chiarabba, and A. Amato (2007), State of stress in the southern tyrrhenian subduction zone from fault-plane solutions, *Geophysical Journal International*, *125*(3), 879–891, doi: 10.1111/j.1365-246X.1996.tb06031.x.

Fujii, Y., K. Satake, S. Sakai, M. Shinohara, and T. Kanazawa (2011), Tsunami source of the 2011 off the pacific coast of tohoku earthquake, *Earth, planets and space*, *63*(7), 815–820.

Fukao, Y., M. Obayashi, H. Inoue, and M. Nenbai (1992), Subducting slabs stagnant in the mantle transition zone, *Journal of Geophysical Research: Solid Earth (1978–2012)*, *97*(B4), 4809–4822.

Funiciello, F., G. Morra, K. Regenauer-Lieb, and D. Giardini (2003), Dynamics of retreating slabs (part 1): Insights from two-dimensional numerical experiments, *Journal of Geophysical Research: Solid Earth (1978–2012)*, *108*(B4).

Funiciello, F., M. Moroni, C. Piromallo, C. Faccenna, A. Cenedese, and H. A. Bui (2006), Mapping flow during retreating subduction: laboratory models analyzed by Feature Tracking, *Journal of Geophysical Research: Solid Earth (1978–2012)*, *111*, doi:10.1029/2005JB003792.

Furlong, K. P., D. S. Chapman, and P. W. Alfeld (1982), Thermal modeling of the geometry of subduction with implications for the tectonics of the overriding plate, *Journal of Geophysical Research: Solid Earth (1978–2012)*, *87*(B3), 1786–1802.

Ganas, A., and T. Parsons (2009), Three-dimensional model of hellenic arc deformation and origin of the cretan uplift, *Journal of Geophysical Research: Solid Earth (1978–2012)*, *114*(B6).

Gardi, A., M. Cocco, A. Negredo, R. Sabadini, et al. (2002), Dynamic modelling of the subduction zone of central mexico, *Geophysical Journal International*, *143*(3), 809–820.

Gérault, M., T. Becker, B. Kaus, C. Faccenna, L. Moresi, and L. Husson (2012), The role of slabs and oceanic plate geometry in the net rotation of the lithosphere, trench motions, and slab return flow, *Geochemistry, Geophysics, Geosystems*, *13*(4).

Gerya, T. (2011), Future directions in subduction modeling, *Journal of Geodynamics*, *52*(5), 344–378.

Giunchi, C., R. Sabadini, E. Boschi, and P. Gasperini (1996), Dynamic models of subduction: geophysical and geological evidence in the tyrrhenian sea, *Geophysical Journal International*, *126*(2), 555–578.

Goes, S., F. A. Capitanio, and G. Morra (2008), Evidence of lower-mantle slab penetration phases in plate motions, *Nature*, *451*(7181), 981–984.

Grand, S. P. (1994), Mantle shear structure beneath the americas and surrounding oceans, *Journal of Geophysical Research: Solid Earth (1978–2012)*, *99*(B6), 11,591–11,621.

Gripp, A., and R. Gordon (2002), Young tracks of hotspots and current plate velocities, *Geophysical Journal International*, *150*(2), 321–361.

Group, I. W., et al. (2010), Italian seismological instrumental and parametric database.

Gudmundsson, Ó., and M. Sambridge (1998), A regionalized upper mantle (rum) seismic model, *Journal of Geophysical Research: Solid Earth (1978–2012)*, *103*(B4), 7121–7136.

Gueguen, E., C. Doglioni, and M. Fernandez (1998), On the post-25 ma geodynamic evolution of the western mediterranean, *Tectonophysics*, *298*(1), 259–269.

Guidoboni, E., G. Ferrari, D. Mariotti, A. Comastri, G. Tarabusi, and G. Valensise (2007), Cfti4med, *Catalogue of Strong Earthquakes in Italy (461 BC-1997) and Mediterranean Area (760 BC-1500). INGV-SGA. Available from http://storing. ingv. it/cfti4med*.

Gung, Y., M. Panning, B. Romanowicz, et al. (2003), Global anisotropy and the thickness of continents, *Nature*, *422*(6933), 707–711.

Gurnis, M., and B. H. Hager (1988), Controls of the structure of subducted slabs, *Nature*, *335*(6188), 317–321.

Gurnis, M., C. Hall, and L. Lavier (2004), Evolving force balance during incipient subduction, *Geochemistry, Geophysics, Geosystems*, *5*(7).

Gvirtzman, Z., and A. Nur (2001), Residual topography, lithospheric structure and sunken slabs in the central mediterranean, *Earth and Planetary Science Letters*, *187*(1), 117–130.

Hager, B. H., and R. J. O'connell (1978), Subduction zone dip angles and flow driven by plate motion, *Tectonophysics*, *50*(2), 111–133.

Hager, B. H., and R. J. O'Connell (1981), A simple global model of plate dynamics and mantle convection, *Journal of Geophysical Research: Solid Earth (1978–2012)*, *86*(B6), 4843–4867.

Hall, C. E., and M. Gurnis (2005), Strength of fracture zones from their bathymetric and gravitational evolution, *Journal of Geophysical Research: Solid Earth (1978–2012)*, *110*(B1).

Hasegawa, A., N. Umino, and A. Takagi (1978), Double-planed structure of the deep seismic zone in the northeastern japan arc, *Tectonophysics*, *47*(1), 43–58.

Hashima, A., Y. Fukahata, and M. Matsu'ura (2008), 3-d simulation of tectonic evolution of the mariana arc–back-arc system with a coupled model of plate subduction and back-arc spreading, *Tectonophysics*, *458*(1), 127–136.

Hassani, R., D. Jongmans, and J. Chéry (1997), Study of plate deformation and stress in subduction processes using two-dimensional numerical models, *Journal of Geophysical Research: Solid Earth (1978–2012)*, *102*(B8), 17,951–17,965.

Hatzfeld, D., and C. Martin (1992), Intermediate depth seismicity in the aegean defined by teleseismic data, *Earth and planetary science letters*, *113*(1), 267–275.

Hayes, G. P., D. J. Wald, and R. L. Johnson (2012), Slab1.0: A three-dimensional model of global subduction zone geometries, *Journal of Geophysical Research: Solid Earth (1978–2012)*, *117*(B1).

Heidbach, O., M. Tingay, A. Barth, J. Reinecker, D. Kurfeß, and B. Müller (2008), The world stress map database release 2008, doi: 10.1594/gfz, *WSM. Rel2008*.

Helffrich, G. R., S. Stein, and B. J. Wood (1989), Subduction zone thermal structure and mineralogy and their relationship to seismic wave reflections and conversions at the slab/mantle interface, *Journal of Geophysical Research: Solid Earth (1978–2012)*, *94*(B1), 753–763.

Herak, D., M. Herak, E. Prelogović, S. Markušić, and Ž. Markulin (2005), Jabuka island (central adriatic sea) earthquakes of 2003, *Tectonophysics*, *398*(3), 167–180.

Herrmann, R. B., L. Malagnini, and I. Munafò (2011), Regional moment tensors of the 2009 l'aquila earthquake sequence, *Bulletin of the Seismological Society of America*, *101*(3), 975–993.

Heuret, A., and S. Lallemand (2005), Plate motions, slab dynamics and back-arc deformation, *Physics of the Earth and Planetary Interiors*, *149*(1), 31–51.

Heuret, A., S. Lallemand, F. Funiciello, C. Piromallo, and C. Faccenna (2011), Physical characteristics of subduction interface type seismogenic zones revisited, *Geochemistry, Geophysics, Geosystems*, *12*(1).

Hollenstein, C., M. Müller, A. Geiger, and H.-G. Kahle (2008), Crustal motion and deformation in greece from a decade of gps measurements, 1993–2003, *Tectonophysics*, *449*(1), 17–40.

Honda, S., and M. Saito (2003), Small-scale convection under the back-arc occurring in the low viscosity wedge, *Earth and Planetary Science Letters*, *216*(4), 703–715.

Houseman, G., and D. Gubbins (1997), Deformation of subducted oceanic lithosphere, *Geophysical Journal International*, *131*(3), 535–551.

Hsui, A. T., and S. Youngquist (1985), A dynamic model of the curvature of the mariana trench, *Nature*, *318*(6045), 455–457.

Huguen, C., J. Mascle, E. Chaumillon, J. M. Woodside, J. Benkhelil, A. Kopf, and A. Volkonskaia (2001), Deformational styles of the eastern mediterranean ridge and surroundings from combined swath mapping and seismic reflection profiling, *Tectonophysics*, *343*(1), 21–47.

Imprescia, P., S. Pondrelli, G. Vannucci, and S. Gresta (2012), Regional centroid moment tensor solutions in cyprus from 1977 to the present and seismotectonic implications, *Journal of seismology*, *16*(2), 147–167.

Irifune, T. (1993), Phase transformations in the earth's mantle and subducting slabs: Implications for their compositions, seismic velocity and density structures and dynamics, *Island Arc*, *2*(2), 55–71.

Isacks, B., and P. Molnar (1969), Mantle earthquake mechanisms and the sinking of the lithosphere, *Nature*, *223*(5211), 1121–1124.

Isacks, B., and P. Molnar (1971), Distribution of stresses in the descending lithosphere from a global survey of focal-mechanism solutions of mantle earthquakes, *Reviews of Geophysics*, *9*(1), 103–174.

Ita, J., and S. D. King (1998), The influence of thermodynamic formulation on simulations of subduction zone geometry and history, *Geophysical research letters*, *25*(14), 1463–1466.

Jackson, J., and D. McKenzie (1988), The relationship between plate motions and seismic moment tensors, and the rates of active deformation in the mediterranean and middle east, *Geophysical Journal*, *93*(1), 45–73.

Jadamec, M. A., and M. I. Billen (2010), Reconciling surface plate motions with rapid three-dimensional mantle flow around a slab edge, *Nature*, *465*(7296), 338–341.

Jarrard, R. D. (1986), Relations among subduction parameters, *Reviews of Geophysics*, *24*(2), 217–284.

Jolivet, L., K. Tamaki, and M. Fournier (1994), Japan sea, opening history and mechanism: A synthesis, *Journal of Geophysical Research: Solid Earth (1978–2012)*, *99*(B11), 22,237–22,259.

Jordan, T. H. (1974), Some comments on tidal drag as a mechanism for driving plate motions, *Journal of Geophysical Research: Solid Earth (1978–2012)*, *79*(14), 2141–2142.

Kalyoncuoğlu, Ü. Y., Ö. Elitok, M. N. Dolmaz, and N. C. Anadolu (2011), Geophysical and geological imprints of southern neotethyan subduction between cyprus and the isparta angle, sw turkey, *Journal of Geodynamics*, *52*(1), 70–82.

Kastelic, V., M. Vrabec, D. Cunningham, and A. Gosar (2008), Neo-alpine structural evolution and present-day tectonic activity of the eastern southern alps: The case of the ravne fault, nw slovenia, *Journal of structural geology*, *30*(8), 963–975.

Kaufmann, G., and K. Lambeck (2000), Mantle dynamics, postglacial rebound and the radial viscosity profile, *Physics of the Earth and Planetary Interiors*, *121*(3), 301–324.

Kawakatsu, H. (1986), Double seismic zones: kinematics, *Journal of Geophysical Research: Solid Earth (1978–2012)*, *91*(B5), 4811–4825.

Kelly, R. K., P. B. Kelemen, and M. Jull (2003), Buoyancy of the continental upper mantle, *Geochemistry, Geophysics, Geosystems*, *4*(2).

Kincaid, C., and P. Olson (1987), An experimental study of subduction and slab migration, *Journal of Geophysical Research: Solid Earth (1978–2012)*, *92*(B13), 13,832–13,840.

Kincaid, C., and I. S. Sacks (1997), Thermal and dynamical evolution of the upper mantle in subduction zones, *Journal of Geophysical Research: Solid Earth (1978–2012)*, *102*(B6), 12,295–12.

King, G. C., R. S. Stein, and J. Lin (1994), Static stress changes and the triggering of earthquakes, *Bulletin of the Seismological Society of America*, *84*(3), 935–953.

King, S. D. (2007), Mantle downwellings and the fate of subducting slabs: constraints from seismology, geoid, topography, geochemistry, and pretrology, in *Treatise on Geophysics*, edited by G. Schubert and D. Bercovici, Elsevier.

King, S. D., S. Balachandar, and J. J. Ita (1997), Using eigenfunctions of the two-point correlation function to study convection with multiple phase transformations, *Geophysical research letters*, *24*(6), 703–706.

Kirby, S. H., S. Stein, E. A. Okal, and D. C. Rubie (1996), Metastable mantle phase transformations and deep earthquakes in subducting oceanic lithosphere, *Reviews of Geophysics*, *34*(2), 261–306.

Kneller, E. A., P. E. Van Keken, S.-i. Karato, and J. Park (2005), B-type olivine fabric in the mantle wedge: Insights from high-resolution non-newtonian subduction zone models, *Earth and Planetary Science Letters*, *237*(3), 781–797.

Kreemer, C., and N. Chamot-Rooke (2004), Contemporary kinematics of the southern aegean and the mediterranean ridge, *Geophysical Journal International*, *157*(3), 1377–1392.

Kukowski, N., S. E. Lallemand, J. Malavieille, M.-A. Gutscher, and T. J. Reston (2002), Mechanical decoupling and basal duplex formation observed in sandbox experiments with application to the western mediterranean ridge accretionary complex, *Marine Geology*, *186*(1), 29–42.

Laigle, M., M. Sachpazi, and A. Hirn (2004), Variation of seismic coupling with slab detachment and upper plate structure along the western hellenic subduction zone, *Tectonophysics*, *391*(1), 85–95.

Lallemand, S., A. Heuret, and D. Boutelier (2005), On the relationships between slab dip, back-arc stress, upper plate absolute motion, and crustal nature in subduction zones, *Geochemistry, Geophysics, Geosystems*, *6*(9).

Le Pichon, X., N. Chamot-Rooke, S. Lallemant, R. Noomen, and G. Veis (1995), Geodetic determination of the kinematics of central greece with respect to europe: Implications for eastern mediterranean tectonics, *Journal of Geophysical Research: Solid Earth (1978–2012)*, *100*(B7), 12,675–12,690.

Li, X., G. Bock, A. Vafidis, R. Kind, H.-P. Harjes, W. Hanka, K. Wylegalla, M. Van Der Meijde, and X. Yuan (2003), Receiver function study of the hellenic subduction zone: imaging crustal thickness variations and the oceanic moho of the descending african lithosphere, *Geophysical Journal International*, *155*(2), 733–748.

Loiselet, C., L. Husson, and J. Braun (2009), From longitudinal slab curvature to slab rheology, *Geology*, *37*(8), 747–750.

Long, M. D., and T. W. Becker (2010), Mantle dynamics and seismic anisotropy, *Earth and Planetary Science Letters*, *297*(3), 341–354.

Long, M. D., and P. G. Silver (2008), The subduction zone flow field from seismic anisotropy: A global view, *Science*, *319*(5861), 315–318.

Long, M. D., and P. G. Silver (2009), Mantle flow in subduction systems: The subslab flow field and implications for mantle dynamics, *Journal of Geophysical Research: Solid Earth (1978–2012)*, *114*(B10).

Lucente, F. P., L. Margheriti, C. Piromallo, and G. Barruol (2006), Seismic anisotropy reveals the long route of the slab through the western-central mediterranean mantle, *Earth and Planetary Science Letters*, *241*(3), 517–529.

Lynner, C., and M. D. Long (2013), Sub-slab seismic anisotropy and mantle flow beneath the caribbean and scotia subduction zones: Effects of slab morphology and kinematics, *Earth and Planetary Science Letters*, *361*(0), 367–378.

Mahadevan, L., R. Bendick, and H. Liang (2010), Why subduction zones are curved, *Tectonics*, *29*(6).

Makris, J., and T. Yegorova (2006), A 3-d density–velocity model between the cretan sea and libya, *Tectonophysics*, *417*(3), 201–220.

Malinverno, A., and W. B. Ryan (1986), Extension in the tyrrhenian sea and shortening in the apennines as result of arc migration driven by sinking of the lithosphere, *Tectonics*, *5*(2), 227–245.

Manea, V., M. Manea, V. Kostoglodov, and G. Sewell (2006), Intraslab seismicity and thermal stress in the subducted cocos plate beneath central mexico, *Tectonophysics*, *420*(3), 389–408.

Mantovani, E., D. Babbucci, D. Albarello, and M. Mucciarelli (1990), Deformation pattern in the central mediterranean and behavior of the african/adriatic promontory, *Tectonophysics*, *179*(1), 63–79.

Mariucci, M. T., and B. Müller (2003), The tectonic regime in italy inferred from borehole breakout data, *Tectonophysics*, *361*(1), 21–35.

Mart, Y., E. Aharonov, G. Mulugeta, W. Ryan, T. Tentler, and L. Goren (2005), Analogue modelling of the initiation of subduction, *Geophysical Journal International*, *160*(3), 1081–1091.

Marton, F. C., C. R. Bina, S. Stein, and D. C. Rubie (1999), Effects of slab mineralogy on subduction rates, *Geophysical research letters*, *26*(1), 119–122.

Marton, F. C., T. J. Shankland, D. C. Rubie, and Y. Xu (2005), Effects of variable thermal conductivity on the mineralogy of subducting slabs and implications for mechanisms of deep earthquakes, *Physics of the Earth and Planetary Interiors*, *149*(1), 53–64.

Mattei, M., F. Cifelli, and N. D'Agostino (2007), The evolution of the calabrian arc: Evidence from paleomagnetic and gps observations, *Earth and Planetary Science Letters*, *263*(3), 259–274.

McAdoo, D., C. Martin, and S. Poulouse (1985), Seasat observations of flexure: Evidence for a strong lithosphere, *Tectonophysics*, *116*(3), 209–222.

McClusky, S., R. Reilinger, S. Mahmoud, D. Ben Sari, and A. Tealeb (2003), Gps constraints on africa (nubia) and arabia plate motions, *Geophysical Journal International*, *155*(1), 126–138.

McKenzie, D. (1978), Active tectonics of the alpine—himalayan belt: the aegean sea and surrounding regions, *Geophysical Journal of the Royal Astronomical Society*, *55*(1), 217–254.

Meier, T., M. Rische, B. Endrun, A. Vafidis, and H.-P. Harjes (2004), Seismicity of the hellenic subduction zone in the area of western and central crete observed by temporary local seismic networks, *Tectonophysics*, *383*(3), 149–169.

Mele, G. (2001), The adriatic lithosphere is a promontory of the african plate: Evidence of a continuous mantle lid in the ionian sea from efficient sn propagation, *Geophysical research letters*, *28*(3), 431–434.

Melosh, H., and A. Raefsky (1980), The dynamical origin of subduction zone topography, *Geophysical Journal of the Royal Astronomical Society*, *60*(3), 333–354.

Miller, K. G., M. A. Kominz, J. V. Browning, J. D. Wright, G. S. Mountain, M. E. Katz, P. J. Sugarman, B. S. Cramer, N. Christie-Blick, and S. F. Pekar (2005), The phanerozoic record of global sea-level change, *Science*, *310*(5752), 1293–1298.

Minelli, L., and C. Faccenna (2010), Evolution of the calabrian accretionary wedge (central mediterranean), *Tectonics*, *29*(4).

Molnar, P., D. Freedman, and J. Shih (1979), Lengths of intermediate and deep seismic zones and temperatures in downgoing slabs of lithosphere, *Royal Astronomical Society Geophysical Journal*, *56*.

Monna, S., and T. Dahm (2009), Three-dimensional p wave attenuation and velocity upper mantle tomography of the southern apennines–calabrian arc subduction zone, *Journal of Geophysical Research: Solid Earth (1978–2012)*, *114*(B6).

Montone, P., and M. T. Mariucci (1999), Active stress along the ne external margin of the apennines: the ferrara arc, northern italy, *Journal of Geodynamics*, *28*(2), 251–265.

Montone, P., M. T. Mariucci, and S. Pierdominici (2012), The italian present-day stress map, *Geophysical Journal International*, *189*(2), 705–716.

Montuori, C., G. B. Cimini, and P. Favali (2007), Teleseismic tomography of the southern tyrrhenian subduction zone: New results from seafloor and land recordings, *Journal of Geophysical Research: Solid Earth (1978–2012)*, *112*(B3).

Morra, G., K. Regenauer-Lieb, and D. Giardini (2006), Curvature of oceanic arcs, *Geology*, *34*(10), 877–880.

Muttoni, G., E. Garzanti, L. Alfonsi, S. Cirilli, D. Germani, and W. Lowrie (2001), Motion of africa and adria since the permian: paleomagnetic and paleoclimatic constraints from northern libya, *Earth and*

Planetary Science Letters, *192*(2), 159–174.

Nakada, M., and K. Lambeck (1989), Late pleistocene and holocene sea-level change in the australian region and mantle rheology, *Geophysical Journal International*, *96*(3), 497–517.

Negredo, A., R. Sabadini, and C. Giunchi (1997), Interplay between subduction and continental convergence: a three-dimensional dynamic model for the central mediterranean, *Geophysical Journal International*, *131*(1), f9–f13.

Negredo, A., S. Barba, E. Carminati, R. Sabadini, and C. Giunchi (1999a), Contribution of numeric dynamic modelling to the understanding of the seismotectonic regime of the northern apennines, *Tectonophysics*, *315*(1), 15–30.

Negredo, A., E. Carminati, S. Barba, and R. Sabadini (1999b), Dynamic modelling of stress accumulation in central italy, *Geophysical Research Letters*, *26*(13), 1945–1948.

Nocquet, J.-M., and E. Calais (2003), Crustal velocity field of western europe from permanent gps array solutions, 1996–2001, *Geophysical Journal International*, *154*(1), 72–88.

Norton, I. O. (2000), Global hotspot reference frames and plate motion, *Geophysical Monograph Series*, *121*, 339–357.

O'Neill, C., D. Müller, and B. Steinberger (2005), On the uncertainties in hot spot reconstructions and the significance of moving hot spot reference frames, *Geochemistry, Geophysics, Geosystems*, *6*(4).

O'Connell, R. J., C. W. Gable, and B. H. Hager (1991), Toroidal-poloidal partitioning of lithospheric plate motions, in *Glacial Isostasy, Sea-Level and Mantle Rheology*, pp. 535–551, Springer.

Pacheco, J., and L. Sykes (1992), Seismic moment catalog of large shallow earthquakes, 1900 to 1989, *Bulletin of the Seismological Society of America*, *82*(3), 1306–1349.

Pacheco, J. F., L. R. Sykes, and C. H. Scholz (1993), Nature of seismic coupling along simple plate boundaries of the subduction type, *Journal of Geophysical Research: Solid Earth (1978–2012)*, *98*(B8), 14,133–14,159.

Panza, G., P. Scandone, G. Calcagnile, S. Mueller, and P. Suhadolc (1992), The lithosphere-asthenosphere system in italy and surrounding regions, *Structural model of Italy, Scale*, *1*(500.000).

Panza, G., A. Peccerillo, A. Aoudia, and B. Farina (2007), Geophysical and petrological modelling of the structure and composition of the crust and upper mantle in complex geodynamic settings: the tyrrhenian sea and surroundings, *Earth-Science Reviews*, *80*(1), 1–46.

Panza, G., C. Doglioni, and A. Levshin (2010), Asymmetric ocean basins, *Geology*, *38*(1), 59–62.

Papadimitriou, E. E., and V. G. Karakostas (2008), Rupture model of the great ad 365 crete earthquake in the southwestern part of the hellenic arc, *Acta Geophysica*, *56*(2), 293–312.

Papazachos, B., C. A. Papaioannou, C. Papazachos, and A. Savvaidis (1999), Rupture zones in the aegean region, *Tectonophysics*, *308*(1), 205–221.

Papazachos, B., V. Karakostas, C. Papazachos, and E. Scordilis (2000), The geometry of the wadati–benioff zone and lithospheric kinematics in the hellenic arc, *Tectonophysics*, *319*(4), 275–300.

Papazachos, B., S. Dimitriadis, D. Panagiotopoulos, C. Papazachos, and E. Papadimitriou (2005), Deep structure and active tectonics of the southern aegean volcanic arc, in *The South Aegean Active Volcanic Arc*, vol. 7, edited by M. Fytikas, pp. 47–64, Developments in Volcanology.

Papazachos, C., and G. Nolet (1997), P and s deep velocity structure of the hellenic area obtained by robust nonlinear inversion of travel times, *Journal of Geophysical Research: Solid Earth (1978–2012)*, *102*(B4), 8349–8367.

Park, J., and V. Levin (2002), Seismic anisotropy: tracing plate dynamics in the mantle, *Science*, *296*(5567), 485–489.

Peacock, S. M. (1996), Thermal and petrologic structure of subduction zones, *Geophysical Monograph Series*, *96*, 119–133.

Peacock, S. M., T. Rushmer, and A. B. Thompson (1994), Partial melting of subducting oceanic crust, *Earth and Planetary Science Letters*, *121*(1), 227–244.

Pepe, F., A. Sulli, G. Bertotti, and F. Cella (2010), Architecture and neogene to recent evolution of the western calabrian continental margin: An upper plate perspective to the ionian subduction system, central mediterranean, *Tectonics*, *29*(3).

Perotti, C. (1991), Osservazioni sull'assetto strutturale del versante padano dell'appennino nord-occidentale, *Atti Ticinensi di Scienze della Terra*, *34*, 11–22.

Peterson, E. T., and T. Seno (1984), Factors affecting seismic moment release rates in subduction zones, *Journal of Geophysical Research: Solid Earth (1978–2012)*, *89*(B12), 10,233–10,248.

Petricca, P., M. Carafa, S. Barba, and E. Carminati (2013), Local, regional, and plate scale sources for the stress field in the adriatic and periadriatic region, *Marine and Petroleum Geology*, *42*, 160–181.

Piana Agostinetti, N., and A. Amato (2009), Moho depth and vp/vs ratio in peninsular italy from teleseismic receiver functions, *Journal of Geophysical Research: Solid Earth (1978–2012)*, *114*(B6).

Piromallo, C., and A. Morelli (2003), P wave tomography of the mantle under the alpine-mediterranean area, *Journal of Geophysical Research: Solid Earth (1978–2012)*, *108*(B2), 2065.

Polonia, A., A. Camerlenghi, F. Davey, and F. Storti (2002), Accretion, structural style and syn-contractional sedimentation in the eastern mediterranean sea, *Marine geology*, *186*(1), 127–144.

Polonia, A., L. Torelli, P. Mussoni, L. Gasperini, A. Artoni, and D. Klaeschen (2011), The calabrian arc subduction complex in the ionian sea: Regional architecture, active deformation, and seismic hazard, *Tectonics*, *30*(5).

Pontevivo, A., and G. F. Panza (2006), The lithosphere-asthenosphere system in the calabrian arc and surrounding seas–southern italy, *pure and applied geophysics*, *163*(8), 1617–1659.

Ranalli, G. (2000), Westward drift of the lithosphere: not a result of rotational drag, *Geophysical Journal International*, *141*(2), 535–537.

Reilinger, R., S. McClusky, P. Vernant, S. Lawrence, S. Ergintav, R. Cakmak, H. Ozener, F. Kadirov, I. Guliev, R. Stepanyan, et al. (2006), Gps constraints on continental deformation in the africa-arabia-eurasia continental collision zone and implications for the dynamics of plate interactions, *Journal of Geophysical Research: Solid Earth (1978–2012)*, *111*(B5).

Reilinger, R., S. McClusky, D. Paradissis, S. Ergintav, and P. Vernant (2010), Geodetic constraints on the tectonic evolution of the aegean region and strain accumulation along the hellenic subduction zone, *Tectonophysics*, *488*(1), 22–30.

Reynolds, S. D., D. D. Coblentz, and R. R. Hillis (2002), Tectonic forces controlling the regional intraplate stress field in continental australia: Results from new finite element modeling, *Journal of Geophysical Research: Solid Earth (1978–2012)*, *107*(B7), ETG 1–1–ETG 1–15, doi:10.1029/2001JB000408.

Ricard, Y., C. Doglioni, and R. Sabadini (1991), Differential rotation between lithosphere and mantle: A consequence of lateral mantle viscosity variations, *Journal of Geophysical Research: Solid Earth (1978–2012)*, *96*(B5), 8407–8415.

Rietbrock, A., and F. Waldhauser (2004), A narrowly spaced double-seismic zone in the subducting nazca plate, *Geophysical Research Letters*, *31*(10), L10,608.

Riguzzi, F., G. Panza, P. Varga, and C. Doglioni (2010), Can earth's rotation and tidal despinning drive plate tectonics?, *Tectonophysics*, *484*(1), 60–73.

Roda, M., A. M. Marotta, and M. I. Spalla (2011), The effects of the overriding plate thermal state on the slab dip in an ocean-continent subduction system, *Comptes Rendus Geoscience*, *343*(5), 323–330.

Rodríguez-González, J., A. Negredo, P. Petricca, and E. Carminati (2009), Modeling with comsol the interaction between subducting plates and mantle flow, in *COMSOL Conference 2009 Milan*.

Rodríguez-González, J., A. M. Negredo, and M. I. Billen (2012), The role of the overriding plate thermal state on slab dip variability and on the occurrence of flat subduction, *Geochemistry, Geophysics, Geosystems*, *13*(1).

Rontogianni, S. (2010), Comparison of geodetic and seismic strain rates in greece by using a uniform processing approach to campaign gps measurements over the interval 1994–2000, *Journal of Geodynamics*, *50*(5), 381–399.

Rontogianni, S., K. Konstantinou, N. Melis, and C. Evangelidis (2011), Slab stress field in the hellenic subduction zone as inferred from intermediate-depth earthquakes, *Earth Planets Space*, *63*(2), 139–144.

Rovida, A., R. Camassi, P. Gasperini, and M. Stucchi (2011), Cpti11, the 2011 version of the parametric catalogue of italian earthquakes. milano, bologna.

Royden, L. H., and L. Husson (2006), Trench motion, slab geometry and viscous stresses in subduction systems, *Geophysical Journal International*, *167*(2), 881–905.

Ruff, L., and H. Kanamori (1980), Seismicity and the subduction process, *Physics of the Earth and Planetary Interiors*, *23*(3), 240–252.

Ruff, L., and H. Kanamori (1983), Seismic coupling and uncoupling at subduction zones, *Tectonophysics*, *99*(2), 99–117.

Russo, R., and P. Silver (1994), Trench-parallel flow beneath the nazca plate from seismic anisotropy, *Science*, *263*(5150), 1105–1111.

Satake, K., and Y. Tanioka (1999), Sources of tsunami and tsunamigenic earthquakes in subduction zones, in *Seismogenic and Tsunamigenic Processes in Shallow Subduction Zones*, pp. 467–483, Springer.

Savage, M. (1999), Seismic anisotropy and mantle deformation: What have we learned from shear wave splitting?, *Reviews of Geophysics*, *37*(1), 65–106.

Schattner, U. (2010), What triggered the early-to-mid pleistocene tectonic transition across the entire eastern mediterranean?, *Earth and Planetary Science Letters*, *289*(3), 539–548.

Schellart, W. (2005), Influence of the subducting plate velocity on the geometry of the slab and migration of the subduction hinge, *Earth and Planetary Science Letters*, *231*(3), 197–219.

Schellart, W., G. Lister, et al. (2004), Tectonic models for the formation of arc-shaped convergent zones and backarc basins, *Orogenic curvature: integrating paleomagnetic and structural analyses*, pp. 237–258.

Schellart, W., J. Freeman, D. Stegman, L. Moresi, and D. May (2007), Evolution and diversity of subduction zones controlled by slab width, *Nature*, *446*(7133), 308–311.

Schellart, W., D. Stegman, R. Farrington, J. Freeman, and L. Moresi (2010), Cenozoic tectonics of western north america controlled by evolving width of farallon slab, *Science*, *329*(5989), 316–319.

Schellart, W., D. Stegman, R. Farrington, and L. Moresi (2011), Influence of lateral slab edge distance on plate velocity, trench velocity, and subduction partitioning, *Journal of Geophysical Research: Solid Earth (1978–2012)*, *116*(B10).

Scholz, C. H. (2002), *The mechanics of earthquakes and faulting*, Cambridge university press.

Scoppola, B., D. Boccaletti, M. Bevis, E. Carminati, and C. Doglioni (2006), The westward drift of the lithosphere: A rotational drag?, *Geological Society of America Bulletin*, *118*(1-2), 199–209.

Scrocca, D. (2006), Thrust front segmentation induced by differential slab retreat in the apennines (italy), *Terra Nova*, *18*(2), 154–161.

Scrocca, D., E. Carminati, and C. Doglioni (2005), Deep structure of the southern apennines, italy: Thin-skinned or thick-skinned?, *Tectonics*, *24*(3).

Selvaggi, G., and C. Chiarabba (1995), Seismicity and p-wave velocity image of the southern tyrrhenian subduction zone, *Geophysical Journal International*, *121*(3), 818–826.

Seno, T., and Y. Yamanaka (1996), Double seismic zones, compressional deep trench-outer rise events, and superplumes, *Geophysical Monograph Series*, *96*, 347–355.

Serpelloni, E., M. Anzidei, P. Baldi, G. Casula, and A. Galvani (2005), Crustal velocity and strain-rate fields in italy and surrounding regions: New results from the analysis of permanent and non-permanent gps networks, *Geophysical Journal International*, *161*(3), 861–880.

Serpelloni, E., G. Vannucci, S. Pondrelli, A. Argnani, G. Casula, M. Anzidei, P. Baldi, and P. Gasperini (2007), Kinematics of the western africa-eurasia plate boundary from focal mechanisms and gps data, *Geophysical Journal International*, *169*(3), 1180–1200.

Serpelloni, E., R. Bürgmann, M. Anzidei, P. Baldi, B. Mastrolembo Ventura, and E. Boschi (2010), Strain accumulation across the messina straits and kinematics of sicily and calabria from gps data and dislocation modeling, *Earth and Planetary Science Letters*, *298*(3), 347–360.

Shaw, B., and J. Jackson (2010), Earthquake mechanisms and active tectonics of the hellenic subduction zone, *Geophysical Journal International*, *181*(2), 966–984.

Silver, P. G. (1996), Seismic anisotropy beneath the continents: Probing the depths of geology, *Annual Review of Earth and Planetary Sciences*, *24*, 385–432.

Sobolev, S. V., and A. Y. Babeyko (2005), What drives orogeny in the andes?, *Geology*, *33*(8), 617–620.

Sodoudi, F., R. Kind, D. Hatzfeld, K. Priestley, W. Hanka, K. Wylegalla, G. Stavrakakis, A. Vafidis, H.-P. Harjes, and M. Bohnhoff (2006), Lithospheric structure of the aegean obtained from p and s receiver functions, *Journal of Geophysical Research: Solid Earth (1978–2012)*, *111*(B12).

Spada, G., Y. Ricard, and R. Sabadini (1992), Excitation of true polar wander by subduction, *Nature*, *360*(6403), 452–454.

Staudigel, H., and S. D. King (1992), Ultrafast subduction: the key to slab recycling efficiency and mantle differentiation?, *Earth and Planetary Science Letters*, *109*(3), 517–530.

Stegman, D., J. Freeman, W. Schellart, L. Moresi, and D. May (2006), Influence of trench width on subduction hinge retreat rates in 3-d models of slab rollback, *Geochemistry, Geophysics, Geosystems*, *7*(3), Q03,012.

Stein, S., and E. A. Okal (2005), Seismology: Speed and size of the sumatra earthquake, *Nature*, *434*(7033), 581–582.

Steinberger, B., R. Sutherland, and R. O'connell (2004), Prediction of emperor-hawaii seamount locations from a revised model of global plate motion and mantle flow, *Nature*, *430*(6996), 167–173.

Stiros, S. C. (2010), The 8.5+ magnitude, ad365 earthquake in crete: Coastal uplift, topography changes, archaeological and historical signature, *Quaternary International*, *216*(1), 54–63.

Strasser, F., M. Arango, and J. Bommer (2010), Scaling of the source dimensions of interface and intraslab subduction-zone earthquakes with moment magnitude, *Seismological Research Letters*, *81*(6), 941–950.

Suckale, J., S. Rondenay, M. Sachpazi, M. Charalampakis, A. Hosa, and L. Royden (2009), High-resolution seismic imaging of the western hellenic subduction zone using teleseismic scattered waves, *Geophysical Journal International*, *178*(2), 775–791.

Taymaz, T., J. Jackson, and R. Westaway (1990), Earthquake mechanisms in the hellenic trench near crete, *Geophysical Journal International*, *102*(3), 695–731.

Tiberti, M., L. Orlando, D. Di Bucci, M. Bernabini, and M. Parotto (2005), Regional gravity anomaly map and crustal model of the central–southern apennines (italy), *Journal of Geodynamics*, *40*(1), 73–91.

Tondi, E., L. Piccardi, S. Cacon, B. Kontny, and G. Cello (2005), Structural and time constraints for dextral shear along the seismogenic mattinata fault (gargano, southern italy), *Journal of Geodynamics*, *40*(2), 134–152.

Torii, Y., and S. Yoshioka (2007), Physical conditions producing slab stagnation: Constraints of the clapeyron slope, mantle viscosity, trench retreat, and dip angles, *Tectonophysics*, *445*(3), 200–209.

Turcotte, D., and E. Oxburgh (1967), Finite amplitude convective cells and continental drift, *J. Fluid Mech*, *28*(1), 29–42.

Uyeda, S. (1981), Subduction zones and back arc basins—a review, *Geologische Rundschau*, *70*(2), 552–569.

Uyeda, S., and H. Kanamori (1979), Back-arc opening and the mode of subduction, *Journal of Geophysical Research: Solid Earth (1978–2012)*, *84*(B3), 1049–1061.

van der Hilst, R. (1995), Complex morphology of subducted lithosphere in the mantle beneath the tonga trench, *Nature*, *374*, 154–157.

van der Hilst, R., and T. Seno (1993), Effects of relative plate motion on the deep structure and penetration depth of slabs below the izu-bonin and mariana island arcs, *Earth and Planetary Science Letters*, *120*(3), 395–407.

van der Hilst, R. D., S. Widiyantoro, and E. R. Engdahl (1997), Evidence for deep mantle circulation from global tomography, *Nature*, *386*, 578–584.

Van Dijk, J., M. Bello, G. Brancaleoni, G. Cantarella, V. Costa, A. Frixa, F. Golfetto, S. Merlini, M. Riva, S. Torricelli, et al. (2000), A regional structural model for the northern sector of the calabrian arc (southern italy), *Tectonophysics*, *324*(4), 267–320.

van Hunen, J., and A. P. van den Berg (2004), Various mechanisms to induce shallow flat subduction: a numerical parameter study, *Physics of the Earth and Planetary Interiors*, *146*, 179–194.

van Hunen, J., A. P. van den Berg, and N. J. Vlaar (2000), A thermo-mechanical model of horizontal subduction below an overriding plate, *Earth and Planetary Science Letters*, *182*(2), 157–169.

Vassiliou, M., and B. Hager (1988), Subduction zone earthquakes and stress in slabs, *Pure and Applied Geophysics*, *128*(3), 547–624.

Vidal, N., J. Alvarez-Marrón, and D. Klaeschen (2000), The structure of the africa-anatolia plate boundary in the eastern mediterranean, *Tectonics*, *19*(4), 723–739.

Vogt, P. (1973), Subduction and aseismic ridges, *Nature*, *220*, 189–191.

Wada, I., K. Wang, J. He, and R. D. Hyndman (2008), Weakening of the subduction interface and its effects on surface heat flow, slab dehydration, and mantle wedge serpentinization, *Journal of Geophysical Research: Solid Earth (1978–2012)*, *113*(B4).

Wdowinski, S., Z. Ben-Avraham, R. Arvidsson, and G. Ekström (2006), Seismotectonics of the cyprian arc, *Geophysical Journal International*, *164*(1), 176–181.

Wegener, A., and J. G. A. Skerl (1922), *The origin of continents and oceans*, Dutton.

Westaway, R. (1990), Present-day kinematics of the plate boundary zone between africa and europe, from the azores to the aegean, *Earth and Planetary Science Letters*, *96*(3), 393–406.

Whittaker, A., M. Bott, and G. Waghorn (1992), Stresses and plate boundary forces associated with subduction plate margins, *Journal of Geophysical Research: Solid Earth (1978–2012)*, *97*(B8), 11,933–11.

Widiyantoro, S., B. Kennett, and R. Van Der Hilst (1999), Seismic tomography with p and s data reveals lateral variations in the rigidity of deep slabs, *Earth and Planetary Science Letters*, *173*(1), 91–100.

Williams, C. A., and R. M. Richardson (1991), A rheologically layered three-dimensional model of the san andreas fault in central and southern california, *Journal of Geophysical Research: Solid Earth (1978–2012)*, *96*(B10), 16,597–16.

Wortel, M., and W. Spakman (2000), Subduction and slab detachment in the mediterranean-carpathian region, *Science*, *290*(5498), 1910–1917.

Wüstefeld, A., G. Bokelmann, G. Barruol, and J.-P. Montagner (2009), Identifying global seismic anisotropy patterns by correlating shear-wave splitting and surface-wave data, *Physics of the Earth and Planetary Interiors*, *176*(3), 198–212.

Yem, L. M., L. Camera, J. Mascle, and A. Ribodetti (2011), Seismic stratigraphy and deformational styles of the offshore cyrenaica (libya) and bordering mediterranean ridge, *Geophysical Journal International*, *185*(1), 65–77.

Zappaterra, E. (1994), Source-rock distribution model of the periadriatic region, *AAPG bulletin*, *78*(3), 333–354.

Zhong, S. (2001), Role of ocean-continent contrast and continental keels on plate motion, net rotation of lithosphere, and the geoid, *Journal of Geophysical Research: Solid Earth (1978–2012)*, *106*(B1), 703–712.

Zhong, S., and G. F. Davies (1999), Effects of plate and slab viscosities on geoid, *Earth and Planetary Science Letters*, *170*, 487–496.

Zhong, S., and M. Gurnis (1994), Controls on trench topography from dynamic models of subducted slabs, *Journal of Geophysical Research: Solid Earth (1978–2012)*, *99*(B8), 15,683–15.

Zhong, S., and M. Gurnis (1995), Mantle convection with plates and mobile, faulted plate margins, *Science*, *267*(5199), 838–843.

Zhong, S., M. Gurnis, and L. Moresi (1998), Role of faults, nonlinear rheology, and viscosity structure in generating plates from instantaneous mantle flow models, *Journal of Geophysical Research: Solid Earth (1978–2012)*, *103*(B7), 15,255–15,268.

Zhou, H.-W., and R. W. Clayton (1990), P and s wave travel time inversions for subducting slab under the island arcs of the northwest pacific, *Journal of Geophysical Research: Solid Earth (1978–2012)*, *95*(B5), 6829–6851.

Zhu, G., T. V. Gerya, D. A. Yuen, S. Honda, T. Yoshida, and J. A. Connolly (2009), Three-dimensional dynamics of hydrous thermal-chemical plumes in oceanic subduction zones, *Geochemistry, Geophysics, Geosystems*, *10*(11).